Microstructural Evolution of Austenite in a Microalloyed Fe30%Ni Alloy

Martin Peter Black

Thesis Submitted for the Degree of Doctor of Philosophy

Department of Engineering Materials

July 2002

ABSTRACT

The study of the physical metallurgy of microalloyed steels has been an important field of research for nearly forty years. During this time the hot working characteristics have been comprehensively investigated, simulated and modelled. Unfortunately, the actual microstructural behaviour during hot working cannot be followed completely due to the unavoidable phase transformation of these steels upon cooling. This transformation prohibits direct study of the deformed austenite, by disordering the dislocation structures developed during hot working.

In order to avoid the problem of transformation, a model alloy has been developed. This allows the retention of the austenitic structure to room temperature, while retaining similar thermodynamic and deformational properties to conventional microalloyed steels. The alloy was based on a matrix of iron with 30wt.% nickel, and niobium and carbon additions to the level of 0.1% and 0.09% respectively. The use of such an alloy to simulate the hot working behaviour of traditional microalloyed steels means that the study of softening and precipitation events in the austenite matrix is possible as the phase transformation is avoided.

The Fe-30%Ni-Nb alloy has undergone thermomechanical processing. Hot plane strain compression tests have been carried out in order to study the precipitation kinetics. Before testing, the material was solution treated at 1250°C to allow supersaturation of the niobium at lower temperatures. Double-deformation plane strain compression testing has been carried out over a range of temperatures (900-1050°C) at a strain rate of $10s^{-1}$ and with delay times between deformations varying from 1s to 1000s. This testing has allowed the study of both the static precipitation and recrystallisation kinetics from the resulting flow stress behaviour. Precipitation has been evident from the stress-strain curves.

Transmission electron microscopy of thin foils of the hot-worked material has been completed to investigate the dislocation structures produced. This shows the presence of a microbanded substructure. The particle populations have been studied using conventional transmission electron microscopy. Direct observation of particles precipitated in the austenite matrix has been achieved by electron spectroscopic imaging studies of the as-deformed material. This is important, as it shows preferential precipitation upon the dislocation structure, and not within the matrix.

The overall study shows that the iron-nickel alloy is a good model austenite in many respects. It has similar hot-working characteristics: deformation behaviour, work hardening response, and recrystallisation behaviour. The present work also reports similar NbC precipitation behaviour to that found in conventional C-Mn based microalloyed steels. It appears that the alloy is an excellent model for microalloyed austenite under hot-working conditions, and should prove to be a valuable material for future investigations.

Acknowledgements

The author is indebted to the Engineering and Physical Science Research Council (EPSRC), Corus (Research and Technology) and the Institute for Microstructural and Mechanical Process Engineering: the University of Sheffield (IMMPETUS) for financial support of the project.

Grateful acknowledgement is given for the encouragement and advice offered by Mark Rainforth, Eric Palmiere, Becky Higginson, Ruth Prentice, Andy Lacey, Peter Morris, John Whiteman and Mike Sellars.

Thanks must also go to my girlfriend Joanne who has provided support and shown much patience during the time taken to complete this work.

1. INTRODUCTION

2. LITERATURE REVIEW

2.1. Microalloyed Steels

2.1.1. Yield Strength and Strengthening Mechanisms
2.1.1.1. Solid Solution Strengthening
2.1.1.2. Grain Size Strengthening
2.1.1.3. Precipitation (Dispersion) Strengthening
2.1.2. Impact Toughness

2.2. Chemical metallurgy of precipitation

2.2.1. Niobium Carbonitride Particles
2.2.2. Solid Solutions and Solution Thermodynamics
2.2.2.1. Solubility Products
2.2.2.2. Solution Kinetics
2.2.3. Precipitation
2.2.3.1. Nucleation of Precipitation
2.2.3.2. Particle Coarsening
2.2.3.3. Quantification of Precipitation and Particle Size
2.2.3.4. Particle Morphologies
2.2.4. Precipitation Kinetics
2.2.4.1. Modelling of Precipitation Behaviour
2.2.4.2. Effect of Other Elements on Precipitation Kinetics

2.3. Microstructural Evolution of the Austenite Matrix During Hot Working

2.3.1. Deformation
2.3.1.1. Deformation Structures
2.3.1.2. Work Hardening
2.3.1.3. Stacking Fault Energy
2.3.2. Recovery
2.3.3. Static Recrystallisation
2.3.3.1 Nucleation of Recrystallisation
2.3.3.2. Nucleus Growth
2.3.3.3. Recrystallisation Kinetics
2.3.3.4. Recrystallised Grain Size
2.3.4. Solute Drag
2.3.5. Particle Pinning
2.3.6. Precipitation-Recrystallisation Interaction
2.3.7. Grain Growth

2.4. Iron-Nickel alloys

2.4.1. The Iron-Nickel System
2.4.2. Suitability as a Model Austenite
2.4.2.1. Hot Working Characteristics
2.4.2.2. Effects of Nickel Addition on the Solubility of Micro-alloy Elements

2.5. Mechanical Testing and Hot Working

2.5.1. Hot Rolling Practices
2.5.2. PSC Testing as a Simulation of Hot Rolling.

3. OVERVIEW

4. EXPERIMENTAL PROCEDURE

4.1. Received material and pre-treatment
4.1.1. Material
4.1.2. Pre-treatment

4.2. Deformation Testing
4.2.1. Test apparatus and control system
4.2.2. PSC Specimens
4.2.3. Test conditions
4.2.4. Data Recording and Flow Curves
4.2.5. Fractional Softening Data
4.2.6. Reheating Simulation

4.3. Optical metallography
4.3.1. Samples
4.3.2. Etchants
4.3.3. Volume Fraction Measurement
4.3.4. Grain Size Measurement

4.4. Electron Microscopy
4.4.1. Samples
4.4.1.1. Carbon Replicas
4.4.1.2. Thin Foils
4.4.2. Microscope Operation
4.4.3. Quantitative Metallography
4.4.3.1. Sample Area
4.4.3.2. Particle Size Distribution, Volume Fraction and Spacing
4.4.3.3. Subgrain size

4.5. Phase Identification: X-ray Diffraction

4.6. Hardness Testing

4.7. Spectroscopic Imaging in Graz

5. RESULTS

5.1. Phases Present

5.2. Plane Strain Compression Testing
5.2.1. Homogeneity of Deformation
5.2.2. Flow Curves
5.2.3. Temperature Data
5.2.3.1. Quench
5.2.3.2. Deformational Heating

5.3. Fractional Softening Curves

1. INTRODUCTION

Customers are increasingly demanding steel that combines high yield strength, a low impact transition temperature (ITT), and good weldability. To optimise these properties, microalloy additions are made to modify microstructural development during hot working. This involves addition of small amounts of the carbide and nitride forming elements: niobium, titanium and vanadium. The result is a uniform fine-grained microstructure giving improved mechanical properties, while the small amounts of alloy added coupled with low carbon contents means that weldability is retained. Commercial steels may have more than one microalloy element added, e.g. Nb + V, but this research will be concerned chiefly with Nb-steels.

With appropriate thermomechanical cycles, niobium in solution can precipitate out in steel, and this is of particular importance during finishing. The composition of such precipitate particles can vary, and depends on a number of factors. The particles found are generally carbides, nitrides, or of compositions between these extremes: carbonitrides.

Niobium microalloyed steels are ferritic at room temperature but are hot worked in the austenite phase field, with processing generally carried out by hot rolling. Before rolling, such steels are first reheated to a high temperature to bring about maximum dissolution of the niobium, which is then available for precipitation at a later stage of processing. The improvement in properties in niobium steels is achieved by one of two controlled rolling processes used to condition the austenite, both of which are established commercial practice. The addition of niobium brings about grain refinement, precipitation hardening, and solid solution hardening effects, depending upon the

processing conditions. The desired microstructure can be gained by conventional controlled rolling, often with large strains below 900°C, where niobium carbonitrides precipitate on the austenite dislocation structure. The presence of such fine-scale particles can pin migrating boundaries, thus retarding recrystallisation and allowing deformation of the austenite grains, or 'pancaking' to occur. This leads to a heavily worked microstructure, with a large grain boundary area, from which a fine ferrite grain size can be obtained upon transformation. Alternatively, improved properties can also be obtained by allowing no precipitation during rolling, whereby full precipitation can occur in the ferrite to give maximum dispersion strengthening in a process known as recrystallisation controlled rolling. Recrystallisation controlled rolling involves rolling at higher temperatures, where full recrystallisation occurs between passes.

Thus, the kinetics and thermodynamics of solution and precipitation are of great significance. The solubility of niobium carbonitride increases with temperature, but also depends on the particle size distribution, as small particles tend to dissolve more quickly. There are a great number of publications concerning the solubility of niobium carbide and niobium carbonitride in austenite, and there is great variance between these publications, although the most cited is that of Irvine *et* al. (1968). Such data are usually presented as a solubility product, from which one can calculate the absolute dissolution temperature or the amount of niobium taken into solution at a particular temperature. Once dissolved, niobium can precipitate out onto the dislocation structure at lower temperature. On cooling from the reheat temperature to the deformation temperature, a supersaturation of niobium exists, as the solubility is lower at the cooler temperature. A large supersaturation gives a greater potential for strain-induced precipitation.

In an attempt to accurately forecast mill loads and predict product properties, modelling of the deformation process is carried out. A model of hot deformation based on physical metallurgy would need to incorporate all of the factors that affect the state of the microstructure. Microstructural change occurs during hot working through the combined action of work hardening, recovery, recrystallisation, grain growth, solute drag, and strain-induced precipitation. The levels to which each of these processes affect the material depend upon the material and processing variables: chemical composition, strain, rate of strain, reheat conditions, deformation temperature, on interpass times between subsequent deformations, and on the cooling schedule. While many authors have considered these principles of microstructural behaviour separately, few integrated models have been put forward. Those that have [e.g. Beynon and Sellars 1992, Hodgson and Gibbs 1992], generally predict some elements of the overall behaviour successfully, while other elements are predicted less well, and can depend heavily on the exact steel chemistry.

A major problem with unified metallurgical models is that they are based on microstructural studies of transformed (non-austenitic) steels. Steels are deformed in the austenite phase field, and the microstructure transforms to ferrite and/or bainite on cooling, where the transformation disorders the dislocation structures seen in microalloyed steels. This is a problem because direct observation of the hot worked microstructure is not possible. Optical studies can reveal the prior austenite structure with reasonable success, but TEM studies are limited as the dislocation structure is thoroughly rearranged. Knowledge of the distribution of the microalloy particles with regard to the deformed austenite dislocation structure is crucial to the understanding upon which a model for the microstructural evolution of microalloyed steels can be based.

Of the methods to look directly at deformed austenite microstructure, perhaps stabilised austenite is the most attractive solution. The addition of nickel to the iron matrix increases the size of the austenite phase field, by suppression of the Ar_3 temperature. With alloy additions in excess of ~28%, nickel forms a solid solution with iron and the austenite is stable at room temperature [Swartzendruber 1991]. This means that such alloys can be worked in the austenitic state, then quenched and observed while still in the austenitic state. This allows a direct microstructural characterisation of worked austenite. If microalloying elements are added to the Fe-Ni matrix, then the detailed study of strain-induced precipitation can be carried out. The Fe-30%Ni alloys have been the subject of many recent studies by the Institute for Mechanical and Microstructural Process Engineering: The University of Sheffield (IMMPETUS) group [e.g. Almaguer *et al.* 2001, Black *et al.* 2001, Higginson *et al.* 2001]. Other model alloys which have been used include Ni-30Fe to study the deformation of austenite [Hurley *et al.* 1998], and austenitic stainless steel to look at niobium carbonitride precipitation in austenite [e.g. Van Aswegen *et al.* 1964].

To form the basis of this research an extensive literature review has been carried out, and is presented in chapter two. In the literature review, it is first necessary to consider the important properties and the strengthening mechanisms operating in microalloyed steels. The chemical metallurgy of niobium carbides and carbonitrides is then given some attention. The physical metallurgy of the hot working of microalloyed steels is considered, then there are sections concerning iron-nickel austenites, mechanical testing and industrial thermomechanical processing practices. Chapter three is an overview of the work carried out, chapter four covers the experimental procedure used during plane strain compression testing and optical/transmission electron microscopy analysis, while the test results are given in chapter five. Chapter six is the discussion of the results

obtained, and of how these compare with the literature. The main emphasis in the discussion is of the precipitation of niobium carbonitrides during simulated plate finish rolling, and of the deformed austenite microstructure, and on the overall performance of the iron-nickel alloy as a model austenite.

2. LITERATURE REVIEW

2.1. Microalloyed Steels

2.1.1. Yield Strength and Strengthening Mechanisms

The strength of steels depends on a number of factors, and all of these factors are based on their ability to impede dislocation motion. As will be discussed later (section 2.3.1.2), work hardening has a large influence on strength. As a material is worked, more dislocations are introduced, which makes further deformation difficult. Thus, work hardening increases the yield strength of the material. Other hardening mechanisms affect the strength of microalloyed steels: solid solution strengthening, grain size control, and dispersion strengthening. The overall strength of a material is a sum of all of these contributing factors. Figure 2.1 shows the strengthening increments attributable to these different mechanisms for a vanadium microalloyed steel [Gladman 1977].

2.1.1.1. Solid Solution Strengthening

The addition of solute elements to the iron matrix brings about strengthening by increasing resistance to dislocation motion. As solutes are introduced to the iron matrix, the lattice becomes elastically distorted, making dislocation motion more difficult. Strength increases with the size difference between the iron atoms and the solute atoms. This means that both smaller atoms (e.g. C and N) and larger atoms (Nb) have a substantial effect upon the strength of steel, while solute additions with a similar atomic radius to Fe, such as Ni, have little affect upon strength. This is emphasised by the plot shown in Figure 2.2 [Pickering 1977]. Strengthening effects can occur together, and Baker (1980) considered the various strength contributions in operation in a niobium microalloyed steel to suggest an equation for the yield strength of hot worked material:

$$\sigma_y = \sigma_0 + \sigma_{ss} + k_y d^{-1/2} + k_s \delta^{-1/2} + \frac{\sigma_p + \sigma_d}{2},$$

(2.1)

where σ_0 is the friction stress, σ_{ss} is the solid solution strengthening, d the grain size, δ is the subgrain size, σ_d is the dislocation strengthening, σ_p is the precipitation strengthening and k_y and k_s are material constants.

2.1.1.2. Grain Size Strengthening

Grain boundaries provide effective barriers to dislocation motion; thus, the increased number of grain boundaries associated with fine grain sizes contributes strengthening to a material. Decreased grain size also gives better brittle fracture resistance. The relation between grain size (*d*) and flow stress (σ_y) was first found empirically by Hall (1951) and Petch (1953):

$$\sigma_y = \sigma_0 + k_y d^{-1/2},$$

(2.2)

where σ_0 is the friction stress that opposes dislocation motion and k_y is the 'unpinning constant'. This equation is known as the Hall-Petch equation, and predicts increased strength with decreased grain size. Such a relation has been seen in many materials under a wide range of processing conditions.

Subgrain strengthening has been detected in ferrite for deformation at lower temperatures [Tanaka *et al.* 1977]. Košík *et al.* (1971) proposed a modified Hall-Petch type relationship for the effect of hot-worked subgrain size (δ) on room temperature strength:

$$\sigma = \sigma_0 + k_y d^{-1/2} + k_s \delta^{-m},$$

(2.3)

where k_s is a constant and m was found to be the order of unity. Mangonon and Heitmann (1977) looked at subgrain strengthening in plain carbon and microalloyed ferrite following hot working, but found a $\delta^{-1/2}$ relation. Most subgrain strengthening work has been in the ferritic state – little work exists for subgrain strengthening in austenite. Fritzmeier *et al.* (1979) looked at subgrain size in stainless steels, concluding that the flow stress was inversely related to subgrain diameter.

2.1.1.3. Precipitation (Dispersion) Strengthening

Morrison and Woodhead (1963) found a strength increase in excess of that expected from grain refinement in Nb-added steels when compared with niobium-free steels and they attributed this to precipitation hardening. The presence of a dispersion of fine second phase particles can have a drastic effect on mechanical properties. Particles hinder dislocation motion, thus causing a strength increase. Dislocations can cut through coherent particles as they move through the material, while they can loop around larger or incoherent particles. These mechanisms both cause strengthening as greater force is required to move the dislocation through the material: see Gladman (1999) for a recent review.

Quantification of precipitation hardening was first successfully considered by Orowan (1948) who derived an equation for strengthening based on dislocation-particle interaction:

$$\Delta\tau_y = \frac{Gb}{\lambda},$$

(2.4)

where $\Delta\tau_y$ is the increase in yield stress due to particles, G is the elastic shear modulus, **b** is the magnitude of the Burgers vector, and λ is the interparticle spacing. This work was built on by Ashby (1966) to give what is known as the Ashby-Orowan equation, which gives the precipitation hardening increment, $\Delta\sigma_y$:

$$\Delta\sigma_y = \frac{0.13Gb}{\lambda}\ln\frac{r}{b},$$

(2.5)

where r is the particle radius. Gladman (1997) applied this equation to precipitation in microalloyed steels, to give an equation for the precipitation hardening increment, $\Delta\sigma_y$ [Gladman 1999] dependent on particle volume fraction, f_V:

$$\Delta\sigma_y = 0.538Gb\frac{\sqrt{f_V}}{X}\ln\frac{X}{2b},$$

(2.6)

where X is the (three-dimensional) particle diameter. This equation predicts the hardening increment for small particles in the low volume fractions seen in niobium steels. Hardening has a square root relation with particle volume fraction. Gladman also proposed an equation for the condition for maximum hardening (cutting vs. looping) at a critical radius, r_{crit}:

$$r_{crit} = \frac{b}{4\varepsilon}$$

(2.7)

where ε is the misfit strain in a coherent lattice. Evidence of hardening due to precipitation in austenite has been detected by the use of double deformation tests [Kwon and DeArdo 1991, Black *et al.* 2000].

2.1.2. Impact Toughness

Ferritic materials (e.g. mild steel) show a transition from ductile to brittle fracture over a temperature range. Below one critical temperature, such as the impact transition temperature (ITT), such materials show very low energy absorption and display brittle cleavage fracture. Above the ITT, the material shows much greater toughness, and fracture is ductile in nature. The ITT is dependent on composition and grain size. In Nb-microalloyed steels, fine Nb(C,N) precipitates form, providing increased strength by dispersion strengthening, these particles also retard grain growth giving a fine grain size, and can therefore help to improve impact properties.

2.2. Chemical metallurgy of precipitation

Precipitation in microalloyed steels involves a reaction whereby a new phase is formed in the lattice of the steel. Such a reaction can occur when a supersaturated solid solution exists, e.g. during cooling. In niobium steels, the precipitation reaction involves solute niobium, which can combine with carbon and/or nitrogen to precipitate niobium carbides, nitrides and carbonitrides, depending on the steel chemistry. Other metal elements present in solid solution (especially titanium) can combine with the niobium to form more complex precipitates.

The amount of an element in solution is governed chiefly by the temperature, as at higher temperatures, solubility is increased. The amount of a compound in solution at a particular temperature is given by the solubility product, which predicts solubility in

relation to the temperature. While the temperature can provide the thermodynamic driving force for dissolution/precipitation, it is the time at temperature that determines whether these processes can proceed, thus the kinetics must also be considered.

Precipitation is a nucleation and growth process. Nucleation occurs within the iron lattice on sites of high local energy. The precipitation kinetics are of interest as the onset of precipitation can be fairly rapid at hot working temperatures, and can occur within the time available between rolling passes. The growth of precipitate particles occurs at high temperature, and is governed by diffusion. As particles increase in size their boundary pinning potency decreases.

2.2.1. Niobium Carbonitride Particles

Figure 2.3 shows the phase diagram for the niobium-carbon system. This shows that the NbC phase exists from approximately 35at.%C to 50at.%C, and from 50-100at.%C in equilibrium with graphite. This γ-niobium carbide has the NaCl type face-centred cubic (FCC) crystal structure, where the Nb atoms sit in the regular FCC lattice, with the C (or N in a carbonitride) in the octahedral interstices. NbC has the lattice parameter of 0.447nm in pure, stoichiometric form. In reality, the stoichiometric NbC phase is not always present, and it has been suggested that niobium carbide is carbon deficient [Nordberg and Aronsson 1968], and that $Nb_{0.87}C$ is the 'average' composition of niobium carbides. Storms and Krikorian (1960) considered the lattice parameter of NbC_x and found that as x decreases, so does the lattice parameter. The compositions seen are further complicated by the presence of nitrogen. NbC and NbN can exist together, are mutually soluble [DeArdo 1984], and are of similar lattice parameter, hence the ternary Nb(C,N) can be thought of. Figure 2.4 shows the niobium-nitrogen phase diagram. This is more complex than the Nb-C phase diagram, with many different

phases existing. NbN occurs at 50at.% nitrogen, while the NbN phase field exists from ~42-51at.% nitrogen. Thus NbN is typically niobium rich. Pure niobium nitride is rarely seen in microalloyed steels, due to the high carbon : nitrogen ratios which are used. The stoichiometry affects the lattice parameter of niobium carbonitride, which varies from 0.447nm for the pure carbide to 0.438nm for the pure nitride, and is also reduced as the vacancy concentration increases. It is of note that the lattice parameter is well in excess of that of austenite (~0.358nm), and there is a mismatch of 22-25%.

As stoichiometry is not always the case, so nomenclature in the literature varies. Niobium carbides, nitrides and carbonitrides have been known as NbC, NbN, Nb(C,N), NbC_x, NbN_y, $Nb(C,N)_z$, NbC_xN_{1-x}, NbC_XN_Y depending on actual composition and the deviance from stoichiometry. The composition of niobium precipitates in steels depends on the relative concentration of nitrogen and carbon present. Nordberg and Aronsson (1968) reported that a C:N ratio of less than ~5 gives a carbonitride precipitate rather than a carbide. Narita (1975) suggested a composition NbC_xN_{1-x}, and found that increased niobium content increases x, increased carbon increases x, and increased nitrogen decreases x. The stoichiometric ratio of niobium : carbon is 1:8 (atomic weights 93 and 12), but often more niobium is added to steels to allow some niobium to remain in solution. Precipitate particles can also contain other metallic elements such as Ti, Mo and Al, and these complicate matters further [Poths *et al.* 2001, Higginson *et al.* 2001].

2.2.2. Solid Solutions and Solution Thermodynamics

Following primary production, niobium exists in steels as carbides, nitrides, and carbonitrides. To be useful, these have to be dissolved during reheating and taken into solid solution before rolling to allow controlled precipitation. The amount of solute in

steels depends on the temperature and on the crystal structure. In steels, carbon is the crucial element. In austenite up to around 2.0% carbon is soluble at 1150°C, while carbon has very low levels of solubility in ferrite (0.024% at 723°C). For the reheating and hot working practices considered in the present work, the austenite phase is the only one of interest, and it is the solubility of solutes in austenite which is of primary concern.

2.2.2.1. Solubility Products

Compounds have limited solubility in the iron matrix, and a solubility product describes the solubility of a compound. For example, consider the dissolution reaction of a compound XY in the iron matrix into its soluble components: $XY \Leftrightarrow [X]+[Y]$. There is a temperature dependent limit on the amount of X and Y in solution, the remainder exists as the compound XY. The mathematical description of the boundary condition (k_s, the solubility product) is of the form:

$$\log k_s = \log[X][Y] = \frac{A}{T} + B \tag{2.8}$$

where A and B are constants, [X] and [Y] are the solute concentration of species X and Y, and T is the absolute temperature. A typical solubility relation is plotted in Figure 2.5. Such equations can be used to calculate both the outright solution temperature, and the amount of an element in solution at a particular temperature, based on compositional data. Many equations of this form exist for different stoichiometries of niobium carbides and nitrides, and are tabulated according to their chemistries in Tables 2.1-2.3 for NbC, NbN, and Nb(C,N) respectively. The corresponding plots are shown in Figures 2.6-2.8, which allow a comparison between the different solubility products found in the

literature. Probably the most often cited solubility product is that suggested by Irvine *et al.* (1967).

Hoogendorn and Spanraft (1977) found that the solution temperature of Nb(C,N) has a strong dependence on steel chemistry, in that strong nitride formers (Ti, V, Al) can affect the solubility. The solubility relations can also be amended for the presence of other components, for example, for mixed metal carbides, nitrides and carbonitrides, see Rios (1998) and Xiaodong *et al.* (1994). The effects of substitutional alloying elements used in microalloyed steels (Mn, Cr, Ni, Si, Mo) on the solubility of niobium carbide and carbonitride have been summarised by Sharma *et al.* (1984).

Solute dissolved at higher temperatures (i.e. during reheating) is available for precipitation at lower temperatures (i.e. during rolling or $\gamma \rightarrow \alpha$ transformation). The 'precipitation potential' in niobium microalloyed steels can be measured by the supersaturation. This quantity is the difference between the amount of soluble niobium at the reheating temperature and the amount of soluble niobium at the deformation temperature. The supersaturation provides the thermodynamic driving force for the precipitation reaction to occur.

2.2.2.2. Solution Kinetics

There is considerably less published work on solution kinetics than there is on the solution temperature of carbonitrides in microalloyed steels. In industry, the solution time is not so important, as long soak times are often used, ensuring maximum dissolution - the long soak times used approach equilibrium. During reheating, both the time and particle size is important. Small particles tend to dissolve more quickly, and at lower temperatures than larger ones, while reprecipitation can occur causing the larger particles present to coarsen (Østwald ripening); although at higher temperatures even

the largest particles are dissolved [Sellars 1986]. Thus, dissolution and particle coarsening can occur concurrently during reheating. Early work considered particle dissolution in the matrix as a reversal of coarsening [Whelan 1969]. A later piece of work was published by Liu *et al.* (1993), who produced a mathematical model for particle size during reheating, based on diffusion controlled growth. This was interesting because it gave particle size distribution and interparticle spacing data during reheating. Recently Cheng *et al.* (2000) reconsidered dissolution theory and put forward a combined dissolution and coarsening model. This model considers particles in the matrix, but also considers precipitates on grain boundaries, where enhanced grain boundary diffusivity exists. This model was applied to AlN particle populations in steels, with good general agreement. The model is also applicable to Nb–containing particles, and gives the growth/dissolution rate of the particle radius, r with time, t as:

$$\frac{dr}{dt} = -k\left[\frac{D}{r} + \frac{\delta D_b}{4r^2} + \left(\frac{D\delta D_b}{r^2 d_0}\right)^{\frac{1}{2}} + \left(\frac{D_b}{\pi t}\right)^{\frac{1}{2}}\right], \tag{2.9}$$

where δ is the grain boundary thickness, D is the bulk matrix diffusivity, D_b is the grain boundary diffusivity, d_0 is the mean grain diameter, and k is given by:

$$k = \frac{C_I - C_M}{C_P - C_I}, \tag{2.10}$$

where C_I is the solute concentration in the matrix at the interface, C_M is the solute concentration in the matrix, and C_P is the solute concentration in the precipitate. Thus dissolution depends on the niobium level, temperature, time available, and also the starting particle size population.

2.2.3. Precipitation

Nucleation of precipitation involves the formation of a stable nucleus within the austenite microstructure. Once formed, the stable nuclei can grow by diffusion. The knowledge of the extent of precipitation and the particle size distribution is important in order to predict the final steel microstructure.

2.2.3.1. Nucleation of Precipitation

For precipitation to occur there needs to be a driving force for nucleation. An overall thermodynamic driving force is provided by temperature change - as the steel cools, Nb solubility is reduced, thus increasing the supersaturation. The thermodynamic driving force varies throughout the microstructure. Local high-energy sites are preferential for nucleation, as their associated energy can be reduced by particle formation. Such high-energy sites include deformation bands, grain boundaries and subgrain boundaries.

During deformation, a dense dislocation network is introduced to the microstructure, and precipitation occurs preferentially upon this. However, many different types of nucleation site for the precipitation of Nb(C,N) in austenite have been observed. These were summarised by Honeycombe (1981). The sites were ranked in order of the likelihood of precipitation as follows: grain boundary nucleation – dislocation nucleation – stacking fault nucleation – matrix nucleation. The relative frequency with which these sites nucleate depends on a number of factors. Grain boundary and dislocation nucleation is likely to occur most often as these sites have high energy associated with them, and can provide vacancies to take up the strain to accommodate the particle as it grows. At grain boundaries and dislocations, diffusion rates are faster,

providing good conditions for growth of the nucleating particle. Stacking fault precipitation is unlikely in austenites, unless they are of very low stacking fault energy (e.g. austenitic stainless steels). Matrix precipitation occurs only when two conditions are met – there is a large excess of supersaturated niobium and insufficient grain boundary/dislocation sites are available. Thus, matrix precipitation can be expected with high Nb solute levels, and the lack of a substantial dislocation structure. Honeycombe (1981) reported that matrix precipitation occurs upon solute atom/vacancy clusters, and only where a high number of vacancies were present (e.g. following quenching).

Kestenbach et al. (1989), using some high niobium steels, found that precipitation in unstrained austenite was confined to grain boundaries, while strain-induced precipitation occurred at deformation temperatures less than 1010°C on subgrain boundaries. Ramaswany and West (1970a,b) looked at precipitate nucleation sites in unstrained and lightly strained 20%Cr-25%Ni-1%Nb austenite. They found matrix precipitation, stacking fault precipitation and precipitation on dislocations in unstrained austenite. With a strain of 10%, no stacking fault precipitation was seen and precipitation occurred primarily on the dislocations formed during deformation.

Both static precipitation and dynamic precipitation have been reported in niobium microalloyed steels. Dynamic precipitation has only been seen at very low strain rates [e.g. Weiss and Jonas 1980], and is unlikely to happen at non-laboratory strain rates due to the limited diffusivity of niobium in austenite.

2.2.3.2. Particle Coarsening

The coarsening of particles is controlled by the diffusion of the slowest moving atomic species. In the case of niobium carbides and carbonitrides, the growth therefore depends

on the rate of niobium diffusion. In austenite at 1250°C, the rate of niobium diffusion is 8.0×10^{-14} m^2s^{-1}, while that of carbon is 2.2×10^{-10} m^2s^{-1} and nitrogen is 1.5×10^{-10} m^2s^{-1} (calculations made from data in Smithell's Metals Reference Book 1983). The particle growth kinetics are described by an equation by Lifshitz and Slyozov (1961):

$$r_t^3 - r_0^3 = \frac{8V_m D\gamma C^S}{9RT} t \qquad (2.11)$$

where r_0 is the mean particle radius at time zero, r_t is the mean particle radius at time t, D is the diffusion coefficient of the solute (Nb) in the matrix, γ is the interfacial energy of the particle/matrix interface, V_m is the molar volume of the precipitate, and C^S is the concentration of the saturated solution. This equation describes particle growth as a function of time.

Relations as those described by Equation 2.11 are actually for bulk diffusion, and show $t^{1/3}$ kinetics. Particles precipitated upon grain boundaries and dislocation structures can undergo enhanced growth. These sites have higher defect concentrations and provide high diffusivity paths; thus, particles situated on such sites can grow faster than particles precipitated in the matrix. Diffusion along high angle grain boundaries was calculated to give $t^{1/4}$ kinetics by Ardell (1972). Ardell also discussed the findings of Kreye (1970) that suggested that diffusion along low angle grain boundaries (dislocation boundaries) was shown to have $t^{1/5}$ kinetics. The $t^{1/5}$ kinetics were found for very small particles only, where they were smaller than the dislocation spacing in the LAGBs, and as the particles grow they revert to $t^{1/4}$ coarsening kinetics.

2.2.3.3. Quantification of Precipitation and Particle Size

There have been several methods used to determine the extent (volume fraction) of precipitation in niobium microalloyed steels. These can be broken down into three groups – electron microscopy, the measurement of physical properties, and actual particle extraction and analysis.

The microscopy of fine particles can be an unreliable measure of volume fraction of precipitate, as thin foils taken may not be of a truly representative area, while extraction replicas do not reliably extract the entire particle population. This problem was highlighted by Ashby and Ebeling (1966) who gave the following equation for precipitated volume fraction, f_V, on the assumption of spherical particles:

$$f_V = \frac{\pi}{6}\left[\frac{N_S'}{\alpha}\left(\bar{x}_A^2 + \sigma_A^2\right)\right], \tag{2.12}$$

where N_S' is the measured number of particles per unit area, α is the extraction efficiency, and $\bar{x}_A$ and σ_A are the mean and standard deviation in particle diameters. Hansen *et al.* (1980) did provide an astute method of avoiding this replication problem. A parameter, k, which is proportional to f_V was defined as such:

$$k = N_S\left(\bar{x}_A^2 + \sigma_A^2\right) = 6\frac{\alpha f}{\pi}. \tag{2.13}$$

This can therefore be used to track any change in particle volume fraction, assuming α remains constant. The measurement of physical properties includes hardness methods to detect the secondary precipitation potential [Le Bon *et al.* 1975, Ouchi *et al.* 1977], changes in electrical resistivity [Simoneau *et al.* 1978] and results obtained from mechanical testing. Mechanical testing used is generally by stress relaxation or double

deformation. Stress relaxation techniques to measure precipitation, first suggested for titanium microalloyed steels by Liu and Jonas (1988), have since been used to detect the onset and completion of precipitation in niobium steels [Arieta 1992, Silveira and Barbosa 1993]. It is unfortunate that the precipitation rate is increased by the application of stress during relaxation, thus accelerating precipitation kinetics [Liu and Jonas 1988]. This factor must be taken into account when considering stress relaxation results. Fractional softening measurements from double deformation testing has been used successfully to determine precipitation events also [Kwon and DeArdo 1991, Dutta and Palmiere 2002].

Particle extraction either by chemical or electrolytic methods involves selective dissolution of the matrix followed by filtration, leaving just the precipitate population. Such techniques provide accurate volume fraction results, although may miss some of the smaller particles. Nevertheless, for a volume fraction measurement, these very fine particles do not make a large contribution to the volume precipitated.

The methods used to determine precipitate volume fraction are not necessarily practical for the measurement of particle size distribution. Quantification of particle size is often determined by transmission electron microscopy studies of carbon extraction replicas. These give an accurate sample of the particle population, but may depend on extraction efficiency. Both Davenport *et al.* (1977) and Janampa (1982) used an x-ray diffraction peak broadening technique of chemically extracted particles to determine precipitate size.

The particle density increases with time as more nucleation occurs. The particle size grows due to coarsening, but while nucleation is still occurring, fine particles are

produced, thus the mean overall size grows at a slower rate, moderated by this new precipitation.

2.2.3.4. Particle Morphologies

Work specifically looking at particle morphology in austenite is limited, so particle morphologies reported in here are from the inspection of micrographs from published work. Niobium-containing particles appear to come in one of two morphologies – cubic or rounded. During the reheating and thermal cycling of Nb-Ti steels, Tian *et al.* (1996) found cubic and rectangular particles, while other publications found rounded particles [Davenport *et al.* 1977] or a combination of spherical and rectangular particles [Siradj *et al.* 1997]. No evidence has been found for a link between particle morphology and precipitation sites, or deformation conditions. The difference may depend on the coherency of the individual particles.

2.2.4. Precipitation Kinetics

Particles precipitate out of solution into the iron matrix when it is both thermodynamically and kinetically viable to do so. Thus, precipitate formation occurs (eventually) on cooling because as the temperature falls, the solubility decreases, providing an increased thermodynamic driving force for precipitation. If the cooling is slow enough, the particles can precipitate out in austenite, but such precipitation in unstrained austenite is very slow and does not occur during normal cooling [Hoogendorn & Spanraft 1977, Begin and Simoneau 1977]. Faster precipitation rates are seen when precipitation is induced either by deformation, or by the austenite-ferrite phase transformation due to enhanced nucleation.

Precipitation kinetics are important when related to typical rolling schedules, as the interpass times can be of the same order as precipitation start times. Precipitation has occasionally been seen during roughing [Davenport and DiMicco 1980], although its overall effect is thought to be minor [Sellars 1986] due to the coarse particle size seen during such high temperature precipitation.

While most work considers precipitation under isothermal conditions, certain workers (e.g. Park *et al.* 1992, Sun *et al.* 1994, Bai *et al.* 1996) have considered precipitation during continuous cooling. Park *et al.* (1992) found that precipitation kinetics were shifted to longer times and lower temperatures during continuous cooling testing compared with isothermal testing.

Sun et al (1993) plotted both the particle size and density vs. time, and this is shown in Figure 2.9. Here torsion experiments were used to simulate multipass rolling during continuous cooling, and this plot shows how the mean particle size and density vary with interpass time.

2.2.4.1. Modelling of Precipitation Behaviour

As the precipitation behaviour has an important effect upon the microstructure, it is important to quantify precipitation, and to try to model precipitation behaviour during the hot working of niobium steels. Plots showing the onset of precipitation, under the effect of temperature and time are known as precipitation-time-temperature (PTT) plots. Figure 2.10 shows a typical PTT plot. Such plots generally show a precipitation start time (P_S) where, typically, 5% of the available precipitation has occurred ($P_{0.05}$), and often show a precipitation finish time (P_f) where 95% of the precipitation event is complete [Dutta and Sellars 1987]. The distinctive shape shows slow precipitation at

high temperatures, where the supersaturation is low, and slow precipitation at low temperatures, where diffusion rates are slow. At intermediate temperatures, the plot shows a 'nose', where the fastest precipitation occurs. Curves of this shape are sometimes referred to as c-curves.

The precipitation start time is effectively the nucleation time, and depends heavily on the state of the deformation microstructure and on diffusion rates. The time for precipitation to reach completion depends on the temperature. Quantitative relations have been constructed to describe precipitation kinetics. Such relations have to incorporate the effects of deformation conditions (ε, ε-rate, deformation temperature etc.), steel chemistry (niobium concentration chiefly), and time. Many quantitative descriptions of precipitation are in the form of precipitation start and finish time equations, which predict the onset and completion of precipitate formation as a function of time. The Dutta and Sellars (1987) model for precipitation gave the following equation for precipitation start time:

$$P_S = A[Nb]^{-1}\varepsilon^{-1}Z^{-0.5}\exp\left(\frac{Q_{def}}{RT}\right)\exp\left(\frac{B}{T^3(\ln k_s)^2}\right), \tag{2.14}$$

where A is a constant dependent on the precipitation detection method given as 3×10^{-6} $s^{1/2}$, Z is the Zener-Holloman parameter, [Nb] is the niobium concentration, Q_{def} is the activation energy for deformation, B is a material constant given as 2.5×10^{10} K^3, while k_s is the solubility product (given by equation 2.8). Thus, it is seen that precipitation is more rapid with increased niobium, increased strain or higher Z conditions. Other workers have suggested similar precipitation start time relations, based on Dutta and Sellars work (e.g. Silveira and Barbosa 1993). Experimentally determined precipitation

data are compared in Table 2.4. The earlier precipitation work was re-examined by Dutta *et al.* (1992) who in particular looked at the coarsening of particles on dislocations due to pipe diffusion. This was again refined by Dutta *et al.* (2001), who put forward a comprehensive model of strain-induced precipitation kinetics in Nb-steels, where heterogeneous precipitation upon dislocation nodes was assumed, with enhanced coarsening via pipe diffusion.

2.2.4.2. Effect of Other Elements on Precipitation Kinetics

The effect of non-microalloy additions on precipitation can be significant in two ways – they can either affect solubility, or affect precipitation. Xiuqiu and Wenxuan (1986) found that Mn retarded precipitation kinetics, although the reasoning given for retardation is unclear, as the paper contradicts itself. Akben *et al.* (1981) also looked at the effect of Mn on precipitation. Kestenbach et al. reported the work of Koyana (1971), which gave a solubility product for Nb steels which incorporates the effects of Si and Mn, but does not incorporate the effect of nickel, which reportedly 'decreases solubility'. Limited work exists on the effect of molybdenum on Nb(C,N) precipitation; Bacroix *et al.* (1982) found that it increased Nb solubility, thus reduced the driving force for precipitation, and so delayed precipitation kinetics, while Andrade *et al.* (1983) considered its effect on recrystallisation when in solution. It appears that silicon affects the carbon activity, and can accelerate strain-induced precipitation [Siciliano and Minami 1996a,b].

2.3. Microstructural Evolution of the Austenite Matrix During Hot Working

This section considers the microstructural change during hot working, and reflects on deformation and its effect upon the microstructure. It then looks at restoration by the

competing processes of recovery and recrystallisation, recrystallisation kinetics, the retarding effects of solute drag and precipitation and also covers grain growth.

2.3.1. Deformation

During deformation, energy is stored as dislocations are accumulated within the worked microstructure. There is a thermodynamic driving force to reduce this energy, and deformation structures form within polycrystals upon straining in order to minimise stored energy. These structures have been termed low energy dislocation structures (LEDS). Such deformation structures can evolve depending on strain and temperature, but also depending on the nature of the material, in particular the stacking fault energy (SFE). Microstructural evolution occurs by dislocation motion and rearrangement into lower energy arrays by recovery and recrystallisation. The hot working of steels is usually carried out in the austenitic condition (at deformation temperatures in excess of ~800°C). At these temperatures the restoration processes (recrystallisation, recovery) may occur dynamically during deformation.

2.3.1.1. Deformation Structures

Plastic deformation is the permanent dimensional change in response to an applied stress. Macroscopically, this is the change in shape of the workpiece. Microscopically, the microstructure also has to change to accommodate the overall deformation. This shape change is taken up by the introduction of dislocations to the structure. Dislocations are discontinuous line defects in the regular crystal lattice which can accommodate the plastic strain as they move through the crystal by progressive slip of atomic planes. The presence of dislocations represents an increase in internal energy, thus energy is stored in the material during deformation. Increased deformation brings about increased dislocation accumulation, the dislocations interact with each other, and

dislocation glide becomes more difficult, therefore plastic flow becomes more difficult. This phenomenon is known as work hardening. As dislocations move and interact, they take on lower energy configurations, forming LEDS. Ideally, during straining all grains are strained homogeneously – taking on the same strain as the strained polycrystalline body [Taylor 1938]. This is a full constraint model. In real materials, strain is not homogeneous and local lattice curvatures exist. LEDS are formed for two reasons: firstly to take up the lattice curvature and thus fill space, and secondly to minimise internal energy.

Historically, lower-energy deformation structures have been given different names by different workers, including cell-blocks, deformation bands (DBs), microbands (MBs), shear bands, kink bands and transition bands. The nomenclature most often followed is the RISØ system [Kuhlmann-Wilsdorf 1989, Bay *et al.* 1992], which clarifies the nomenclature for cold worked dislocation structures. A recent review of this system was by Hansen and Juul Jensen (1999).

During hot working, the microstructure is in a state of dynamic change and deformation structures do not appear to be identical to cold-worked features. No corresponding system to the RISØ nomenclature has been generally agreed upon for hot worked microstructures, although a report by the IMMPETUS group summarises their latest thinking [IMMPETUS 2001]. This report discusses the "statistically stored" boundaries introduced by Taylor deformation, and the "geometrically necessary" boundaries required to take up the lattice curvature. The importance of LEDS is that they are potent nucleation sites, due to their associated energy, and this makes their study of great interest. The IMMPETUS group, like many others, has recently focussed upon the presence of microbands in deformed microstructures. Microbands are elongated

collections of cell-blocks bounded by dense dislocation walls. These cell blocks are geometrically necessary dislocations to minimise work done during deformation. During testing, microbands have been found to form at ±35° to the 'rolling direction' [Duly *et al.* 1996].

Recently, the deformed state has been described by the internal state variable model [Nes 1995, Sellars 1997]. This is an alternative means of considering the microstructure, based on the dislocation structure. Microstructural formulae can be expressed in terms of easily measured parameters: subgrain size, misorientation, and dislocation density.

Microstructural evolution by recovery or recrystallisation nearly always occurs to some extent during deformation, certainly during periods of hot working. The dislocations are rearranged to form a cell structure, or subgrain structure during recovery, whereafter recrystallisation may occur. Early stages of recovery involve polygonization where some dislocations of opposite sign are annihilated and low angle grain boundaries (LAGBs) are formed as dislocations tangle and interact. As recovery progresses the dislocation tangles' walls consolidate to become cells or, with further recovery, subgrain boundaries, which are walls of high dislocation density surrounding a region of low dislocation density, with a misorientation between adjacent subgrains up to ~5°. The LAGB structure developed depends on the deformation and the extent of recovery, both of which depend on the stacking fault energy of the material.

2.3.1.2. Work Hardening

As dislocations are introduced to the worked material, the strength increases – this is known as work hardening. This phenomenon occurs because, during deformation, the dislocations interact with each other, making further deformation by slip more difficult.

Work hardening is seen in the flow curves for plastic deformation (see Figure 2.11), the stress initially increases upon deformation as the material work hardens. This can be balanced by dynamic recovery, which reduces the stress level, because the microstructure evolves during straining. Low stacking fault energy materials exhibit higher levels of work hardening as they recover to a lesser extent than higher stacking fault energy materials.

2.3.1.3. Stacking Fault Energy

The stacking fault energy (SFE) of a material is not an important parameter in itself, but it has proved a valuable way of classifying metals according to their deformation behaviour. SFE is the energy associated with the formation of a stacking-fault in a perfect crystal by the dissociation of dislocations into partial dislocations. Materials with high SFE recover to a greater extent than those with lower SFE as they have greater scope for dislocation glide as more slip systems are in operation. Dynamic recovery occurs readily in high SFE materials, while low SFE materials, such as austenite, show limited dynamic recovery, and dynamic recrystallisation can be induced if deformation conditions allow. Temperature has a large effect on SFE, in that at high temperature the energy required to create a stacking-fault is immense. This would imply that SFE is of limited importance during high temperature deformation.

2.3.2. Recovery

The microstructure of a worked material is composed of deformed grains, containing high levels of dislocations. As discussed earlier, these dislocations take on lower energy configurations in order to lower the internal energy. During recovery, these dislocation cells are further rearranged resulting in lower dislocation density within the subgrain interior. Recovery occurs initially by annihilation and combination of dislocations as

structural relaxation occurs, then by polygonization where the walls become sharper and low angle subgrain boundaries are formed by climb and cross-slip. The process is summarised in Figure 2.12.

Recovery is a thermally activated process, and the extent of recovery depends on the strain rate, temperature, and the stacking fault energy of the material. The SFE governs the potential of the dislocations to leave their slip planes, with limited potential for cross-slip or climb in low SFE metals. Thus, materials of high SFE promote dynamic recovery (DRV) which occurs concurrently with work hardening during hot deformation. Flow curves of dynamically recovering material show a characteristic increase in flow stress to a plateau as the material work hardens, after which the flow stress remains approximately constant during steady state deformation. This is seen in Figure 2.11 a) [Sellars 1990]. The extent of DRV is promoted by increased strain, increased temperature and strain rate. Niobium addition has been shown to slow the rate of DRV [Petkovic *et al.* 1975, Everett 1980]. Beyond a critical strain (ε_c) dynamic recrystallisation commences. Such behaviour is shown in Figure 2.11 b). The flow curve of such materials shows an initial increase in stress as the material work hardens to a stress peak at ε_c, whereupon dynamic recrystallisation can start, with a characteristic fall in flow stress [Jonas *et al.* 1969]. Dynamic recrystallisation is beyond the confines of this report. Furthermore, dynamic recrystallisation does not happen under the deformation conditions used during industrial finishing rolling for Nb-microalloyed plate steels.

Static recovery (SRV) occurs post-deformation, and has no incubation period. Recovery can occur alone for small strains, while at higher strains the onset of static recrystallisation can halt the progression of recovery. Recovery and recrystallisation are

competing processes, and often recovery occurs first and is then overcome by recrystallisation. The extent of recovery is advanced by fine precipitate particles and solid solutions as they hinder boundary motion, thus delaying the onset of static recrystallisation although, conversely, solute additions may also lower the SFE, so promoting recrystallisation. Petkovic *et al.* (1975) found an activation energy for SRV in austenite of ~134kJ/mol and the rate of recovery was found to increase with strain and temperature, but decreased considerably with the niobium concentration. Arieta (1992) determined SRV activation energy values for Nb-steels during stress relaxation, finding that increased niobium content and lower strain rates increased the activation energy, and also that the activation energy increased with the extent of recovery. Values given were 184kJ/mol and 155kJ/mol for a 0.1%Nb-0.06%C-1.51%Mn-37ppm N steel after deformation under strain rates of 0.1/s and 0.01/s respectively. Technically the recovery during stress relaxation is dynamic in nature, as there is a small constant stress applied during testing.

Hot worked subgrain sizes are most often determined in aluminium, as austenite transforms on cooling. Fritzmeier *et al.* (1979) considered DRV and austenite subgrains in stainless steel, and found that subgrain size decreases with either decreased deformation temperature or increased strain rate.

2.3.3. Static Recrystallisation

Recrystallisation is a nucleation and growth process during which deformed material is replaced by new strain-free grains. The deformed state has high stored energy associated with it, and there is a thermodynamic need to reduce this energy. Nucleation of recrystallisation is initiated heterogeneously at sites of particularly high energy, such as on grain boundaries, twin boundaries, and on deformation bands. Such nucleation

requires an incubation time. Once new grains have nucleated, they can grow into the deformed regions, increasing in volume and consuming the deformed material. Kinetics of such growth have been studied, leading to quantitative relations to describe the kinetics of recrystallisation, which are time, temperature and strain dependent.

2.3.3.1 Nucleation of Recrystallisation

Nucleation involves the formation of stable dislocation-free nuclei within the deformed microstructure. Such nuclei need to be above a critical size, and to have a larger than average misorientation to allow rapid boundary motion. Sites which have these two requirements are subgrains in regions of high local energy. Nucleation occurs heterogeneously at these preferred sites within the deformed matrix – such as grain boundaries and the dislocation structures discussed in section 2.3.1.1.

Grain boundary nucleation occurs by strain induced boundary migration (SIBM) where part of an existing grain boundary bulges into a neighbouring grain [Beck and Sperry 1950, Bailey and Hirsch 1962]. This is shown schematically in Figure 2.13 [Humphreys and Hatherly 1996], where an energy difference across a boundary provides a driving force for growth. Thus, a cap grows from a region of low stored energy into one of higher stored energy leaving a region of low dislocation density.

An alternative hypothesis to nucleation by boundary migration is nucleation by subgrain coalescence [Hu 1962, Li 1962]. This nucleation mechanism involves the attainment of the critical nucleus size by the convergence and rotation of contiguous subgrains. This theory is not wholly accepted [Jones 1980]. A subgrain coalescence model for nucleation in niobium steels was suggested by Sun and Hawbolt (1995) to account for

the incubation times measured. Subgrain coalescence was the only nucleation mechanism which fitted their data.

2.3.3.2. Nucleus Growth

Once a stable nucleus has been established it can grow into the surrounding deformed microstructure at the expense of smaller subgrains, due to its size advantage. Growth involves the migration of subgrain boundaries, and it is calculated [Humphreys and Hatherly 1996] that subgrain radius growth rate is directly proportional to the misorientation and inversely proportional to the subgrain radius.

The driving pressure for recrystallisation (P_R) is given by [Humphreys and Hatherly 1996]:

$$P_R = \frac{1}{2} G \mathbf{b}^2 \rho, \tag{2.15}$$

where G is the shear modulus, **b** is the magnitude of the Burgers vector (0.25nm in austenite) and ρ is the dislocation density. Opposing this is the pressure due to boundary curvature (P_C):

$$P_C = \frac{\gamma_b}{d}, \tag{2.16}$$

where d is the grain diameter and γ_b is the grain boundary energy. This equation is only appropriate in the earliest stages of recrystallisation, as P_C diminishes with increased grain size.

2.3.3.3. Recrystallisation Kinetics

The recrystallisation kinetics comprise two processes: an incubation time while nuclei form, and a 'transformation' time associated with recrystallisation growth to consume the deformed microstructure in its entirety. The incubation time is generally ignored in the literature, as it is assumed to be small compared to the overall time, and the recrystallisation time is often given as that taken for the growth to proceed from 0% to 100%. This is perhaps unfortunate, as during the incubation time, recovery occurs to a greater extent. This may account for the differences seen between actual experimental recrystallisation rates and models developed to describe recrystallisation kinetics. One publication that did look at incubation time was by Sun and Hawbolt (1995), who incorporated an incubation time into their model for recrystallisation kinetics.

The recrystallisation process is gradual, and the kinetic description was described by several workers independently at around the same time: Johnson and Mehl (1939), Avrami (1939, 1941), and Kolmogorov (1937), and is now known as the JMAK model. The important equation from this theory governs recrystallisation rate, and it relates the fraction recrystallised, $X(t)$, with time, t:

$$X(t) = 1 - \exp\left(-Bt^n\right) \tag{2.17}$$

where B is a material constant and n is the Avrami exponent. This equation shows a characteristic sigmoidal plot; a schematic recrystallisation curve is shown in Figure 2.14. The value of the exponent is expected (theoretically) to be 3 or 4, depending on the nature of the nucleation, falling throughout the recrystallisation until it is complete [Humphreys and Hatherly 1996]. Values seen experimentally are generally less than theory predicts due to recovery events and inhomogeneous nucleation. Fernandez *et al.*

(1999) found the value of the Avrami exponent in microalloyed steels to be between 0.8 and 1.3, while Janampa (1982) found n values of ~0.5-0.65 for various Nb-steels in the temperature range where precipitation occurs (T_{def}<1000°C).

A considerable amount of work has been carried out on recrystallisation kinetics for both C-Mn and microalloyed steel grades. One useful method of quantifying static recrystallisation kinetics was the t_{50} concept, as suggested by Sellars and Whiteman (1979). This was a modification of the JMAK equation to give a time for 50% recrystallisation, t_{50} (or any other selected percentage value) as a function of the deformation variables for C-Mn steel grades:

$$t_{50} = \mathrm{A} Z^{-0.375} d_0^2 \varepsilon^{-4} \exp\left(\frac{Q_{\mathrm{rex}}}{\mathrm{R}T}\right) \tag{2.18}$$

where A is a material constant (Sellars and Whiteman suggested 3.54×10^{-21}s$^{0.625}$μm^{-2}), Z is the Zener-Hollomon parameter, d_0 is the initial grain size, ε is the strain, R the gas constant, Q_{rex} the activation energy for recrystallisation, and T is the hold temperature. The time t_{50} is marked on Figure 2.14. This type of equation indicates that t_{50} values increase with increased initial grain size, and decrease with increased strain, strain rate, or temperature, and can be thought of in the general power-law form:

$$t_{50} = \mathrm{A}\dot{\varepsilon}^{\mathrm{p}} d_0^{\mathrm{q}} \varepsilon^{\mathrm{r}} \exp\left(\frac{Q_{\mathrm{rex}}}{\mathrm{R}T}\right), \tag{2.19}$$

where A and the exponents (p,q,r) are material-dependent constants. Table 2.5 gives values from the literature for these constants in this general equation form. This type of equation has been amended to incorporate different deformation variables and steel

grades, although many t_{50} equations are based on C-Mn data, but amended for niobium steels. A t_{50} relation specifically for niobium steels and was suggested by Hodgson and Gibbs (1992):

$$t_{50} = (-5.24 + 550[\mathrm{Nb}]) \times 10^{-18} d_0^2 \varepsilon^{(-4+77[\mathrm{Nb}])} \exp\left(\frac{330000}{RT}\right) \quad (2.20)$$

where [Nb] is the niobium in solution in weight%. It is of note that this equation has no Z-dependence. Medina and co-workers have suggested that below a critical temperature (dependent on composition), the activation energy, Q_{rex} increases with temperature [Medina and Mancilla 1993, Medina 1995, Medina and Quispe 1996].

The effect of temperature and time on recrystallisation kinetics is most easily summarised using a recrystallisation-temperature-time (R-T-T) plot, as shown in Figure 2.15 for a C-Mn steel. In microalloyed grades, precipitation strongly effects the recrystallisation kinetics and this is covered in a later section.

2.3.3.4. Recrystallised Grain Size

The recrystallised grain size is important, because mechanical properties (strength, impact toughness) are governed by grain size. A fine grain size is generally desirable for most applications, and forming processes are usually tailored to achieve as fine a grain size as possible. Microalloyed steels are ferritic or bainitic, but are worked in the austenite phase field, and a fine austenite grain size promotes a fine transformation product. Fine grain sizes are brought about by small initial grain sizes and increased deformation. The recrystallised grain size, d_{rex} is a function of the deformation conditions, and is described by a power law, with the general equation:

$$d_{rex} = \alpha d_o^{\ a} \varepsilon^{-b} Z^{-c},$$

(2.21)

where α, a, b, and c are constants. Typical values found for α, a, b, and c for microalloyed steels, are 0.9, 0.67, 0.67, 0 [Sellars 1980], while other workers have found different values.

Cuddy (1981), working on the hot rolling of microalloyed steels, found that reheated grain size had a large effect on product grain size and uniformity, in that in order to break down coarse initial microstructures, extremely large reductions were required.

2.3.4. Solute Drag

Substitutional alloy elements in solution in the matrix can affect grain boundary mobility by a phenomenon known as solute drag. Niobium in solid solution can suppress recrystallisation during hot deformation by impeding boundary motion. An important publication on solute drag in microalloyed steels was given by Akben *et al.* (1983). They considered the effects of microalloy additions on recovery and recrystallisation in austenite, and defined a solute retarding parameter (SRP):

$$\text{SRP} = \log\left(\frac{t_x}{t_{ref}}\right) \times \frac{0.1}{\text{at.\%(x)}} \times 100$$

(2.22)

where t_x and t_{ref} are the times to initiate static recrystallisation in the steel containing the element x and a reference C-steel respectively. The SRP for Nb addition was high, indicating a high boundary dragging pressure associated with such an addition. This is borne out by the drastic effect that Nb has on recrystallisation in steels. This equation

allows a direct comparison of the relative potency of elements in solution on retarding recrystallisation.

A more recent publication on solute drag compares its effect in Nb-steels with pinning obtained by Nb particles [Suehiro 1998]. This work considered solute drag in a microalloyed ultra low carbon steel, and found a large retarding effect on grain boundary velocity above a critical Nb concentration level. Calculations revealed that this reduction in mobility was due to solute drag. This work involved cold working and annealing rather than the more usual hot working simulation, and it was suggested that precipitate pinning would be much more likely in a hot working situation as the grain boundary driving force would be smaller due to dynamic recovery.

2.3.5. Particle Pinning

Particles interact with grain boundaries by imposing a retarding force on the boundary migration. This phenomenon is known as Zener drag, named after Clarence Zener whose original work was first published by Smith (1948). He considered the drag imparted upon a moving grain boundary due to interaction with an array of particles, giving an expression for the Zener pinning pressure exerted by a distribution of particles (P_Z):

$$P_Z = \frac{3}{2}\frac{f_V \gamma_b}{r} \qquad (2.23)$$

where f_V is the volume fraction of particles, γ_b is the grain boundary energy per unit volume and r is the particle radius. Boundary motion would be retarded by particles when a critical grain size (d_{Zener}) is reached:

$$d_{Zener} = \frac{4r}{3f_v} \tag{2.24}$$

This equation implies that in order to limit grain size a large volume of very fine precipitates is needed. These two equations have been a subject for disagreement and modification for a number of years, although the equation form and value of the numerical constants given by Zener is still considered to be reasonably accurate. More recent reviews of particle pinning exist [Nes *et al.* 1985, Manohar *et al.* 1998]. These publications have also considered other important factors, e.g. the particle shape effect.

It is possible for sufficiently large particles to bring about increased recrystallisation in worked materials. Humphreys (1977) has considered particle stimulated nucleation, whereby existing large, hard particles in the matrix form local highly deformed zones, within which, nucleation rates are enhanced. This phenomenon generally occurs only for very large particles (greater than ~1μm) and at lower deformation temperatures – thus it rarely occurs in microalloyed steels, as it is unlikely that a sufficient quantity of large particles will be present in a commercial microalloyed grade.

2.3.6. Precipitation-Recrystallisation Interaction

The precipitation-recrystallisation interaction has a profound effect on the hot worked microstructure. The order in which these processes occur dramatically changes the condition of the austenite. The question of which process occurs first depends on the relative recrystallisation and precipitation kinetics, which are highly temperature dependent.

As discussed in sections 2.2.3. and 2.3.3., both the nucleation of precipitation and the nucleation of recrystallisation is initiated at high energy sites in the microstructure.

These nucleation sites are essentially the same for both processes, thus there is competition for such sites. The process with the fastest kinetics will establish itself at these nucleation sites. Figure 2.16 shows the three possible cases, dependent on temperature and strain. Consider the three regions separately: Region 1 – high temperature, here recrystallisation can occur above a critical strain, while precipitation does not occur and the niobium remains in solution. Region 2, recrystallisation occurs before precipitation. Precipitation eventually occurs in a partially recrystallised microstructure, preventing further recrystallisation. This is undesirable as the partially recrystallised structure produces a mixed grain size upon transformation with poor associated mechanical properties. Region 3 – low temperatures, here recrystallisation kinetics are slow, so precipitation occurs before recrystallisation, preventing any recrystallisation and the grains become deformed. During rolling, the deformed grains become elongated, taking on a form known as pancaking. Further deformation at low temperature introduces substructure and LEDS into the austenite microstructure. Softening by recovery can still occur within this region.

The relative rates of precipitation and recrystallisation have been plotted together in a recrystallisation-precipitation-time-temperature (RPTT) plot. Figure 2.17 shows a typical example of an RPTT. This shows the effect of precipitation on recrystallisation. At higher temperatures recrystallisation occurs unhindered by precipitation, although niobium in solid solution will have a drag effect on recrystallising boundaries. At lower temperatures, precipitation affects recrystallisation by increasing the strain, for a given temperature, at which recrystallisation can commence.

It is perhaps useful at this point to discuss the important temperatures concerned with recrystallisation, and the nomenclature used. Initially Jonas and co-workers defined a

no-recrystallisation temperature (T_{NR}). This was the critical temperature where recrystallisation did not occur (fully). Other workers have since carried out similar experiments, and renamed the critical temperature with their own name. This behaviour has resulted in a number of names for what is effectively the same temperature. The name 'no-recrystallisation temperature' is possibly an unfortunate title, as recrystallisation can happen at the no recrystallisation temperature if there is sufficient time available. It also appears that T_{NR} is not a single value, but has a complex relation with interpass time [Sun *et al.* 1993]. It appears that it would be more sensible to define two critical temperatures; one below which recrystallisation does not occur (recrystallisation stop temperature, RST) and one above which, the material can completely recrystallise (recrystallisation limit temperature, RLT). This has also been suggested by Dutta and Sellars (1987), who defined these two critical temperatures as equating to 5% (RST) and 95% (RLT) recrystallisation. This makes good sense, as deformation in this region is undesirable due to the partially recrystallised microstructures formed, thus hot working should be carried out above the RLT or below the RST.

Work by Sun *et al.* (1993) considered the effect of interpass time on T_{NR} during 17 pass torsion deformation schedules under continuous cooling. T_{NR} was determined as the point of deviation in the equivalent stress vs. reciprocal temperature plot. This yielded the plot of temperature vs. interpass time, as shown in Figure 2.18, with T_{NR} and measured precipitation start and finish temperatures (T_{PS}, T_{PF}) plotted. The apparently erratic T_{NR} response was accounted for by considering three separate behavioural regions. In region I, recrystallisation occurs (unhindered) before precipitation. In region II, precipitation drives T_{NR} up as precipitation occurs at higher temperature, so that $T_{NR} \approx T_{PS}$ in this region. In region III, T_{NR} decreases with time due to particle coarsening

before the completion of recrystallisation. In follow up work to that of Sun *et al.*, equations were given for T_{NR} in regions I and II [Bai *et al.* 1996].

Another method of representing the precipitation/recrystallisation interaction exists. Medina and co-workers have found irregular softening kinetics in some microalloyed grades under certain conditions. They found a response that did not show the conventional sigmoidal shape usually associated with recrystallisation kinetics, but showed a plateau on the curve. This is where recrystallisation commences, then precipitation occurs, preventing further recrystallisation, leaving a partially recrystallised microstructure. They defined the static recrystallisation critical temperature (SRCT), which is effectively the same as T_{NR}, as this point. Figure 2.19 shows a typical curve [Medina and Mancilla 1993].

The attainment of a partially recrystallised structure is better illustrated in Figure 2.16 a), which shows the effect of strain and temperature on the microstructure during hot working. The three different regions of recrystallisation/precipitation interaction are clearly seen in such a plot. Figure 2.16 b) also shows the effect of niobium content on the PRX region.

The recrystallisation driving force was calculated earlier (section 2.3.3.2). The Zener pinning force operating against this can also be calculated. The pinning force due to randomly distributed particles on a rigid boundary (RBM) was given by equation (2.23).

$$P_Z = P_{RBM} = \frac{3 f_v \gamma_b}{2r} \tag{2.25}$$

where γ_b is the grain boundary energy, f_V is the volume fraction of particles, and r is the mean particle size. This equation is valid for incoherent particles; coherent particles offer twice the pinning pressure [Humphreys and Hatherly 1996]. Further work on particle pinning force considers the nature of the particle/boundary interaction. Two other models exist for boundary pinning. The flexible boundary model (FBM) allows local boundary curvature between particles, and the pinning pressure exerted by a particle distribution on a flexible boundary [reported in Kwon and De Ardo 1991] is given by:

$$P_{\mathrm{FBM}} = \frac{3\gamma_b f_V^{2/3}}{\pi r} \tag{2.26}$$

Perhaps a more realistic model than the RBM for hot worked structures is the subgrain boundary model (SBM). As discussed earlier, nucleation occurs preferentially on grain boundaries and subgrain boundaries, thus it is necessary to take the subgrain structure into account. Hutchinson and Duggan (1978) suggested a model for subgrain boundary pinning by particles that lie inhomogeneously on boundaries. Hansen *et al.* (1980) applied this to microalloyed steels and proposed a model for the pinning of austenite subgrain boundaries by precipitates. The equation for the pinning pressure due to subgrain boundary (P_{SGB}) precipitation is given by:

$$P_{\mathrm{SGB}} = \frac{\gamma_b f_V \delta}{4r^2}, \tag{2.27}$$

where γ_b is the grain boundary energy, f_V is the volume fraction of particles, δ the subgrain size, and r is the mean particle size.

A number of workers have attempted driving pressure/pinning pressure calculations. Their results have been summarised in Table 2.6. Hansen *et al.* (1980) suggested that the SBM fitted his data. Meanwhile, Kwon and DeArdo (1991) calculated pinning pressure values less than the driving pressure for recrystallisation for all but the FBM. Arieta (1992) found no subgrain boundary precipitation, and suggested that the SBM was not valid for his work, and instead used the RBM. Thus, the three different models have been validated by different workers. The calculations are open to interpretation by the user, and values can be achieved by whichever method to fit their data by selecting constants appropriately, choosing coherency/incoherency or imprecise experimental determination. For this reason, they cannot give a definite key to pinning behaviour. The pressure due to boundary curvature (equation 2.16) is often neglected from such calculations. This is a factor in the early stages of recrystallisation, where pinning of the low mobility LAGBs has a large influence. This leads to the question as to whether pinning has an effect on the nucleation of recrystallisation or on growth during recrystallisation.

2.3.7. Grain Growth

Grain boundaries have an associated energy. There is a thermodynamic driving force to reduce this energy, so grain boundary area is minimised by the diffusion of atoms. Grain growth has strong temperature dependence, as at elevated temperatures atoms are more mobile, and can diffuse into lower energy configurations more easily. Sellars and Whiteman (1979) reviewed data for C-Mn steels and formulated an equation for grain growth as a function of absolute temperature, T:

$$d^{10} = \mathrm{d}_{rex}^{10} + \mathrm{A}t\exp\left(\frac{-\mathrm{Q}_{gg}}{\mathrm{R}T}\right) \qquad (2.28)$$

Here, d and d_{rex} are the mean grain sizes of the coarsening grains and initial grains respectively, A and Q_{gg} are material constants and R is the gas constant. This equation suggests that grain growth is accelerated at higher temperature, and requires an activation energy to begin. Atkinson (1988) gives a comprehensive review of grain growth. Grain growth can be inhibited by the pinning of grain boundaries by fine particles. During steel processing, grain growth affects the microstructure most severely during reheating, but also during any other holding periods at high temperature.

Grain growth during the reheating of Nb-microalloyed steels can occur conventionally, or if conditions allow, abnormally. At low reheating temperatures (~<1050°C) normal grain growth occurs, as is seen in plain carbon steels - but the grain sizes are finer in microalloyed steels due to the presence of second phase particles pinning boundary motion. As the temperature increases, smaller particles begin to dissolve, while others begin to coarsen by Østwald ripening, thus lessening the pinning potential. This then leads to the preferential coarsening of some grains, which undergo extreme growth consuming the smaller grains. It is desirable to avoid this type of growth, and this can be achieved by the addition of titanium (which dissolves at a higher temperature), or the addition of an excess of Nb. Gladman (1966) suggested that abnormal grain growth is prevented by the presence of fine particles in sufficient quantity, defining a critical particle radius value (r_{crit}), dependent on particle volume fraction (F_V), above which abnormal grain growth can occur:

$$r_{crit} = \frac{6R_0 F_V}{\pi}\left(\frac{3}{2} - \frac{2}{z}\right)^{-1}, \qquad (2.29)$$

where z is the heterogeneity factor, or size ratio of the growing grain compared with the matrix grain. This means that r_{crit} is going to vary from region to region in the microstructure due to local variations in z – this gives abnormal grain growth. At temperatures in excess of ~1200°C, most of the particles have dissolved and normal grain growth can then resume. Palmiere *et al.* (1994) studied grain coarsening in Nb-microalloyed steels and defined a grain coarsening temperature (T_{GC}), a temperature above which grain coarsening occurs:

$$T_{GC} = T_{DISS} - 125°C, \tag{2.30}$$

where T_{DISS} is the temperature for complete dissolution, as calculated from their solubility product determined by atom probe analysis (see Table 2.1).

2.4. Iron-Nickel alloys

Nickel is added in small quantities (<1%) to many steel grades. Stainless steels contain larger nickel additions, along with large chromium additions (e.g. type 316 stainless contains typically 16% chromium and 12% nickel). The addition of 36% nickel to iron is a valuable alloy in its own right, known as Invar. Invar was developed earlier in the 20th century and is important because of its especially low thermal expansion coefficient. It is thought that the anomalous properties shown by Invar are because it is not in true equilibrium [Swartzendruber 1991]. The nickel addition to Invar-type compositions suppresses the Ar_3 temperature to around –30°C, and thus stabilises the austenite. As the transformation temperature is below room temperature, then such alloys can be used to study the austenite-to-martensite transformation in detail. Most published work on such alloys concerns the transformation properties and only a limited amount of work on mechanical testing of Invar-type alloys exists. High nickel alloys

have (also) been used to simulate the hot working characteristics of austenite [Hurley *et al.*, 1998].

It has been proposed that an iron-30wt% nickel steel could be used as a high temperature quenchable austenite to allow the study of hot worked microstructures, or microalloyed to look at precipitation nucleation sites [Sellars 1998].

2.4.1. The Iron-Nickel System

Figure 2.20 shows the iron-nickel phase diagram. This shows that the melting points of pure (FCC) iron and (FCC) nickel are 1538 and 1455°C respectively, with complete solid solubility between these compositions. At lower temperatures a eutectoid reaction occurs at the composition 49% nickel:

$$\gamma\,(Fe,Ni) \Rightarrow \alpha\,Fe + FeNi_3, \tag{2.31}$$

but as the temperature is low, diffusion is very slow, the reaction does not go to equilibrium and the γ-(Fe,Ni) remains in metastable austenitic form.

At the composition Fe-30Ni, on cooling from the melting temperature (~1460°C), a single phase FCC Fe-30Ni solid solution exists throughout the temperature range down to room temperature, albeit below ~510°C it is metastable. It is because the γ-α phase change is avoided that this alloy can be used as an austenite analogue. Below room temperature, a martensite transformation can occur, although this is a diffusionless transformation and the kinetics do not depend on temperature. Such alloys have been used for the controlled study of the martensite transformation [e.g. Abe and Sellars 1991].

The lattice parameter of iron austenite is 0.358nm. The effect of solutes on this value has been studied in detail by Dyson and Holmes (1970). They considered the effect of substitutional solid solution additions on lattice parameter using x-ray techniques and multiple regression analysis. In their equation for the lattice parameter of austenite (valid only to 24.5at.% nickel), the coefficient for the effect of nickel addition was - 2×10^{-4} /at.%. Extrapolating this to 30% nickel predicts a lattice parameter of ~0.357nm for the Fe-30at.%Ni composition; thus the lattice parameters or iron austenite and Fe-30%Ni austenite are similar.

2.4.2. Suitability as a Model Austenite

It is desirable to look directly at the hot worked microstructure of microalloyed steels. Hot working occurs in the austenite range and upon cooling a phase transformation occurs from austenite either to α-iron transformation products or to martensite. Such a phase change drastically alters both the microstructure and the dislocation structure formed during hot working. The use of steel with increased nickel content provides an austenite stable at lower temperatures. The addition of in excess of ~28wt% nickel reduces the effective transformation temperature to below room temperature. This means that following hot processing of such iron-nickel alloys, the materials may be quenched with transformation, while retaining the hot worked structure. This allows a full investigation of the austenite structure, providing that the alloy can reproduce the behaviour of iron austenite.

There are two major criteria for the use of such an alloy as a valid austenite analogue. Firstly, the alloy must show similar deformation behaviour to microalloyed steels (i.e.

similar work hardening and softening characteristics). Secondly, the solution and precipitation characteristics must also be similar to those of microalloyed steels.

2.4.2.1. Hot Working Characteristics

A limited amount of work exists on the hot working of iron-nickel alloys. Pluhar and Zuna (1968) considered the deformation at very high strain rates (~100s^{-1}) of Fe-36Ni. Work by Almaguer (2001) has looked at the hot working of an iron-30%nickel alloy. The mechanical responses have been similar to those seen in iron austenites. Static recrystallisation has been seen at lower deformation temperatures, while at higher temperatures dynamic recrystallisation occurs at higher strains. The activation energy for hot working was found to be ~300kJ/mol – a figure similar to that for C-Mn steels (Jonas *et al.* (1969) found 312kJ/mol for C-Mn steel). Activation energy for microalloyed steels is higher (e.g. Foster (1981) found 401kJ/mol for 0.04%Nb steel). There is little to suggest that the hot working characteristics are significantly different to conventional C-Mn steels. Cho et al. (1997) found a T_{NR} for non-microalloyed Fe-36Ni steels. This was given as a function of the deformation conditions:

$$T_{NR} = \alpha + \exp(\beta\varepsilon). \tag{2.32}$$

Values given for α and β were 103.8 and –0.25, giving a T_{NR} value for their alloy of ~1000°C. This appears to give very high values for, what is a non-microalloyed steel, and in disagreement with other published literature. Maki *et al.* (1982) looked at DRX in a range of steels including Fe-31%Ni and a 0.04%Nb C-Mn grade. They found values for the activation energy of DRX, and for these two grades were 335 and 327 kJ/mol respectively. This compares with their values of ~260kJ/mol for C-Mn steel. They concluded that niobium retards DRX, as does nickel and considered the onset of

DRX as a function of Z. Ohtsuka *et al.* (1987) used an iron-31%nickel steel to observe warm-worked deformation structures formed in austenite during rolling and compression.

Deformation is thought to be governed by the SFE of the material, however limited work on SFE exists. Charnock and Nutting (1967a,b) produced the most comprehensive work available, in looking at the SFE of the Fe-Ni system by quantifying annealing twin frequency as a function of nickel content. The data suggested that, contrary to results seen in stainless steels, SFE falls with nickel addition from 75 J/m^2 at pure iron, to a minimum of 35 J/m^2 at around 36%Ni, rising to 120 J/m^2 for pure nickel. These results are shown in Figure 2.21. The effect of composition on SFE for other elements is patchy, and work on the effect of Nb additions to austenite vary. Van Aswegen *et al.* (1964) found no effect with a 1% Nb addition to 18/10 austenitic stainless steel, while Martinez *et al.* (1992) found a significant drop in SFE with Nb addition to austenitic Fe-15%Cr-15%Ni. This apparent difference can be explained by the fact that one of these studies was on niobium in solution, while the other as particles.

2.4.2.2. Effects of Nickel Addition on the Solubility of Micro-alloy Elements

The atomic radii of iron and nickel are similar (0.121 and 0.125nm respectively) and the lattice parameters of FCC Fe and FCC Ni are also similar – i.e. there is little difference. The size of the tetrahedral interstices in the austenite lattice may be a little larger in the Fe-Ni alloy, due to the smaller atomic size of nickel, this would suggest a slightly greater solubility.

For the microalloyed Fe-30%Ni to be a good model steel, it is important to understand the effect of a large Ni addition on Nb(C,N) solubility, yet no work exists in this field.

The most obvious effect that a nickel addition has is the larger γ-phase field, and the suppression of the Ar_3 temperature. This means that there is greater carbon solubility, and hence more Nb(C,N) can be taken into solution during reheating. Some thermodynamic calculations (unpublished) have been carried out at the University of Sheffield to design the model alloy. These studies compared Fe-30Ni base alloys with Fe base alloys of otherwise equivalent composition (C, Mn, Si). Figure 2.22 (a, b) compares solubility calculations in the two materials at a temperature of 1150°C.

2.5. Mechanical Testing and Hot Working

Hot working involves the change of shape of a material by deformation at a temperature greater than $0.6T_M$. Many metal forming processes involve hot working, as high temperature deformation is beneficial compared with cold working due to the relative ease of deformation, and therefore the lower working loads required. By far the most common method of metal forming is by hot rolling. Industrial rolling involves a series of passes, and the microstructure developed depends on both the static and dynamic changes occurring during the deformation sequence. Rolling is such an important process that modelling has been carried out in an attempt to understand microstructural change during periods of rolling and to allow prediction of the final properties.

Improvements in knowledge have led to more advanced hot rolling techniques in order to achieve desirable microstructures. Thermomechanical processing (TMP) involves the application of both thermal and deformational cycles to metals, leading to improved microstructural control.

Laboratory-based simulations of the thermomechanical processing by hot rolling are also discussed in this section.

2.5.1. Hot Rolling Practices

Hot rolling is the most widely used metal forming procedure. The material is reheated to ~$0.9T_M$ and worked above $0.6T_M$ as the forces are lower and softening processes can fully occur. Rolling involves shape change (ideally) by plane strain. The stock material passes through driven rolls, where it undergoes compression and elongation (plane strain), but often some width change is also seen.

The industrial process of the thermomechanical processing of microalloyed steels involves three main stages: reheating, controlled hot rolling, and accelerated cooling. The reheating schedule is designed to solutionise niobium, and in practice, schedules are long enough to approach equilibrium. During reheating, grain growth also occurs – this is undesirable. The steel then undergoes controlled rolling, usually in the austenite phase field in order to condition the austenite, to achieve the desired microstructure.

Hot rolling practices are split into two stages: roughing and finish rolling; each of these involves a series of passes. Roughing breaks down the large reheated structure to give a uniform, and relatively fine grain size. Roughing is carried out in the high temperature range where work hardening is followed by rapid recrystallisation. A minimum critical pass strain is required to ensure full recrystallisation [Sellars 1980].

Finish rolling conditions vary depending on the gauge of the product. Two important finish rolling techniques exist for microalloyed steels, and these depend on the recrystallisation and precipitation kinetics of the steel. Finish rolling must be carried out at temperatures where either full recrystallisation occurs (recrystallisation kinetics faster than precipitation kinetics) or no recrystallisation occurs (precipitation kinetics faster

than recrystallisation kinetics), as discussed in section 2.3.6. If finish rolling occurs between these temperatures then a partially recrystallised austenite is formed, leading to a mixed microstructure in the transformation product, with poor mechanical properties. Rolling at temperatures above the RLT is known as Recrystallisation Controlled Rolling (RCR), here full recrystallisation occurs, while no precipitation occurs during finishing, and the precipitation can occur later in the ferrite to enhance precipitation hardening. Rolling below RST is known as conventional controlled rolling (CCR); here full grain pancaking occurs, with large S_V values, ensuring a fine grain size in the transformation product.

An attempt to quantify the 'amount of deformation' involves the creation of the S_V parameter, a measure of boundary area. This approximates the grain boundary area, but must also incorporate deformation bands and twin boundaries. In fully recrystallised equiaxed grain structures, S_V is given by:

$$S_V = \frac{3}{D_\gamma}, \tag{2.33}$$

where D_γ is the austenite grain size. Upon deformation, grains are no longer equiaxed, are elongated and flattened, and contain deformation bands. For deformed materials, the true S_V value is a combination of both the grain boundary contribution, $S_V(GB)$ and the intragranular defect contribution, $S_V(DB)$:

$$S_V = S_V(GB) + S_V(DB). \tag{2.34}$$

Equations exist for these two contributions based on cubic grains [Gray and DeArdo 1986]:

$$S_V(GB) = \frac{1}{D}\left(1 + \frac{1}{R} + R\right), \tag{2.35}$$

$$S_V(\mathrm{DB}) = 0.63(\%R - 30), \tag{2.36}$$

where D is the cube grain size, R is the original-to-final-thickness ratio and %R is the reduction as a percentage. These equations imply that for deformed microstructures the S_V increases with strain. The importance of the S_V value is that these boundary areas are potent nucleation sites, and materials with high S_V values have higher nucleation densities, and produce finer grain sizes upon transformation. Thus, during thermomechanical processing, it is desirable to produce a material with a high S_V value to ensure a fine transformation product. This can be achieved by a fine recrystallised grain size (RCR), or by a heavily deformed microstructure (CCR). Because of the lower temperatures employed, CCR involves the use of high rolling loads, which may not be within the capability of many mills. Cuddy (1984) carried out a comprehensive study of the experimental hot rolling of Nb and Nb-Ti steels. In this work, an attempt was made to modify the rolling temperature range by altering steel chemistry, but this was unsuccessful.

Following rolling, accelerated cooling techniques are often employed to gain the maximum advantage by controlling the transformation temperature and kinetics.

2.5.2. PSC Testing as a Simulation of Hot Rolling.

There are several different methods of laboratory-based mechanical testing of metals. These include laboratory rolling, axisymmetric compression, plane strain compression,

torsion, and tension testing. All of these methods have been used to study the hot working of metals, and all have their own merits and drawbacks. Unfortunately, there is no published work seriously comparing these different test methods, and not promoting one specific method over the others.

The plane strain compression (PSC) testing can be used as a laboratory simulation of hot rolling. Following reheating to the desired temperature, the testpiece is placed between two parallel platens. These then come together under computer control, and the material is deformed under compressive stress. The geometry of the set-up is such that the platens are wider than the testpiece, so constricting the strain in the width direction. Ideally, the deformation is plane strain – in the direction of motion of the platens, and in the length direction. In reality, some lateral spreading occurs, although this can be corrected for mathematically. The plane strain deformation achieved using PSC is similar to the plane strain achieved during hot rolling. In Sheffield, a substantial amount of PSC testing has been carried out [e.g. Beynon 1979, Foster 1981], and the system has been developed for routine PSC testing. The test machine can be servo-hydraulically controlled to provide a constant true strain rate. Such a system is good as it can be used to high true strain rates (up to 100/s). The achievement of high strain rates is important as these are typical of values used in industry. It is perhaps unfortunate that many published papers claiming to simulate industrial practice are carried out at unrealistic strain rates, making their relevance inadequate.

Deformation during PSC is inhomogeneous through the specimen thickness, due to inhomogeneous strain, strain rate and temperature distribution. Finite element modelling work in Sheffield has shown that the strain and strain rate in the central region is approximately uniform-see Figure 2.23. Regions along the diagonals from the specimen

centre to the edge of the tool show high strains. This highlights the importance of careful selection of areas for taking specimens. The central regions undergo the desired strain, with a greater likelihood of approaching plane strain; this makes the PSC method a good simulation of hot rolling.

Different measuring methods have been used to determine microstructural events and their kinetics during hot working. Stress relaxation involves deforming the material (by compression, torsion, tension etc.) and by holding the tools in place under a small strain and allowing the material to deform, effectively by creep. This method is especially useful for detecting the onset and completion of recrystallisation [Karjalainen 1995]. Liu and Jonas (1988) first presented the stress-relaxation method for the detection of precipitation events in microalloyed steel. The main drawback of the technique is that the interpretation of the softening curves is open to misinterpretation, as precipitation events show up as a very small inflexion on the curve.

Double hit testing involves carrying out a single deformation on one specimen, followed by two deformations on another specimen to the same overall strain, with a timed strain interruption between deformations. The single-hit and double-hit curves are then compared. Following the interpass interruption time, if no microstructural change occurred, then the stress level on the second deformation would be equivalent to the single hit curve. Typically softening by recovery and recrystallisation occurs between deformations, and the stress after the delay is below the control curve. This method can be used to study softening as a function of time between passes [Cordea and Hook 1970]. This method has also been shown to be effective for the measurement of precipitation events, and the kinetics of precipitation by taking quantitative

measurements of fractional softening from the flow curves [Kwon and DeArdo 1986, Palmiere *et al.* 1996].

Various methods have been used to determine fractional softening from the flow curves, and Fernandez et al. (1999) compared the different methods of fractional softening measurement, finding that back extrapolation and the mean flow stress (area) methods most reliably measured the recrystallised fraction.

3. OVERVIEW

The study of the physical metallurgy of microalloyed steels has now been an important field of research for nearly forty years. During this time the hot working characteristics have been comprehensively investigated, simulated and modelled. Unfortunately, the actual microstructural behaviour during hot working cannot be followed completely due to the unavoidable phase transformation of these steels upon cooling. This transformation prohibits direct study of the deformed austenite, by disordering the dislocation structures developed during hot working. Thus, an absolute characterisation of the deformed state cannot be completed.

In order to avoid the problem of transformation, a model austenite alloy has been developed to allow the retention of the austenite structure to room temperature, while retaining similar thermodynamic and deformational properties to conventional microalloyed steels. The alloy was based on a matrix of iron with 30wt.% nickel, and niobium and carbon additions to the level of 0.1% and 0.09% respectively. The use of such an alloy to simulate traditional microalloyed steels means that the study of softening and precipitation events in the austenite matrix is possible as the phase transformation is avoided.

This Fe-30%Ni-Nb alloy has undergone thermomechanical processing. The material was subjected to high temperature preheating (1250°C) to allow supersaturation of the niobium. Double-deformation plane strain compression testing has been carried out over a range of temperatures (900-1050°C) at a strain rate of $10s^{-1}$ and with delay times between deformations varying from 1s to 1000s. During deformation, strain induced precipitation of NbC particles occurs depending on the processing conditions.

This thermomechanical processing has allowed a quantitative TEM study of precipitation of NbC particles in the austenite matrix. TEM thin foil analysis of the hot worked matrix has also been completed to investigate the dislocation structures produced.

The objectives of the present research were as follows:

- to look at the Fe-Ni-Nb alloy and determine whether it is a feasible model alloy for low carbon microalloyed steels,
- to investigate the strain-induced precipitation of NbC in this alloy,
- to analyse the hot worked austenite microstructure as a function of deformation temperature and delay time.

4. EXPERIMENTAL PROCEDURE

4.1. Received material and pre-treatment

4.1.1. Material

The material was received from Corus Research, Development and Technology (Swinden Technology Centre) as forged 30mm square bar, with the chemical composition given in Table 4.1. The microstructure of the as-received material was partially recrystallised with the recrystallisation inhomogeneously distributed through the section.

4.1.2. Pre-treatment

The material was soaked at 1200°C for 60 minutes before being hot rolled down to 11mm in several passes with reheating to the soak temperature in between passes. The rolled product was then allowed to air cool to room temperature.

4.2. Deformation Testing

4.2.1. Test apparatus and control system

All mechanical testing was carried out by plane strain compression (PSC) using the Sheffield University Servotest servo-hydraulic testing facility. This machine allows precise deformation under temperature conditions which are appropriate to those found in industrial plate rolling, and at a strain rate of up to $100s^{-1}$. The PSC machine at Sheffield is shown schematically in Figure 4.1, and has been used routinely for more than twenty years.

The PSC machine records the load, displacement, and temperature data, and is able to deform material at a constant true strain rate. The PSC output data are produced as

computer text files. These raw data can be post-processed on a PC-compatible desktop computer. The detailed use of this machine and PSC testing has been described elsewhere [Sellars *et al.* 1976, Loveday *et al.* 1999]. Figure 4.2 shows a schematic diagram of the tool geometry.

4.2.2. PSC Specimens

PSC specimens were machined from the rolled material to the dimensions 50×10×30mm. A schematic diagram of the test specimens is shown in Figure 4.3. K-type thermocouples (chromel/alumel) were inserted in a hole drilled to half the specimen breadth to allow temperature measurement during testing. The PSC samples were coated in a glass lubricant to minimise the effect of friction during testing.

4.2.3. Test conditions

The PSC specimens were scheduled to undergo a series of interrupted compression tests under different conditions, as given in Table 4.2. During the timed interruption between deformations, static microstructural changes (precipitation, recovery, and recrystallisation) were anticipated. Single deformation tests were also carried out as a control, designated with an interpass time of zero.

Specimens were first reheated to a temperature of 1250°C for 15 minutes to bring about niobium carbonitride dissolution. The reheated specimens were allowed to air cool to 15°C above the test temperature (T_{def}), after which the deformation fell under computer control. Samples were deformed at a constant true strain rate of $10s^{-1}$ to a pre-strain of 0.25, unloaded for a set interpass time, then reloaded to a total strain of 0.5, and quenched to room temperature in running water. Figure 4.4 shows the time temperature schedules employed.

Throughout this text the nomenclature for specimens was as follows: test specimens were designated by the test temperature and the interpass time, followed by either SD, DD or HHQ to signify a single-deformation, double deformation or hit-hold-quench test. Thus, 950-100DD refers to a double-deformation specimen deformed at 950°C, held for 100 seconds, then restrained; while 1050-SD refers to a single-hit specimen deformed at 1050°C. Table 4.2 shows the principal test matrix, but other tests were necessary also. Where discussed in the text, these will be described fully, giving all deformation conditions. Other tests included testing to higher strain levels, testing at different strain rates, and some stress relaxation work.

4.2.4. Data Recording and Flow Curves

Raw data were handled using the Terrapin software developed in the University of Sheffield. This program was specifically written to deal with PSC test data. Terrapin corrects, the recorded load and displacement data for machine compliance, and determines the origin. Load–displacement data are converted to true stress-true strain flow curves, which are then corrected for temperature variation due to isothermal heating during deformation. Terrapin can also give strain-rate and temperature evolution data.

4.2.5. Fractional Softening Data

The flow curves were converted to fractional softening data using the mean flow stress method as used by Kwon and DeArdo (1991). This method compares the area under the flow curves using single- and double-deformation curves. This is shown schematically in Figure 4.5. Fractional softening (FS) is calculated using the equation:

$$FS = \frac{\bar{\sigma}_s - \bar{\sigma}_2}{\bar{\sigma}_s - \bar{\sigma}_1} \tag{4.1}$$

where $\bar{\sigma}_1$ and $\bar{\sigma}_2$ are the mean stress values for deformation 1 and 2 for the double-hit (interrupted deformation) test and $\bar{\sigma}_s$ is the stress of the corresponding single-hit stress. Mean stress values are calculated by the area under the flow curve:

$$\bar{\sigma} = \frac{1}{\varepsilon_2 - \varepsilon_1} \int_{\varepsilon_1}^{\varepsilon_2} \sigma . d\varepsilon \tag{4.2}$$

This method is reliable, as the determination of softening is based upon an area, rather than upon single stress values as is used in other fractional softening measures.

4.2.6. Reheating Simulation

Specimens were reheated in a furnace to different temperatures and for different times. The reasons for this were two-fold. Firstly, the reheat simulations allowed the determination of the most appropriate reheat conditions, up to the test furnace maximum temperature of 1250°C. Secondly, reheat simulations allowed characterisation of the microstructure developed from these conditions.

4.3. Optical metallography

4.3.1. Samples

Samples were hot-press mounted in Bakelite and then subjected to a sequence of grinding stages on successively finer silicon carbide abrasive papers (120, 240, 400, 800, 1200 grit). Polishing was then carried out on a series of lubricated cloths impregnated with fine diamond pastes (6μm, 1μm, and 0.25μm). This was followed by a final surface polish using a colloidal silica suspension (~0.04μm).

4.3.2. Etchants

Etching the material proved difficult and therefore several etchants were investigated. Samples were initially etched using Schaftmeister's reagent; although this provided a satisfactory etch, it did take around 30 minutes. Other chemical and electrolytic etchants were used in an attempt to find a more rapid etch; these are described in Table 4.3. Once a successful etch was found it was to be used for all quantitative metallography to ensure equivalence between specimens. The preferred etchant for optical work was 10% nitric acid in water. This was chosen because it was quick, easy and gave a good, clear etch, and appeared to etch up all grain boundaries. Other working etchants include ammonium persulphate solution, Kalling's reagent, and concentrated nitric acid, although the nitric acid additionally etched the substructure.

4.3.3. Volume Fraction Measurement

Samples were viewed optically, and photomicrographs were taken. Fraction recrystallised was measured using a Swifts point counter on a travelling stage microscope. The fraction recrystallised was measured by linear analysis along through-thickness lines at predetermined distances through the section, counting at least 600 points. Counting was carried out over the whole of the section to allow for the local microstructural inhomogeneities found in PSC specimens. Error in the volume fraction was calculated using the following equation:

$$value = \bar{x} \pm \frac{\sigma_{n-1}}{\sqrt{n}} t_{(n-1,0.05)} \qquad (4.3)$$

where $\bar{x}$ is the sample mean and σ_{n-1} is the standard deviation in the measured data, n is the number of observations and $t_{(n-1,\ 0.05)}$ is the value of the t-distribution on n-1 degrees of freedom at a 95% confidence interval.

4.3.4. Grain Size Measurement

The mean grain size values were measured using a Swifts point counter on a travelling stage microscope. Grain sizes were determined by the mean linear intercept method. As with the fraction recrystallised metallography, counting was carried out over the whole of the section to allow for local microstructural inhomogeneities. Where possible, quantitative metallography was carried out in the manner set out by Orsetti-Rossi and Sellars (1997). Sample sizes were of at least 500 grains where possible. Errors were estimated using the t-distribution, as given in equation 4.3.

4.4. Electron Microscopy

4.4.1. Samples

4.4.1.1. Carbon Replicas

Carbon extraction replicas were used to remove precipitates from the surface of the samples, allowing a study of these particles. Specimens were sectioned parallel to the deformation axis, prepared metallographically by grinding and polishing, and lightly etched in Kalling's No.2 reagent. A thin coating of carbon was deposited on the sample surfaces, which was then cut up into 2×2mm squares. The extraction replicas were detached from the sample surface using 10% Nital, floated off in distilled water and placed on copper grids for TEM observation.

4.4.1.2. Thin Foils

Thin foils were produced from both annealed, rolled and PSC test specimens. They were produced by manual grinding on silicon carbide papers to a thickness of <500μm, finishing at 1200grit. The ground material was then further thinned using a grinding block to a thickness of 80-100μm. Samples 3mm in diameter were then either punched out or spark eroded as disks. The disks were then electropolished to electron transparency, using a Struers Tenupol-3 electropolishing unit with a solution of 5% perchloric acid-35% butoxyethanol-60% methanol. Operating conditions varied, but were nominally as follows: temperature –35°C, flowrate 4, current 0.1A, with a time of typically ~90 seconds. Specimens were intermittently checked on an optical microscope during the electropolishing process, and the current was controlled depending on the condition of the sample. Before insertion into the microscope, samples underwent final cleaning using a Gatan PIPS ion beam miller to remove much of the oxide film found on the as-electropolished samples.

4.4.2. Microscope Operation

TEM was carried out on either the Philips EM400 or EM420 electron microscopes, operating at 100kV. For the carbon replicas, both bright field and dark field imaging was used to investigate precipitation, and in all cases a selected area diffraction (SAD) pattern was obtained to verify that the particles found were NbC. For thin foils a variety of different diffraction conditions were used, although g vectors around the [110] zone were found to be particularly useful. EDS (energy dispersive spectroscopy) analysis was carried out using the LINK XL system to determine the presence of microalloyed elements in these precipitates.

4.4.3. Quantitative Metallography

4.4.3.1. Sample Area

To allow a quantitative metallographic study of the precipitated particles, random areas in the replicas were selected and photographed. These random photograph samples were printed and examined by eye. Measurements were made of particle size, inter-particle spacing and precipitate volume fraction.

Sample areas in foils were possibly less random, as the amount of area available to study was much lower compared with replicas. Areas of subgrain structure were photographed, from which the subgrain size was measured.

Prior to quantitative work, the microscope magnification was calibrated using a standard grid of known spacing. Micron markers given throughout this text refer to the corrected values.

4.4.3.2. Particle Size Distribution, Volume Fraction and Spacing

Particles were measured from TEM micrographs by use of an optical Lupe magnifying scale. These particles were measured in two directions; this allowed a measure of particle aspect ratio. At least 100 particles were counted to give reasonable statistical relevance. Typically, 200 particles were counted per sample, and errors were calculated as given in equation 4.3.

The particle volume fraction was measured from TEM micrographs of replicas. This was done by measuring the area fraction from micrographs. This method of volume fraction determination is fraught with danger, as the extraction efficiency in replication is never 100%. Thus, volume fraction measurements underestimate the true volume

fraction; nevertheless, they can be used as comparative reference between different test conditions if the extraction efficiency remains constant. This assumption is not unreasonable, as all samples were made by the same person, using the same equipment, preparation method, and etchants. Measurements of volume fraction were not completed for all test specimens.

The inter-particle spacing was also measured. The average spacing between particles was determined from random photomicrographs, where the distance from each particle centre to that of its nearest neighbour was measured. Errors were handled using equation 4.3. Measurements of inter-particle spacing were not completed for all test specimens.

4.4.3.3. Subgrain size

A quantitative assessment of the subgrain size in the deformed material was carried out using thin foils. These specimens were from tests at the lower deformation temperatures, and commonly showed microband structures. Measurement of subgrain size in these structures was carried out both parallel and perpendicular to the dominant microband walls – thus measuring the spacing of the dense dislocation walls and the size of the cell blocks. Typically, 200 subgrains were counted per sample, and error bars calculated using equation 4.3.

4.5. Phase Identification: X-ray Diffraction

In order to verify that the structure of the Fe-30%Ni-Nb alloy was fully austenitic, x-ray diffraction was undertaken. A specimen approximately 25×15×4mm was prepared from the as-received material. This was ground to a 1200-grit flatness on silicon carbide

paper, and then underwent a 2-theta scan using the Siemens x-ray texture goniometer. Output was as a plot of intensity vs. angle.

4.6. Hardness Testing

The hardness testing of deformed testpieces was carried out on the Leco-400 microhardness testing machine, using a load of 0.25kgf. Sampling was carried out at random on the specimens, and errors were calculated by using equation 4.3. Errors would be large as only 12 indents per sample were taken.

4.7. Spectroscopic Imaging in Graz

An opportunity arose to carry out some spectroscopic imaging of Fe-30%Ni-Nb samples in the laboratories of Professor Hofer, in the Department of Engineering in Graz University, Austria. Their previous work had used spectroscopic imaging to produce elemental maps [e.g. Hofer *et al.*, 1996]. Work was carried out in Graz by the Hofer group in conjunction with Professor Mark Rainforth from Sheffield University, using a Philips CM20 transmission electron microscope operating at 200kV, with a LaB_6 filament, and fitted with a Gatan Imaging Filter (GIF). This work involved conventional imaging and energy filtered imaging using the relevant absorption edges (e.g. Nb K-edge). This process would be useful for the study of small Nb-containing particles [Rainforth *et al.* 2002].

The work presented here was carried out using thermomechanically-processed specimens of Fe-30%Ni-Nb. The deformation conditions for these samples were as follows: reheated for 900s at 1250°C, air cooled to 950°C, deformed to a strain of 0.45, held for 100s, re-strained to an overall strain of 0.9, then quenched. Testing was carried

out under a constant true strain rate of $10s^{-1}$. From this testpiece, conventional TEM thin foil specimens were prepared by grinding, thinning, and electropolishing.

Zero-loss bright field images were collected, along with filtered images of the corresponding microstructural region. This results in Nb and Fe maps of these regions of interest.

5. RESULTS

5.1. Phases Present

Figure 5.1 shows the x-ray diffraction data. This shows peaks corresponding to γ-iron only. The importance of this is that the only phase present is an iron-nickel solid solution of austenite, and that no α-iron or intermetallic phases were present in a measurable volume fraction. This result was confirmed in TEM studies, as detailed later. This is expected when considering the kinetics of phase change – the phase diagram suggests that transformation should occur (see Figure 2.20), but austenite is stable to temperatures below which diffusion is very slow, thus the metastable iron-nickel austenite only is present.

5.2. Plane Strain Compression Testing

5.2.1. Homogeneity of Deformation

Figure 5.2 is a collage of optical micrographs showing the plastic flow in a typical PSC test specimen to a strain of 0.5 at a deformation temperature of 950°C. The flow lines show the inhomogeneous nature of the flow. This collage can be compared with results from finite element modelling techniques, as seen in Figure 2.23 for a stainless steel specimen of comparable geometry [Mirza and Sellars, 2001]. This shows the local inhomogeneity of strain, strain rate and temperature distribution. Regions in the corners of the specimen show higher strain rate values, along with the diagonals to the midplane, where a peak in the strain and temperature also exist. This means that more rapid recrystallisation could be expected along these channels. These regions are referred to as the slip-line field. Meanwhile, central regions show strain and strain rate values much nearer the desired values. This inhomogeneous distribution is important when selecting the location for TEM specimens for microstructural characterisation. In

the present work, all TEM specimens were taken from the central region, with an almost uniform strain distribution, except where noted otherwise.

5.2.2. Flow Curves

All flow curves displayed within this section are true stress-true strain plots, and were carried out at a constant true strain rate.

The single-compression stress-strain curves are shown in Figure 5.3. These curves show the single-compression flow curves for deformation at temperatures between 900 and 1050°C. The temperature effect on flow stress is as expected, that at lower temperatures the material is stronger. Note that there is no evidence of dynamic recrystallisation during deformation at any temperature.

Figure 5.4 shows the flow curves resulting from double deformation PSC testing (for a constant delay time of 10s) at temperatures between 900 and 1050°C. As seen in the single-deformation data, deformation at lower temperatures shows increased flow stress. Appreciable hardening occurs on the second deformation at low temperatures (900 and 950°C).

The double deformation curves at specific temperatures, shown in Figures 5.5-5.8, vary only in interpass delay time and give a representation of softening/hardening kinetics. These can be compared with the double deformation schematic, Figure 4.5, where areas relating to softening and hardening are identified.

The flow curves for deformation at 900°C are shown in Figure 5.5. All of the interrupted tests at this temperature show an increased flow stress compared with the

single-deformation curve following the delay. The amount of hardening following the delay was considerable, and hardening occurs for all interpass delay times. With reference to Figure 4.5, the area A is very small in this case for all delay times; this shows the slow progression of softening at 900°C.

Figure 5.6 shows the flow curves for deformation at 950°C. As with the 900°C tests, hardening is seen following the delay for all interpass times. The 1000s test also shows appreciable softening upon restraining. Hardening was still occurring, as seen by the increased flow stress following the strain delay – area B in Figure 4.5 increases, but appreciable interpass softening also occurs, signified by the size of area A, which is increased when compared to the 900°C results.

Figure 5.7 shows the flow curves for deformation at a test temperature of 1000°C. Here, no hardening is observed following the strain delay, and all of the curves fall back upon the control curve. The extent of the interpass softening seen increases with hold time (area A increases).

Figure 5.8 shows the flow curves for 1050°C tests. Here the double-deformation curves are approximately coincident with the single-deformation curve, showing only softening (area B is non-existent). The softening increases with increased interpass delay time (area A gets larger).

5.2.3. Temperature Data

There are two important temperature considerations during deformation testing other than the nominal test temperature; these are the time-to-quench and the effect of deformational heating.

5.2.3.1. Quench

Typical quench data are shown in Figure 5.9. This shows that there is a finite time between the finish of deformation and the quench. This occurs as the test machinery retracts the tools, removes the sample, and turns on the water spray. This series of events, or 'transfer time', takes around two seconds. A further time is then required to cool the material to a temperature low enough that no further structural change can occur: typically 1-2 seconds to go below 800°C. The mean transfer time was 2.3 seconds, while the mean water quench time was 1.4 seconds, giving a mean total time of 3.7 seconds. The water quench time was found to be a weak function of temperature, so the overall quench time (t_q) determined by regression was given by:

$$t_q(\text{seconds}) = 2.29 + (0.0111T_{test} - 9.326), \tag{5.1}$$

where T_{test} is the test temperature in °C. This means that the material is held at high temperature for a significant amount of time, which is clearly important, because static change can occur within such periods, and therefore quenched microstructures are not truly representative of the final deformation condition.

5.2.3.2. Deformational Heating

During a double-deformation test, the heating which occurs on the first deformation can raise the temperature appreciably for the second deformation, especially when testing at low temperatures, and with short interpass times. Therefore, the stress-strain data are corrected for temperature by calculating the parameter β, which is defined by the flow stress (σ)/Zener-Holloman parameter (Z) relationship:

$$Z = \dot{\varepsilon} \exp\left(\frac{Q_{def}}{RT}\right) = A \exp \beta\sigma, \tag{5.2}$$

where Q_{def}, R, A and β are constants. For constant strain rates, this can be used to relate stress values at different absolute temperature values (subscripts 1 and 2) by:

$$\sigma_1 = \sigma_2 + \frac{Q}{\beta R}\left(\frac{1}{T_1} - \frac{1}{T_2}\right) \tag{5.3}$$

This involves obtaining data at two different strain rates to allow a determination of β. Q_{def} was determined using Arrhenius-type plots to be 400kJ/mol. This correction was used to compensate for small discrepancies between the actual test temperature and desired test temperature to ensure direct comparisons between tests. The value of β during testing was determined as 0.06. This correction was used to correct temperatures in all results shown here. As an example, the correction at 900°C would be ±5.8MPa for a 10°C temperature discrepancy.

5.3. Fractional Softening Curves

Fractional softening values, determined from the flow curves, were calculated for all test conditions. The fractional softening values are plotted as a function of delay time in Figure 5.10. This shows the softening/hardening occurring between passes during double deformation testing. At high test temperatures (1000 and 1050°C) the material softens between passes, with increased softening seen at longer delay times. At low temperatures (900 and 950°C) no softening is seen, but interpass hardening occurs, increasing with time to a peak, then falling off. The peak hardening for both 900 and 950°C tests corresponds to an interpass time of 100 seconds.

The microhardness values measured from test specimens are shown graphically in Figure 5.11. The error bars are quite large as only a small number of tests were carried out. The hardness values were used to calculate the fractional softening based on hardness, using the equation:

$$FS = \frac{H_{one-hit} - H_{test}}{H_{one-hit} - H_{soft}}, \tag{5.4}$$

where the hardness value subscripts refer to the one-hit hardness, the double-hit test hardness and the hardness in the 'soft', or annealed state. These data give the fractional softening as a function of delay time, as shown in Figure 5.12. This shows a similar shape to the fractional softening as determined from the flow curves, Figure 5.10. Note that this plot was based on only twelve hardness measurements per sample.

5.4. Optical Microscopy

5.4.1. Imaging

5.4.1.1. Reheated Material

The rolled material was reheated and water quenched in order to determine the initial austenite grain size, and check niobium solubility. The maximum reheat temperature available before PSC testing was 1250°C, thus reheat trials were conducted at 1200 and 1250°C. Figure 5.13 shows optical micrographs of the resulting grain sizes from some of the reheating trials. It would appear that the niobium was not taken fully into solution at either of these temperatures. A reheat schedule of 15 minutes at 1250°C was used for all deformation tests. The corresponding original austenite grain size (d_0) was measured as 393±15μm.

These data can also be plotted as a function of time to give grain growth kinetics during reheating, see Figure 5.14. The data show no evidence for abnormal grain growth during reheating, although a full investigation of grain growth kinetics was not carried out.

5.4.1.2. Deformed Material

Optical microscopy was used to evaluate the state of the microstructure following different thermomechanical cycles. Figure 5.15 shows the effect of temperature on recrystallisation kinetics. At low test temperatures, the recrystallisation was very limited, as seen in a) and b), and is typically confined to those regions of higher relative strain and strain rate, discussed in Section 5.2.1. Grain pancaking and elongation was seen at these lower temperatures. At higher temperatures, recrystallisation was much more extensive, and occurred more homogeneously. Figure 5.16 shows deformed twin boundaries in the 900-1-DD sample, while Figure 5.17 shows the presence of microbands in the deformed material.

5.4.1.3. Nature of Recrystallisation

Although macroscopically the recrystallisation was seen in the slip-line field regions, recrystallisation nucleated preferentially on grain boundaries, grain triple points and deformation bands was also found upon microscopic examination. Such heterogeneous nucleation is shown in Figure 5.18, where recrystallisation is localised on grain boundaries. At high temperature, recrystallisation appeared to nucleate on all grain boundaries, although those in the slip-line field regions were in operation first. Figure 5.19 shows nucleation on deformation bands and twin boundaries, while Figure 5.20 shows grain boundary nucleation in more detail.

5.4.2. Quantitative Optical Metallography

5.4.2.1. Fraction Recrystallised

The fraction recrystallised was measured for all test specimens, and the resulting data are given in Table 5.1. Note that these values were taken following the quench. Fraction recrystallised data are probably best illustrated graphically, as shown in Figures 5.21-5.24.

Figure 5.21 shows the effect of strain on the extent of recrystallisation for all test temperatures. It is apparent that increased strain increases the fraction recrystallised.

Figure 5.22 shows the same data plotted as a function of delay time. This shows that the fraction recrystallised is insensitive to delay time but, as expected, is sensitive to the test temperature. As the recrystallisation occurs during the quench time, it may be that this has the dominant effect upon recrystallisation, and what is seen is due to slight variations in either quench time or strain.

Figures 5.23 and 5.24 show the fraction recrystallised data from the hit-hold-quench specimens. Figure 5.23 shows the effect of temperature on the extent of recrystallisation, with the hold time constant at 10 seconds. At low test temperatures (900 and 950°C), only a small percentage recrystallised is seen, while at high test temperatures, recrystallisation has advanced to a much greater extent. Figure 5.24 shows the effect of hold time on recrystallisation kinetics during isothermal tests at 950°C. Recrystallisation occurs to around 5% within 1 second. This level of recrystallisation remains constant as a function of hold time, until above 100 seconds. After 100 seconds, the extent of recrystallisation increases, to reach 20% by 1000 seconds.

5.4.2.2. Deformed and Recrystallising Grain Size

Although a full study of the recrystallising grain size was never intended, Orsetti-Rossi style measurements were carried out on some specimens [Orsetti Rossi and Sellars, 1997]. These gave full details of both the deformed and recrystallising grain sizes, which have been summarised in Table 5.2. Figure 5.25 shows the effect of temperature on deformed grain size and aspect ratio for double deformation samples. These data show how the grain size changes with temperature during double deformation testing. At a deformation temperature of 900°C, the mean deformed grain size was 494×210μm, while at 950°C it was 347×152μm, and at 1050 it was 77.5×77.9μm. For a material of initial grain size of 393μm undergoing plane strain compression, the grain size after deformation can be calculated. The predicted deformed grain size during PSC testing is shown in Table 5.3 for different levels of strain, and taking into account lateral spreading; predicted aspect ratios are also shown.

5.5. TEM Observations

5.5.1. TEM Imaging

TEM work has been carried out using both carbon replica and thin foil samples. Images from thin foils have been used to look at the deformed matrix, the subgrain structure therein and precipitation in the matrix. Carbon replicas show no microstructural features, and are used only for study of the precipitate population. Much of the TEM work carried out has concentrated on specimens tested at lower deformation temperatures - this is because when strain-induced precipitation occurs, it does so at these lower temperatures.

5.5.2. TEM Investigation of the Deformed Matrix

TEM micrographs of thin foils show the microstructure of the deformed matrix. Figures 5.26-5.34 show the microstructure following testing atdifferent temperatures. It is of note that the substructure is dominated by the presence of microbands. It can be seen that these elongated structures are made up of cell-blocks bounded by dense dislocation walls. The cell-block size measured both parallel and perpendicular to the microbands is given in Table 5.4. At 900°C, the microbands formed are narrow, and show relatively few internal cell walls. At 950°C, the microband width is greater, and many more cell blocks exist within these microbands; thus the dense dislocation walls are of a similar spacing to the internal cell walls. This can often give an equiaxed look to the micrograph images, although definite microband walls are prominent in many images. At 1050°C, fewer data were collected, as the specimens showed a greater amount of recrystallisation. The microband width was 0.57μm, while the cell-block length was 1.02μm – much larger volume elements than seen at lower temperatures, while the recrystallised material showed an equiaxed subgrain structure, of mean size 0.42μm, as shown in Figure 5.33.

It has been suggested [Duly *et al.*, 1996] that the angle that the microbands make to the deformation axis is around ±30° to the rolling direction, thus the angle to the effective rolling direction was measured from TEM specimens of known 'rolling direction'. The microband angle was measured, and was found to be at 25.4±4.6° to the longitudinal plane, the effective rolling direction. Sets of crossed microbands were frequently seen, and these can give the appearance of an equiaxed subgrain structure; Figure 5.32 shows crossed microbands. Where two sets of microbands crossed, the angle between them was measured as 60.0±3.9°.

5.5.3. Strain Induced Precipitation

Strain induced precipitation was seen to occur following deformation at temperatures below 1000°C. TEM images of strain-induced precipitation for different thermomechanical conditions are shown in Figures 5.35 to 5.42. The indexed diffraction pattern in Figure 5.35 shows that the reflections indicate that the particles present were NbC. It is of note that the precipitation seems to occur non-randomly, whether in a cell-like manner as in Figure 5.37, or in a more linear configuration as seen in Figure 5.36. Both of these images show heterogeneous precipitation.

EDS analysis was also carried out for many particles, to verify the presence of niobium. Some of these scans are shown in Figures 5.43 to 5.46, where EDS analysis was carried out for the different particle morphologies seen (most particles were either rounded or cuboid in nature). The EDS analysis showed that niobium was present in all of these morphologies.

5.5.4. Quantitative Metallography of Precipitates

Particle size distributions frequently showed different-sized populations within specimens; this is shown visually in Figure 5.38, which shows two different sized particle populations. The different precipitate populations are due to different precipitation events, and are discussed later. In a double-deformation test, precipitation occurs twice: between deformations, and again after the second deformation.

It was found that quantitative data collected from images at different magnifications produces different results – finer particles were seen at higher magnifications (175-300,000×), while larger ones were imaged at lower magnifications (>60,000×). This happens because the finest particles are not clearly seen at the lower magnifications. As

an example, Figure 5.47a) shows the particle size distribution for the 950-1000-DD sample, which is bimodal. These data were separated by using high and lower magnification imaging, to obtain the two distributions seen in Figure 5.47b) and c). This bimodal precipitation was typical of all 950°C double-deformation specimens; at 900°C, while such fine precipitates could not be distinctly resolved, it is probable that they are present. It was also found that the 1 second data were unreliable, thus results for 1 second delay times are not presented. This was due to both the difficulty of imaging small populations, and the lack of reliability of extraction replicas to successfully remove particles <5nm in size.

The presence of the fine particle population is attributable to the second precipitation event, occurring between the second deformation and quenching. Single-deformation testing sees this type of precipitation event only. Such fine-scale precipitation is shown in Figure 5.40, where the specimen has been subjected to a single-deformation test. This fine-scale precipitation has occurred between testing and quenching, and the precipitation is shown clearly, without any distraction by larger particles.

The larger particle population, seen in the double-deformation specimens, has precipitated following the first deformation, and then subsequently grew during the interpass hold time. The size distribution of this population is therefore dependent on the hold time. It is this distribution that is primarily of interest in the present work, as this is the particle population which affects recrystallisation events between passes. The presence of two populations can give a deceptive measure of the particle size data. In order to avoid this, the particle size data for the double-deformation tests were taken from images at a magnification of 60,000×, thus counting only the particles precipitated between deformations. The size distribution data are shown in Figures 5.48 to 5.58. The

effect of hold time on the mean particle size at both 900°C and 950°C is summarised in Figure 5.59. This shows the particle growth kinetics, and allows a comparison of particle sizes between tests. It appears that, for equivalent times, the particle size is in the order: 950-DD > 950-HHQ > 900-DD.

The particle volume fraction was calculated for the samples shown in Table 5.5. These values are the apparent volume fractions; nevertheless, they allow a comparison between the test specimens here. These values cannot be taken as actual volume fraction values due to the problems associated with the extraction efficiency of carbon replicas.

The inter-particle spacing was measured for the 950-100-DD specimen. This was found to be 56±6nm. This has allowed a calculation of the expected strength increment due to precipitation hardening, using Equation 2.5. The value of the shear modulus at elevated temperature (absolute) was given by [Frost and Ashby 1982]:

$$G = 8.1\times10^{4}\left[1-0.91\left(\frac{T-300}{1810}\right)\right]\text{MPa}. \qquad (5.5)$$

The modulus at 950°C is therefore 42.9GPa, so the increment in yield strength due to precipitation under these conditions is calculated as 57.3MPa.

5.6. Spectroscopic Imaging

Some of the results of the TEM work carried out in Graz have been published [Rainforth *et al.* 2002], while some of the images are seen in Figures 5.60 and 5.61. These each show a zero loss filtered bright field (BF) image, and electron spectroscopic images, of the same region in the sample. The spectroscopic images, b) and c), show

jump ratio images for iron and niobium. This technique shows the presence of fine precipitates, and these particles unquestionably contain niobium. This work was carried out using a double-deformation specimen which had been reheated to 1250°C for 15minutes before testing at 950°C. The pre-strain was to 0.45, then a hold of 100s, followed by a further strain of 0.45, to a total strain of 0.9; the strain rate used was $10s^{-1}$.

This method shows precipitation in foils on a very fine scale – for example, of the five particles seen on a subgrain boundary in Figure 5.61, the three larger ones are ~5nm in size, while there are two very fine particles in between these. Particles like this are thought to be of the size directly responsible for the pinning of boundary motion.

6. DISCUSSION

6.1. Introduction

An understanding of the precise deformation mechanisms that occur during the hot deformation of steel has been a long-standing objective. Unfortunately, the direct study is impossible due to the unavoidable phase transformation that occurs in steels upon cooling from hot working temperatures. Therefore, thermomechanical testing of the Fe-30%Ni-Nb alloy has been carried out to simulate the hot working of a microalloyed steel austenite. In this alloy, the austenitic structure is stabilised to room temperature by the presence of 30wt% nickel. This means that such iron-nickel alloys can be studied in the as-deformed state, allowing a full characterisation of the hot-worked microstructure.

For such alloys to be useful as an austenite analogue, they must behave in a similar manner to C-Mn based steels. This means they must show similar deformation and recrystallisation behaviour during hot working to C-Mn based steels and, in the case of the present work, must show similar precipitation characteristics. The ability of the Fe-30%Ni-Nb alloy to follow the microstructural behaviour of conventional C-Mn based microalloyed steels is fundamental to its further use for the study of the structure of worked austenite. Thus, the comparative behaviour of the Fe-30%Ni-Nb and conventional microalloyed steels are thoroughly discussed in a later section.

6.2. Microstructural Behaviour during Hot Working

The Fe-30%Ni-Nb was deformed by hot plane strain compression. This was carried out mainly by double deformation testing, where the material is deformed, held, deformed again, and then quenched. Investigations were carried out on the alloy to follow microstructural change in the material during the different stages of hot working.

Reheating phenomena are discussed in this section, then recrystallisation and precipitation following deformation.

6.2.1. Reheating

Reheating was carried out in order to dissolve as much of the niobium as possible into the austenite. The reheating schedule chosen was limited by the maximum temperature of the PSC reheating furnace, which was 1250°C. Only partial solution was anticipated at this temperature from the solubility calculations [Whiteman and Argent 1998], which suggested that approximately 0.08wt.% Nb (i.e. around 80% of total Nb) would be in solution at 1250°C. Thus, due to this temperature limit, and the relatively large niobium content of the alloy (0.1 wt.%), not all of the niobium was taken into solution during reheating. A full solubility study was not undertaken during the present work, although TEM examination of carbon replicas showed the presence of undissolved niobium carbide following heat treatment at 1250°C.

The presence of these undissolved particles would not be expected to have a major effect on the strain-induced precipitation in the alloy. Large undissolved particles would be expected to act as nucleation sites for precipitation following deformation at lower temperatures, and during reheating, the accelerated coarsening of any large undissolved particles present can occur [Gladman 1997]. This will reduce the niobium available for fine-scale precipitation, and less fine-scale precipitation is expected than if all of the niobium were dissolved. However, these particles were widely dispersed and therefore the effect would be local. Given the numerous heterogeneous nucleation sites offered by the dislocation substructure, which were, in comparison, much more uniformly distributed, it seems highly unlikely that the undissolved particles would have much effect.

The reheating trials allowed the selection of an appropriate reheating time, to maximise the niobium in solution without substantial grain growth. The fifteen-minute reheat time selected was seen to take sufficient niobium into solution, while the initial austenite grain size grew from 67μm to 393μm during reheating. This grain size is quite large, especially when compared to reheated grain sizes seen in some of the literature for C-Mn steels. The grain sizes found during industrial processing can be of this order, and some experimental work on grain size during reheating shows reheated austenite grain sizes nearly this large. For instance, work by Kosazu *et al.* (1977) and Tanaka *et al.* (1977) found that the austenite grain size in conventional microalloyed steels, with comparable Nb levels, reheated at 1250°C were in the size range 250-300μm. The large grain size is of concern however, in that the present work is meant to be simulating finish rolling of microalloyed steels, where the starting grain size is generally below 50μm. It would perhaps have been prudent to put in a roughing deformation at a temperature of ~1100-1150°C to induce recrystallisation and reduce the starting grain size to a value nearer to those encountered industrially. Another point of view is that the present work is a simulation of process conditions, and is concerned with the relative changes to the original microstructure, and the starting grain size is therefore of less concern.

6.2.1.1. Grain Growth during Reheating

From analysis of the grain growth data shown in Figure 5.14, a grain growth relationship was calculated for this material:

$$d^{4.55} = d_{rex}^{4.55} + At\exp\left(\frac{Q_{gg}}{RT}\right) \qquad (6.1)$$

where $A=1.75\times10^{25}s^{-1}$ and $Q_{gg}=-493900$ kJmol^{-1}. This relation, along with the actual data and some of the published relationships for C-Mn based steels from the literature, is shown for comparison in Figure 6.1. The present data compare well with the published work, in that they fall between the predictions of other authors, although there is a large variance between the values found by other workers. This is useful, as it suggests that although this alloy is not a C-Mn based steel, it does behave in a manner similar to C-Mn based steels.

6.2.1.2. Abnormal Grain Growth.

No abnormal grain growth was seen during the reheating tests; at 1200 and 1250°C only equiaxed grains were seen with a normal grain size distribution. The absence of abnormal grain growth suggests that it has either not occurred, or has finished at a temperature below 1200°C. Gladman (1966) suggested that abnormal grain growth is prevented by a distribution of fine particles (see Equation 2.29). If abnormal grain growth has not occurred here, then despite partial dissolution, there must still be enough particles of sufficiently small size to prevent it. The Gladman equation (2.29) predicts that a particle size as large as 50nm ($R_0=150\mu m$, $F_V=3\times10^{-5}$ and $z=1.5$) would prevent abnormal grain growth. At higher temperatures still, further dissolution would occur, giving a lower particle density, also the remaining particles may coarsen due to Østwald ripening, thus allowing abnormal grain growth. Using the Palmiere *et al.* (1994) solubility product, and their relationship between grain coarsening temperature and the dissolution temperature (equation 2.30), gives a T_{DISS} value of 1377°C, and a T_{GC} value of 1252°C. This would suggest a higher reheat temperature than the 1250°C used would result in the onset of abnormal grain growth in this material, although in reality the T_{DISS} value would be lower due to the effect of Ni. Interestingly, Palmiere *et al.* (1994) found that in an industrial C-Mn steel of comparable Nb-content (0.08%C-1.43%Mn,

0.09%Nb, 0.0008%N) that the grain coarsening temperature was 1200°C. This may therefore suggest that in the present material, such coarsening is complete below 1200°C. Either way, following reheating at 1250°C (and also at 1200°C) a coarse, uniform equiaxed austenite grain structure was developed.

6.2.2. Flow Curves

In this section, the PSC flow curves are discussed and in particular the relationships between the flow curves and the microstructures developed are of interest. The stress-strain curves for the Fe-30%Ni-Nb alloy have been studied at length, and are discussed below. Figures 5.3 and 5.4 show the effect of deformation temperature on flow behaviour for single- and double-deformation testing respectively. The single-deformation curve shows increased flow stress with lower deformation temperatures. The same temperature effect is seen in the double-deformation curves, with increased flow stress at lower temperatures, but there is an additional temperature effect following the strain delay. The stress levels in the second deformation vary following the delay, depending on the temperature.

6.2.2.1 Effect of Temperature on Flow Stress - 1000-1050°C

At high deformation temperatures (1050 and 1000°C), the flow stress found upon reloading increases to the level which would have been achieved in a single deformation test to the same strain, as seen in Figures 5.7 and 5.8. Some inter-pass softening is often seen, as recovery and recrystallisation occur during the static hold period. The extent of softening can be determined from the flow curves by many methods, but in this case, by measuring the area under the flow curve. If a material were to fully soften between passes, then the second deformation flow curve would fall directly back on that of the first deformation. Optical microstructural investigations revealed that specimens tested

at these higher temperatures (1000 and 1050°C) show much more advanced recrystallisation than low temperature specimens (900 and 950°C), see Figure 5.22. The recrystallising grains were equiaxed, and were finer than the original austenite grain size (393μm). As recorded in Table 5.2, the material recrystallised to a grain size of ~80μm after the first deformation, and recrystallised to ~35μm following the second pass. This inter-pass recrystallisation may bring about an increase in flow stress during the second deformation of a double hit test, through a Hall-Petch effect. This would lower the amount of softening recorded during fractional softening measurements.

6.2.2.2. Effect of Temperature on Flow Stress – 900-950°C

At lower temperatures (950 and 900°C), the flow stress responses seen following the interpass delay show a hardening effect, where the strain in the second deformation is increased above the value of a single deformation (Figures 5.5 and 5.6). The hardening effect observed can be directly attributable to strain-induced precipitation between deformations. This strain-induced precipitation provides a fine network of precipitate particles, which pin boundary motion. This makes recrystallisation difficult in these low temperature specimens, with limited recrystallisation seen at 950°C, and effectively none at 900°C. The maximum hardening increment at both 900 and 950°C appears to be ~30-35MPa which is just over half the 57MPa calculated in section 5.5.4. This may be within the limits of experimental error, and is likely to be due to inaccuracies in the measurement of interparticle spacing from carbon replicas. Precipitation events are discussed in more detail below.

6.2.2.3. Dynamic Recrystallisation

No dynamic recrystallisation was seen at any of the test temperatures. This was perhaps unexpected, as it has been seen in the non-microalloyed Fe-30%Ni, even at fairly low

temperatures [Almaguer 2002], and is often seen in microalloyed steels at higher test temperatures. The lack of dynamic recrystallisation may be because the strain rate used was fairly high ($10s^{-1}$), which, along with the presence of niobium in solution, prevents dynamic recrystallisation at the strain values used here. Le Bon *et al.* (1975) found that at high strain rates (12.5 and 33.3 s^{-1}), then a supersaturated austenite can prevent dynamic recrystallisation even after very large strains. Some test samples were tested to higher strain, and higher temperature, and eventually dynamic recrystallisation was seen to occur in the present material at 1050°C under a strain rate of $10s^{-1}$.

6.2.2.4. Effect of Strain on Flow Stress

Although not in the main test matrix, double-deformation tests to higher strains were carried out, Figure 6.2. These true stress-true strain curves show an even greater strengthening increment than the ε=0.25+0.25 tests for both 10s and 100s hold times, with an increase in the flow stress of ~50-60MPa; this is due to NbC precipitation. Although no study was attempted, it is anticipated that the increased hardening is because there is a greater volume fraction of precipitates formed following deformation to higher strains. This would be expected due to the higher stored energy in the matrix associated with increased deformation, with more deformation bands and dislocations introduced to the matrix. These would act as potent sites for the nucleation of precipitated particles, thus increasing the precipitate density. Hence, the hardening increment is larger than values seen at the lower strain. Due to the difficulties in particle volume fraction determination [Ashby and Ebeling 1966], only limited experimental work has been carried out on the effect of strain on precipitate volume fraction. Much more work has been carried out on the effect of strain on precipitation kinetics, with faster precipitation seen with increased strain, e.g. Medina and Quispe (1996b).

6.2.3. Fractional Softening – Time Curves

Double-deformation tests have been used for many years to detect softening kinetics [Cordea and Hook 1970] and precipitation events [Kwon and DeArdo 1986]. During such testing, both a single-deformation and double-deformation test are carried out under identical conditions. The flow curves are then compared, and any difference in flow stress between the second-deformation of the double-deformation test and the single-deformation test is due to events that have occurred during the delay time between deformations. Such differences are quantified as fractional softening values, and are directly attributable to static microstructural events occurring during the strain delay. Inter-pass softening is due to recovery and recrystallisation, while hardening is due to precipitation between deformations. By varying the testing conditions, the effect of changing deformation variables on this hardening/softening can then be studied. The delay time has a profound effect on the flow curve, and this has been quantified by the fractional softening measurement. Figure 5.10 shows the fractional softening as a function of interpass time. This graph is the key to understanding the microstructural changes which occur during the hot working of this alloy. This plot shows two different softening regimes, dependent on the deformation temperature.

6.2.3.1. Fractional Softening at Temperatures ≥1000°C

At high temperatures (T_{def}≥1000°C), the materials showed only softening – with increased softening observed with increased time, presumably with Avrami kinetics. In these high temperature regions, niobium is present in solution, and this may slow the recrystallisation kinetics by solute drag on the boundary [Akben *et al.* 1981]. No precipitation was expected at this temperature as the supersaturation was low, and thus the driving force for precipitation was low. No strain-induced precipitation was found during TEM investigations at these temperatures. Recrystallisation occurred rapidly

(Figure 5.15), as it was unimpeded by precipitation at these temperatures. It is also of note that the higher the temperature, the faster the softening kinetics, due to the increased boundary mobility.

6.2.3.2. Recrystallisation Kinetics Determined from Fractional Softening Plot

The fractional softening-time plot can also be used to give a rough estimation of the recrystallisation kinetics. The overall fractional softening measurement includes a contribution from recovery, and this has been estimated at between ~20-40% [Djaic and Jonas 1973, Petkovic *et al.* 1975]. If 20% softening is attributed to recovery, then half of the remaining 80% softening would give the time to 50% recrystallisation value (t_{50}), which is therefore equivalent to 60% overall softening (i.e. the time taken for 60% softening = time taken for 50% recrystallisation). Similarly, for a 40% softening contribution due to recovery, then the t_{50} would be equivalent to 70% overall softening. This is shown in Figure 6.3, which shows the same data as Figure 5.10, but normalised so that the maximum softening recorded is set at 100%. Reading from the graph gives t_{50} values of ~9s and ~20s for 1000°C and ~6s and ~10s at 1050°C deformation temperatures respectively. Table 6.1 compares these values with some calculations made using the deformation variables used here, and using t_{50} relationships for C-Mn based steels from the literature (Table 2.5). Although the alloy has a high nickel content, the t_{50} values still compare with most of those in the literature. The recrystallisation kinetics of the present alloy are perhaps a little faster than the values calculated for C-Mn based steels. The values calculated from the literature show a lot of spread, thus no real comparison can be made. The actual recrystallisation values measured from the hit-hold-quench experiments were 49.8 and 69.9% for a nominal hold time of 10s. This suggests that the values for recrystallisation kinetics derived from the fractional softening-time plot in the present study are accurate. Previous work by Palmiere *et al.*

(1993, 1996) had also used quantitative optical microscopy in order to verify fractional softening data, thus proving that the technique is good.

6.2.3.3. Fractional Softening and Hardening at Lower Temperatures

At lower temperatures (950°C and below), no softening is seen in the fractional softening-time plot, while hardening occurs and varies as a function of time. This observation arises from precipitation hardening. Figure 5.10 shows that, initially, no significant softening occurs, and with increased delay time, the hardening increases to a peak at 100s. Following this peak, the material does begin to soften, and the hardening increment is seen to fall off with increased time at both 900 and 950°C. This response is indicative of the precipitation kinetics, as discussed below. The hardening peak in the plot occurred at 100s for both temperatures, while the hardening increment recorded was greater at 900°C than at 950°C. The shape of these two curves has been further verified by the measurement of fractional softening from hardness data (Figure 5.12). The hardness data show similar hardening, increasing to a peak at 100s, followed by softening.

6.2.4. Precipitation Kinetics

The time-dependent hardening response is a representation of the precipitation kinetics. Precipitation hardening was detected after 1s at 900°C, and after 10s at 950°C, indicating that strain-induced precipitation had commenced within these times. Precipitation density increased with time, providing a greater hardening increment. As the isothermal delay time increases, the particles are increasing in size, and larger particles have a less potent effect on precipitation hardening (equation 2.5). Thus a trade-off between fresh fine-scale precipitation and growth of the existing particles occurs. This gives a peak in the hardening plot – in this case at 100s, which suggests

that much of the precipitation is complete by that time. This indicates that precipitation starts within 1 or 10s (depending on the temperature) and is nearly complete at ~100s. Precipitation this fast is certainly possible – Arieta (1992) using a conventional microalloyed steel of similar composition (0.06%C-0.1%Nb-1.5%Mn-0.03%Si-33ppm N) to the present alloy found precipitation at 920°C in 1.5s (and at other temperatures between 900 and 1000°C in 1-3s). Other workers have found comparable precipitation times; often depending on the detection method used (see Table 2.4).

The present findings tie in with the work of Sun *et al.* (1993), who found that the particle number density increases with time to a maximum at around 60s, after which the density decreases as coarsening occurs. This suggests that precipitation was complete by ~60s, and this figure compares well with the peak at 100s found in the present study. The completion of precipitation seen in the present study at around 100s cannot be due to solute depletion, because further precipitation was witnessed following the second hit. This would suggest that it might be due to local solute depletion around the precipitate nucleation sites. Work by Dutta *et al.* (1992) discussed the effect dislocations have upon precipitate coarsening. They suggested that precipitation occurs at dislocation nodes in the microstructure. This then leads to rapid coarsening by pipe diffusion along the connected dislocations, leaving zones depleted of Nb. Subsequent deformation passes provide a new dislocation structure in regions where the solute remains, upon which further precipitation can occur. This is shown in Figure 6.4 [Dutta *et al.* 1992]. Recently, Dutta *et al.* (2001) advanced the earlier work, as they put forward a precipitation kinetics model which encompasses that work. This model assumed heterogeneous nucleation of precipitates on dislocation nodes, and accelerated coarsening due to pipe diffusion along dislocations. Work by Rainforth *et al.* (2002) on the alloys used in the current study has shown that precipitation does occur

preferentially on the dislocation structure, and not in the matrix. This would leave regions of solute niobium available for further precipitation during subsequent deformation. The present work appears to fit in with the literature; the mechanisms described above would explain the precipitation behaviour observed, and particle growth kinetics in accordance with dislocation pipe diffusion were observed (discussed below).

A consideration of the particle size as a function of time can be used to give information on the nucleation time. This is shown in Figure 6.5, where the particle size data have been extrapolated back to find the time for a particle size of zero for the three data sets available: 900DD, 950HHQ and 950DD. The intercepts are at ~0.5, ~0.8 and ~2 seconds. These values suggest that the nucleation of precipitation occurs within two seconds under the present test conditions.

Dynamic precipitation was not anticipated in the present work and it is generally accepted that precipitation occurs between passes. Dynamic precipitation has only ever been recorded at low strain rates (e.g. $1.2\times10^{-3}s^{-1}$, Weiss and Jonas 1980), while the strain rates used here ($10s^{-1}$) eliminate the possibility.

6.2.4.1. TEM Evidence of Precipitation Kinetics

Direct evidence of strain-induced precipitation has been seen in TEM studies of the present alloy. The data after 1s hold times are inconclusive, due to the fine size of the particles, and reliability of the replication technique. Images of hit-hold-quench specimens in this work show strain-induced precipitation after 10s, and particle size data are given for this time. Particles were seen after 1s, but were very fine, and could not be counted reliably (e.g. Figure 5.40). The double hit specimens show two levels of

precipitation. Firstly, interpass precipitation occurs following the first deformation, within the delay time. These first precipitates are of direct interest in the present study. Following the second deformation, further fine-scale precipitation occurs before the quench, while the first particle population coarsens. This gives two particle populations, as seen in Figures 5.38 and 5.47. As mentioned earlier, the first precipitation is of primary interest here, as these particles affect the interpass softening, and provide the precipitation hardening seen in the second deformation. The hit-hold quench tests provide a simulation of the precipitation and recrystallisation state between passes.

6.2.5. Recrystallisation Kinetics

6.2.5.1. Recrystallisation Kinetics – Effect of Precipitation

The presence of strain-induced precipitates at temperatures below 1000°C has a dramatic effect on the recrystallisation kinetics. These fine particles pin advancing boundaries, preventing recrystallisation. It is useful to study the isothermal FRX-hold time plot for the hit-hold-quench tests (Figure 5.24). This shows the recrystallisation kinetics at 950°C, where limited recrystallisation (~5%) is seen after 1s. Precipitation then occurs, and prevents any further recrystallisation; hence the recrystallisation is still only ~5% after both 10s and 100s. At 1000s, more extensive recrystallisation is observed – thus, a plateau is seen in the recrystallisation plot. Such a plateau could be similar to the plateaux reported by Medina and co-workers [Medina *et al.* 1993, Medina 1995, Medina *et al.* 1996]. Between 100s and 1000s, particle coarsening begins to dominate and recrystallisation can recommence, so the volume fraction recrystallised rises to ~21% at 1000s. This would provide further evidence for precipitation finishing at ~100s.

The sluggish static recrystallisation kinetics seen at 950°C were similar to those found by Janampa (1982) for a 0.06%Nb-0.09%C steel, in which all niobium was in solution following reheating. In that work the fraction recrystallised at 127s was 5%, at 5000s was 34%, and 70% recrystallised at a hold time of 61000s. The recrystallisation kinetics of the present alloy were a little faster than those of the Janampa steel.

6.2.5.2. Recrystallisation Kinetics – Effect of Deformation Temperature

Figure 5.23 shows the effect of temperature on recrystallisation kinetics for a 10s hold in the HHQ tests, for otherwise similar deformation conditions. As with the fractional softening plot (Figure 5.10), this shows two regions of behaviour depending upon the deformation temperature. At low temperature very little recrystallisation occurs (0% and 6% at 900 and 950°C respectively), while at high temperature much more recrystallisation occurs (50% and 70% recrystallisation at 1000 and 1050°C). The large increase in the extent of recrystallisation is because different processes are in operation to influence recrystallisation kinetics. At high temperatures, no fine-scale precipitation occurs following deformation and the slow recrystallisation cannot be explained by precipitation [Le Bon *et al.* 1975]. Nb in solution will provide a solute drag effect, slowing recrystallisation a little. At lower temperatures, strain-induced precipitation occurs providing a fine network of particles which pin advancing boundaries. This has a much more severe effect on recrystallisation than solute drag during hot working [Hansen *et al.* 1980, Suehiro 1998]. In between these responses falls the recrystallisation-stop-temperature (RST). This is the temperature at which sufficient precipitation has occurred in order to prevent any recrystallisation (or less than 5%), and is dependent on deformation conditions. The RST for the present alloy can be estimated directly from the fractional softening-temperature plot shown in Figure 6.6. By allowing 20% softening to account for recovery [Palmiere *et al.* 1998], then the RST for a delay

time of 10s is calculated as 973°C. This value is similar to those found under comparable working conditions in a C-Mn-Nb-steel in work by Dutta and Palmiere (2002), and is supported by the metallographic investigations made (Figure 5.23).

6.2.6. Precipitation

6.2.6.1. Particle Growth Kinetics

The particle size data, Figure 5.59, show the particle growth kinetics. The particles were larger at 950 than at 900°C, as expected. It was also anticipated that the double deformation (DD) specimens would have particles a little larger than the equivalent hit-hold-quench test specimens, as they have spent very slightly longer at the elevated temperature. The particle size data are separated, plotted against ln (time), and curve-fitted for each temperature in Figure 6.7. The slope of these plots gives a growth exponent for particles at that temperature. The data suggest that the particles grow with the $t^{1/5}$ kinetics associated with dislocation pipe diffusion, as first suggested by Kreye (1970). The exponent for 900-DD tests was 0.19, which implies pipe diffusion controlled growth. The 950-HHQ tests showed a growth exponent of 0.21, which again suggests $t^{1/5}$ kinetics. The 950-DD data exponent was somewhat higher at 0.27, predicting $t^{1/4}$ kinetics, but this is consistent with the findings of Kreye, in that as the particles coarsen, the exponent is reduced. These plots are only based on three data points each, and are by no means conclusive. However, this interesting result provides further evidence for the strain induced precipitation of fine NbC heterogeneously upon the dislocation network in austenite, as suggested in the literature [Davenport *et al.* 1977, Hansen *et al.* 1980, Palmiere *et al.* 1996, Sellars 1998, Rainforth *et al.* 2002]. This localised precipitation gives a much more potent pinning force than random matrix precipitation.

6.2.6.2. Precipitate Location – Nucleation Sites

The location of precipitates is important, as they provide much more pinning potential if they are located on subgrain boundaries rather than located randomly throughout the matrix [Hansen *et al.* 1980]. The extraction replica images in the present work show non-random precipitation, either in a cell-like manner, or in more linear arrays (e.g. Figures 5.37 and 5.36). This would suggest precipitation upon subgrain boundaries (SGBs), or upon the dense dislocation walls of microbands, depending on the substructure present. This would make sense, as these areas have a high associated energy, and would make preferential nucleation sites for precipitation. Deformed regions found in the microstructure have shown both microbands and regions containing equiaxed subgrains, which is why both linear and cell-like precipitate arrays were found in the present work. The spatial distribution of the particle strings was similar to the cell widths both for cell-like and microbanded substructures, thus providing further evidence for heterogeneous precipitation upon the substructure. When considering the linear arrays, although no quantitative measurement was undertaken, the strings of particles appear to suggest more extensive precipitation on the dense dislocation walls (DDW) of microbands, with less precipitation on the perpendicular dislocation boundaries which make up the cell-blocks. This is of interest, as it suggests that the DDWs are preferential nucleation sites, and will be subject to increased pinning when compared with the perpendicular walls.

6.2.6.3. Heterogeneous Precipitation on Dislocation Substructure

The preferential precipitation of fine NbC particles on subgrain boundaries has been thought to occur for a number of years. Davenport *et al.* (1977) reported fine-scale precipitation within 4 seconds in a 0.09%Nb-steel following hot rolling. They carried out a dark field (DF) TEM analysis of thin foils and found precipitates heterogeneously

distributed in a cell-like manner, suggesting precipitation on subgrain boundaries. Unfortunately, this method of precipitate detection can be deficient, because the dislocations also provide contrast in the DF images, and these may be confused with particles. DF analysis of carbon replicas was used by Kwon and DeArdo (1991), who found Nb(C,N) precipitation in 'localised arrays' and suggested precipitation upon austenite grain boundaries and deformation bands. Again, there are problems with such a technique, as this involves the use of carbon replicas, which do not reliably extract fine particles (less than ~5nm), and are not suitable for volume fraction determination [Ashby and Ebeling 1966]. Indeed, it is difficult to use TEM analysis to resolve fine-scale precipitation on dislocation structures, and the associated drawbacks were discussed recently [Rainforth *et al.* 2002]. This is why the present study includes results from the electron spectroscopic imaging (ESI) work carried out at the University of Graz, Austria (e.g. Figures 5.60 and 5.61). The conventional TEM work carried out for this project (replica analysis and DF imaging of foils) is subject to the limitations suggested above, while the ESI images are not limited. The ESI images clearly show fine NbC particles precipitated on subgrain boundaries and not precipitated within the austenite matrix: proof of heterogeneous nucleation. Although the particle size distribution measured during this work shows that no particles were measured of less than 2nm in diameter, it is shown by Rainforth *et al.* (2002) that the resolution of the technique was ~2nm and therefore smaller particles, expected to be present, were not detected. Subsequently to this, similar work carried out at Sheffield using a FEGTEM which has inherently better resolution, suggests that ESI can be used to image precipitates down to 0.7nm [Higginson *et al.* 2001]. Another method of studying fine precipitates is using atom probe field ion microscopy (APFIM). A study of precipitation in hot rolled microalloyed steel was carried out by Burke *et al.* (1988) using APFIM. This technique allowed detection of particles less than 1nm, but could not detect

particles larger than 5nm, thus supporting the belief that particles <2nm were present, but were not detected. APFIM has since been used by Palmiere *et al.* (1994) to detect fine Nb(C,N) strain-induced precipitates (<1nm) in microalloyed steels.

6.2.7. Precipitated Particles

6.2.7.1. Particle Size Data

The particle size distributions found using the extraction replica technique were typical of strain-induced precipitation in microalloyed steels. Other workers have found particles of similar size, and details are given in Table 6.2 for precipitation at 900°C, along with the present results for the 900-DD tests. This shows that the particles in the current investigation are of approximately the same size as other workers investigating conventional microalloyed steels under similar test conditions.

There was a distribution of much finer particles present (mean size 2-3nm), as shown in Figure 5.47. These particles had precipitated between deformation and quenching. These are of the size that can pin boundaries, but were largely neglected in the present study. As explained earlier, this was due to their fine size and the unreliability of the carbon replica extraction process, and also because the main interest was the particle population precipitated between deformations, as these are the particles that affect softening between passes.

The 950-DD and 950-HHQ particles were of a similar size, but with the particles originating from double deformation being slightly larger. This is as expected, as the particles in 950-HHQ have had slightly longer to grow, with the time of the second deformation, and the applied strain during the second deformation is expected to advance growth. The fact that these two populations are similar, despite being separated

by an additional deformation, means that the 900-DD measurements are also valid, despite no hit-hold-quench tests at 900°C. It has been suggested recently that in multipass deformation situations, the moving of dislocations away from particles by subsequent rolling passes can isolate these particles, which can then only coarsen by bulk diffusion [Dutta *et al.* 2001]. Bulk diffusion is slower than pipe diffusion and therefore the particle coarsening rate is reduced. No direct evidence either in support or against this can be gained from the present work, although the finding that the 950-DD are of similar size to the 950-HHQ particles may suggest that growth is slowed by the consequences of the second deformation. Further work could be carried out to investigate this by using a hit-hold-hit-hold test schedule.

6.2.7.2. Particle Volume Fraction

The precipitate volume fractions measured vary from 8.7×10^{-4} to 5.8×10^{-3} (see Table 5.5). These values appear to be high, especially when compared with values calculated from the literature, and the expected values using the equation:

$$f_v = \frac{(\mathrm{Nb})+(\mathrm{C})}{100}\left(\frac{\rho_{\mathrm{Fe-30Ni}}}{\rho_{\mathrm{NbC}}}\right) \qquad (6.2)$$

where (Nb) and (C) refer to the amount (in wt.%) of niobium and carbon precipitated, and $\rho_{\mathrm{Fe\text{-}30Ni}}$ and ρ_{NbC} refer to the density of the iron-nickel matrix and the NbC particles. The actual and calculated values are compared in Table 6.3. The actual values are around ten times higher than those calculated from solubility data, and a little higher than the value using equation 6.2, estimating (Nb) and (C) levels to be ~0.05. The higher values obtained are presumably an artefact of carbon replication, as this can pull out more than just the surface particles, giving false volume fraction readings [Ashby

and Ebeling 1966]. Although the values obtained are not dramatically different, they cannot be accepted wholly.

6.2.8. A Driving Pressure Consideration of Recrystallisation-Precipitation Interaction

The fractional softening data presented show that strain-induced precipitation affects softening behaviour between deformations. It can slow recrystallisation and grain growth rates by pinning subgrain and grain boundaries. This effect has been studied quantitatively in previous work [e.g. Hansen *et al.* 1980, Kwon and DeArdo 1991, Palmiere *et al.* 1996]. These previous publications have considered the driving pressure for recrystallisation and the pressure pinning grain boundaries. The driving pressure for recrystallisation (P_R) is calculated by using equation 2.15:

$$P_R = \frac{1}{2} G\mathbf{b}^2 \rho \qquad (2.15)$$

This depends upon the estimation of dislocation density often using the Keh equation, which relates the increase in flow stress due to work hardening ($\Delta\sigma$) and dislocation density ($\Delta\rho$) [Keh 1962]:

$$\Delta\sigma = 0.2\mathrm{Gb}(\Delta\rho)^{1/2} \qquad (6.3)$$

where G is the shear modulus of the material, and **b** is the magnitude of the Burgers vector. Values of P_R found in the literature are shown in Table 2.6. Errors in estimation of the driving pressure are large, as is evident by the variance in the data in Table 2.6. This diversity is because the hot worked dislocation density values used vary between ~10^{14} and 10^{17} dislocation lines/m^2, while the values of the shear modulus used are

often the room temperature values and should be values at the hot working temperature (given by equation 5.5). Using this method for the present material, with flow stress increments of ~100 and 110MPa at 950 and 900°C, yields driving pressure values of 2.9 and 3.4MPa at 950 and 900°C respectively. These figures are at the lower end of values calculated in the literature, but it is important to note that a small change in the dislocation density estimate can cause a large effect in P_R. The force opposing recrystallisation is provided by fine particles pinning boundary motion. It is generally accepted that the SGB model of Hansen *et al.* (1980) is the most appropriate model for pinning. This should be appropriate, as no matrix precipitation was recorded during the present investigation. Thus, for recrystallisation to be inhibited, then $P_R < P_{SGB}$ and the following inequality must be true:

$$\frac{Gb^2\Delta\rho}{2} \leq \frac{3\gamma f_v \ell}{2\pi r} \qquad (6.4)$$

Thus, small diameter particles and high particle volume fractions promote pinning. Using the present data to calculate P_{SGB} values at 900°C, and at 950°C as a function of hold time, yields the values seen in Figure 6.8. For the purposes of this calculation, a volume fraction of 2.1×10^{-3} was assumed, as this was the estimated value, and is probably a more reliable guide than the experimental data collected. The particle size data were estimated at 7nm at 900°C (assuming a 10s hold), while the actual data from the 950–HHQ specimens were used, with the mean microband cell (subgrain) sizes of 0.41 and 0.54μm respectively, and a grain boundary energy of $0.8J/m^2$ [L'Ecuyer and L'Esperance 1989]. The plot also shows the P_R values at 900 and 950°C, which are shown as constant but in reality, would diminish with increased time as recrystallisation commences. This plot shows that the pinning force is reduced as a function of time. The

plot also shows that recrystallisation is expected to be pinned at 950°C for delay times up to and including 100s, and also at 900°C following a hold time of 10s. There may be errors in the measurements, especially in the dislocation density, while it may be more appropriate to use the subgrain boundary energy (~0.5J/m^2, but depends on misorientation) rather than the grain boundary energy, as the SGB pinning model involves the pinning of subgrain boundaries. These findings are backed up by the low volume fraction recrystallised values recorded during quantitative optical microscopy, and suggest that precipitation prevents recrystallisation while the particles are small, but as they grow, the balance swings towards recrystallisation, as the pinning ability diminishes. No precipitation was seen at 1000°C and above, which would imply that only solute drag can slow recrystallisation at these temperatures.

This kind of treatment to estimate recrystallisation and pinning pressures may be invalid. It has generally been assumed in the literature that $P_R=1/2Gb^2\Delta\rho$, which is valid when one assumes recrystallisation by SIBM. This may not be the case if it is assumed that precipitation affects nucleation, rather than the recrystallisation process overall. During the early stages of recrystallisation, subgrains coarsen to form the recrystallisation nuclei, thus the driving force for recrystallisation in a subgrain structure, $P_{REX(SG)}$ is given by [Humphreys and Hatherly 1996]:

$$P_{REX(SG)} = \frac{3\gamma_s}{\delta} \qquad (6.5)$$

where γ_s is subgrain boundary energy, and δ the subgrain diameter. This is assuming that recovery has occurred to such an extent that most of the dislocations exist within the subgrain walls, and are not loose in the subgrain interior. The subgrain boundary energy is related to the subgrain misorientation via the Read-Shockley equation, and

this means that more highly misorientated subgrains nucleate preferentially. This kind of work is beyond the scope of the present investigation, requiring detailed misorientation studies, although further work would be interesting to see whether precipitation affects the growth of these subgrains into recrystallising grains.

6.2.9. Precipitation Hardening Increments

The peak hardening was seen at 100s at both 900 and 950°C, this means that the precipitation hardening increment is at its greatest at this time. While the actual precipitation strengthening increment was ~30-35MPa, the calculated value using the Ashby-Orowan equation (equation 2.5) was 57MPa. These values are reasonably close, and the difference may be due to errors in the precise measurement of interparticle spacing from carbon replicas. As the precipitation hardening increment peaks at 100s, and the pinning of recrystallising grains peaks at 1s (Figure 6.8), then this suggests that these do not operate entirely in unison. From the data in the present study, it appears that grain boundary pinning is much more sensitive to particle size, while the hardening increment depends more upon the interparticle spacing.

6.2.10. Undissolved Particles and their Effect on Precipitation

It must also be noted that some larger particles do exist (50-300nm). As discussed earlier (section 6.2.1), these are undissolved particles, which were not taken into solution during reheating. It is likely that these have coarsened significantly during the test as, in addition to normal $t^{1/3}$ coarsening [Kreye 1970], solute niobium will 'precipitate' onto these pre-existing particles [Gladman 1997]. These particles play no active part in precipitation strengthening or the pinning of subgrain or grain boundaries.

6.2.11. Particle Morphologies

Many different particle morphologies were observed. All morphologies contained niobium, although some of the particles were also showing copper and silicon signals in the EDS spectra. These were not believed to be 'real' readings, and were respectively due to the copper grid, and contamination picked up in the carbon film. There was no apparent link between the particle morphologies found and particle size, or the deformation temperature.

Although not confirmed in the present work, it is much more likely that the particles are highly carbon-rich. As reported earlier (section 2.2.1), work by Nordberg and Aronsson (1968) suggested that a carbon to nitrogen ratio of greater than five gives a carbide, rather than a carbonitride. As the C:N ratio here is ~57, then a carbide is anticipated.

6.3. Deformed Microstructure

Following deformation at low temperatures (900 and 950°C), the microstructures showed little or no recrystallisation. With the present alloy, the deformed structure can be studied in detail, whereas in previous work on conventional microalloyed steels no such study is possible. The optical images of the unrecrystallised material show deformed, elongated austenite grains (Figures 5.16 to 5.19). Within these grains, deformation bands and deformed twin boundaries are clearly seen. Deformation bands contain the dislocations that are introduced to take up the shape change. These, along with existing austenite grain boundaries are shown to be highly effective recrystallisation nucleation sites.

There has been considerable recent interest in deformed microstructures, in particular microbanded structures [Duly *et al.* 1996, Hansen and Juul Jensen 1999, Zhu and Sellars 2000, Zhu and Sellars 2001]. The austenite dislocation structure in Fe-30%Ni is

of interest with respect to nucleation of recrystallisation and precipitation, as it is suggested [Hughes and Hansen 1991] that during hot working of microalloyed steels precipitation occurs preferentially upon the dislocation substructure. A more detailed analysis of the deformed Fe-30%Ni matrix is published elsewhere.

6.3.1. Microband Structures seen at Low Temperatures

A microband structure was produced by hot deformation of Fe-30%Ni, as seen in the TEM images shown in this publication. A "microband" is an elongated structure comprising cell-blocks bounded by dense dislocation walls (DDWs). These cell-blocks are comprised of walls of geometrically necessary dislocations, and are thought to minimise work done during deformation, rather than the more commonly accepted need to store energy [IMMPETUS 2001].

Microbands were seen in the deformed microstructure at all temperatures, but were particularly prevalent at low temperature. The low temperature (900, 950°C) microstructure in the Fe-30%Ni-Nb was affected by the precipitation of fine-scale NbC particles. The presence of particles, coupled with the relatively low temperature allows only limited boundary motion; thus, no recrystallisation can occur. The microbands seen are formed as recovery-only structures, necessary to accommodate the strain at lower temperatures. Some regions in the samples deformed at the lower temperatures also contained a cell-structure and subgrain structures that were approximately equiaxed. It is suggested that this variety of substructural feature may be due to local strain inhomogeneities. Zhu and Sellars (2000) found such variance in hot worked aluminium alloys during strain reversal tests, where monotonic deformation produced microbands while strain reversal produced a more equiaxed subgrain structure.

The TEM images show the presence of regions of more diffuse-walled cells and subgrain boundaries (Figures 5.27 and 5.28). This suggests variance in the extent of recovery, in that some regions are only partially recovered. Recovery in this alloy will be slowed by the presence of niobium and low temperatures [Petkovic *et al.* 1975]. It may also be possible that the regions where these images came from were subjected to a higher or lower than average level of strain or strain rate – this is certainly a possibility in PSC testing.

Some regions showed a more equiaxed substructure, rather than the microbanded structure. The more equiaxed subgrains seen (Figure 5.31) may be due to the orientation of the microstructure with respect to the applied stress. Other regions of equiaxed substructure (Figure 5.30b) look as if they could be the product of sets of intersecting microbands. If this is the case, then all four walls in this region would be DDWs. Interestingly, the subgrain boundaries at 900 and 950°C look different to each other. At 900°C the boundaries appear to be more diffuse-walled structures with individual dislocations more clearly visible. Again, this may also be an artefact of reduced boundary mobility, in that the lower temperature limits the extent of recovery.

The microband populations are interesting, and would make an excellent topic for further study, and the present alloy would provide an excellent material for such study. Such work would be of prime importance as the recrystallised structure forms from the deformed microband structure. The key issue would be one of boundary mobility, namely which of the dislocation walls are mobile, and which are stored? This would allow a determination of which dislocations are driving recrystallisation, and would give more insight into the recrystallisation process in austenite. Microbands were studied in a hot-worked Fe-31%Ni alloy by Ohtsuka *et al.* (1987). This work showed

optical images of microbands, but no TEM study was undertaken. This early work found that microband width and length increased with increased deformation; this has since been contradicted by Zhu and Sellars (2001) who found that the overall microband size in Al-alloys remained unaltered with strain, but that the misorientation continues to change with strain. Microband structures in austenite have also been studied in hot- and warm-worked Ni-30%Fe alloys [Adachi and Hinotani 2001, Hurley *et al.* 1998, Ohtsuka *et al.* 1987], and warm-worked nickel [Wierzbinski *et al.* 1992].

6.3.2. Microband Structures seen at High Temperatures

TEM investigations of the high temperature worked microstructure show an equiaxed subgrain structure in sample 1050-SD (Figure 5.33). The subgrains in this image show sharp, well-defined boundaries, with a mean subgrain size of ~0.4μm. Conventional subgrain structures have been studied comprehensively in the past [e.g. Jonas *et al.* 1969, McQueen and Jonas 1975]. The dynamically recovered subgrain size is related to the flow stress, with larger subgrains formed at lower stress values. This implies that at higher temperatures, larger subgrain sizes are seen [McQueen and Jonas 1975]. Fritzmeier *et al.* (1979) found that the hot worked subgrain size in type 304 stainless steel increased with decreased Z values (higher temperature, lower strain rates). They found subgrains of around 1-2μm in diameter at 1000°C. The subgrain size in the present alloy (0.4μm) is of similar magnitude to those found by Fritzmeier *et al.* for the type 304 stainless steel, although a direct comparison is not valid due to difference in materials. Sun *et al.* (1996) gave an equation for the subgrain diameter (d_{SUB}) dependent on initial grain size, strain and Z-value:

$$d_{SUB} = A d_0^{1/2} \varepsilon^{-1/3} Z^{-1/6} \qquad (6.6)$$

where A is a constant (value ~5). This gives a d_{SUB} value of ~0.50μm for the present material and test conditions. The microband structure seems to be a common feature in all deformed specimens, and was seen at both high and low temperatures. Microbands were perhaps unexpected at a temperature as high as 1050°C [Adachi and Hinotani 2001], although they are seen in Figure 5.34. Their presence may be as a result of the second deformation.

It is tentatively suggested that the microbands seen in Fe-30%Ni-Nb form at low temperature (900, 950°C) and are a result of the low boundary mobility, while at higher temperature (1000°C and above) a more conventional equiaxed subgrain structure is formed due to the enhanced mobility available, and greater scope for recovery. This thinking has been supported by work by Adachi and Hinotani (2001) who carried out warm and hot working on a Ni-30%Fe austenite. They found that microbands formed at low temperatures, while at higher temperature, equiaxed subgrains and recrystallised grains were seen to form. Work that considered subgrains in hot worked type 304 stainless steel found that at lower temperature the subgrains were more elongated [Fritzmeier *et al.* 1979]. This is again in accordance with the possibility of a temperature effect on the substructure developed. It remains unknown whether the presence of NbC particles has an effect of its own on substructural development, or whether it just has a general effect on boundary mobility through pinning.

6.3.3. Microband Angles

The angles made by the microbands to the 'effective rolling direction' (RD) was found to be ~25°. This is lower than values previously found in PSC work [Baxter *et al.* 1997], which found microbands in Al-alloys at ±35° to the simulated rolling direction. The difference may not be significant, and could be within the margin of experimental error,

combined with the further error from the possibility of the TEM thin foil not being taken exactly perpendicularly to the effective rolling plane. An inspection of images published by Wierzbinski *et al.* (1992) of uniaxial compressive warm-working of nickel, the microbands appeared to be ~50° to the compression axis. This compares with the ~65° found in the present study. It is suggested that the difference may be due to the constraints of uniaxial compression compared with deformation by PSC, and the microband angle could be a function of strain path. In the present work, the angle measured between crossed sets of microbands was ~60°. This is interesting as 60° is the angle between [111] directions, and suggests that the microbands may be crystallographically aligned.

6.4. Model Alloy Capability

6.4.1. Introduction

This particular alloy was chosen as a model austenite above other materials such as nickel, austenitic stainless steel, and Ni-30%Fe. It has been previously suggested [Hurley 1998] that the Ni-30%Fe matrix provides a better austenite matrix than the Fe-30%Ni, as it has the same stacking fault energy (SFE) as that of iron austenite [Charnock and Nutting 1967b]. The reasons behind the alloy selection were based not only on the provision of a stable austenite and the SFE, but also on the solubility of Nb in the matrix. The calculations made using Metadex at the University of Sheffield [Whiteman and Argent 1998] on Nb solubility implied that niobium solubility increased as nickel content increased. This is expected as nickel is an austenite stabiliser and, as such, it expands the austenite phase field (to below room temperature in this case), thus there is increased niobium (and carbon) solubility. The nickel atoms are larger than iron atoms, thus allowing substitutional atoms into the lattice more easily, with a lower misfit strain. In addition, the interstices in the FCC crystal lattice are larger, so allowing

more interstitial carbon atoms. Thus Ni-30Fe alloys have a very high solubility (of both Nb and C), and are unrepresentative of iron austenite. Thus when the present alloy was selected, the required alloy was one with as little Ni as possible, while remaining in the austenite phase field to give a stable austenite to room temperature. The minimum amount of Ni for stability is ~30%, hence the alloy Fe-30%Ni was selected. This was the prime reason for the alloy selection, as the investigation of strain-induced NbC precipitation was of great interest, while Ni-30Fe alloys are of great use for a study of the deformed microstructure due to their preferred SFE. Another problem with the Ni-30%Fe alloy is that it shows a large solid solution hardening increment, where the flow stresses can be nearly double those of a comparable C-Mn based steel [Hurley 1998].

6.4.2. *Deformation Behaviour*

Many different materials have been used to simulate (iron) austenite during hot working. Stainless steels are perhaps the obvious choice, but have very low stacking fault energy (SFE). Nickel, nickel-cobalt and nickel-iron alloys are other possibilities, and these appear to acceptably simulate the deformation behaviour of iron austenites.

Ni-30%Fe alloys have been used to investigate hot worked austenite microstructures [Hurley *et al.* 1998, Hurley *et al.* 2001]. It has been suggested that the Ni-30%Fe alloy is a better model austenite than the Fe-30%Ni as its SFE is nearer the value of austenite [Hurley 2001]. The reasoning behind this is based on the Charnock and Nutting (1967b) paper, which considered SFE in Fe-Ni alloys as a function of nickel content, the main result of which is shown in Figure 2.21. Pure iron austenite was found to have a SFE value of 75mJ/m^2, while a Ni-30%Fe alloy was found to have a similar value to that of iron, while the Fe-30%Ni composition had a SFE of~35mJ/m^2. SFE is a useful parameter, as it has been used to classify metals and alloys according to their

deformational and restoration behaviour during hot working. However, the data collected by Charnock and Nutting (1967a,b) were based on counting twin boundaries, and an empirical relationship between twin frequency and SFE. The Fe-30%Ni-Nb alloy shows no evidence of having a low SFE, and shows hot working characteristics more similar to copper and nickel – FCC metals with medium SFE values (~40-100mJ/m^2) - in that dynamic recrystallisation occurs, fast static recrystallisation is seen, and that the dislocation structures show tangled dislocations, cells and microbands. It can also be argued that the SFE of Fe-30%Ni, although thought to be around half that of iron austenite, is of minimal significance at the temperatures used during thermomechanical processing.

Comparisons can be drawn between the behaviour of this material with the behaviour of *conventional C-Mn-Nb steels.* Figure 6.9 shows a comparison between the flow behaviour of the Fe-30%Ni-Nb alloy during hot working, and an industrial Nb-microalloyed steel of similar niobium content. The comparison alloy was from work by Palmiere (1991), and was deformed under axisymmetric compression, so the Fe-30%Ni-Nb data have been amended to give an equivalent strain. The deformation conditions were otherwise identical (strain rate, temperature, delay times). These flow curves display the true stress-true strain response of these materials at test temperatures between 900 and 1050°C, and show the similarity between the hot working responses of the two austenites:

- No dynamic recrystallisation seen at these temperatures.
- Similar work hardening behaviour.
- Similar temperature effect on relative strength.
- Identical precipitation hardening responses seen following the interpass delay.

The major difference is that the Fe-30Ni shows increased strength compared with the C-Mn steel. This may be due to the addition of 30 wt.% nickel to the iron matrix, as discussed earlier. Although it is generally accepted that nickel addition brings about little solid solution hardening [Pickering 1977], the addition of a large amount of nickel does have a profound effect on carbon solubility by expanding the austenite phase field. With more carbon dissolved, then the material shows increased strength, as seen in the flow curves. This comparison shows that the Fe-30%Ni-Nb is a good model alloy for austenite, where the deformational characteristics are concerned.

As the hot-working behaviour appears to be similar to that of C-Mn based steels, then it is a reasonable assumption that the Fe-30%Ni-Nb alloy shows similar deformation structures to those present in the microstructure of microalloyed steels. Obviously no work has been carried out on hot worked substructures in C-Mn based steels, but based on the similar behaviour it may be that a microband structure dominates in the deformed matrix. It is of interest that microband structures have also been found in the Ni-30%Fe alloys also [Adachi and Hinotani 2001, Hurley *et al.* 1998, Ohtsuka *et al.* 1987].

6.4.3. Recrystallisation Behaviour

As no detailed recrystallisation study was carried out during the present work, then a direct comparison between the recrystallisation behaviour of the Fe-Ni based alloy and C-Mn based steels cannot be made. Such a comparison can be difficult due to differences in the test method used (PSC, torsion, rolling simulation), in measurement of recrystallisation (stress-relaxation, optical measurement, fractional softening), in test parameters (reheat conditions, strain, rate, deformation temperatures), and differences in steel composition. The recrystallisation kinetics do appear to be slightly faster than

those of C-Mn based steels, although the effect that solute niobium has on recrystallisation kinetics masks this, as the niobium effect somewhat dwarfs other compositional factors.

Work on the Nb-free Fe-30%Ni has shown rapid recrystallisation kinetics, which compare well with C-Mn steels, although the flow stress appears to be more temperature sensitive [Almaguer 2002]. Work is ongoing within IMMPETUS at Sheffield with Fe-30Ni-Mo alloys. The molybdenum is added to slow recrystallisation kinetics [Sekine *et al.* 1982]. This will perhaps give a closer reproduction of the recrystallisation kinetics seen in C-Mn steel grades.

6.4.4. Precipitation Behaviour

As no solubility study was carried out in the present work, it is difficult to compare the Nb solubility in the present alloy with the solubility data for C-Mn based microalloyed steels. As discussed earlier, it is suspected that Nb solubility is slightly increased in the Fe-30%Ni matrix. A solubility study of this alloy would be required before a full comparison of solubility could be made.

The precipitation events investigated show a good comparison with conventional C-Mn-Nb steels. Precipitation occurs at similar temperatures, under testing with similar thermomechanical variables, and in similar precipitation times. The particles are of comparable size to those found in conventional microalloyed steels, and show similar growth kinetics upon holding. The localised precipitation which is thought to occur heterogeneously on subgrain boundaries in microalloyed steels has been seen, actually in the deformed austenite, using the Fe-30%Ni-Nb alloy. This shows that the Fe-

30%Ni-Nb is a very promising model material for the study of strain-induced precipitation in microalloyed steels.

7. CONCLUSIONS

1. The hot working of a model austenite has been carried out to simulate the finish rolling of microalloyed steels. Thermomechanical processing of a Fe-30%Ni-1.6%Mn-0.1%C-0.1%Nb was performed at temperatures of between 900-1050°C, at strain rate $10s^{-1}$ and true strain values of between 0.25 and 0.9. Testing was carried out by double-deformation plane strain compression (PSC).

2. Mechanical test data were collected in the form of true stress-true strain flow curves, from which fractional softening values were determined. Quantitative optical and transmission electron microscopic studies have allowed characterisation of the deformed matrix, the recrystallising matrix and of the precipitated NbC particles.

3. This is the first work of this type on what is effectively a 'new' alloy. This alloy is fully austenitic from room temperature up to the hot working temperature, which means that hot worked microstructures can be quenched in, without martensitic transformation.

4. The deformed material was found to have a predominantly microbanded substructure. There has been increased recent interest in microbands in hot worked materials. Microbands were found at all temperatures, especially at the lower deformation temperatures (900 and 950°C). Some equiaxed subgrain structure was also seen in this alloy, although this was seen mainly at higher temperatures.

5. Microband size varied with temperature: 0.87 ×0.19μm at 900°C, 0.60×0.50μm at 950°C, and 1.0×0.57μm at 1050°C for double deformation to an overall strain of 0.5

(0.25 + 0.25). Where subgrains existed, they were equiaxed and 0.42μm in size. These values are similar to data in the literature for type 304 stainless steel.

6. The microband boundaries (i.e. dense dislocation walls) were found to make an angle of ~65° to the compression direction. Where two microband populations crossed, they did so at an angle of ~60° to each other.

7. During reheating, the grain growth characteristics were similar to those of comparable C-Mn based steels in the literature. Reheating gave a coarse, but uniform, equiaxed austenite structure. Reheating brought about partial dissolution of the Nb.

8. Analysis of the PSC flow stress data has allowed an appreciation of the recrystallisation and precipitation processes. Two distinct responses were seen, depending upon the temperature. At temperatures of 1000°C and above, softening processes (recrystallisation, recovery) occurred. At lower temperatures, the recrystallisation kinetics were much slower – this was due to pinning by the strain-induced precipitation of fine NbC particles.

9. Precipitation hardening was observed at 900 and 950°C and quantified as a function of delay time. Hardening peaked after 100s, implying that much of the precipitation was complete by that time. This was later confirmed by the TEM study of carbon extraction replicas.

10. Two separate precipitation events were seen: one during the static hold between deformations, and the other between the second deformation and quenching. The

particles in the second population were very fine (<2-3nm) and were not quantified. The first population was the one of primary interest, as these particles affect the interpass hardening and softening behaviour. Quantitative microscopy of these particles was undertaken. Large undissolved NbC particles were also found, although these play no part in grain boundary pinning.

11. The precipitation kinetics were studied. Precipitation was found to start in less than 1 second at 900°C, and within 10 seconds at 950°C, and to be complete by ~100s in both cases. No precipitation was seen at temperatures of 1000°C and above.

12. Recrystallisation was more rapid at higher temperatures, and at greater strains as expected. Recrystallisation-precipitation interaction meant that recrystallisation was very limited at lower temperatures (<1000°C), and the recrystallisation kinetics were found to be dependent on the precipitation kinetics. This interaction between recrystallisation and precipitation has been considered, and calculations have been made for the driving pressure necessary for recrystallisation and particle pinning pressure opposing this. No dynamic recrystallisation or dynamic precipitation was seen during the current work.

13. Fine-scale NbC precipitation was found to occur heterogeneously upon subgrain boundaries. The particle size data have been quantified as a function of time, and rapid particle growth kinetics have been seen, assumed to be associated with dislocation pipe diffusion.

14. The iron-nickel microalloyed steel appears to be a good model austenite in both precipitation and deformational behaviour. The alternative materials to the iron-

nickel are stainless steels, high-manganese steels, and nickel-alloys. Major problems render these alternatives unsuitable; such problems include unrealistic stacking-fault energy values that give invalid hot working characteristics and deformation structures, and unsuitable niobium solution thermodynamics, which can be substantially different from the solution behaviour in austenite.

15. The potential of this material as a model material is substantial – the work presented here is only a preliminary study of a 'new' material. Much further research is required using Fe-30%Ni and similar alloys, and many areas of new research are possible, a few of which are mentioned in the next section.

8. FURTHER WORK

- Before any further precipitation studies are conducted, it may be prudent to perform some comprehensive solubility studies. This would lead to an experimentally determined solubility product relation for the dissolution of Nb in the Fe-Ni matrix, and would give a better idea on precipitation and supersaturation.

- Fe-30%Ni would make an excellent material for the study of the nucleation of recrystallisation. A TEM study of nucleating grains could be carried out, and this could be followed as a function of time, giving data on nucleus growth and location.

- This alloy would also be good for an investigation into the nucleation of precipitation. Some of this work has already been carried out [Higginson *et al.* 2001, Rainforth *et al.* 2002], while an APFIM study of precipitation may provide better detail.

- With a stabilised austenite, a full microstructural study of the deformed (or recrystallised) matrix could be carried out. This would allow further characterisation of the microband structures seen. Perhaps this would first require the completion of a true stacking-fault energy determination.

REFERENCES

- Abe, T. and Sellars, C.M. (1991), Mater. Sci. Technol., **7**, 1108.
- Adachi, Y. and Hinotani, S. (2001), "Proceedings of THERMEC 2000", Eds. T.Chandra, K.Higashi, C.Suryanarayana and C.Tome, CD-Rom, TMS.
- Akben, M.G., Weiss, I. and Jonas, J.J. (1981), Acta Metall., **29**, 111.
- Almaguer, S. (2001), to be published, in Conf. Proc. "Recrystallisation and Grain Growth 2001, Aachen".
- Almaguer, S. (2002), PhD Thesis, University of Sheffield, to be submitted.
- Andrade, H.L., Akben, M.G. and Jonas, J.J. (1983), Metall. Trans. A, **14A**, 1967.
- Ardell, A.J. (1972), Acta Metall., **20**, 601.
- Arieta, F.G. (1992), "Precipitation Kinetics of Nb(C,N) in Austenite for the Low C High Nb HSLA Steels", PhD Thesis, University of Sheffield.
- Ashby, M.F. (1966), Acta Metall., **14**, 679.
- Ashby, M.F. and Ebeling, R. (1966), Trans. Metall. Soc. AIME, **236**, 1396.
- Atkinson, H.V. (1988), Acta Metall., **36**, 469.
- Avrami, M. (1939), J. Chem. Phys., **7**, 1103.
- Avrami, M. (1941), J. Chem. Phys., **9**, 177.
- Bacroix, B., Akben, M.G. and Jonas, J.J. (1982) in Conf. Proc. "Thermomechanical Processing of Microalloyed Austenite", Eds. DeArdo, Ratz and Wray, The Metallurgical Society of AIME, Warrendale, 293.
- Bai, D.Q., Yue, S., Maccagno, T. and Jonas, J.J. (1996), ISIJ Int., **36**, 1084.
- Bailey, J.E. and Hirsch, P.B. (1962), Proc. Roy. Soc. Lond., **A267**, 11.
- Baker, T.N. (1980), in Conf. Proc. "Hot Working and Forming Processes" Eds. Sellars, C.M. and Davies G.J., Metals Society, London, 32.
- Baxter, G.J., Furu, T., Zhu, Q., Whiteman, J.A., and Sellars, C.M. (1997), Acta Mater., **47**, 2367.
- Bay, B. Hansen, N., Hughes, D.A. and Kuhlmann-Wilsdorf, D. (1992), Acta Metall. Mater., **40**, 205.
- Beck, P.A. and Sperry, P.R. (1950), J. Appl. Phys., **21**, 150.
- Begin and Simoneau (1977), in Conf. Proc. "Microalloying '75", Ed. Korchinsky *et al.*, Union Carbide Corp., N.Y., 85.
- Beynon, J.H. (1979), PhD Thesis, University of Sheffield.
- Beynon, J.H. and Sellars, C.M. (1992), ISIJ Int., **32**, 359.

- Black, M.P., Rainforth, W.M. and Palmiere, E.J. (2001): "Proceedings of THERMEC 2000", Eds. T.Chandra, K.Higashi, C.Suryanarayana and C.Tome, CD-Rom, TMS.
- Burke, M.G., Cuddy, L., Piller, J., and Miller, M.K. (1988), Mater. Sci. Tech., **4**, 113.
- Charnock, W. and Nutting, J. (1967a), Metal Sci., **1**, 78.
- Charnock, W. and Nutting, J. (1967b), Metal Sci., **1**, 123.
- Cheng, L.M., Hawbolt, E.B. and Meadowcroft, T.R. (2000), Metallurgical and Materials Transactions A, **31A**, 1907.
- Cho, S.H., Kim, S.I. and Yoo, Y.C. (1997); Journal of Material Science Letters, **16**, 1836.
- Cordea, J.N. and Hook, R.E. (1970), Metall. Trans., **1**, 111.
- Cuddy, L.I. (1981), Metall. Trans. A, **12**, 1313.
- Cuddy, L.I. (1984), Metall. Trans. A, **15A**, 87.
- Davenport, A.T., Miner, R.E., and Kot, R.A. (1977), in Conf. Proc. "Hot Deformation of Austenite", Ed. J.B.Balance, A.I.M.E., Warrendale, 186.
- Davenport and DiMicco (1980), in Conf. Proc. "Proceedings of the International Conference on Steel Rolling", ISIJ, Tokyo, 1237.
- DeArdo, A.J., Gray, J.M. and Meyer, L. (1984), in Conf. Proc. "Niobium - Proceedings of the International Symposium", Ed. H.Stuart, The Metallurgical Society of AIME, Warrendale, 685.
- Djaic, R.A.P. and Jonas, J.J. (1973), Metall. Trans., **4**, 621.
- Duly, D., Baxter, G.J., Shercliff, H.R., Whiteman, J.A., Sellars, C.M. and Ashby, M.F. (1996), Acta Mater., **44**, 2947.
- Dutta, B. and Palmiere, E.J. (2002), submitted to Acta Mater.
- Dutta, B., Palmiere, E.J. and Sellars, C.M. (2001), Acta Mater., **49**, 785.
- Dutta, B. and Sellars, C.M. (1987), Mater. Sci. Tech., **3**, 197.
- Dutta, B. (1987), PhD Thesis, University of Sheffield.
- Dutta, B., Valdes, E. and Sellars, C.M. (1992), Acta Metall. Mater., **40**, 653.
- Dyson, D.J. and Holmes, B. (1970), JISI, **208**, 469.
- Everett, J.R., Gittins, G., Glover, G. and Toyama, M. (1980) in Conf. Proc. "Hot Working and Forming Processes" Eds. Sellars, C.M. and Davies G.J., Metals Society, London, 16.
- Fang, B. (2002), unpublished ongoing work.
- Fernandez, A.I., Lopez, B., Rodriguez-Ibabe, J.M. (1999), Scripta Mater., **40**, 543.

- Fitzsimons, G., Tiitto, K., Fix, R. and DeArdo, A.J. (1984), Metall. Trans. A, **15A**, 241.
- Foster, S.R. (1981), PhD Thesis, University of Sheffield.
- Fritzmeier, L., Luton, M.J. and McQueen, H.J. (1979), in Conf. Proc. "Fifth International Conference on the Strength of Metals and Alloys, ICSMA5", 95.
- Frost and Ashby (1982), "Deformation Mechanism Maps", Pergamon Press, Oxford.
- Gladman, T. (1966), Proc. Roy. Soc. A., **204**, 298.
- Gladman, T. (1977), in Conf. Proc. "Microalloying '75", Ed. Korchinsky *et al.*, Union Carbide Corp., N.Y., 25.
- Gladman, T. (1997), "The Physical Metallurgy of Microalloyed Steels", Institute of Materials, London.
- Gladman, T. (1999), Mater. Sci. Tech., **15**, 30.
- Gladman, T. and Walker, F. (1984), in Conf. Proc. "Niobium - Proceedings of the International Symposium", Ed. H. Stuart, The Metallurgical Society of AIME, Warrendale, 1061.
- Gray, J.M. and DeArdo, A.J. (1986), in Conf. Proc. "HSLA steels: metallurgy and applications", Eds. J.M. Gray, T. Ko, Z. Shouhua, B. Wu and X. Xie, Beijing, ASM International, 83.
- Hall, E.O. (1951), Proc. Phys. Soc., **643**, 747.
- Hansen, N. and Juul Jensen, D. (1999), Phil. Trans. R. Soc. Lond., **A357**, 1447.
- Hansen, S.S., VanderSande, J.B. and Cohen, M. (1980), Metall. Trans., **11A**, 387.
- Hashimoto, Y. and Shinohara, K. (1992), Steel Res., **63**, 219.
- Higginson, R.L. Rainforth, W.M. Palmiere, E.J. and Sellars, C.M. (2001), "Proceedings of THERMEC 2000", Eds. T.Chandra, K.Higashi, C.Suryanarayana and C.Tome, CD-Rom, TMS.
- Hodgson, P.D. and Gibbs, R.K. (1992), ISIJ Int., **32**, 1329.
- Hofer, F., Warblicher, P., Buchmayr, B. and Kleber, S. (1996), Journal of Microscopy, **184**, 163.
- Honeycombe, R.W.K. (1981), "Steels: Microstructure and Properties", Edward Arnold, London.
- Hoogendoorn, T.M. and Spanraft, M.J. (1977), in Conf. Proc. "Microalloying '75", Ed. Korchinsky *et al.*, Union Carbide Corp., N.Y., 75.
- Hu, H. (1962), Trans. Metall. Soc. A.I.M.E., **224**, 75.
- Hughes, D.A. and Hansen, N. (1991), Mater. Sci. Technol., **7**, 544.

- Humphreys, F.J. (1977), Acta Metall., **25**,1323.
- Humphreys, F.J. and Hatherly, M. (1996), "Recrystallisation and Related Annealing Phenomena", Pergamon, Oxford.
- Hurley, P.J., Muddle, B.C., Hodgson, P.D., Davies, C.H.J., Wynne, B.P., Cizek, P. and Hickson, M.R. (1998) in Proc. Int. Conf. on "Microalloying in Steels", Eds. Rodríguez-Ibabe *et al.*, Trans Tech Publications Ltd., Switzerland, 159.
- Hurley, P. J. (2001), private communication.
- Hurley, P. J., Hodgson, P.D. and Muddle, B.C. (2001), Scripta Mater., **45**, 25.
- Hutchinson, W.B. and Duggan, B.J. (1978), Metal Sci., **12**, 372.
- IMMPETUS (2001), "IMMPETUS Deformation Microstructure Glossary 2001", Version 0.5, Unpublished work, University of Sheffield.
- Irvine, K.J., Pickering, F.B. and Gladman,T. (1967), JISI, **205**, 161.
- Janampa, C.J. (1982), "The Role of Nitrogen in the Hot Working of Niobium Microalloyed Steels", PhD Thesis, University of Sheffield.
- Johnson, W.A. and Mehl, R.F. (1939), Trans. Metall. Soc. AIME, **135**, 416.
- Jonas, J.J., Sellars, C.M. and Tegart, W.McG. (1969), Met. Rev., **14**, 1.
- Jones, A.R. (1980), in Conf. Proc. "Grain Boundary Structure and Kinetics", Ed. Balluffi, ASM, Ohio, 379.
- Karjalainen, L.P. (1995), Materials Science and Technology, **11**, 557.
- Karjalainen, L.P. and Perttula, J.S. (1996), in Conf. Proc. "ReX '96", Ed. McNelly, 413.
- Keh, A.S. (1962), Direct Observation of Imperfections in Crystals, Eds. Newkirk and Wernick, Wiley-Interscience, New York, 213.
- Kestenbach, H-J., Rodrigues, J.A. and Dermonde, J.R. (1989), Mater. Sci. Tech., **5**, 29.
- Kolmogorov, A.N. (1937), Izv. Akad. Nauk. USSR-Ser-Matemat., **1(3)**, 355.
- Kosazu, I., Ouchi, C., Sampei, T., Okita, T. (1977), in Conf. Proc. "Microalloying '75", Ed. Korchinsky *et al.*, Union Carbide Corp., N.Y., 120.
- Košík, O., Abson, D.J. and Jonas, J.J. (1971), JISI, **209**, 624.
- Koyana (1971), as reported in Kestenbach *et al.* (1989).
- Kreye, H. (1970), Z. Metallkunde, **61**,108; as reported in Ardell (1972).
- Kuhlmann-Wilsdorf, D. (1989), Mater. Sci. Eng., **A113**, 1.
- Kwon, O. and DeArdo, A.J. (1986), in Conf. Proc. "HSLA steels: metallurgy and applications", Eds. J.M. Gray, T. Ko, Z. Shouhua, B. Wu and X. Xie, Beijing, ASM International, 287.

- Kwon, O. and DeArdo, A.J. (1991), Acta metall. mater., **39**, 529.
- Laasraoui, A. and Jonas, J.J. (1991), Metall. Trans. A, **22A**, 151.
- Lakshmanan, V.K. and Kirkaldy, J.S. (1984): Metall. Trans. A, **15A**, 541.
- Le Bon, A., Rofes-Vernis, J. and Rossard, C. (1975), Metal Sci., **9**, 36.
- L'Ecuyer, J.D. and L'Esperance, G.L. (1989), Acta Mater., **37**, 1023.
- Li, J.C.M. (1962), J. Appl. Phys., **33**, 2958.
- Lifshitz, I.M. and Slyozov, J.V. (1961), J. Phys. Chem. Solids, **19**, 35.
- Liu, W.J., Hawbolt, E.B. and Samarasekera, I.V. (1993), in Conf. Proc. "Modelling of Coarsening and Grain Growth", Eds. S.P. Marsh and C.S. Pande, TMS, Warrendale.
- Liu, W.J. and Jonas, J.J. (1988), Metall. Trans. A, **19A**, 1403.
- Loveday, M.S., Nahon, G.J., Roebuck, B., Sellars, C.M., Silk, N.J., and Van der Winden, M.R. (1999), "Measuring flow stress in plane strain compression tests", Measurement Good Practice Guide No.27, National Physical Laboratory, Department of Trade and Industry, UK.
- Maki, T., Akasaka, K. and Tamura, I. (1982), in Conf. Proc. "Thermomechanical Processing of Microalloyed Austenite", Eds. DeArdo, Ratz and Wray, The Metallurgical Society of AIME, Warrendale, 218.
- Mangonon, P.L. and Heitmann, W.E. (1977), in Conf. Proc. "Microalloying '75", Ed. Korchinsky *et al.*, Union Carbide Corp., N.Y., 49.
- Manohar, P.A., Chandra, T., and Dunne, D.P. (1996), in "Proceedings of ReX '96 Third Int. Conf. on Recrystallisation and Related Phenomena", ed. T.R. McNelley, Monterey Institute of Advanced Studies, Monterey, California, 445.
- Manohar, P.A., Ferry, M., and Chandra, T. (1998), ISIJ International, **38**, 913.
- Martinez, L.G., Imakuma, K. and Padilha, A.F. (1992), Steel Research, **63**, 221.
- McQueen, H.J. and Jonas, J.J. (1975), Plastic Deformation of Materials, Vol.6, Ed. R.J.Arsenault, Academic Press, New York, 393.
- Medina, S.F. and Mancilla, J.E. (1993), ISIJ Int., **33**, 1257.
- Medina, S.F. (1995), Scripta Metall. et Mater., **32**, 43.
- Medina, S.F. and Quispe, A.F. (1996), Steel Res., **67**, 257.
- Medina, S.F. and Quispe, A.F. (1996b), ISIJ Int., **36**, 1295.
- Mirza, S. and Sellars, C.M. (2001), Mater. Sci. Tech., **17**,
- Morrison, W.B. and Woodhead, J.H. (1963), JISI, **201**, 43.
- Narita, K. (1975), Trans. ISIJ, **15**, 145.
- Nes, E. (1995), Scripta Metall. et Mater., **33**, 225.

- Nes, E., Ryum, N. and Hunderi, O. (1985), Acta Metall., **33**, 11.
- Nordberg, H. and Aronsson, B. (1968), JISI, **206**, 1263.
- Ohtsuka, H., Umemoto, M. and Tamura, I. (1987), Trans. ISIJ, **27**, 408.
- Orowan, E. (1948), "Internal Stress in Metals and Alloys", Institute of Metals, London, 451.
- Orsetti-Rossi, P.L. and Sellars, C.M. (1997), Acta Mater., **45**, 137.
- Ouchi, C., Sanpei, T., Okita, T. and Kosazu, I. (1977), in Conf. Proc. "Hot Deformation of Austenite", ed. Balance, TMS-A.I.M.E., Warrendale, 316.
- Palmiere, E.J. (1991), PhD Thesis, University of Pittsburgh, USA.
- Palmiere, E.J., Garcia, C.I. and DeArdo, A.J. (1993), in Conf. Proc. "Low Carbon Steels for the 90s", Eds. R.Asfahani and G.Tither, TMS, Warrendale, 121.
- Palmiere, E.J., Garcia, C.I. and DeArdo, A.J. (1994), Metall. Mater. Trans., **25**, 277.
- Palmiere, E.J., Garcia, C.I. and DeArdo, A.J. (1996), Metall. Trans., **27**, 951.
- Palmiere, E.J., Garcia, C.I. and DeArdo, A.J. (1998), in Proc. Int. Conf. on "Microalloying in Steels", Eds. Rodríguez-Ibabe *et al.*, Trans Tech Publications Ltd., Switzerland, 151.
- Park, S.H., Yue, S. and Jonas, J.J. (1992), Metall. Trans. A, **23A**, 1641.
- Petch, N.J. (1953), JISI, **173**, 25.
- Petkovic, R.A., Luton, M.J., and Jonas, J.J. (1975), Canadian Metallurgical Quarterly, **14**, 137.
- Pickering, F.B. (1977), in Conf. Proc. "Microalloying '75", Ed. Korchinsky *et al.*, Union Carbide Corp., N.Y., 9.
- Pluhar, J. and Zuna, P. (1969), JISI, **207**, 58.
- Poths, R.M., Higginson, R.L. and Palmiere, E.J. (2001), "Proceedings of THERMEC 2000", Eds. T.Chandra, K.Higashi, C.Suryanarayana and C.Tome, CD-Rom, TMS.
- Rainforth, W.M., Black, M.P., Higginson, R.L., Palmiere, E.J., Sellars, C.M., Prabst, I., Warbichler, P., Hofer, F., (2002), Acta Mater., **50**, 735.
- Ramaswany, V. and West, D.R.F. (1970a), J.I.S.I., **208**, 391.
- Ramaswany, V. and West, D.R.F. (1970b), J.I.S.I., **208**, 395.
- Rios, P.R. (1998), Mater. Sci. Tech., **4**, 324.
- Swartzendruber, L.J. (1991), Journal of Phase Equilibria, **12**, 288.
- Sekine, H., Maruyama, T., Kageyama, H. and Kawashima, Y. (1982) in Conf. Proc. "Thermomechanical Processing of Microalloyed Austenite", Eds. DeArdo *et al.*, 141.

- Sellars, C.M. (1980), in Conf. Proc. "Hot Working and Forming Processes" Eds. Sellars, C.M. and Davies G.J., Metals Society, London, 3.
- Sellars, C.M. (1986), in Conf. Proc. "HSLA steels: metallurgy and applications", Eds. J.M. Gray, T. Ko, Z. Shouhua, B. Wu and X. Xie, Beijing, ASM International, 73.
- Sellars, C.M. (1997), in Conf. Proc. "THERMEC '97", Eds. T.Chandra and T.Sakai, TMS, Warrendale, Volume 1, 3.
- Sellars, C.M. (1998), in Proc. Int. Conf. on "Microalloying in Steels", Eds. Rodríguez-Ibabe *et al.*, Trans Tech Publications Ltd., Switzerland, 73.
- Sellars, C.M. and Whiteman, J.A. (1979), Metal Sci. J., **13**, 187.
- Sellars, C.M., Sah, J.P., Beynon, J.H. and Foster, S.R. (1976); "Plane Strain Compression Testing at Elevated Temperatures", Report on research work supported by Science Research Council grant B/RG/1481.
- Sharma, R.C., Lakshmanan, V.K. and Kirkaldy, J.S. (1984), Metall. Trans. A, **15A**, 545.
- Siciliano, F. and Minami (1996a), ISIJ Int., **36**, 1500.
- Siciliano, F. and Minami (1996b), ISIJ Int., **36**, 1507.
- Silveira e Silva, J.M. & Barbosa, R. (1993), Scripta Metall. et Mater., **29**, 881.
- Simoneau, R., Begin, G. and Marquis, A.H. (1978), Metal Sci., **12**, 381.
- Siradj, E.S. (1997), "Strain Induced Precipitation Kinetics of Nb(C,N) in Nb-HSLA Steel as a Function of Thermomechanical History" PhD Thesis, University of Sheffield.
- Smith, C. (1948), Trans. AIME, **175**, 15.
- Smithell's Metals Reference Book (1983), "Smithell's Metals Reference Book", 6th Edition, Ed. Brandes, Butterworths, London.
- Storms, E.K and Krikorian, N.H. (1960), J. Phys. Chem., **64**, 1747.
- Suehiro, M. (1998), ISIJ Int., **38**, 547.
- Sun, W.P. and Hawbolt, E.B. (1995), ISIJ Int., **35**, 908.
- Sun, W.P., Hawbolt, E.B. and Meadowcroft, T.R. (1996), in Conf. Proc. "37th Mechanical Working and Steel Processing", ISS-AIME, Warrendale, 680.
- Sun, W.P., Militzer, M., Bai, D.Q. and Jonas, J.J. (1993), Acta Metall., **41**, 3595.
- Sun, W.P., Jonas, J.J., Hawbolt, E.B., Samarasekera, I.V., Brimacombe, J.K. and Yue, S. (1994), in Conf. Proc. "Advances in Hot Deformation Textures and Microstructures", Eds. Jonas, Bieler and Bowman, The Minerals, Metals & Materials Society, Warrendale, Pennsylvania , 1.

- Tamura, I. (1987), ISIJ International, **27**, 763.
- Tanaka, T., Tabata, N., Hatomura, T. and Shiga, C. (1977), in Conf. Proc. "Microalloying '75", Ed. Korchinsky *et al.*, Union Carbide Corp., N.Y., 107.
- Taylor, G.I. (1938), J. Inst. Met., **62**, 307.
- Tian, D.W., Karjalainen, L.P., Bainian Qian and Xiaofeng Chen (1996), Metall. Trans. A,**27A**, 4031.
- Valdes, E. and Sellars, C.M. (1991), Mater. Sci. Tech., **7**, 622.
- Van Aswegen, J.S.T., Honeycombe, R.W.K. and Warrington, D.H. (1964), Acta Metall., **12**, 1.
- Weiss, I. and Jonas, J.J. (1980), Metall. Trans. A, **11A**, 403.
- Whelan, M.J. (1969), Metal Sci. J., **3**, 95.
- Whiteman, J.A. and Argent, B. (1998), Unpublished Thermodynamic Calculations, The University of Sheffield.
- Wierbinski, S., Korbel, A. and Jonas, J.J. (1992), Mater. Sci. Technol., **8**, 153.
- Xiadong, L. , Solberg, J.K., Gjengedal, E. and Kluken, A.O. (1994), Scripta Metall. et Mater., **31**, 1607.
- Xiuqui, L. and Wenxuan, C. (1986), in Conf. Proc. "HSLA steels: metallurgy and applications", Eds. J.M. Gray, T. Ko, Z. Shouhua, B. Wu and X. Xie, Beijing, ASM International, 235.
- Yamamoto, S., Ouchi, C. and Osuka, T: (1982) in Conf. Proc. "Thermomechanical Processing of Microalloyed Austenite", Eds. DeArdo, Ratz and Wray, The Metallurgical Society of AIME, Warrendale, 613.
- Zhu, Q and Sellars, C.M. (2000), Materials Science Forum, **331-337**, 409.
- Zhu, Q and Sellars, C.M. (2001), Scripta Mater., **45**, 41.

Table 2.1: Solubility products found in the literature for niobium carbide.

Author (s)	Year	Solubility Product	Detection method
Narita	1975	$\log [Nb][C] = 3.42-7900/T$	Chemical separation and analysis
Nordberg and Aronsson	1968	$\log [Nb][C]^{0.87} = 3.11-7520/T$ $\log [Nb][C] = 2.96-7510/T$ $\log [Nb][C]^{0.87} = 3.43-7200/T$	Averaged existing equations Averaged existing equations Thermodynamic calculations
Palmiere et al	1996	$\log [Nb][C] = 2.06-6700/T$	Atom probe microscopy
Smith et al	1966	$\log [Nb][C] = 3.7-9100/T$	Gas mixtures equilibrium
Sharma et al	1984	$\log [Nb][C]^{0.87} = 2.81-7019.5/T$	Thermodynamic calculations
Lakshmanan and Kirkaldy	1984	$\log [Nb][C]^{0.87} = 3.4-7920/T$	Gas mixtures equilibrium
Hoogendorn and Spanraft	1977	$\log [Nb][C] = 3.89-8030/T$	Gas mixtures equilibrium

Table 2.2: Solubility products from the literature for niobium nitride.

Author (s)	Year	Solubility Product	Detection method
Narita	1975	$\log [Nb][N] = 2.8\text{-}8500/T$	Chem separation and analysis
Smith et al	1966	$\log [Nb][N]^{0.87} = 2.86\text{-}7927/T$	Thermodynamic calc
Hoogendorn and Spanraft	1977	$\log [Nb][N] = 3.7\text{-}10800/T$	Chem separation and analysis

Table 2.3: Solubility products from the literature for niobium carbonitride.

Author (s)	Year	Solubility Product	Detection method
Irvine et al	1967	$\log [Nb][C+12/14N] = 2.26\text{-}6770/T$	Chem separation and analysis
Nordberg and Aronsson	1968	$\log [Nb][C+N] = 1.54\text{-}5860/T$ $\log [Nb][C]^{0.83}[N]^{0.14} = 4.46\text{-}9800/T$	Data Analysis
Hashimoto and Shinohara	1992	$\log [Nb][C+0.86[N-(Ti/3.43)]] = 0.36\text{-}4770/T$	Chem separation and analysis

Table 2.4 : Experimentally measured precipitation start times from the literature.

Author (s)	Steel Chemistry			Deformation Conditions			Detection Method	Nose temp	Ps (sec)
	%Nb	%C	N (ppm)	T_{def}	ε	ε-rate			
Davenport *et al.* (1977)	0.09	0.08	200	870-1200	0.22-0.92	-	Chemical extraction / XRD peak broadening/thin foil TEM	870	within 4sec
Dutta & Palmiere (2001)	0.03	0.1	54	850-1050	0.1 0.2 0.3 0.4	10	Based on fractional softening measurements	920 920 920 850	1.9 3.3 3.6 4.3
Fitzsimmons *et al.* (1984)	0.07	0.08	200	800-925	0.6-0.9	2	Thin foil TEM	850	0.4
Hansen *et al.* (1980)	0.095	0.1	100	900 950	0.69	2.6	TEM of extraction replicas	~950 ~950	2-3 10
Herman *et al.* (1992)	0.08	0.1	33	900	0.44	11 ?		-	10
Janampa (1982)	0.12	0.081	141	800-1000	0.29	4.2	Electrolytic extraction / centrifuge and TEM	1000 900 850	0.2 0.2 0.7
Kang *et al.* (1997)	0.03	0.076	61	900	0.3	10	Mechanical testing		3
Medina & Quispe (1996)	0.093	0.1	119	1000?	0.35	3.63	Mechanical testing	1000	25
Ouchi *et al.* (1977)	0.031	0.16	54	-	0.69	-	Hardness drop	880	10
Silveira & Barbosa (1993)	0.11	0.026	10	850-1050	0.1	0.1	Stress relaxation	950	20
Park *et al.* (1992)	0.04	0.067	60	900	0.05	0.1	Dilatometry	~900	12
Watanabe *et al.* (1977)	0.084	0.063	58	980	0.36	-	Electrolytic extraction	925	10
Yamamoto *et al.* (1982)	0.095	0.02	28	-	0.69	10	TEM of extraction replicas		10
Hoogendorn and Spanraft (1977)	0.040	0.1	80	- -	0 0.8		Electrolytic extraction		
Le Bon *et al.* (1975)	0.04	0.17	90	900	0.75	12.5	Microhardness testing		
Simoneau *et al.* (1978)	0.04 0.058	0.07 0.19	103 72	- -	0	0	Electrical resistivity	900 900	2000 700

Table 2.5: Values from the literature of t_{50} components for static recrystallisation of Nb-microalloyed steels.

Author	Steel Chemistry (wt%)			Exponents					Notes
	Nb	C	N (ppm)	D_o	ε	ε-rate	Const	Q_{rex}	
Sellars (1980)	< 0.04	-	-	2	-4	0	2.52×10^{-19} 5.94×10^{-38} 9.24×10^{-9}	325000 780000 130000	T>1004°C 1004>T>891°C T<891°C
Medina and Mancilla (1993)	0.041 0.093	0.11 0.11	112 119	1	-1.96	-0.44	3.94×10^{-13}	262000 272000	T>1030°C T>1060°C
Karjalainen and Perttula (1996)	0.046	0.07	72	2	-3.3	-0.25	6.5×10^{-19}	330000	T<1000°C
Hodgson and Gibbs (1992)	<0.03	-	-	2	-4+77[Nb]	0	$(-5.24+550[Nb])\times10^{-18}$	330000	For ε ≥0.3
Cho *et al.* (2001)	-	-	-	2	-2.8	-0.41	1.9×10^{-18}	324000	
Laasraoui and Jonas (1991)	0.055	-	-	0	-3.81	-0.36	1.27×10^{-18}	404000	T> strain-induced pptn temp.

Table 2.6: Pinning force calculations made in the literature.

Author (s)	Recrystallisation Driving Force (MPa)	Pinning Force			wt%Nb in steel	notes
		RBM	FBM	SBM		
Hansen *et al.* (1980)	14	0.5	-	20-40	0.03-0.21	
Kwon and DeArdo (1991)	9	3.66	16.32	2.86	0.04	Wrong equations used. Data from 100s hold.
Arieta (1992)	0.61	1.14	-	-	0.1	Taken at T=1000°C.
Palmiere *et al.* (1996)	22-30	19.5 24.9	-	30.1 44.9	0.02 0.09	F_{rex} is T dependent – increases at lower temp.
Dutta and Palmiere (2001)	2	-	-	~10	0.03	Taken at t_i=10s. F_{PIN} increases with time.
Poths *et al.* (2001)	20	-	-	13	0.03	F_{PIN} varies with time.

Table 4.1: Steel composition.

Element	Wt%	± Error
C	0.097	0.01
S	0.003	0.001
P	<0.005	-
Si	0.03	0.02
Mn	1.61	0.02
Cr	<0.02	-
Ni	30.0	0.2
Mo	<0.02	-
V	<0.02	-
Ti	<0.02	-
Nb	0.10	0.02
Al	<0.005	-
N	.0017	0.0005
Fe	(Balance)	-

Table 4.2: Main test conditions matrix used during mechanical testing.

Variable	T_{reheat}	T_{def}	Strain	Strain Rate	Interpass Time
Range of values	1250°C	900-1050°C	0.25+0.25	10/sec	0,1,10,100,1000 sec

Table 4.3: Etchants used for Fe-30%Ni-0.1Nb.

Etchant	Composition	Etch time	Problems
Schaftmeister's Reagent	45% HCl 5% HNO_3 50% H_2O.	~30 mins.	Slow. Staining occurs.
Kalling's No.2 Reagent	100mL HCl 100mL alcohol 5g $CuCl_2$.	4/5 mins, swabbed.	Staining occurs.
Saturated Ammonium Persulphate	Ammonium persulphate in H_2O.	10 mins, swabbed.	Does not etch all grain boundaries. Shows strain lines.
Nital 5	5% HNO_3 95% alcohol.	5 mins, swabbed.	Does not etch all grain boundaries. Shows strain lines.
Electrolytic Nitric	40%HNO_3 60% H_2O. 3 Volts, 3 amps.mm^{-2}.	10-50 seconds.	Erratic results.
Conc. Nitric Acid	HNO_3.	~1 min, swabbed.	Etches up substructure.
10% Nitric in Tap Water	10% HNO_3 90% Tap Water.	~20 seconds, swabbed.	None.

Table 5.1: Measured Fraction Recrystallised Values.

Test	% X_V	± Error
900sd	0	0
900hw	0	0
900-1dd	0	0
900-10dd	0	0
900-100dd	0	0
900-1000dd	3.4	2.6
900-10hhq	0	0
950sd	9.2	5.0
950hw	0.9	1.2
950-1dd	17.8	4.5
950-10dd	6.0	3.0
950-100dd	8.0	3.3
950-1000dd	9.4	4.6
950-1hhq	4.2	2.0
950-10hhq	5.6	1.8
950-100hhq	5.8	2.0
950-1000hhq	20.6	4.0
1000sd	45.4	3.5
1000hw	14.3	3.7
1000-1dd	35.2	4.6
1000-10dd	33.8	5.9
1000-100dd	26.0	5.4
1000-1000dd	39.0	2.0
1000-10hhq	49.8	5.9
1050sd	74.0	7.0
1050hw	29.8	9.0
1050-1dd	52.7	5.1
1050-10dd	67.5	7.3
1050-100dd	61.0	7.6
1050-1000dd	71.9	4.0
1050-10hhq	69.9	4.9

Table 5.2: Deformed and recrystallising grain sizes measured in double-deformation plane strain compression specimens.

Deformation Temperature	Recrystallised grain size (μm)		Aspect Ratio	Deformed grain size (μm)		Aspect Ratio
	RD	ND		RD	ND	
900°C	-	-	-	494±130	210±19	2.4
950°C	41±21	28±5	1.4	347±180	152±31	2.3
1050°C	36±7	32±6	1.1	78±31	78±32	1

Table 5.3: Expected deformed grain size and aspect ratio for a 393μm original grain size material deformed in plane strain compression.

Strain	RD grain size (μm)	ND grain size (μm)	Aspect Ratio
0	393	393	1
0.25 in PSC	505	306	1.7
0.5 in PSC	647	239	2.7
0.5 inc 5% spread	615	239	2.6

Table 5.4: Substructure size measurements in hot worked Fe-30%Ni-Nb.

Sample	Cell-Block Length	Microband Width
900-10-dd	0.87±0.16μm	0.19±0.02μm
950-100-dd	0.60±0.01μm	0.50±0.01μm
1050-100-dd	1.00±0.12μm	0.57±0.12μm
1050-sd	0.42±0.06μm	equiaxed subgrains

Table 5.5: Particle volume fractions measured from TEM images of carbon replicas for various test conditions.

Sample	Volume Fraction Measured
900-10-DD	0.0039
900-10-HHQ	0.00087
900-100-DD	0.0058
950-1-DD	0.0012
950-10-HHQ	0.0028
950-1000-DD	0.0049

Table 6.1: Calculation of t_{50} values for static recrystallisation during the present processing conditions using valid t_{50} relations from the literature for C-Mn microalloyed steels. All of these relations refer to static recrystallisation, in the absence of precipitates.

AUTHOR	t_{50}(1000°C)	t_{50}(1050°C)
Sellars (1980)	216	68
Laasraoui and Jonas (1991)	4	1
Medina and Mancilla (1993)	48	19
Karjalainen and Perttula (1996)	190	59
Cho et al. (2001)	109	34
Actual t_{50} data from Figure 5.10	**~9-20**	**~6-10**

Table 6.2 Particle size data measured during thermomechanical processing of Fe-30%Ni-Nb compared to values found in the literature on C-Mn-Nb steels.

Author(s)	Hold Time (s)	Mean Particle Diameter (nm)
Janampa (1982)	2	8.0
Kwon and DeArdo (1991)	10	4.1
Kwon and DeArdo (1991)	100	6.5
Kwon and DeArdo (1991)	1000	9.8
Poths *et al.* (2001)	10	8.5*
Poths *et al.* (2001)	1000	11.1*
Actual data	10	7.2
Actual data	100	10.2
Actual data	1000	16.9

* Poths data estimated from frequency distributions in publication.

Table 6.3: A comparison between particle volume fraction expected and that actually measured from carbon replicas of deformed material.

Source	Volume Fraction Expected
Irvine *et al.* (1967) equation at 900°C.	6.7×10-4
Palmiere *et al.* (1994) equation at 900°C.	4.6×10-4
Irvine *et al.* (1967) equation at 950°C.	6.4×10-4
Palmiere *et al.* (1994) equation at 950°C.	4.4×10-4
Estimated value using equation 6.2.	0.0021
Measured value from *e.g.* 900-10-DD	0.0039

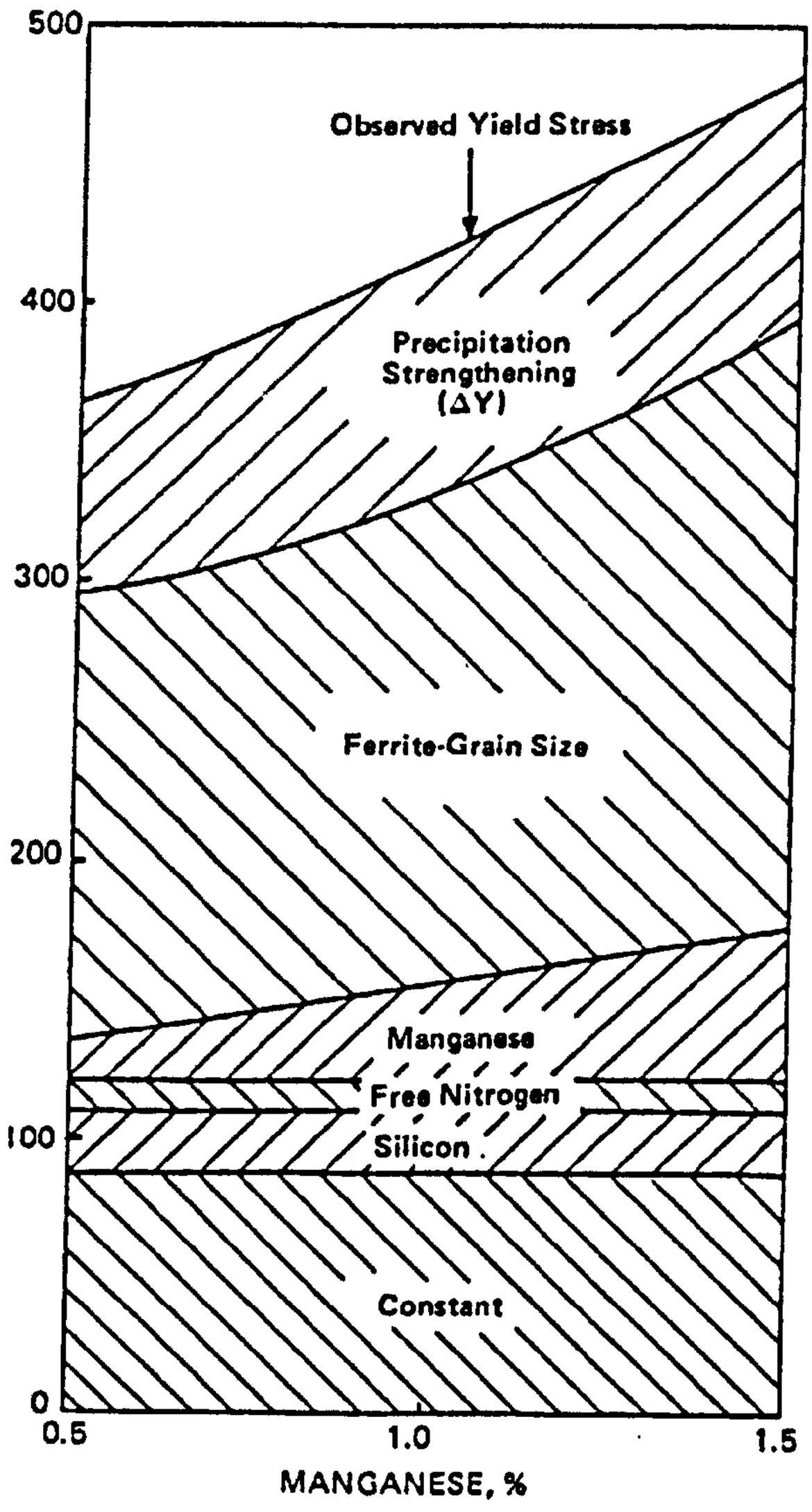

Figure 2.1: Strengthening attributable to different mechanisms in a 0.2%C-0.2%Si-0.15%V-0.015%N microalloyed steel [from Gladman 1977].

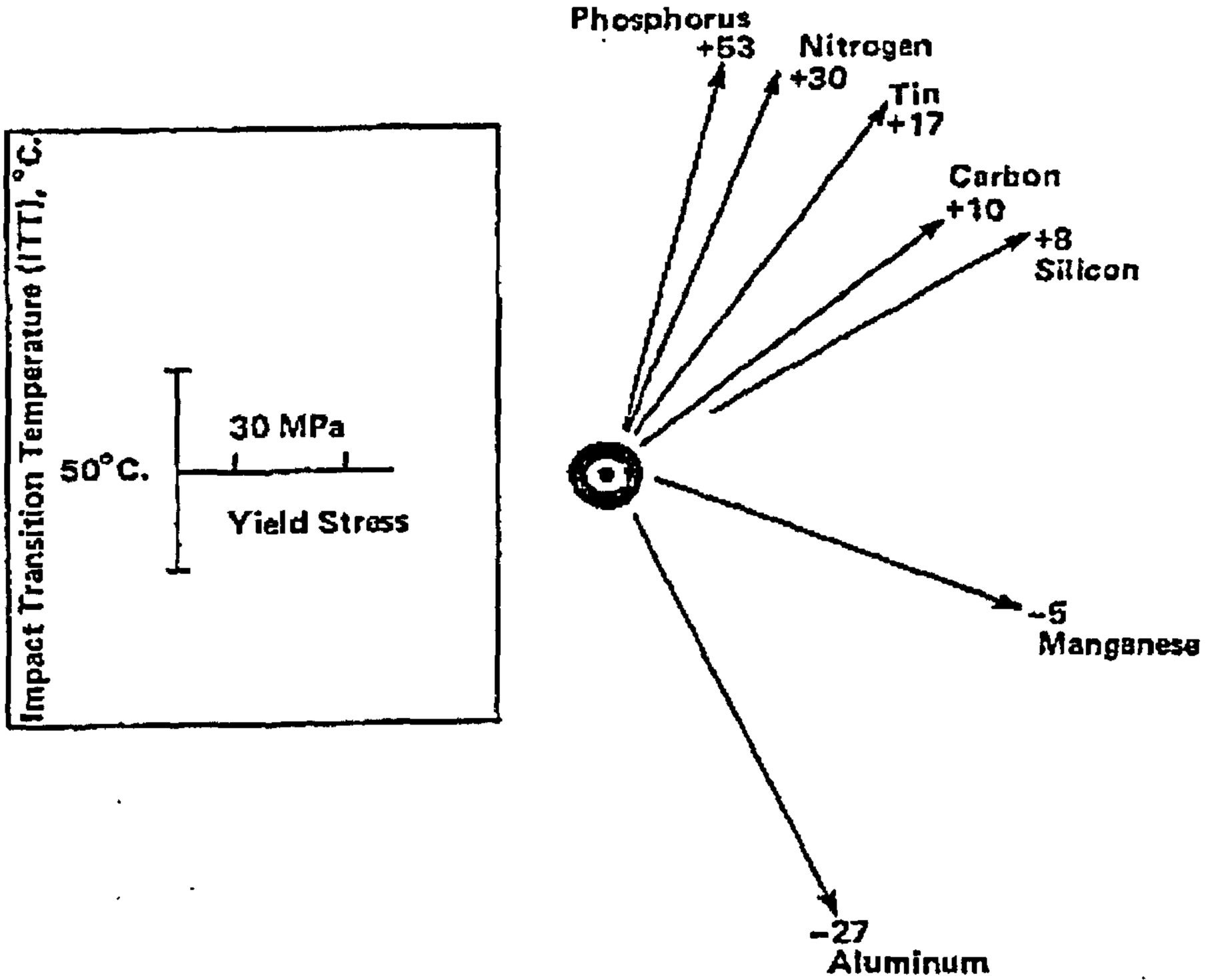

Figure 2.2: Effect of alloying additions on yield strength and impact transition temperature [from Pickering 1977]. The numbers refer to the change in ITT per 15MPa increase in yield strength.

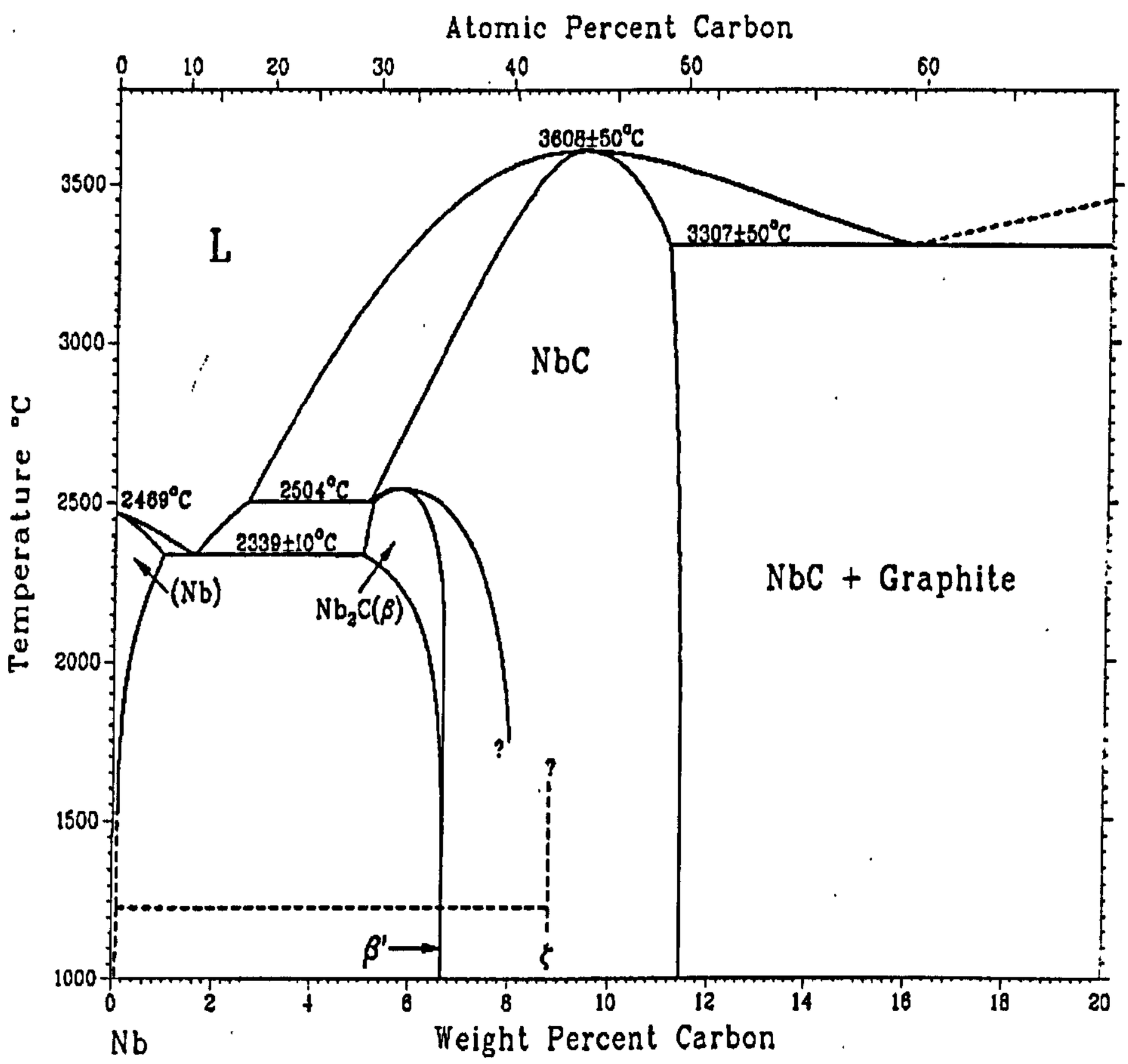

Figure 2.3: Equilibrium phase diagram for the Nb-C system [from Binary Alloy Phase Diagrams 1986].

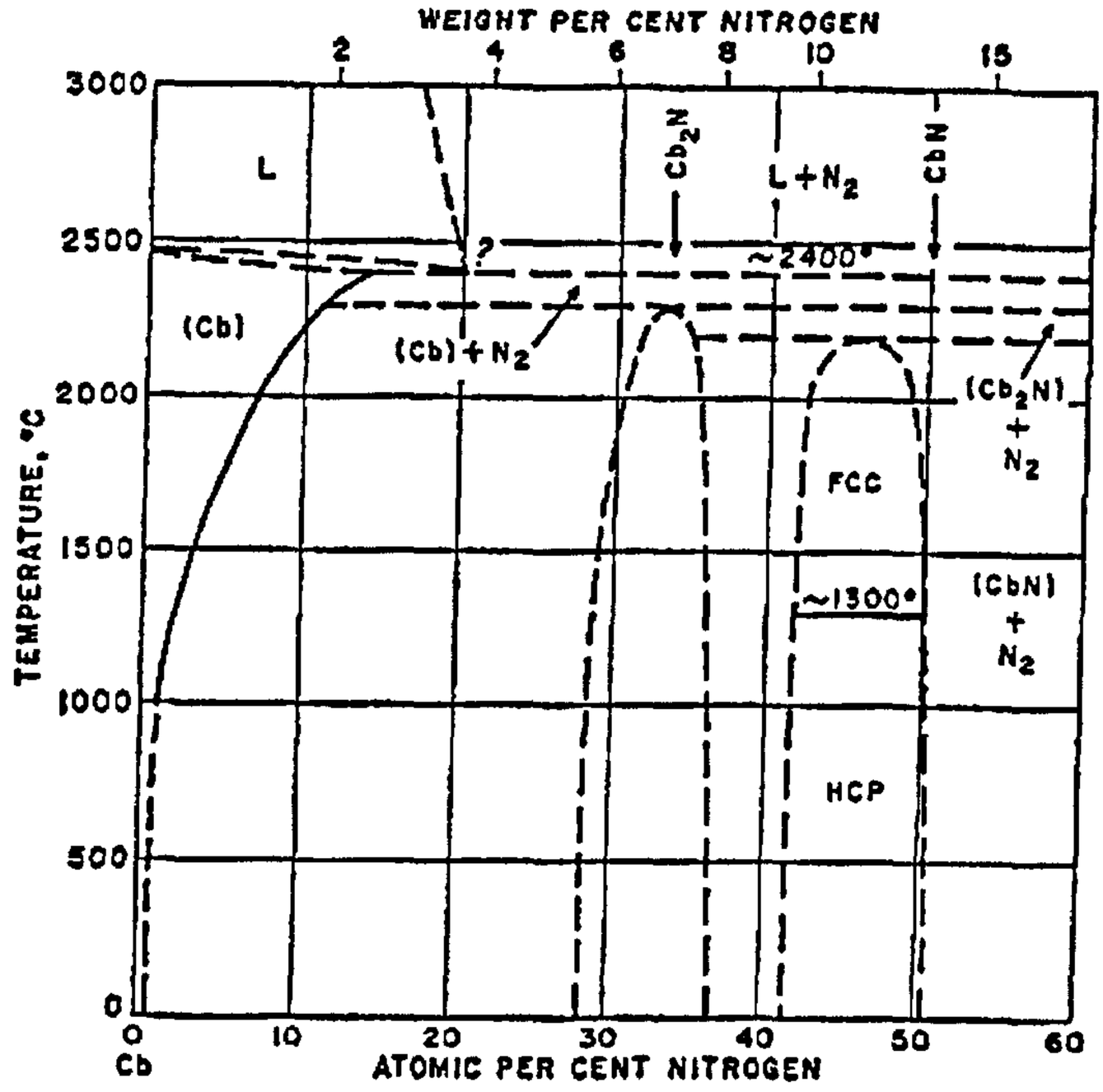

Figure 2.4: Equilibrium phase diagram for the niobium (columbium)-nitrogen system [from Constitution of Binary Alloys 1965].

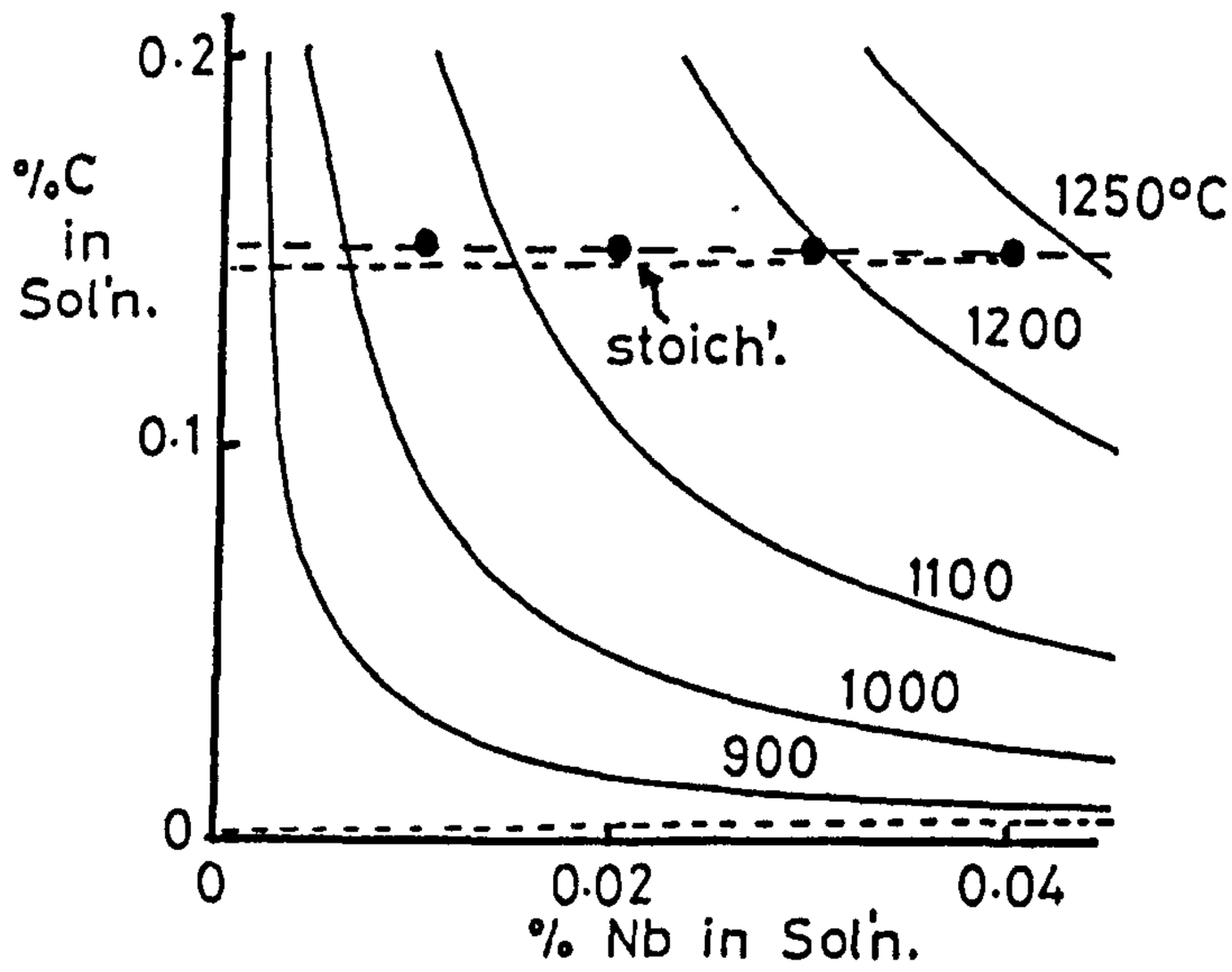

Figure 2.5: Plot showing NbC solubility product relation as a function of temperature [from Gladman and Walker 1984].

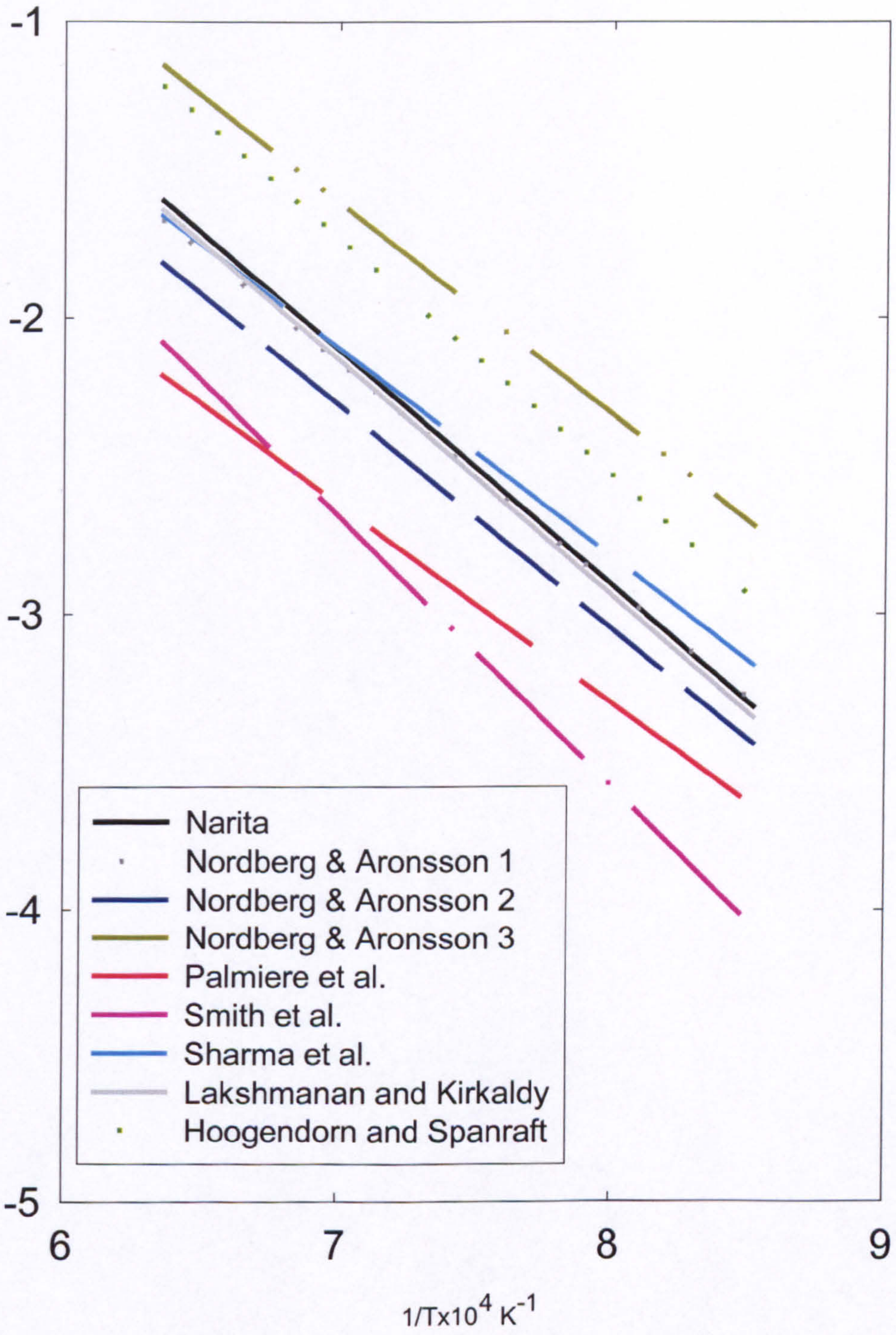

Figure 2.6: A comparison of NbC solubility products found in the literature.

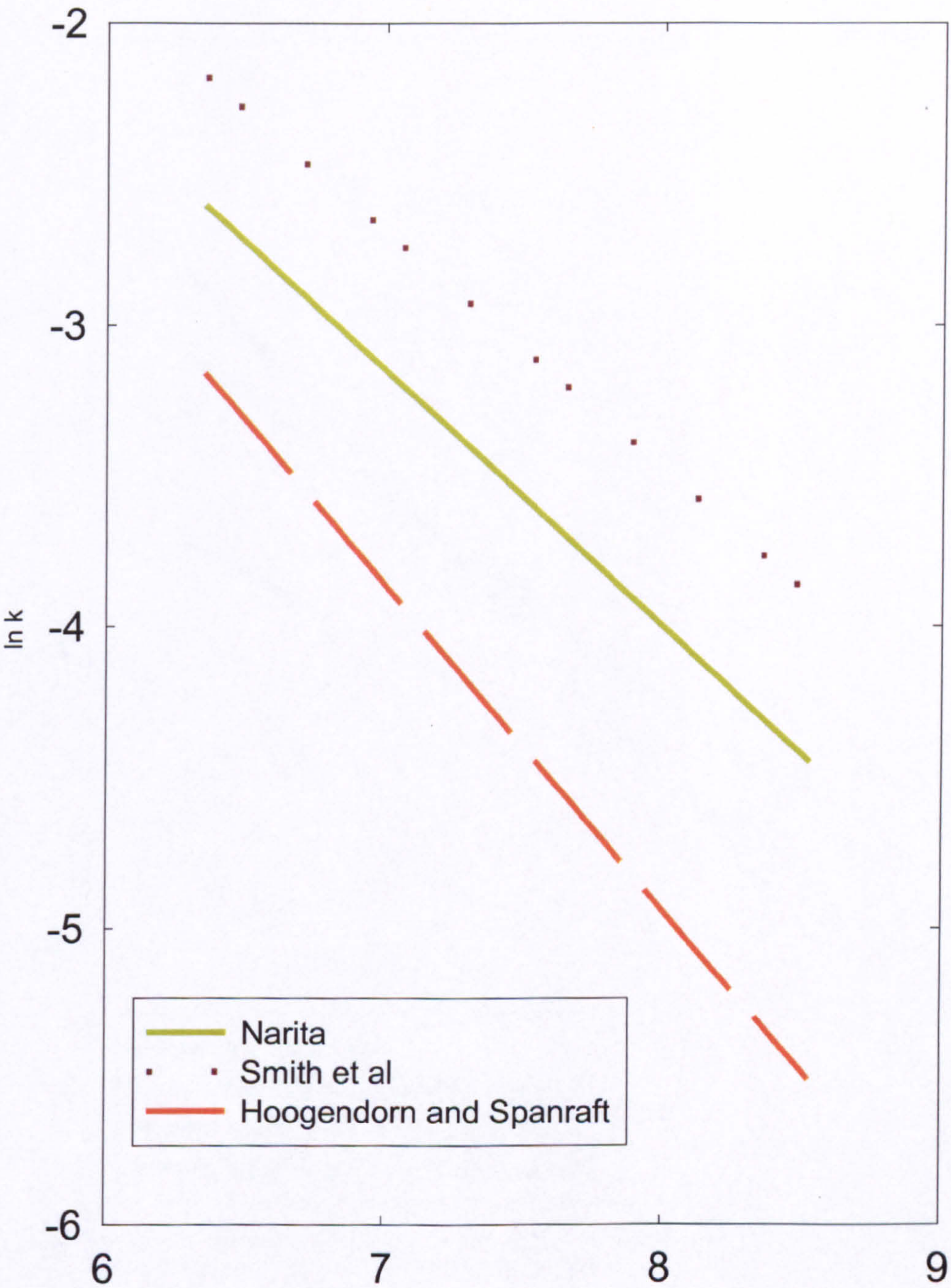

Figure 2.7: A comparison of NbN solubility products found in the literature.

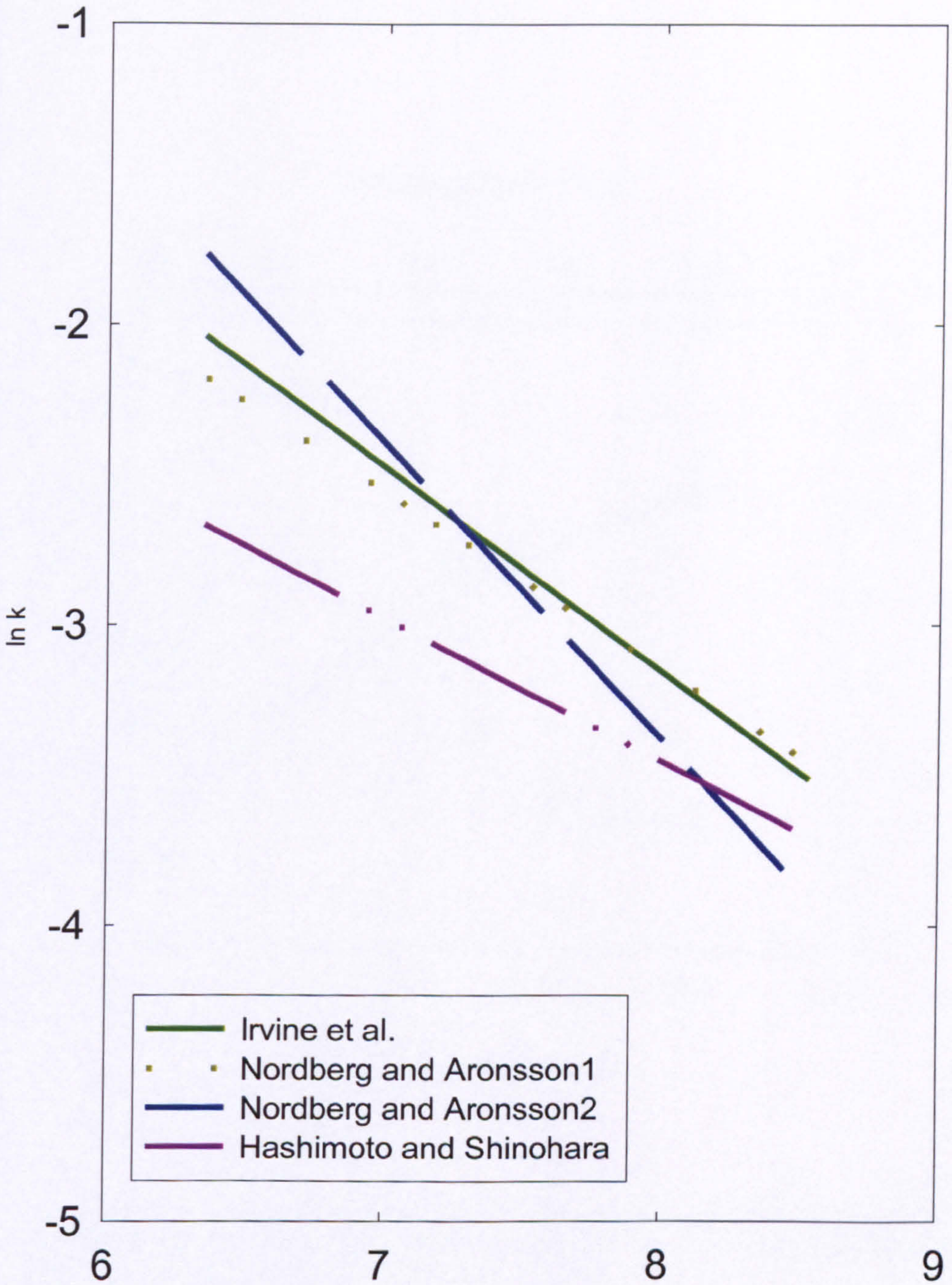

Figure 2.8: A comparison of NbCN solubility products found in the literature.

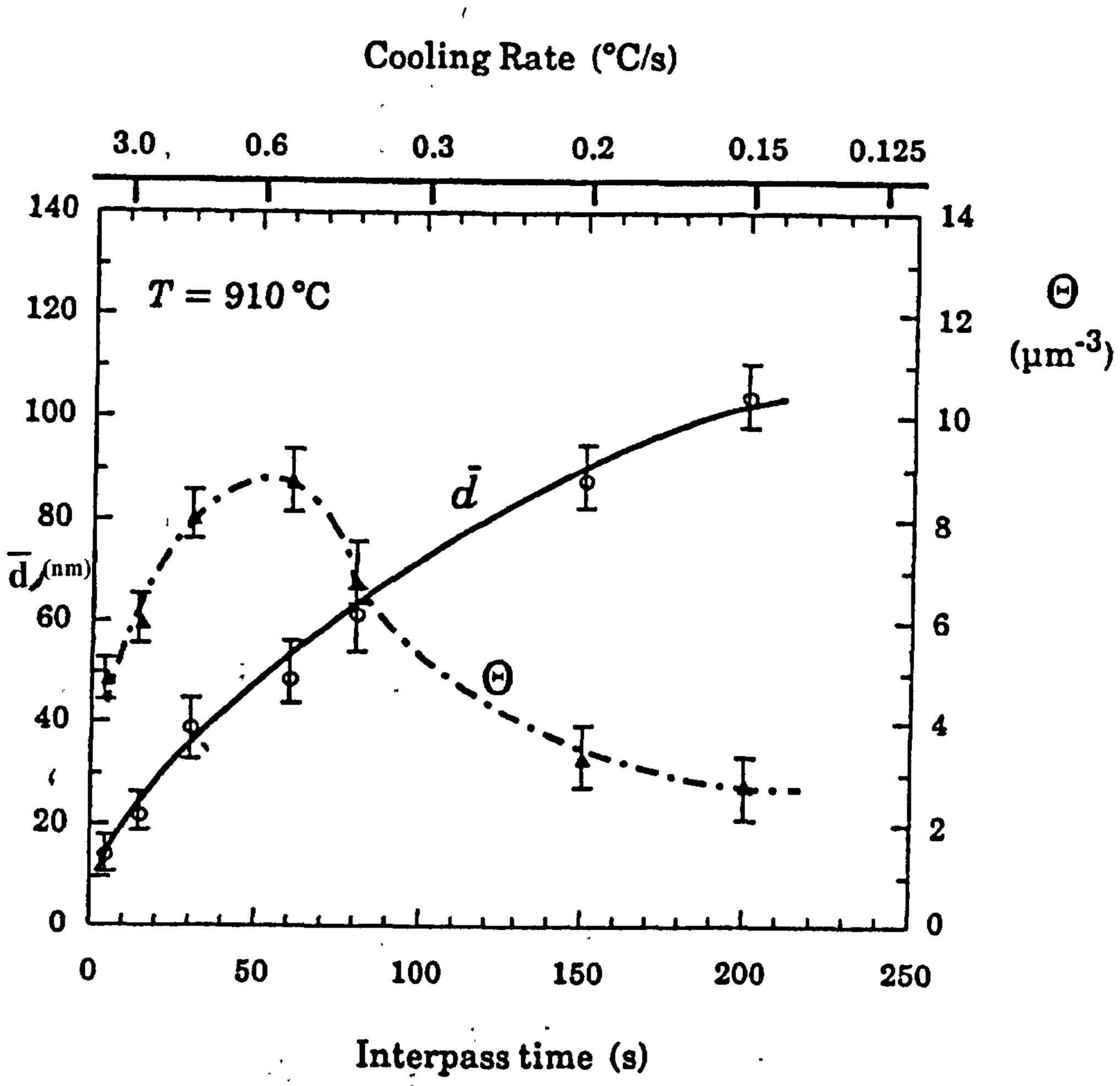

Figure 2.9: Plot showing precipitate particle size variance ($\bar{d}$) with isothermal hold time and precipitate density (Θ) as a function of time during a rolling simulation under continuous cooling conditions [from Sun *et al.* 1993].

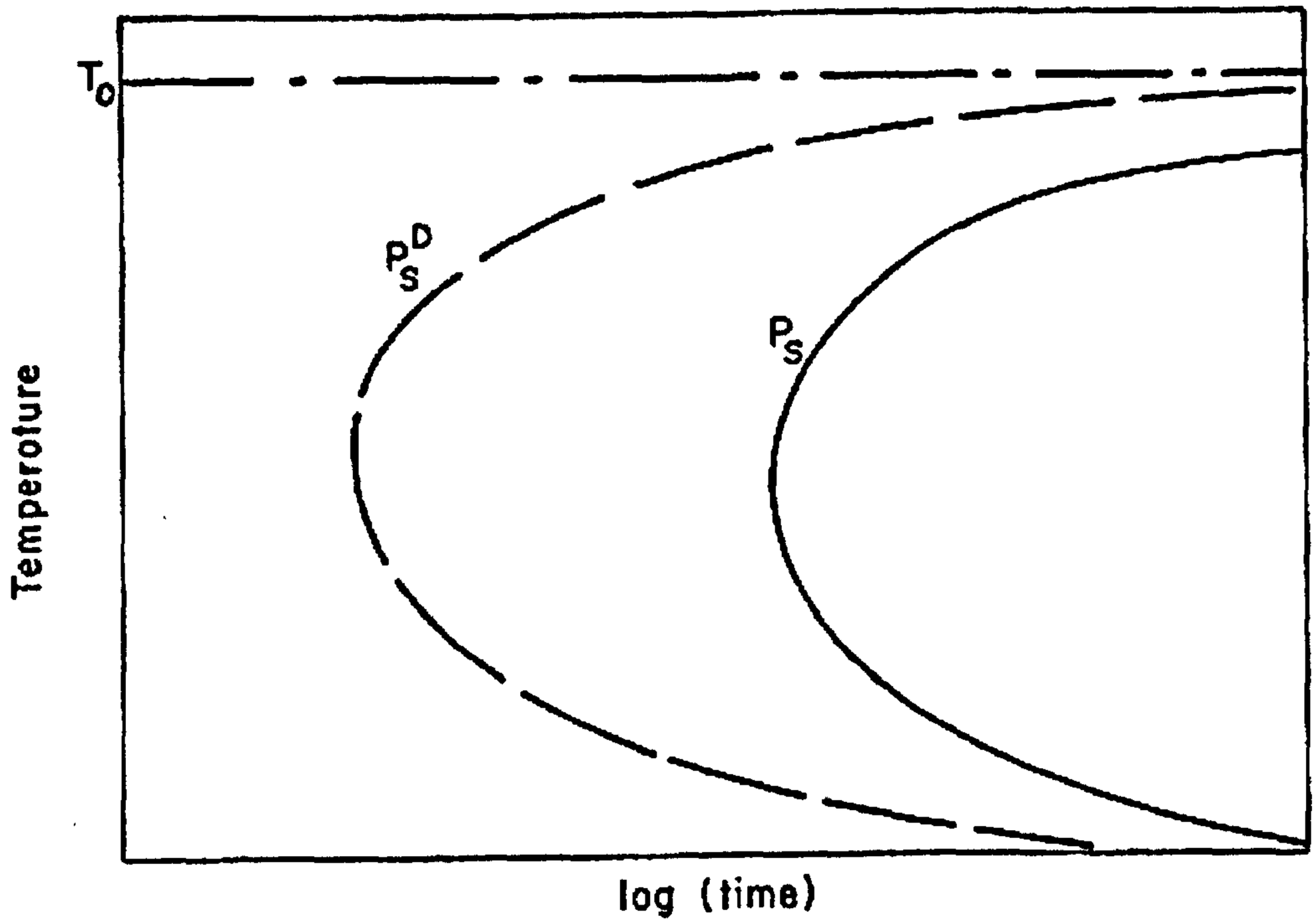

Figure 2.10: Precipitation-time-temperature (PTT) schematic showing precipitation kinetics in a microalloyed steel. Precipitation start times with ($\mathbf{P_S^D}$) and in the absence of (P_S) deformation are marked. Often such diagrams also show completion times (P_F) [from Hansen *et al.* 1980].

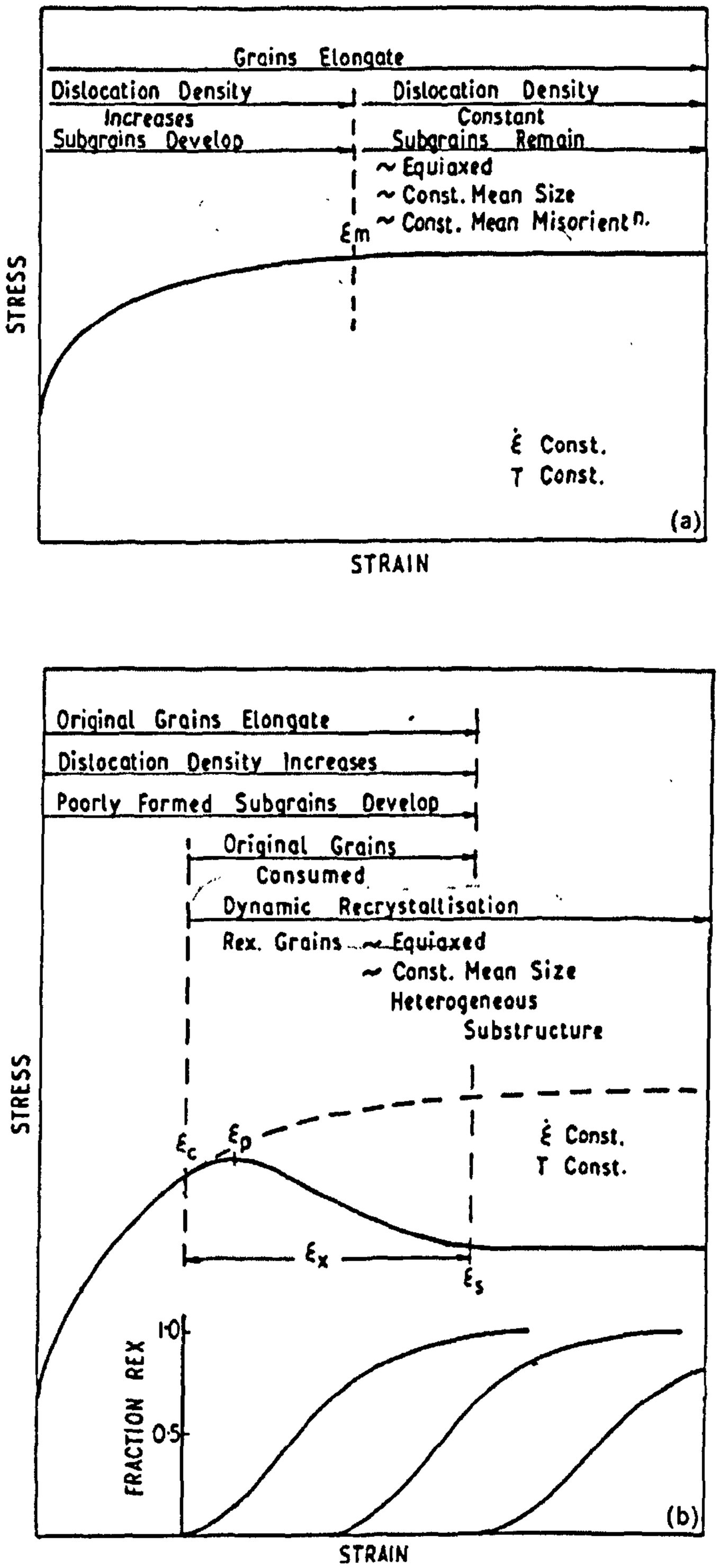

Figure 2.11: High temperature flow behaviour of metals during hot working for: a) high SFE materials which show a dynamic recovery (DRV) response, and b) low SFE materials which exhibit dynamic recrystallisation (DRX) beyond a critical strain [from Sellars 1990].

(a)

Dislocation tangles

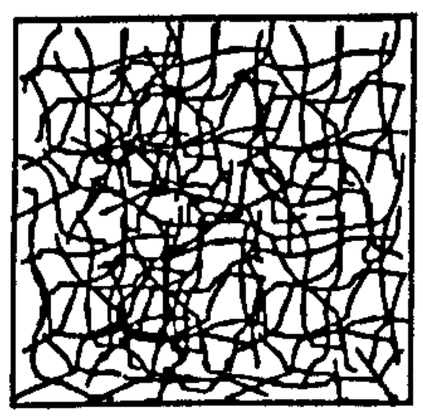

(b)

Cell formation

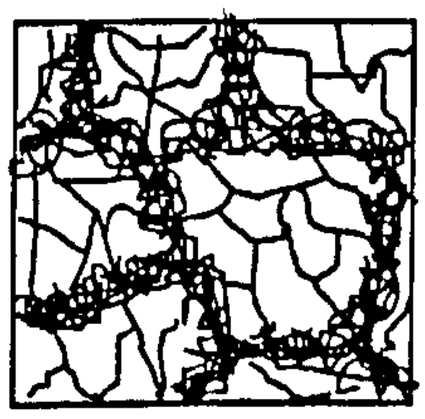

(c)

Annihilation of dislocations within cells

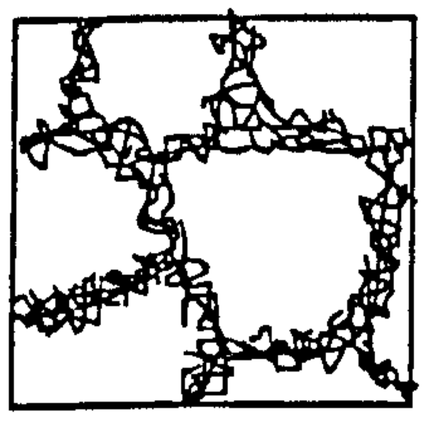

(d)

Subgrain formation

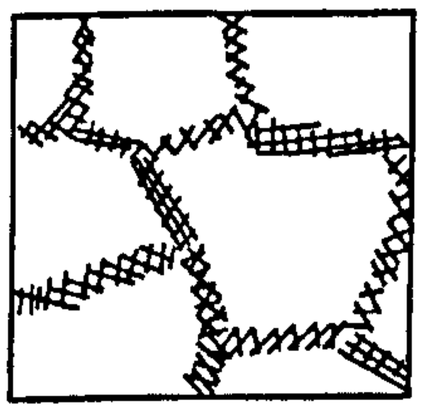

(e)

Subgrain growth

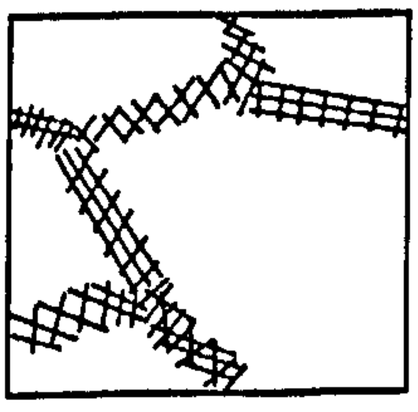

Figure 2.12: The recovery process in metals: a) the introduction of dislocations during deformation, and b) the formation of a loose-walled cell structure, c) further re-arrangement by dislocation annihilation and combination, d) the cell walls consolidate to form compact subgrain boundaries, e) subgrain growth and the early stages of recrystallisation [from Humphreys and Hatherly 1996].

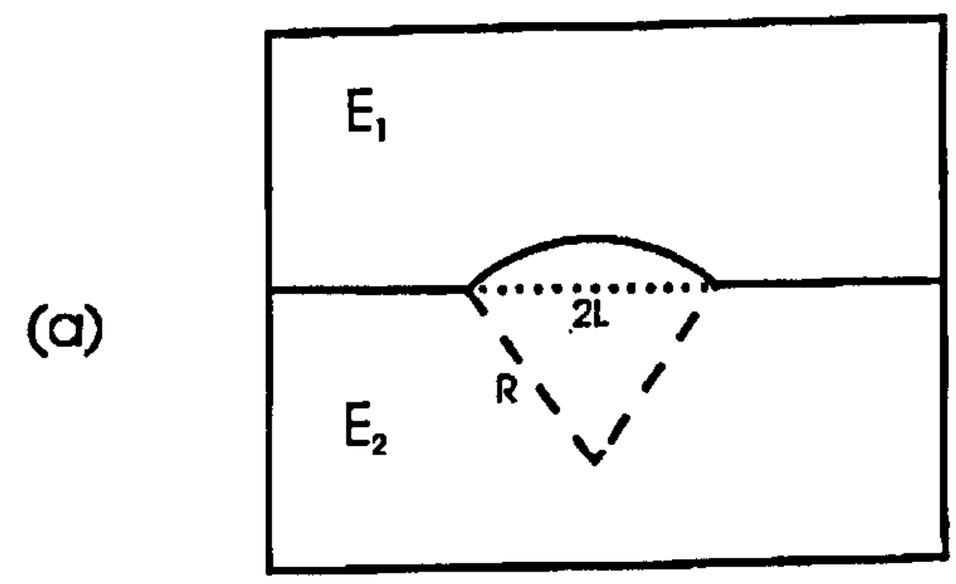

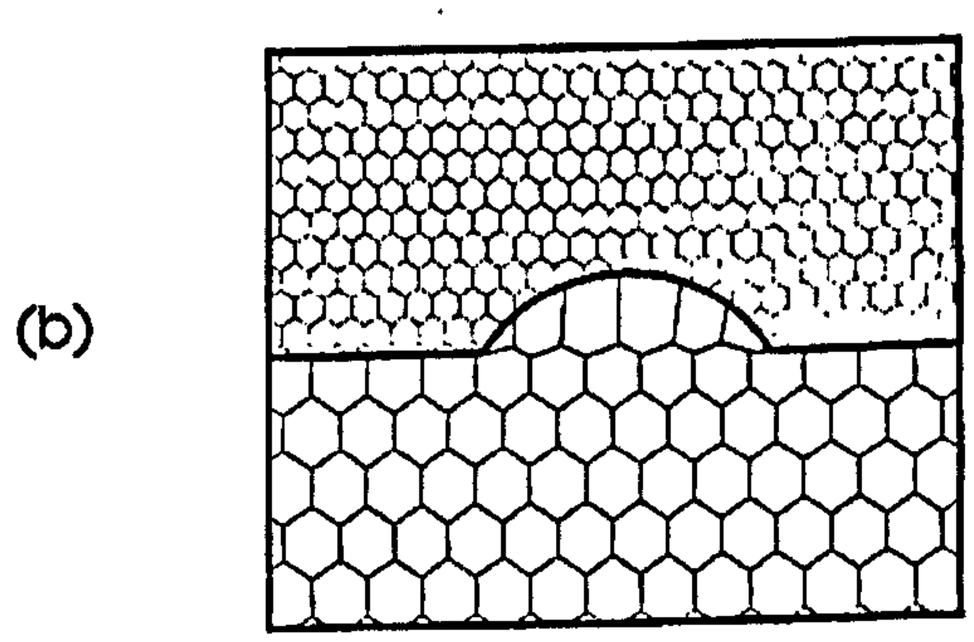

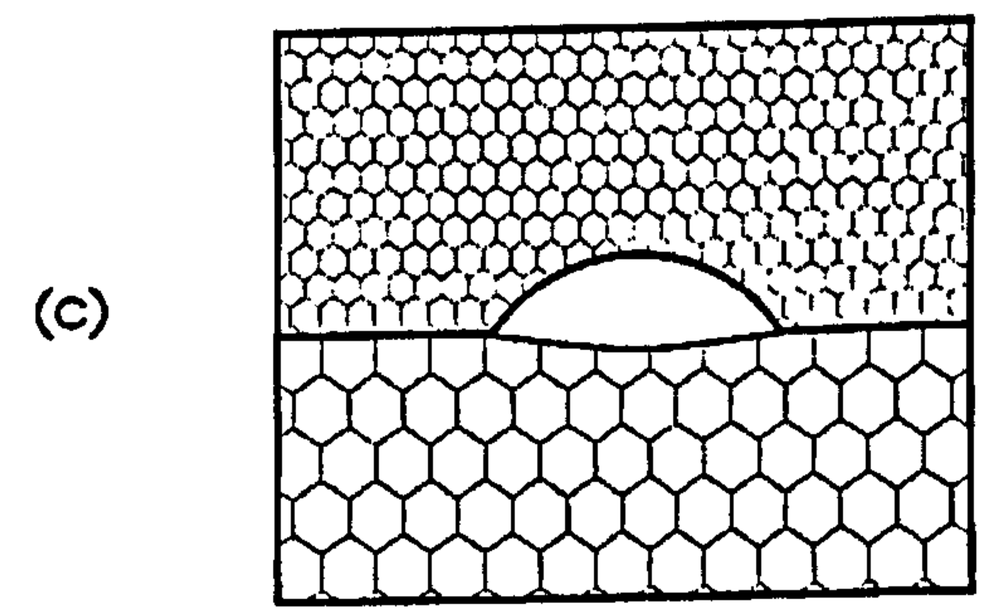

Figure 2.13: Schematic showing the strain induced boundary migration (SIBM) nucleation mechanism in metals: a) shows two contiguous grains of differing stored energy ($E_2<E_1$) with a cap from grain 1 bulging in grain 2. b) Shows the subgrains in the cap elongating as they grow into the lower energy grain; c) shows the newly formed recrystallisation nucleus [from Humphreys and Hatherly 1996].

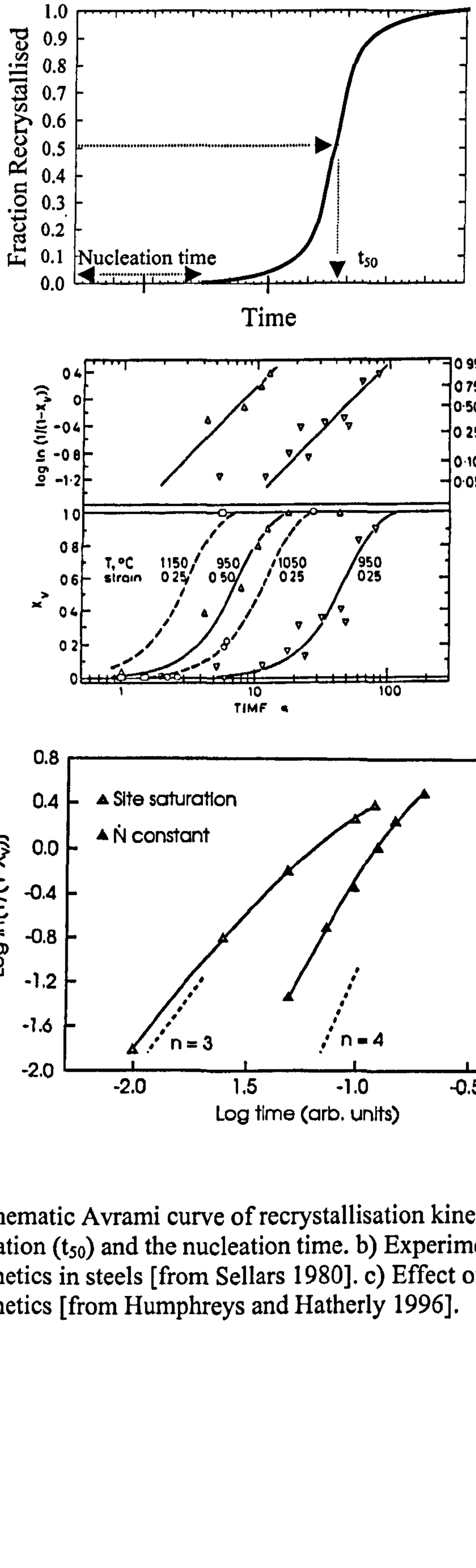

Figure 2.14: a) Schematic Avrami curve of recrystallisation kinetics, showing the time to 50% recrystallisation (t_{50}) and the nucleation time. b) Experimentally determined recrystallisation kinetics in steels [from Sellars 1980]. c) Effect of Avrami exponent on recrystallisation kinetics [from Humphreys and Hatherly 1996].

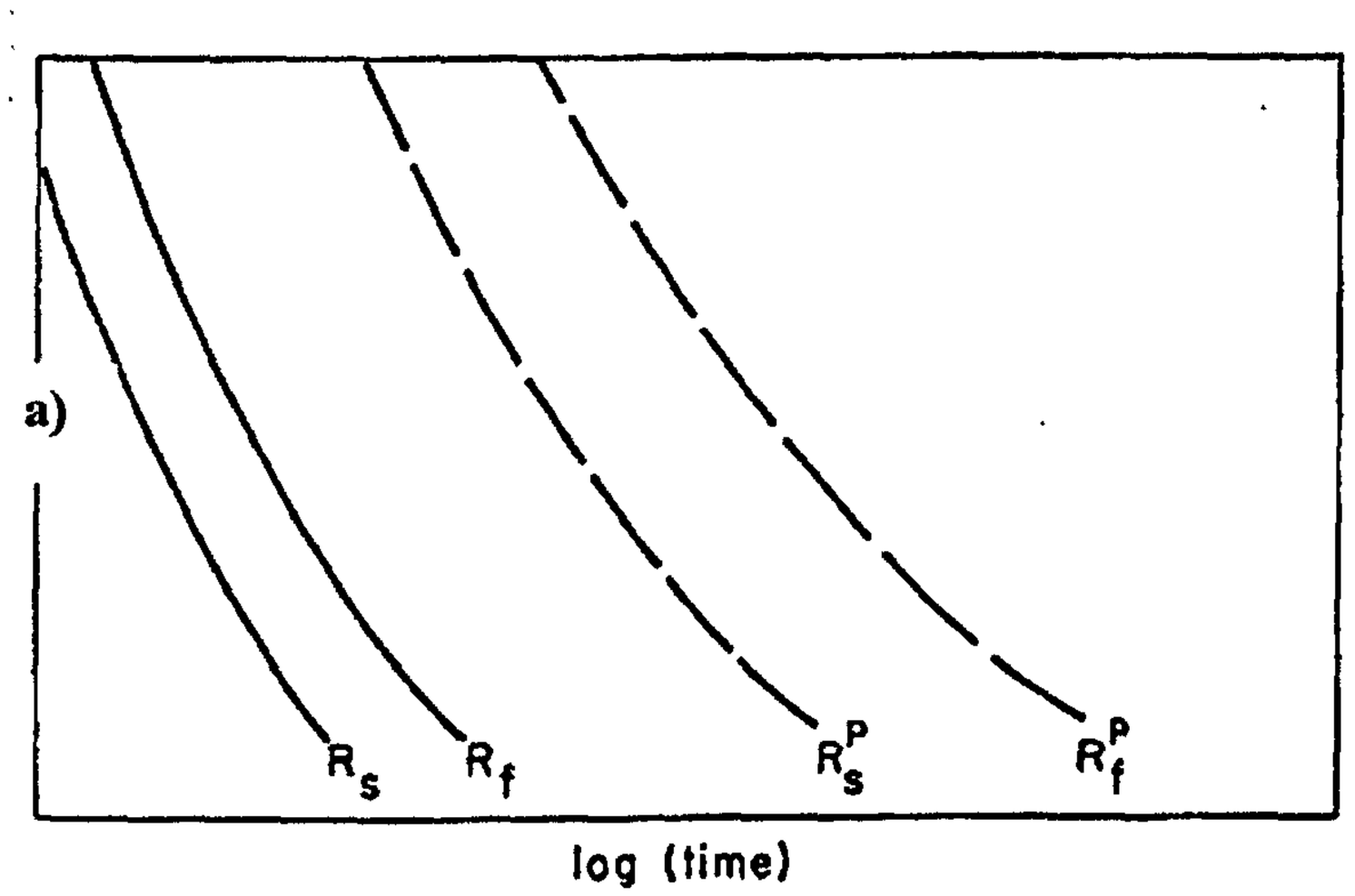

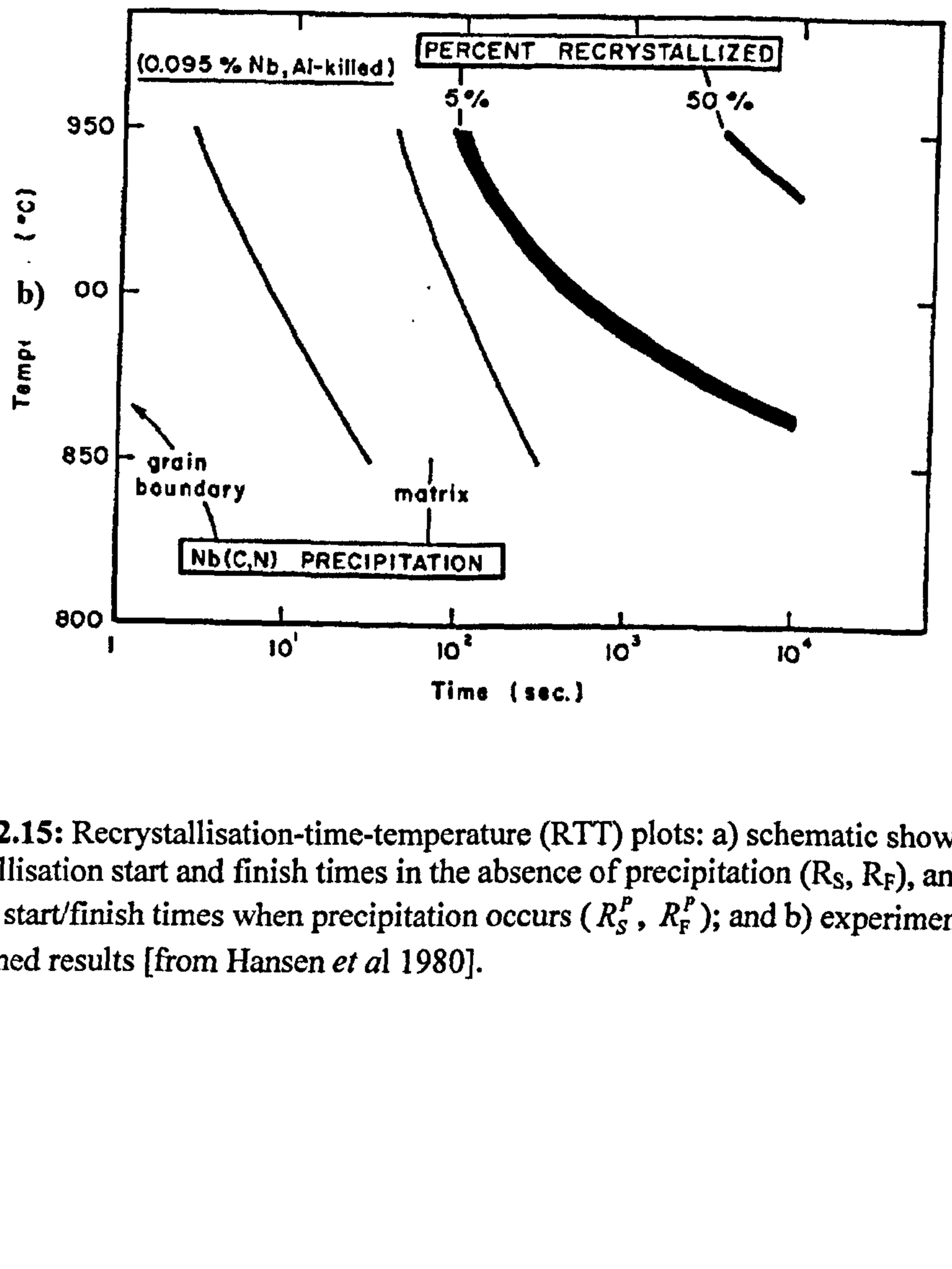

Figure 2.15: Recrystallisation-time-temperature (RTT) plots: a) schematic showing recrystallisation start and finish times in the absence of precipitation (R_S, R_F), and delayed start/finish times when precipitation occurs (R_S^P , R_F^P); and b) experimentally determined results [from Hansen *et al* 1980].

a)

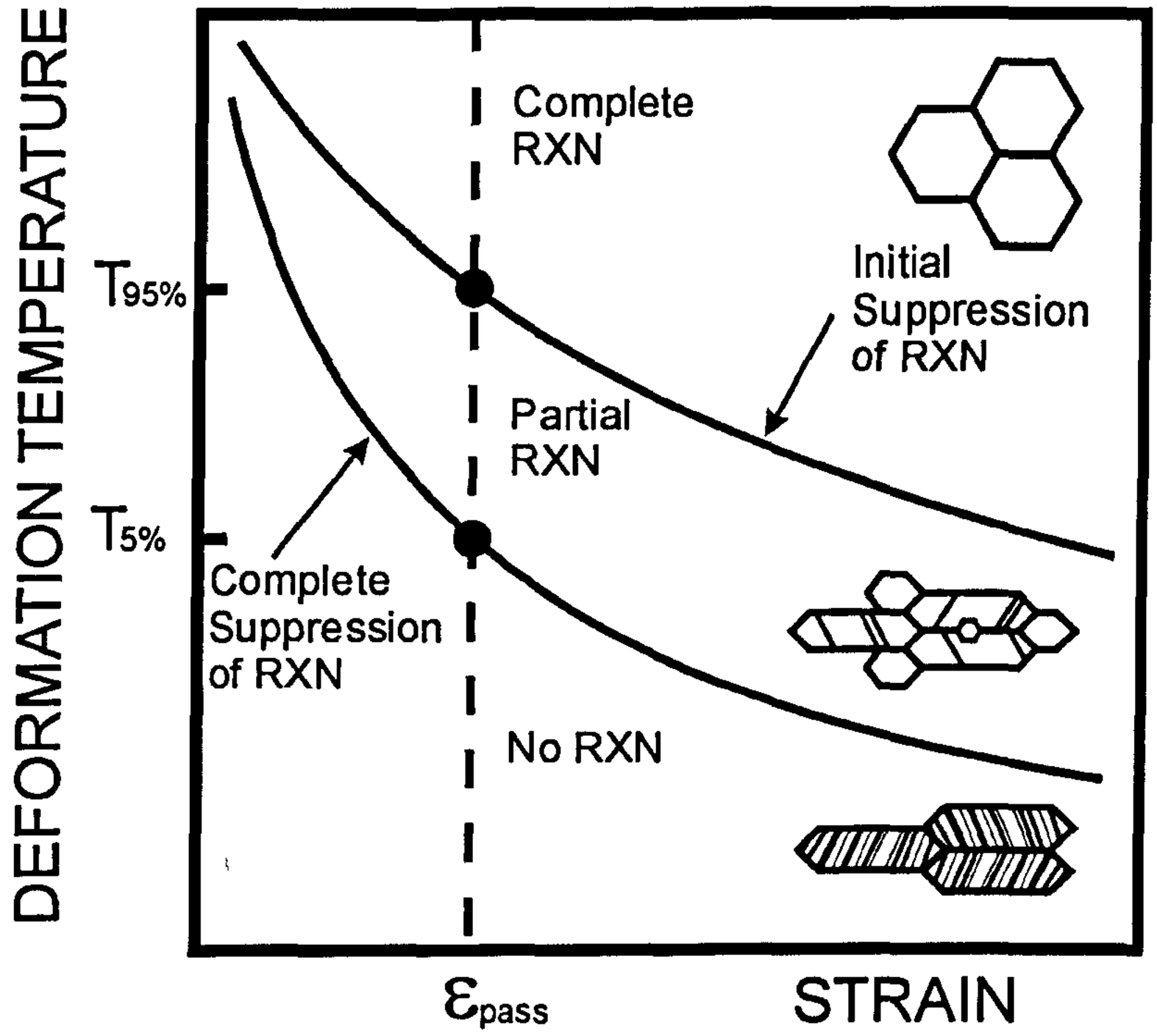

b)

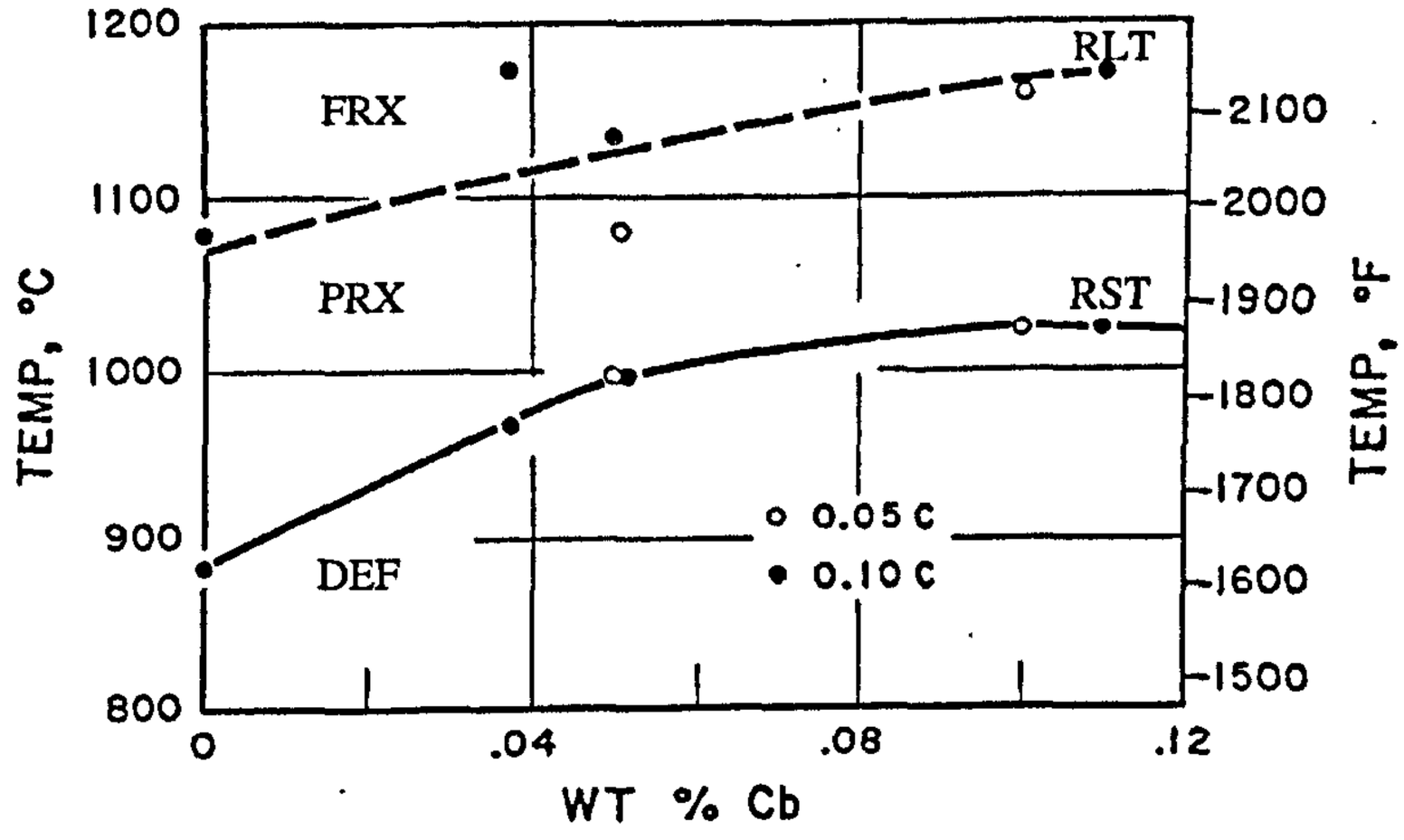

Figure 2.16: Effect of deformation variables on recrystallisation. a) Shows the effect of strain and deformation temperature on recrystallisation [Palmiere *et al.* 1996]. b) Shows the effect of niobium content as a function of deformation temperature - note the regions of full recrystallisation (FRX), partial recrystallisation (PRX) and pancaking (DEF). The recrystallisation limit temperature and recrystallisation stop temperature are also marked [Davenport and DiMicco 1980].

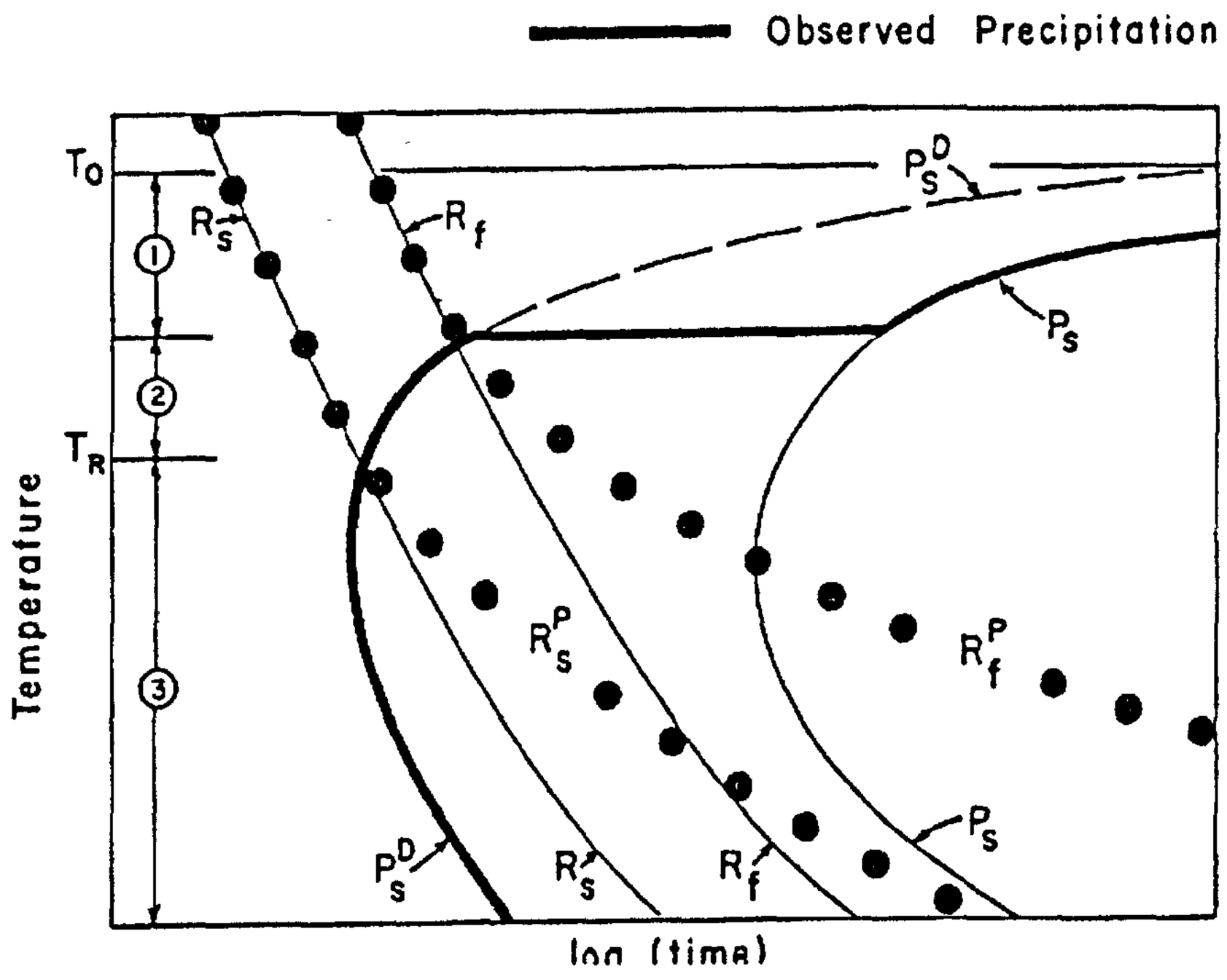

Figure 2.17: Recrystallisation-precipitation-time-temperature (RPTT) plot showing the interaction between precipitation and recrystallisation. Recrystallisation start/finish times are labelled R_F/R_S, while the superscript P indicated recrystallisation in the presence of precipitate particles. P_S is the precipitation start time, and the superscript D refers deformation-induced precipitation [from Hansen *et al.* 1980].

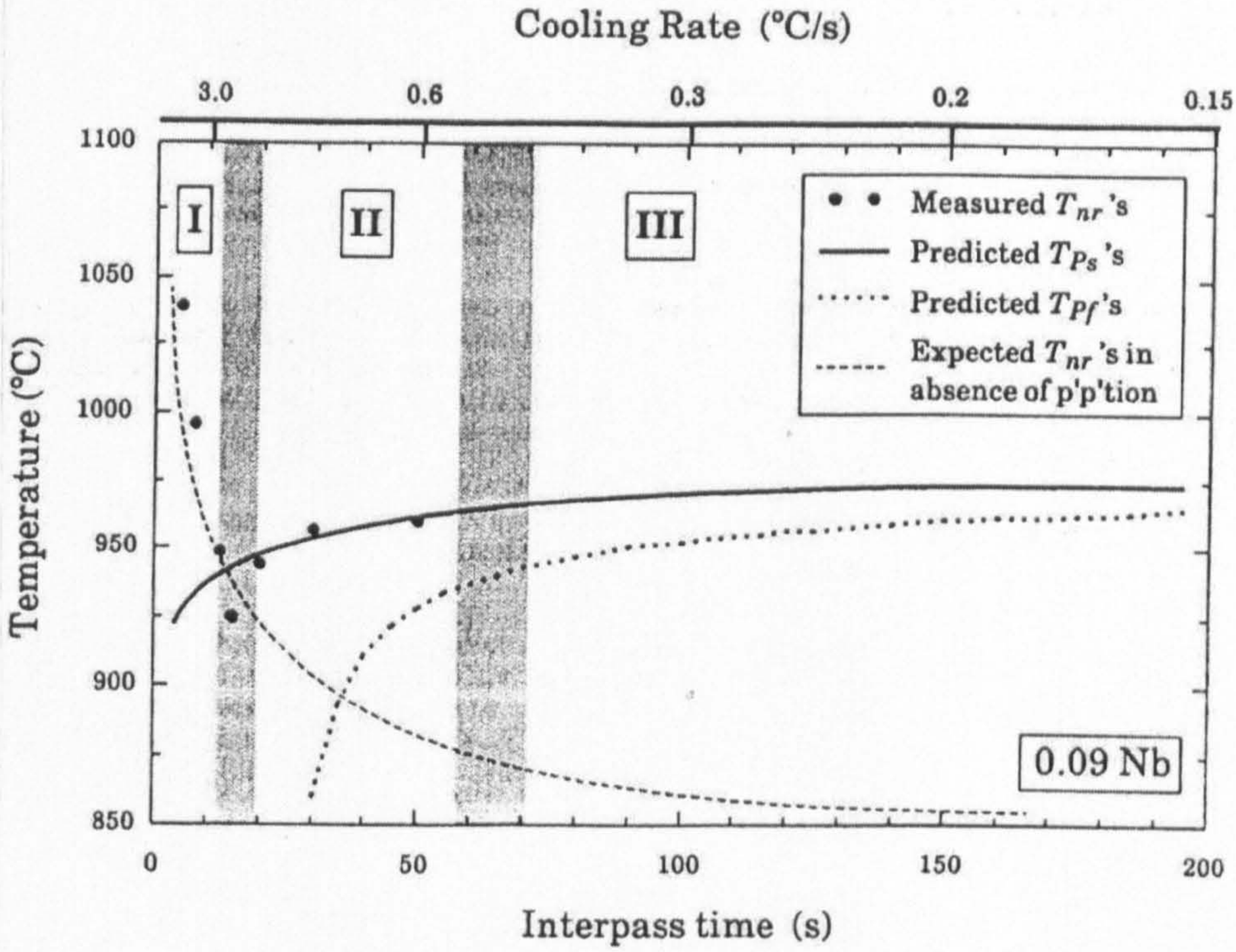

Figure 2.18: Plot showing the change in T_{NR} as a function of interpass time during a continuous cooling simulation of hot rolling for different niobium concentrations [from Sun *et al.* 1993].

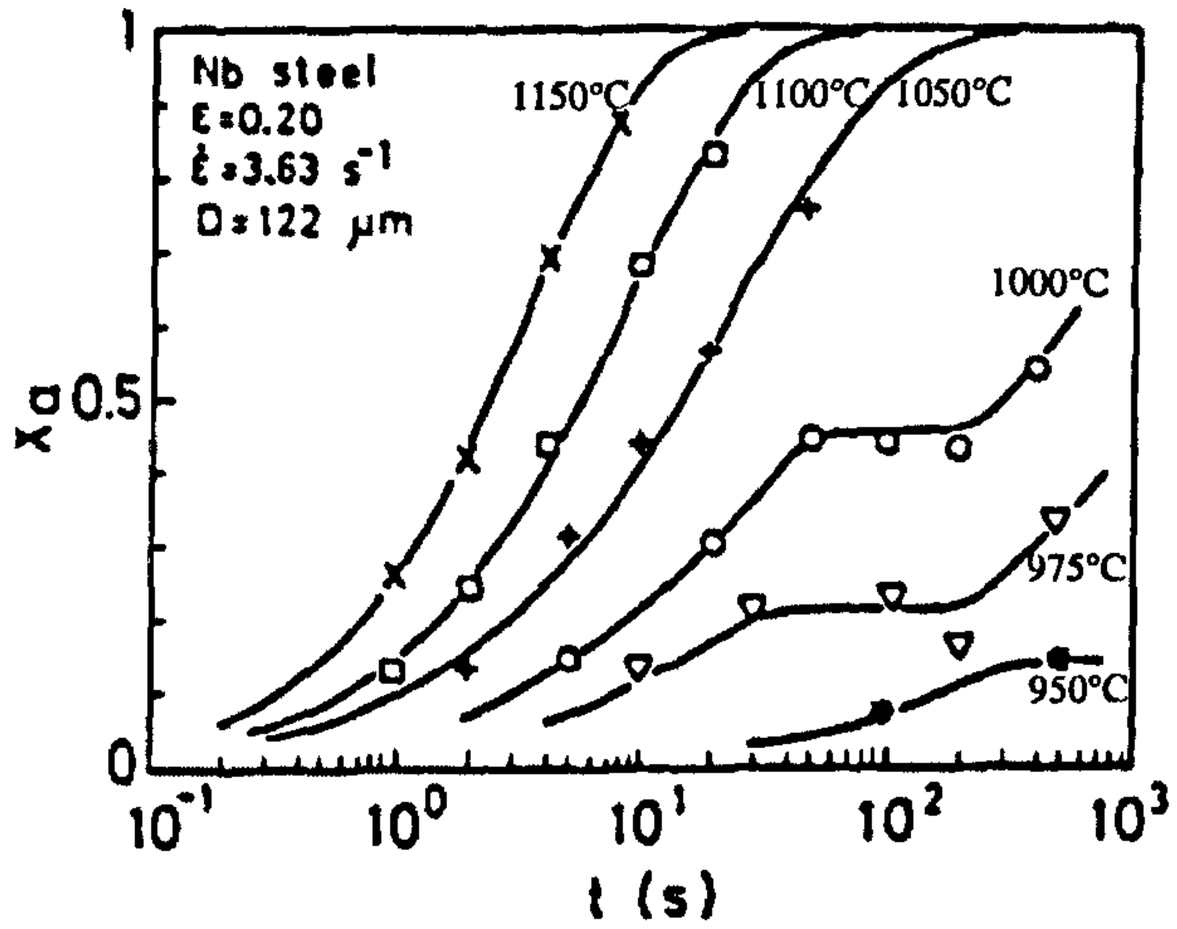

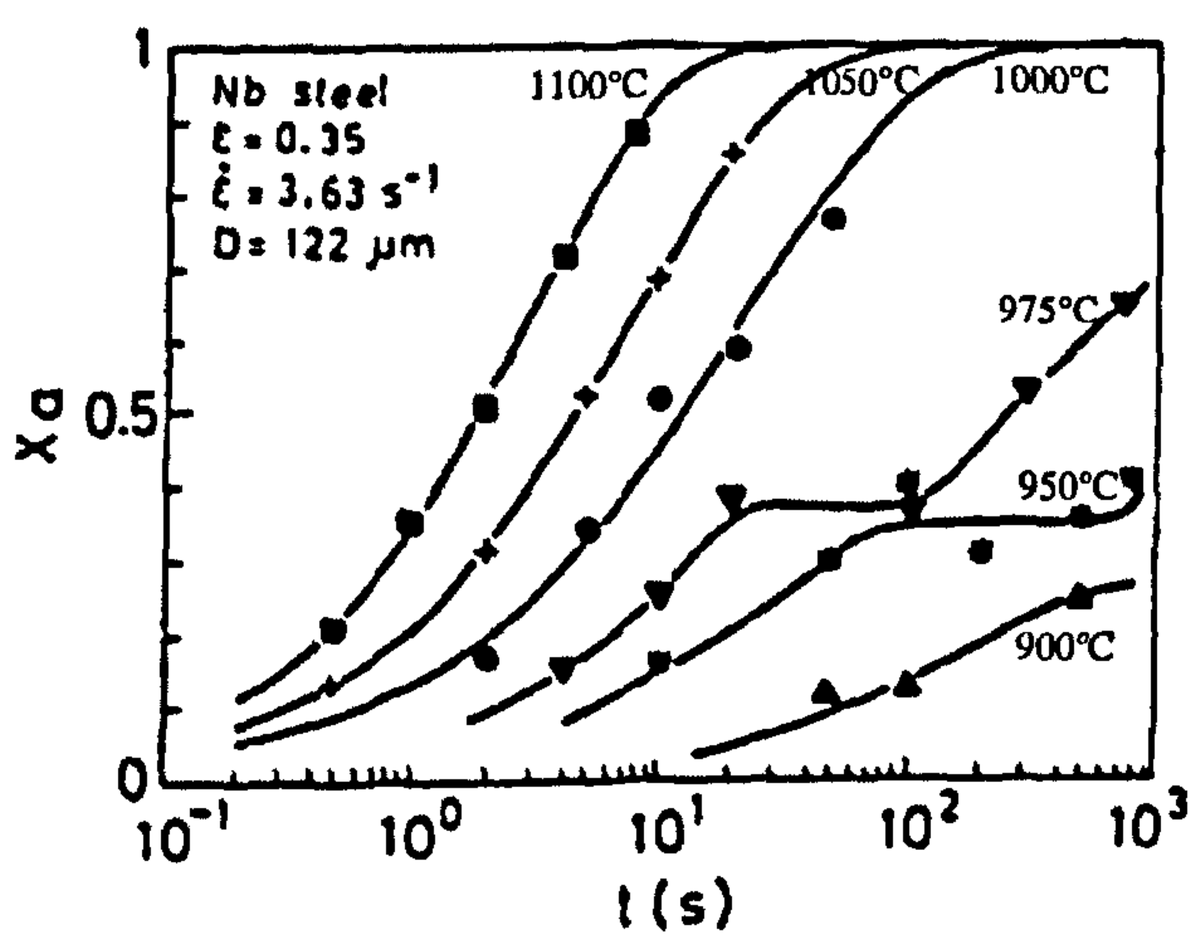

Figure 2.19: Recrystallisation kinetics as a function of temperature, highlighting the effect of precipitation on recrystallisation at lower deformation temperatures, where plateaux show the arrest of recrystallisation for a) strain of 0.2 and b) strain of 0.35 [from Medina and Mancilla 1993].

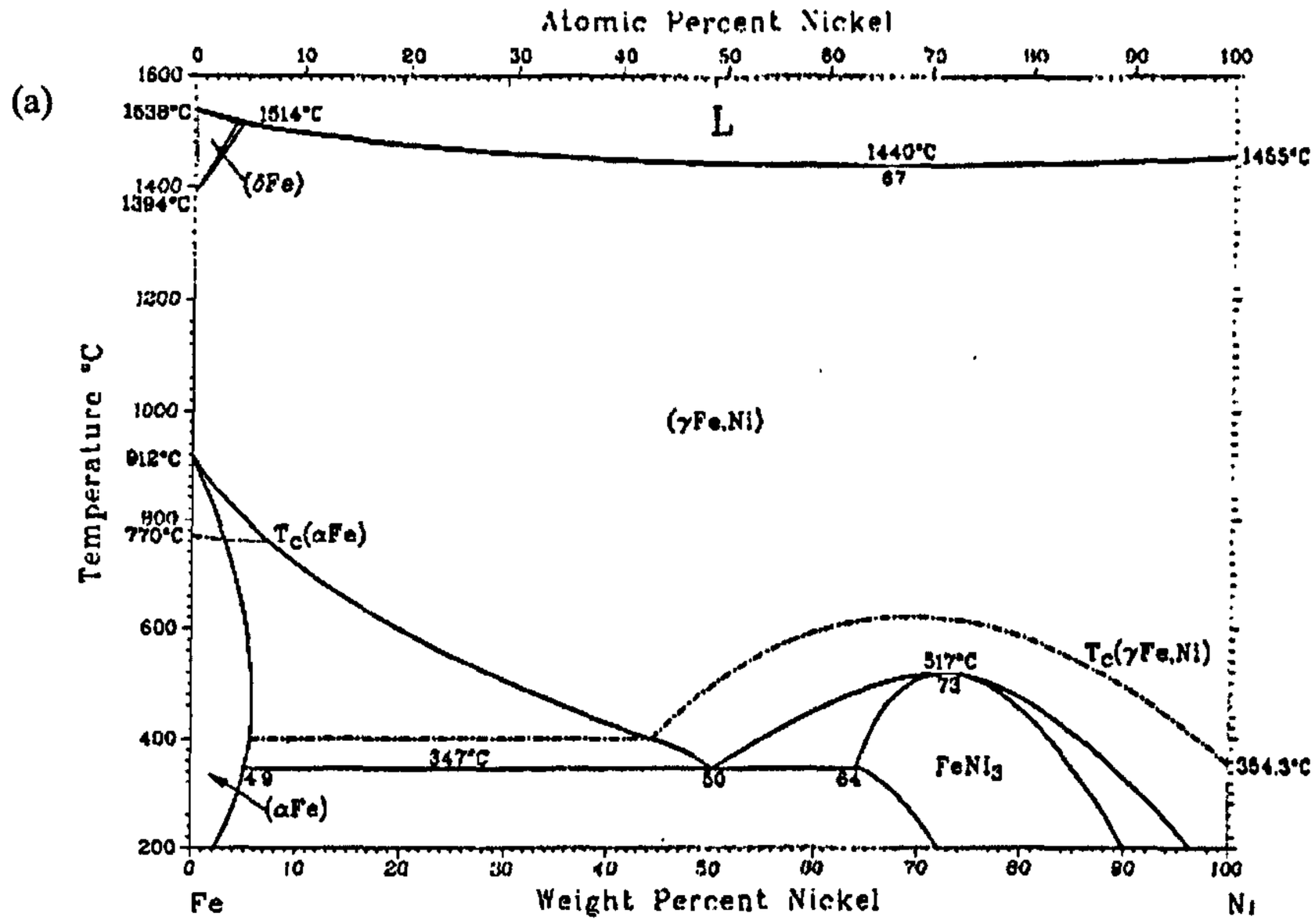

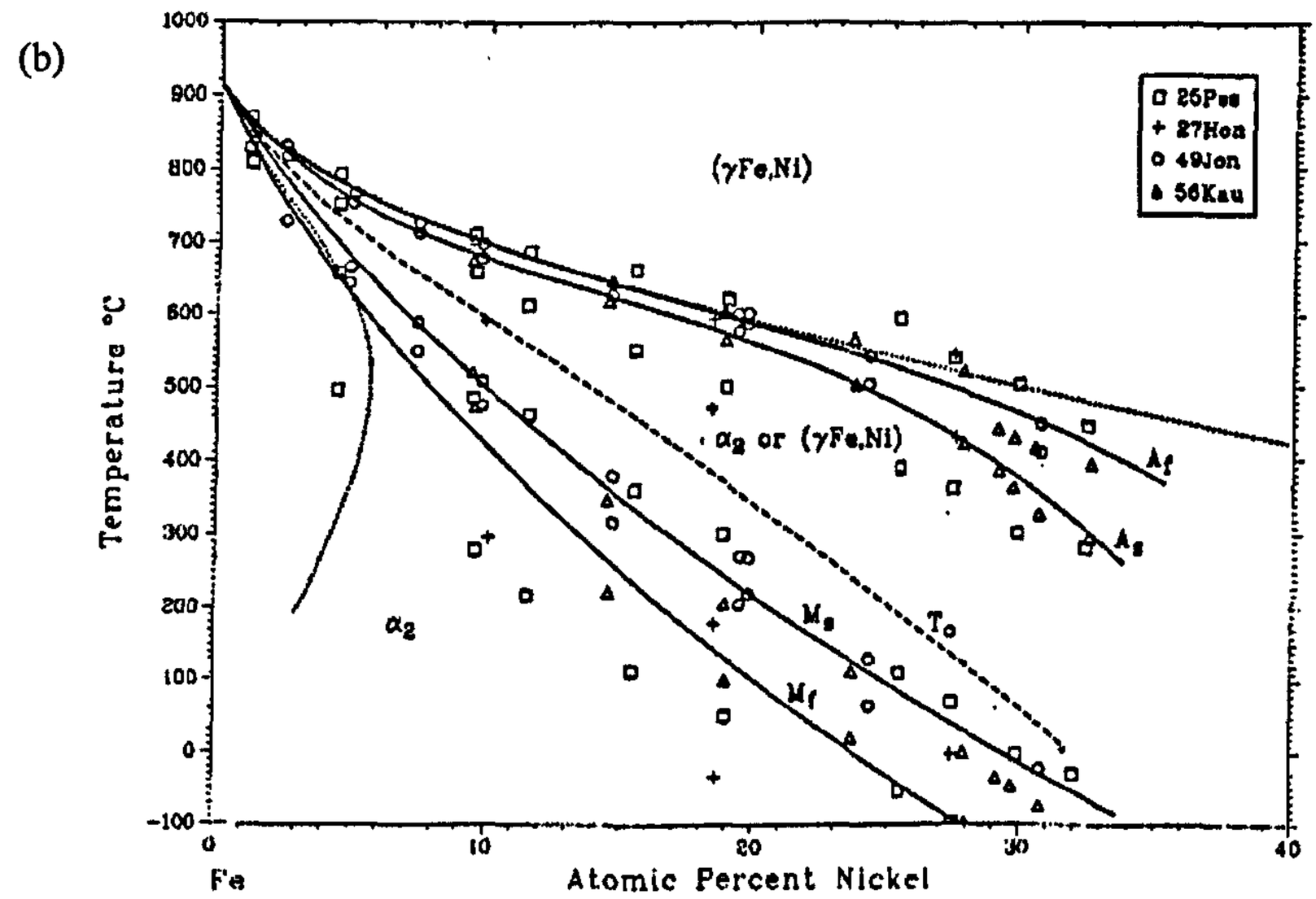

Figure 2.20: a) Equilibrium phase diagram for the Fe-Ni system, b) transformation diagram for Invar alloys [from Swartzendruber 1991].

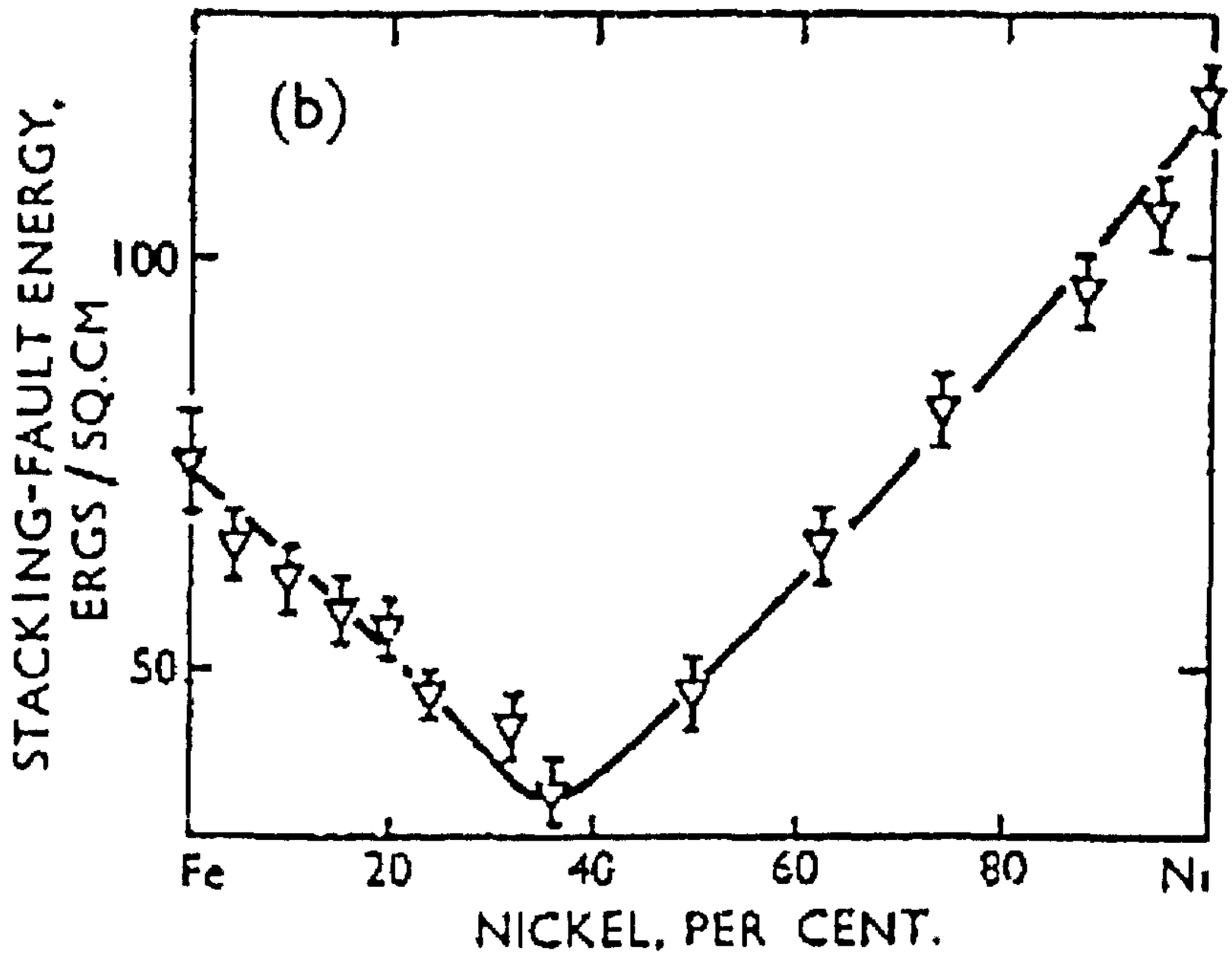

Figure 2.21: Variation in stacking fault energy with composition in the Fe-Ni system [from Charnock and Nutting 1967b].

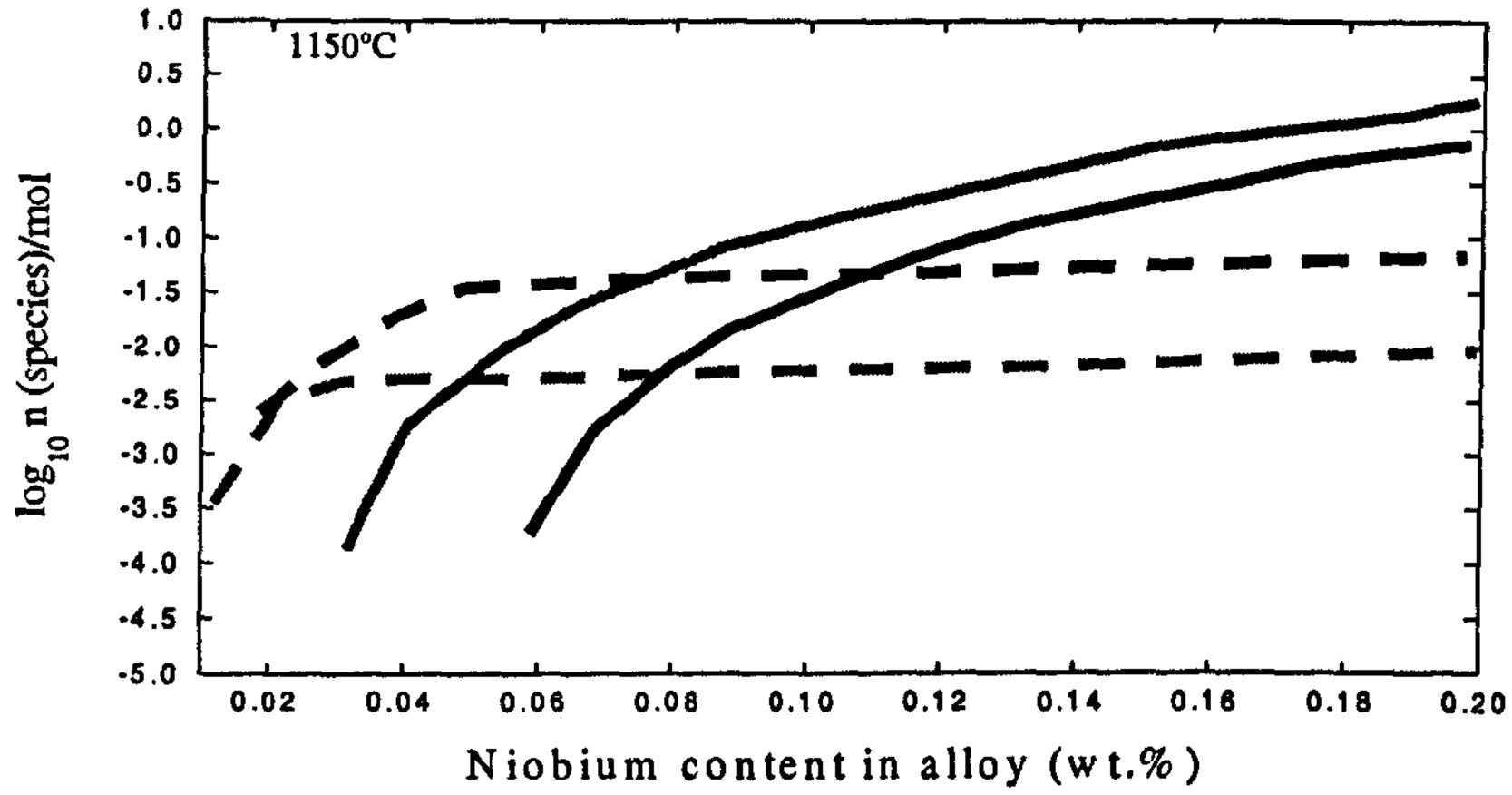

Figure 2.22: Plot determined from Thermocalc equilibrium solubility plots for C-Mn based and Fe-Ni-C-Mn based microalloyed steels of otherwise similar composition at 1150°C. The y-axis shows the number of chemical species present (equates to at.% concentration) for NbC and solute Nb, while the x-axis shows wt.% niobium in the alloy.

This allows a comparison of the relative solubility of NbC in these two alloys. This shows that for a given amount of Nb in the steel (e.g. 0.1wt.%), then the Fe-30%Ni matrix has more solute niobium than an equivalent C-Mn based steel. The dotted lines are approximately 0.4 units apart, which corresponds to a factor of ~2.5. It is because of this higher solubility (and therefore reduced supersaturation) at lower temperatures that the Sheffield experimental alloy requires such a large amount of niobium, when compared with typical niobium levels found in conventional microalloyed steels.

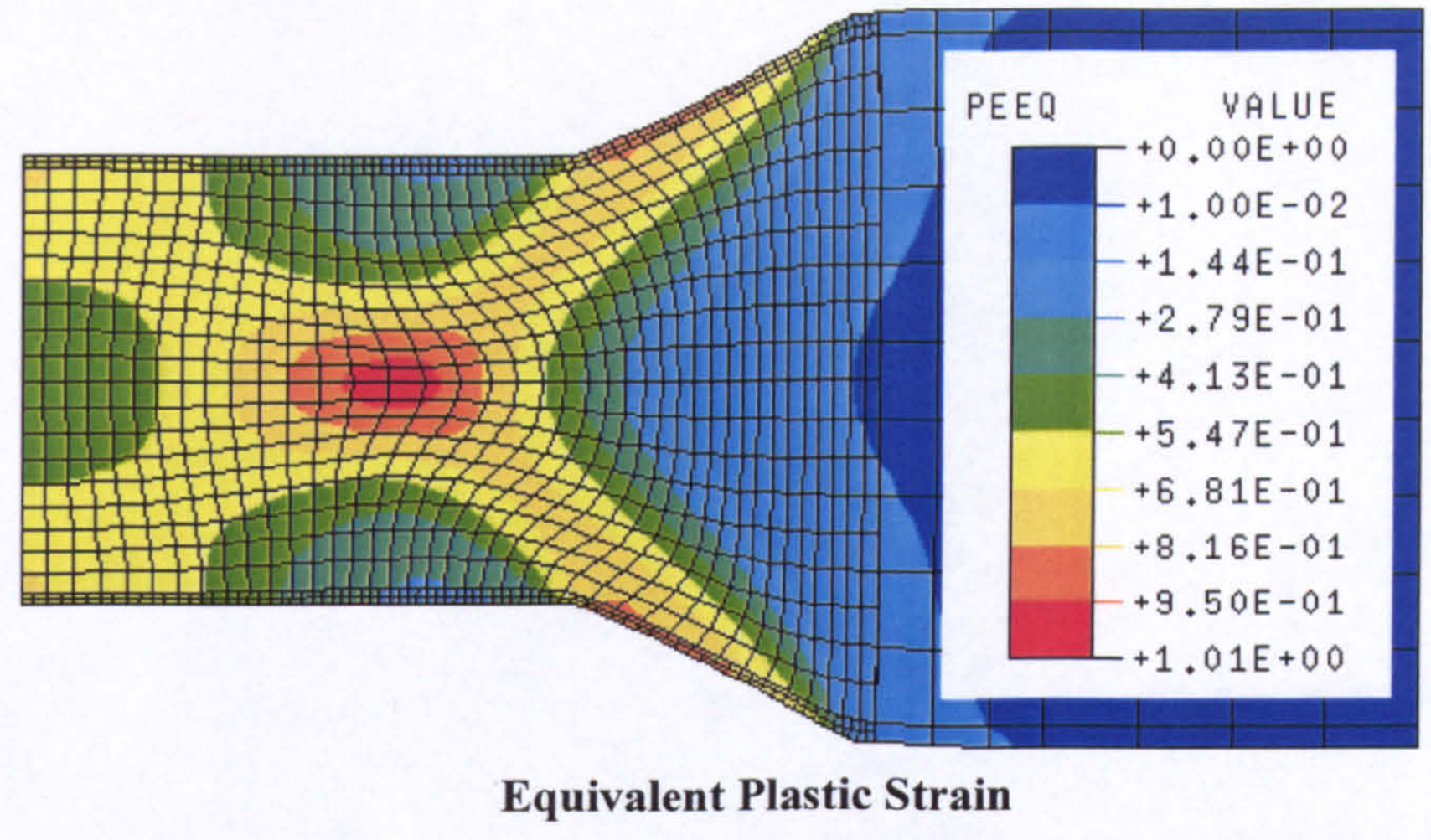

Equivalent Plastic Strain

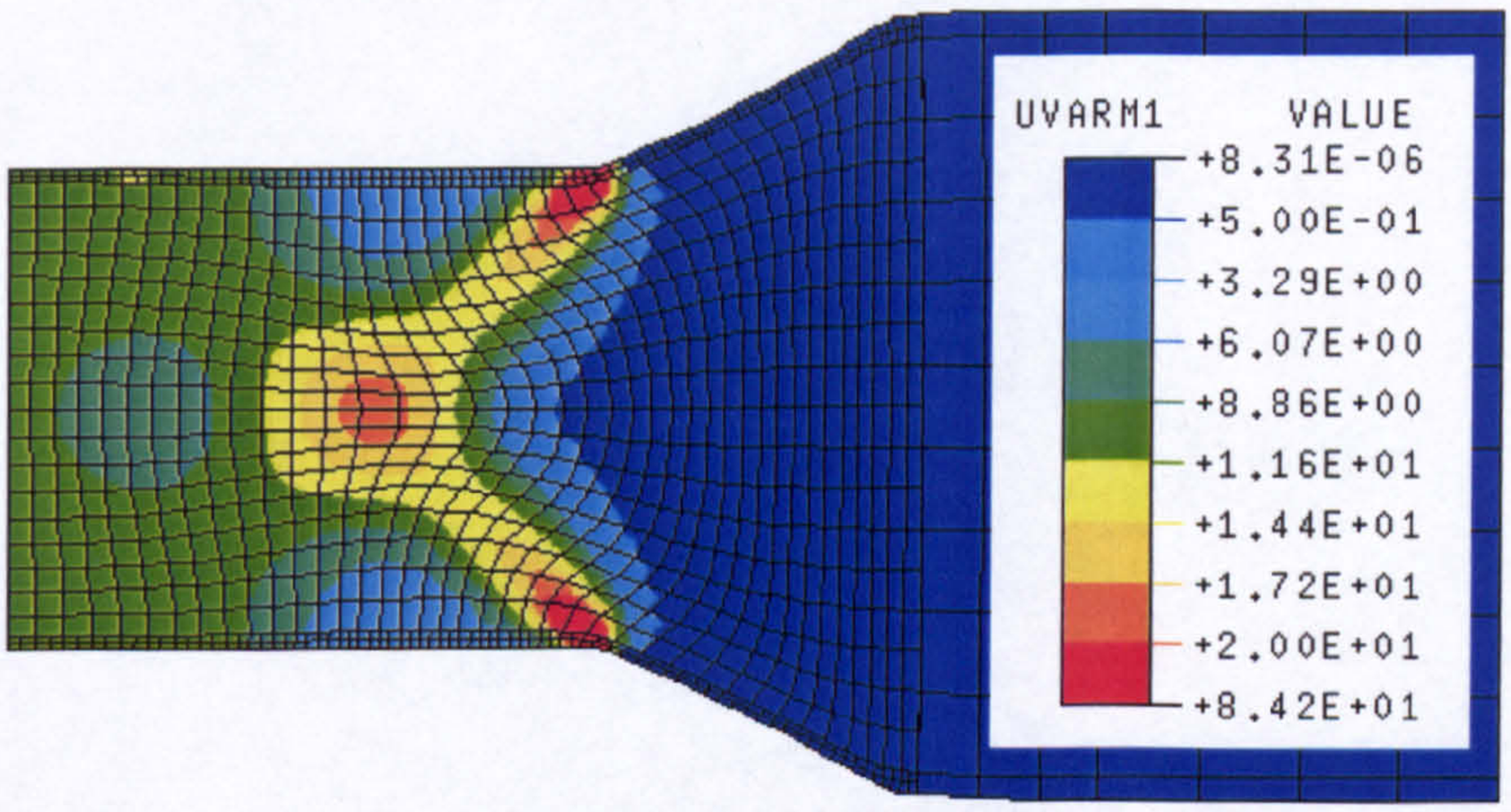

Instantaneous Strain Rate

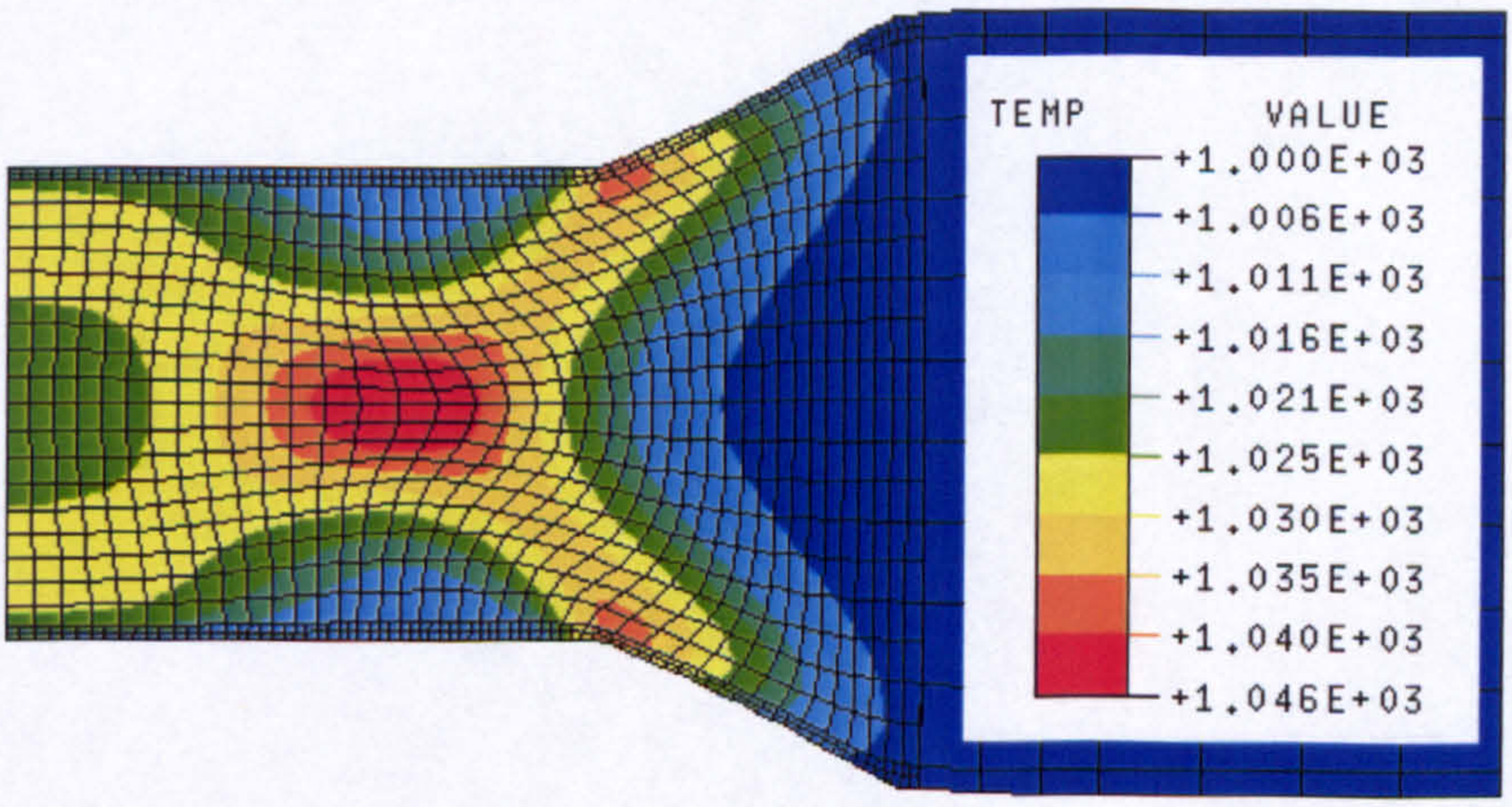

Temperature

Figure 2.23: Finite element modelling analysis of deformation inhomogeneities. These images were calculated for 316 stainless steel tested at 1000°C at a strain rate of 10 s^{-1}, and specimen geometry identical to that used in the present work. [from Mirza 2001].

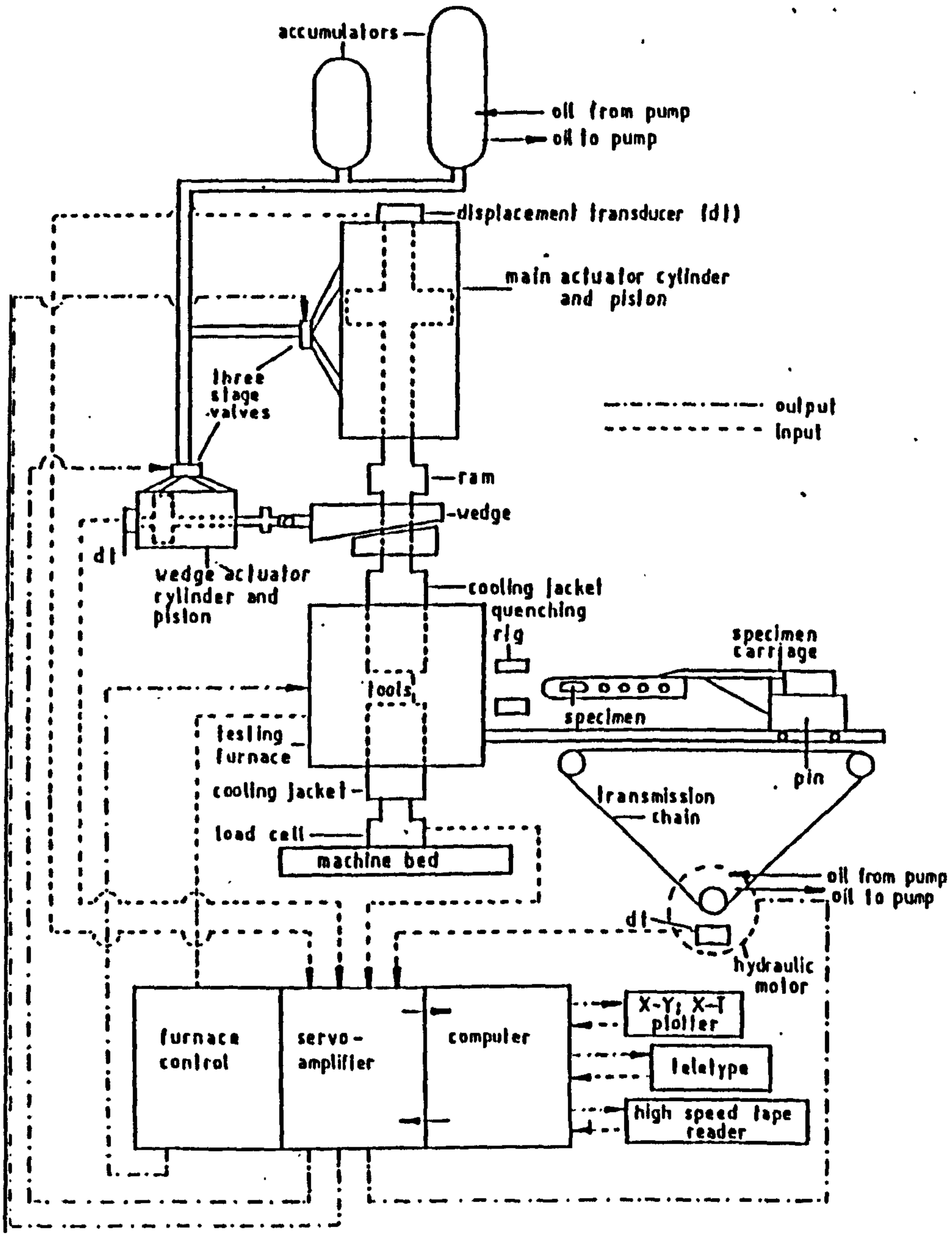

Figure 4.1: Schematic showing PSC test apparatus used at Sheffield [from Dutta 1987].

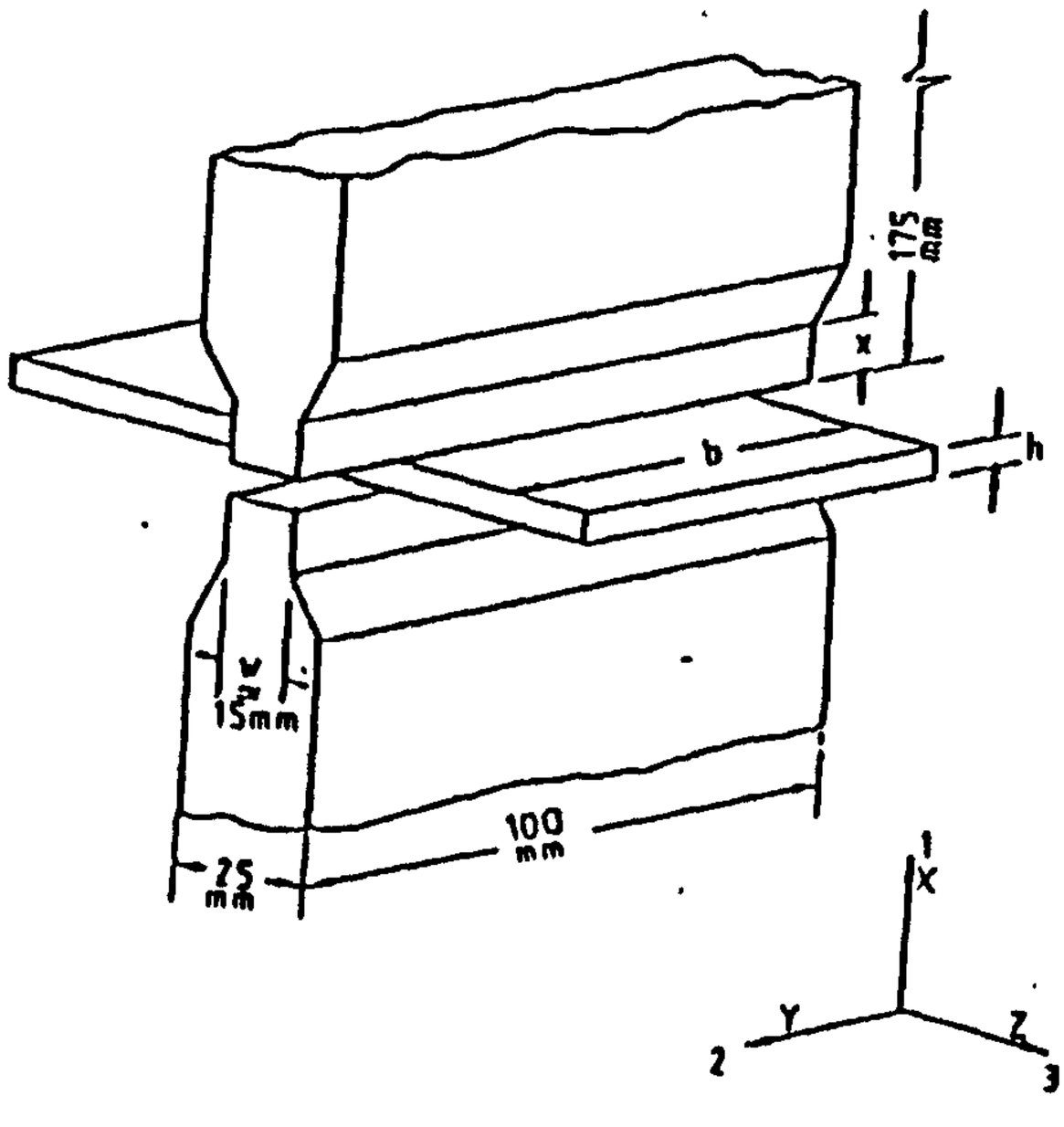

Figure 4.2: Schematic showing the testing tools set-up in the Sheffield PSC facility, and the location of the specimen. Specimens used in the present work were all 50mm long, 30mm wide and 10mm high [from Dutta (1987)].

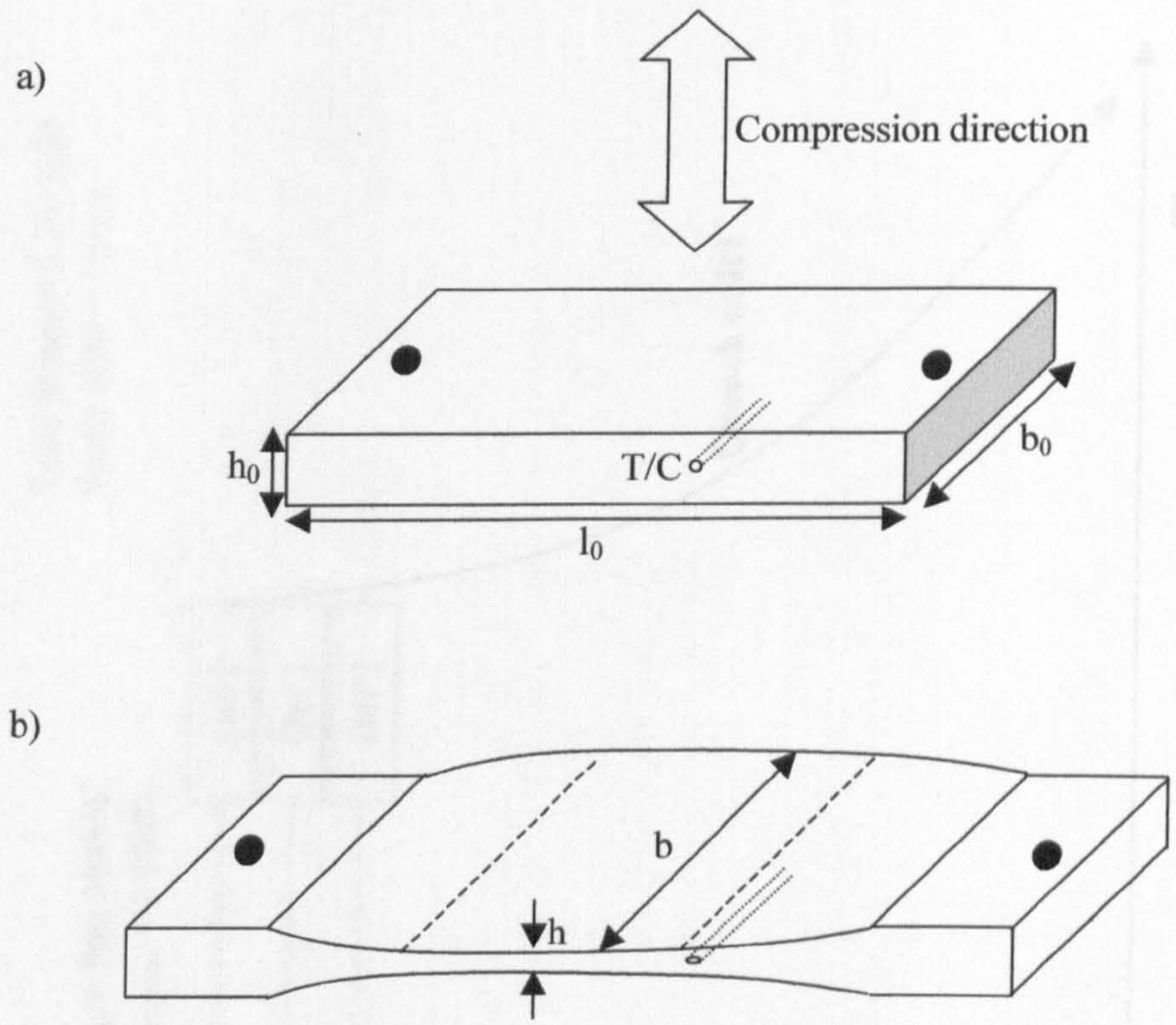

Figure 4.3: Schematic diagram of PSC testpiece: a) prior to deformation, and b) after deformation. Initial testpiece dimensions were h_0=10mm, b_0=30mm, l_0=50mm. The location of the thermocouple is marked T/C.

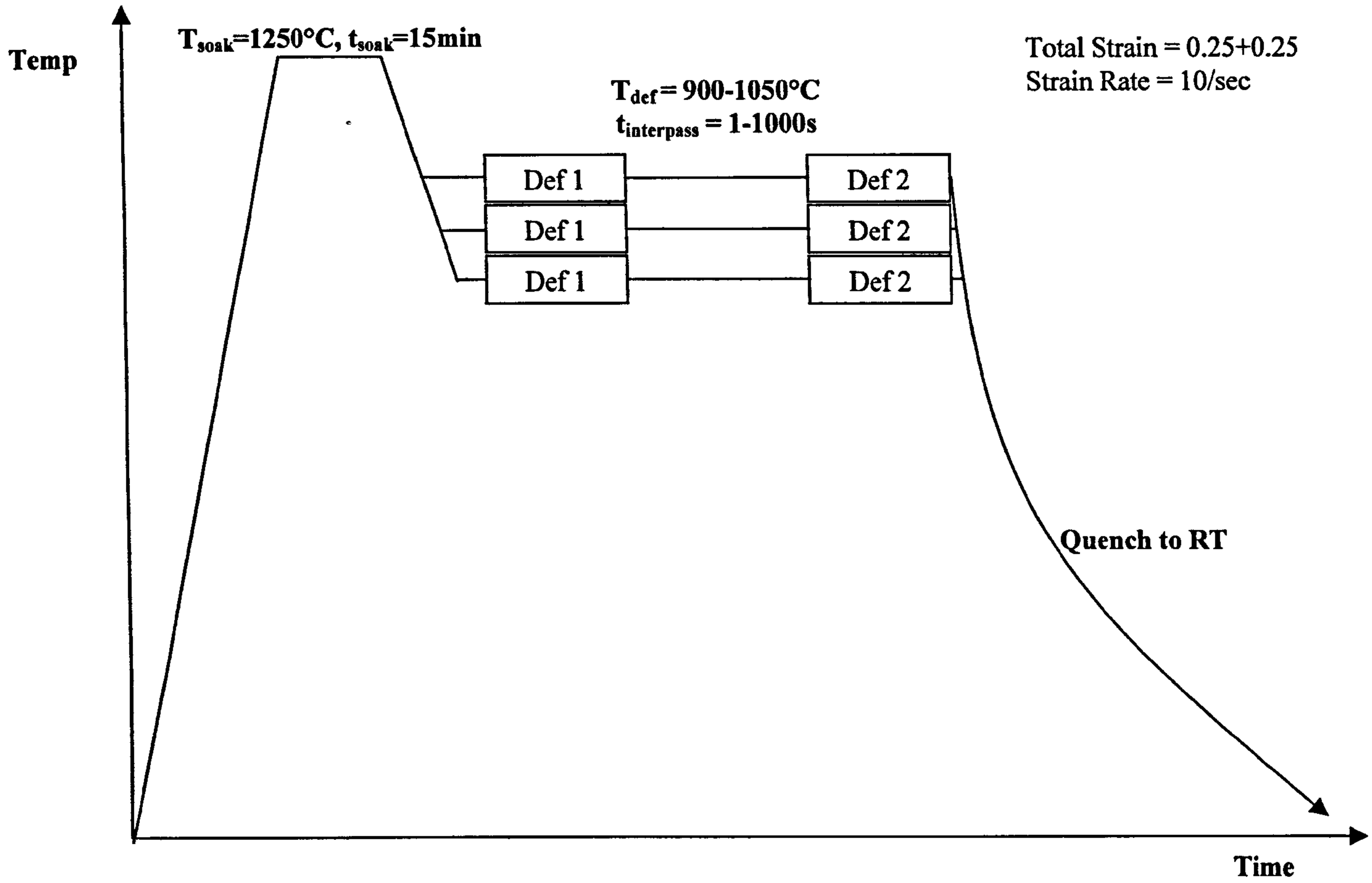

Figure 4.4: Schematic diagram showing the time-temperature profile used during testing.

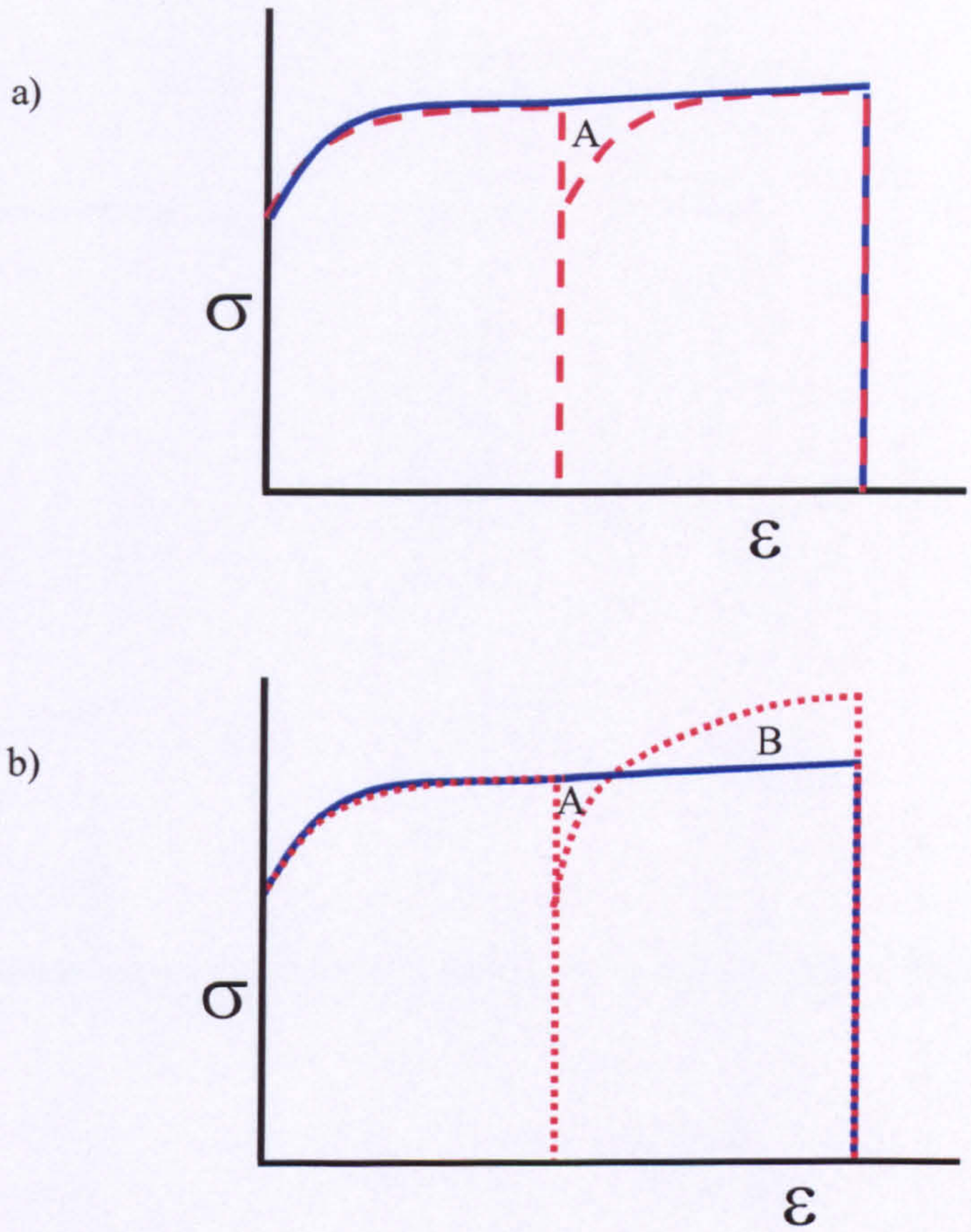

Figure 4.5: Schematic diagram of double deformation flow curves. In each case the solid line shows a single-hit curve to the total strain, while the dotted or dashed line shows the double deformation. Regions marked A and B show the relative softening and hardening contributions. Case a) shows a material undergoing full softening between passes, where the curve on the second deformation is identical to that on the first deformation. Case b) shows an overall hardening, where area B is greater than A.

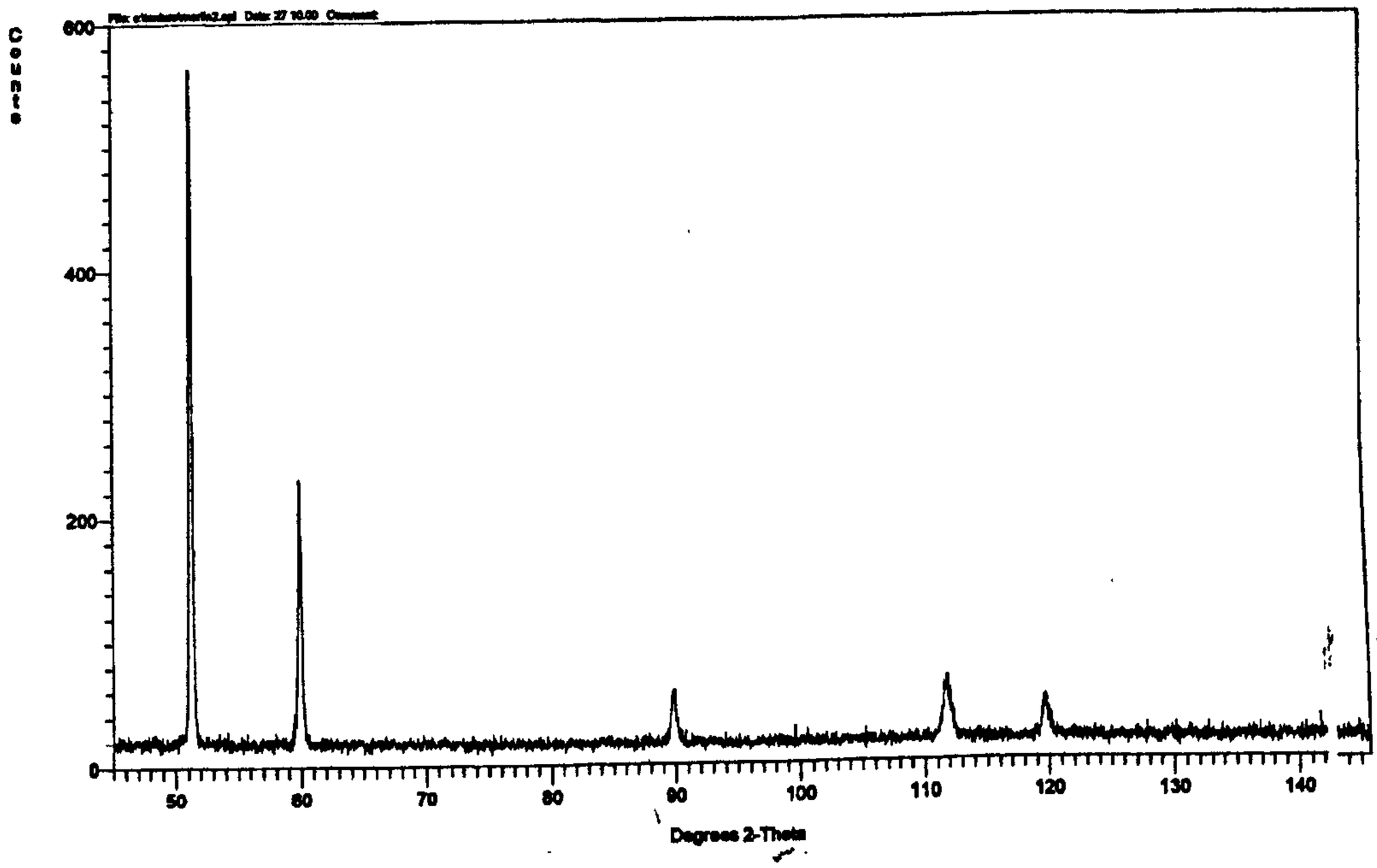

Figure 5.1: Figure showing the 2θ scan, as determined by texture goniometer of Fe-30%Ni-Nb. The peaks correspond to austenite, and show that no other phases exist.

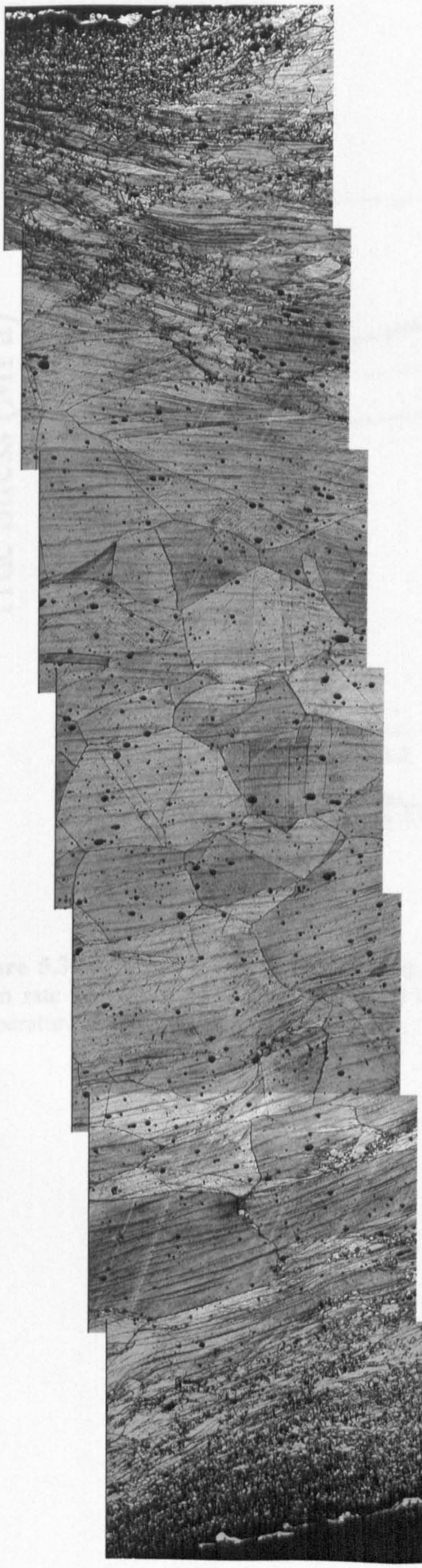

Figure 5.2: Optical collage taken through PSC specimen at the shoulder. Note that more extensive recrystallisation is present at the surface, and on the diagonals, as shown in Figure 2.23. This is due to the inhomogeneous strain distribution under PSC testing. The test specimen shown here is 950-1000DD.

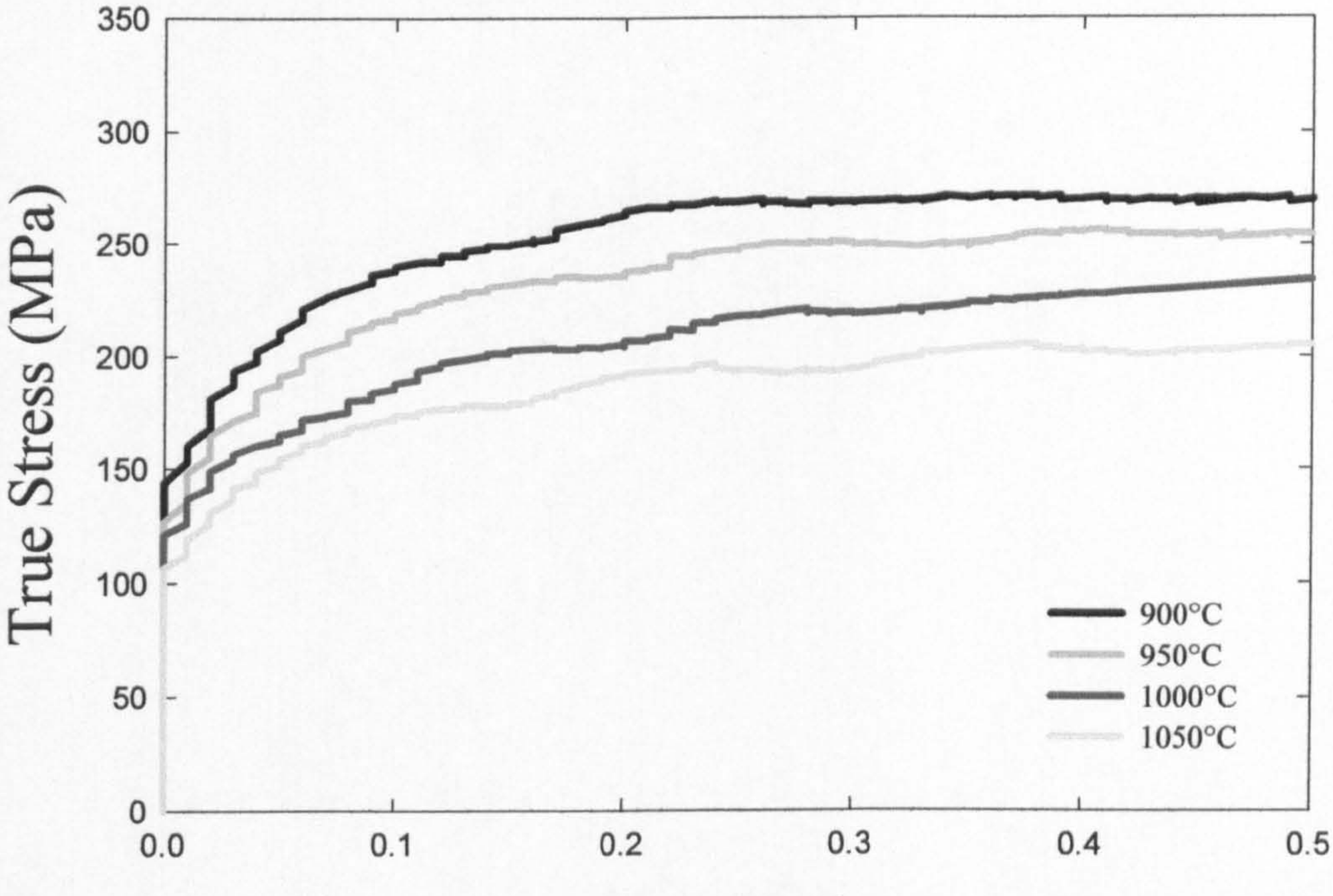

Figure 5.3: Flow curves from PSC testing of Fe-30Ni-Nb, deformed at a constant true strain rate of 10 sec^{-1} to an overall strain of 0.5. This shows the effect of deformation temperature on flow behaviour.

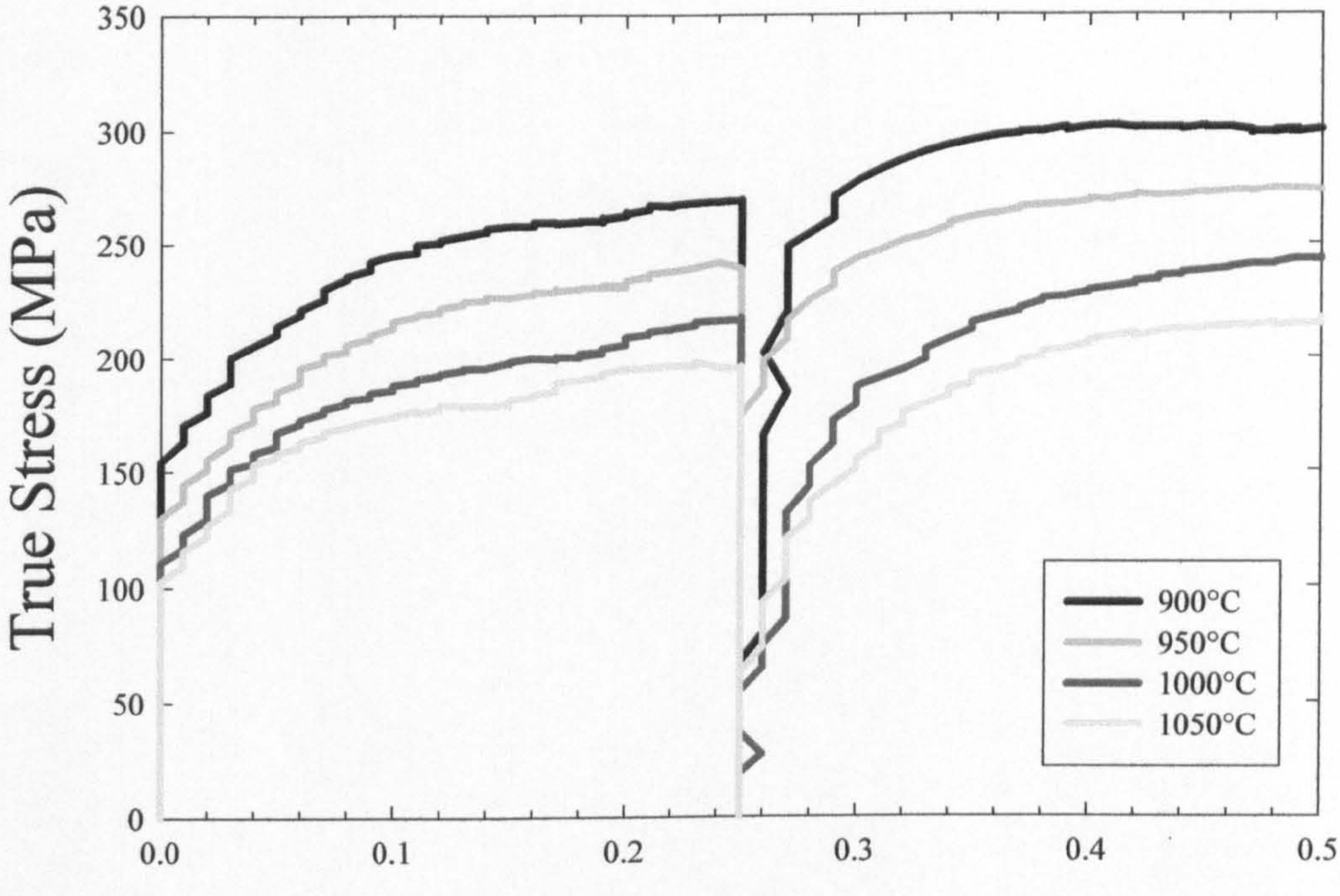

Figure 5.4: Double deformation flow curves from PSC testing of Fe-30Ni-Nb, deformed at a constant true strain rate of 10 sec^{-1}. The material was pre-strained to ε=0.25, held isothermally at the test temperature for 10s, and restrained to an overall strain of 0.5. This shows the effect of deformation temperature on flow behaviour during double deformation testing.

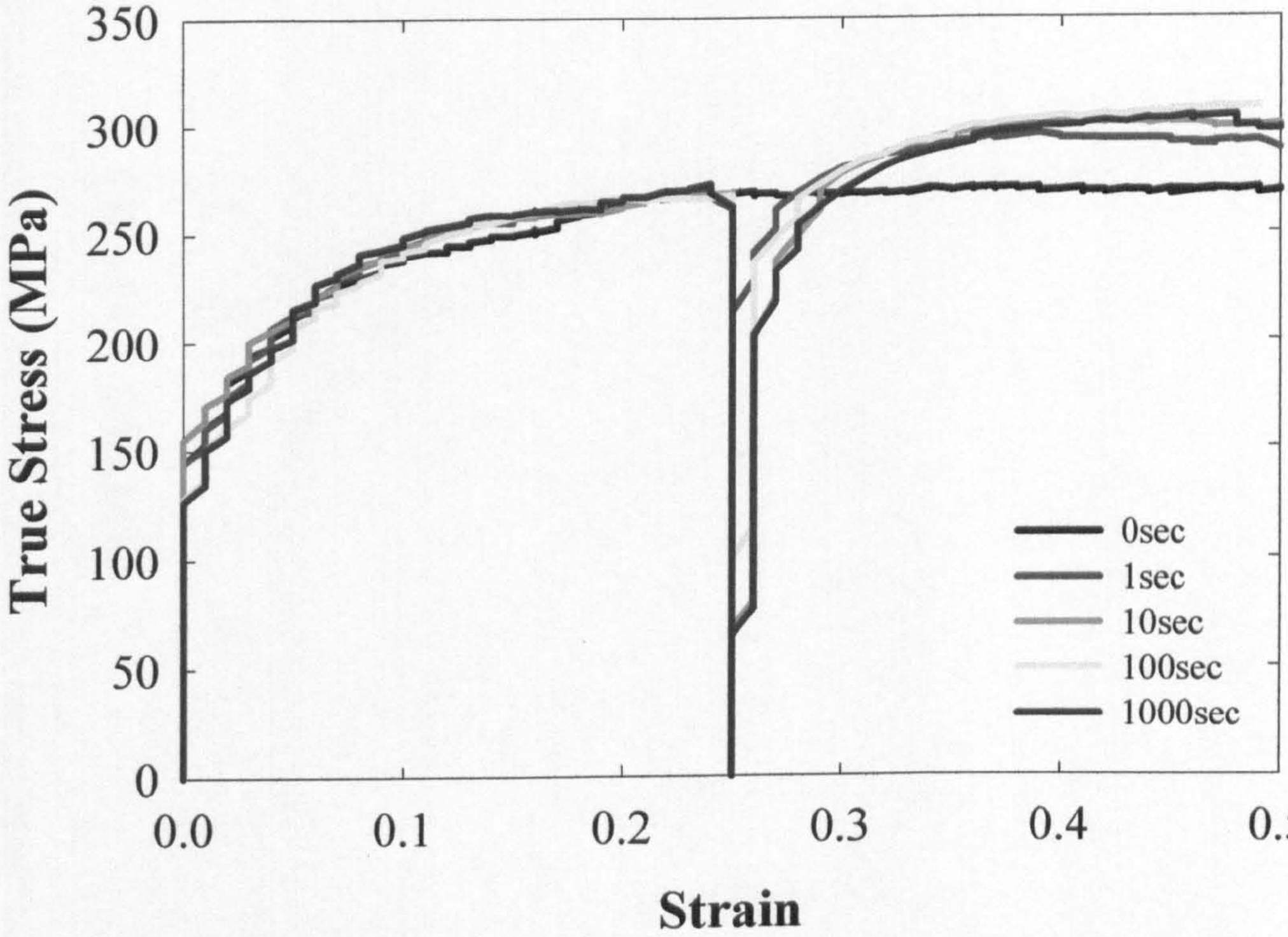

Figure 5.5: Interrupted testing at 900°C to a total strain of 0.5, under a constant true strain rate of $10s^{-1}$. This shows the effect of increased interpass delay time at this temperature.

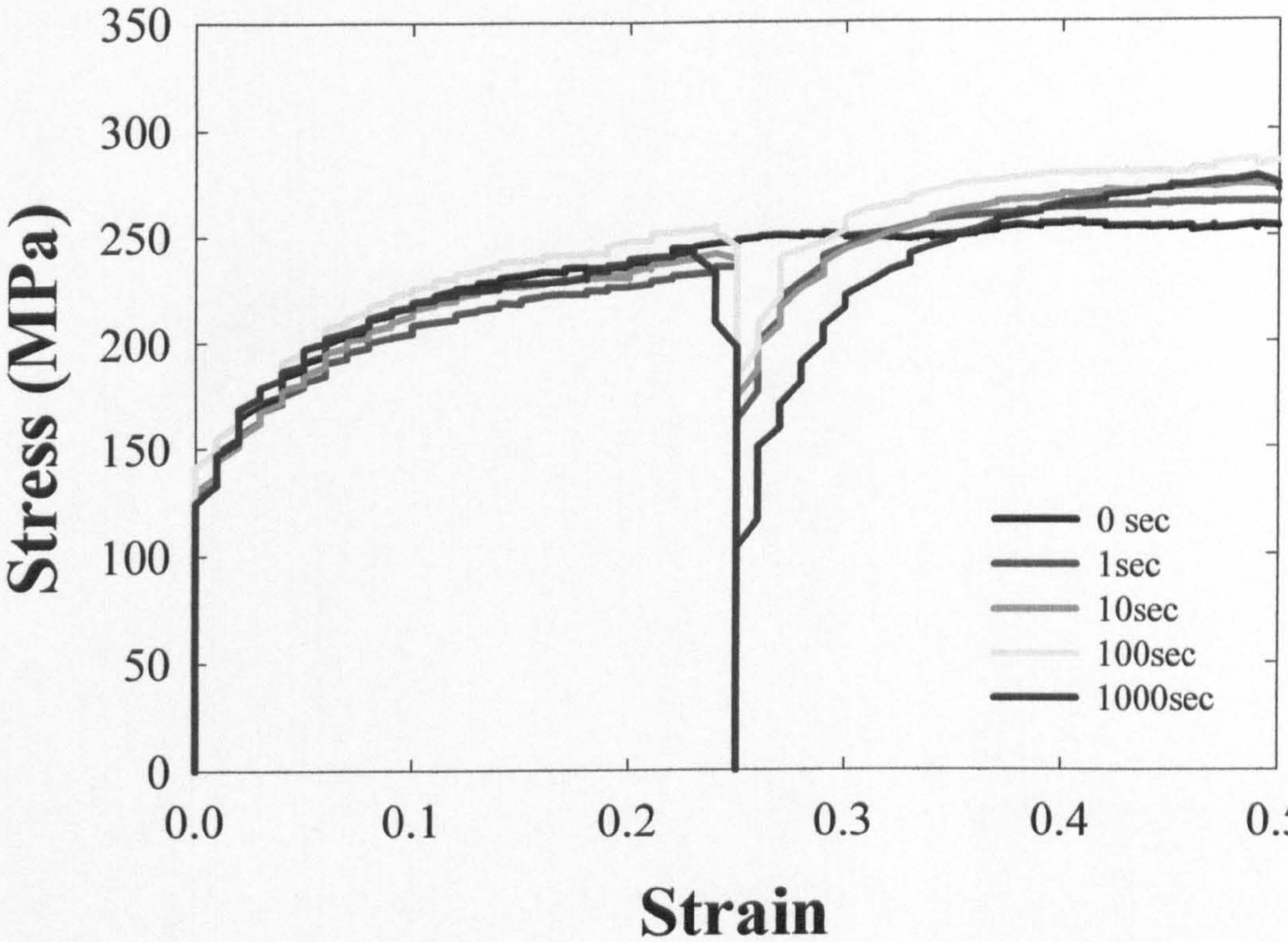

Figure 5.6: Interrupted testing at 950°C to a total strain of 0.5, under a constant true strain rate of $10s^{-1}$. This shows the effect of increased interpass delay time at this temperature.

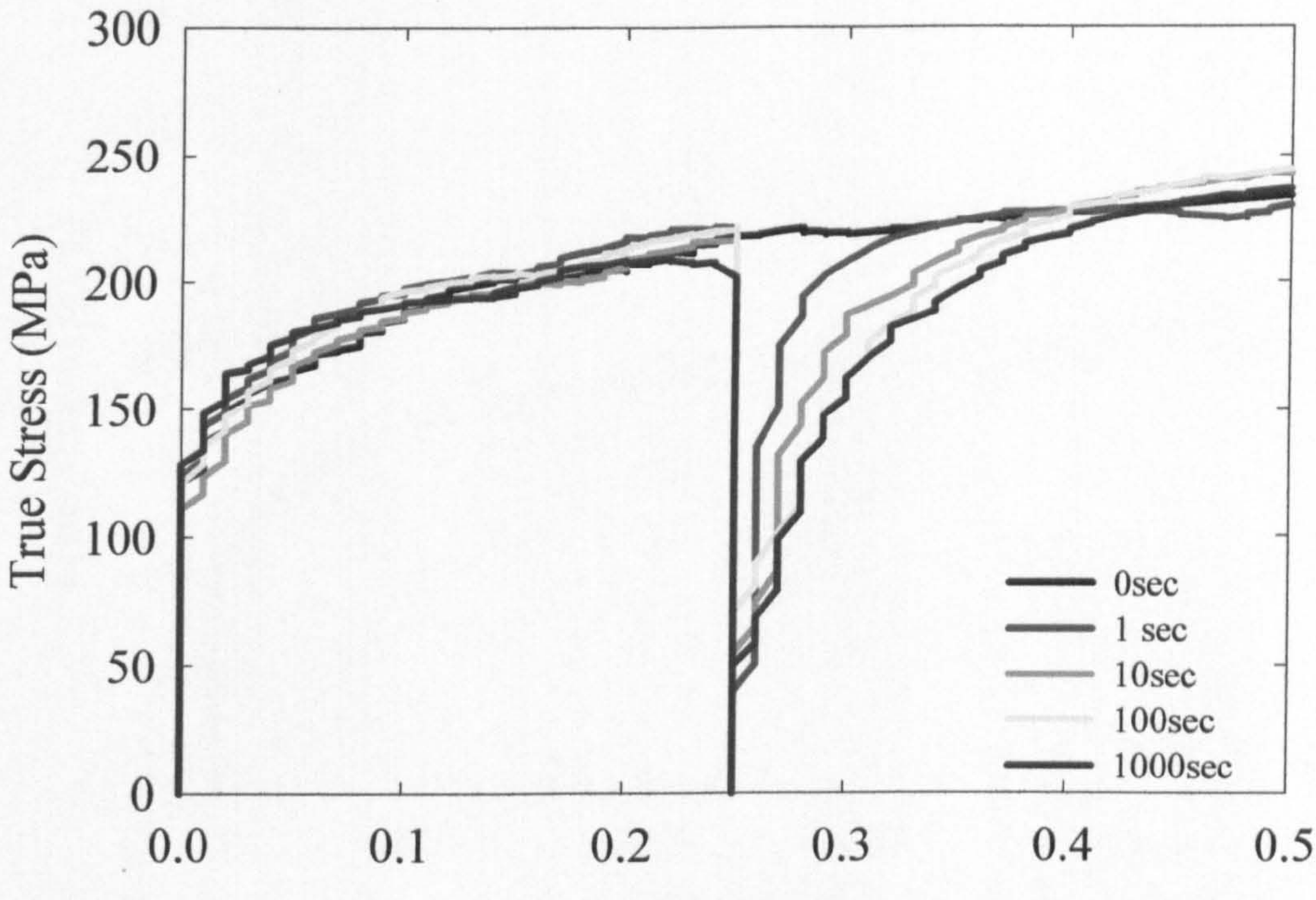

Figure 5.7: Interrupted testing at 1000°C to a total strain of 0.5, under a constant true strain rate of $10s^{-1}$. This shows the effect of increased interpass delay time at this temperature.

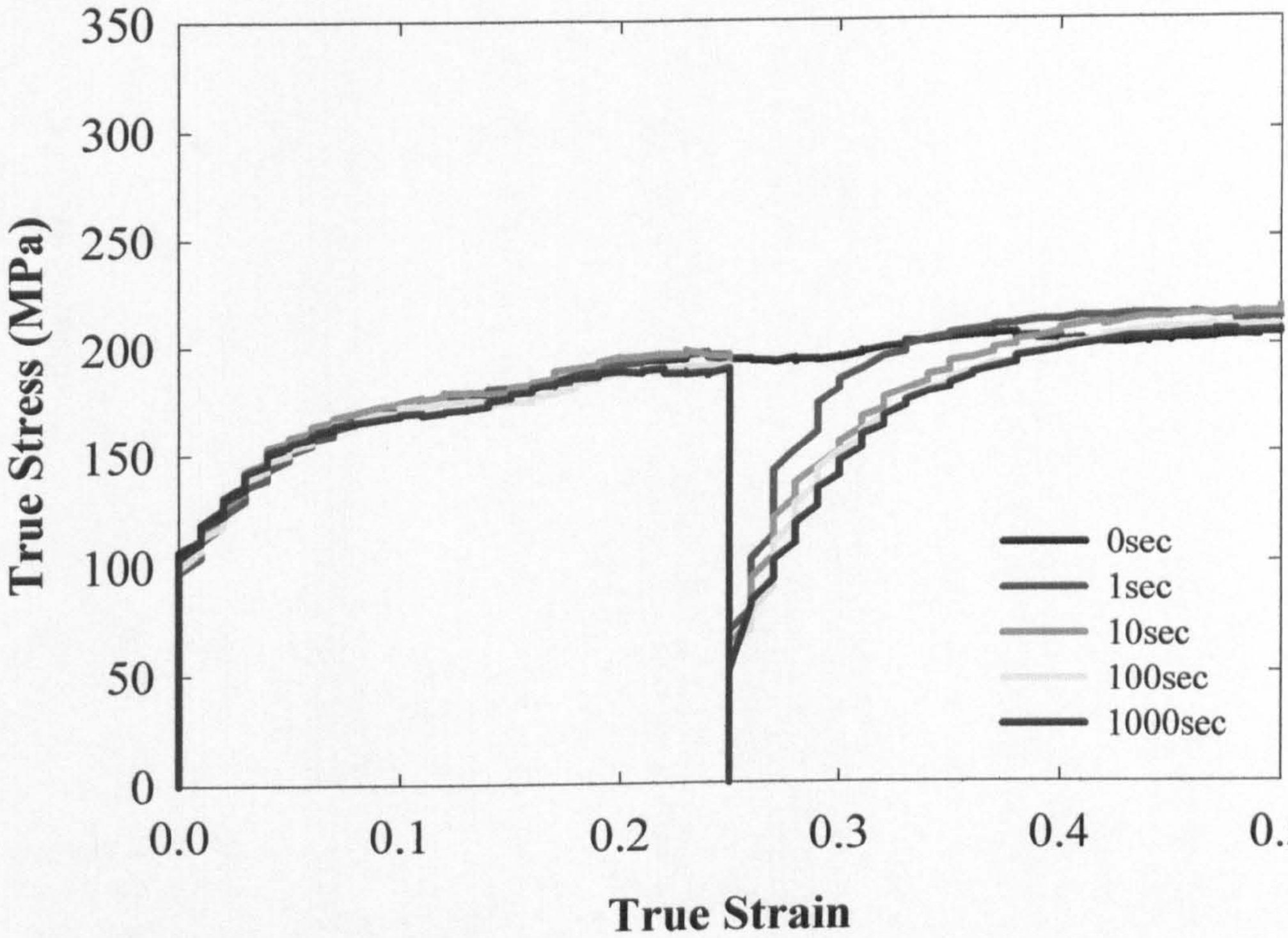

Figure 5.8: Interrupted testing at 1050°C to a total strain of 0.5, under a constant true strain rate of $10s^{-1}$. This shows the effect of increased interpass delay time at this temperature.

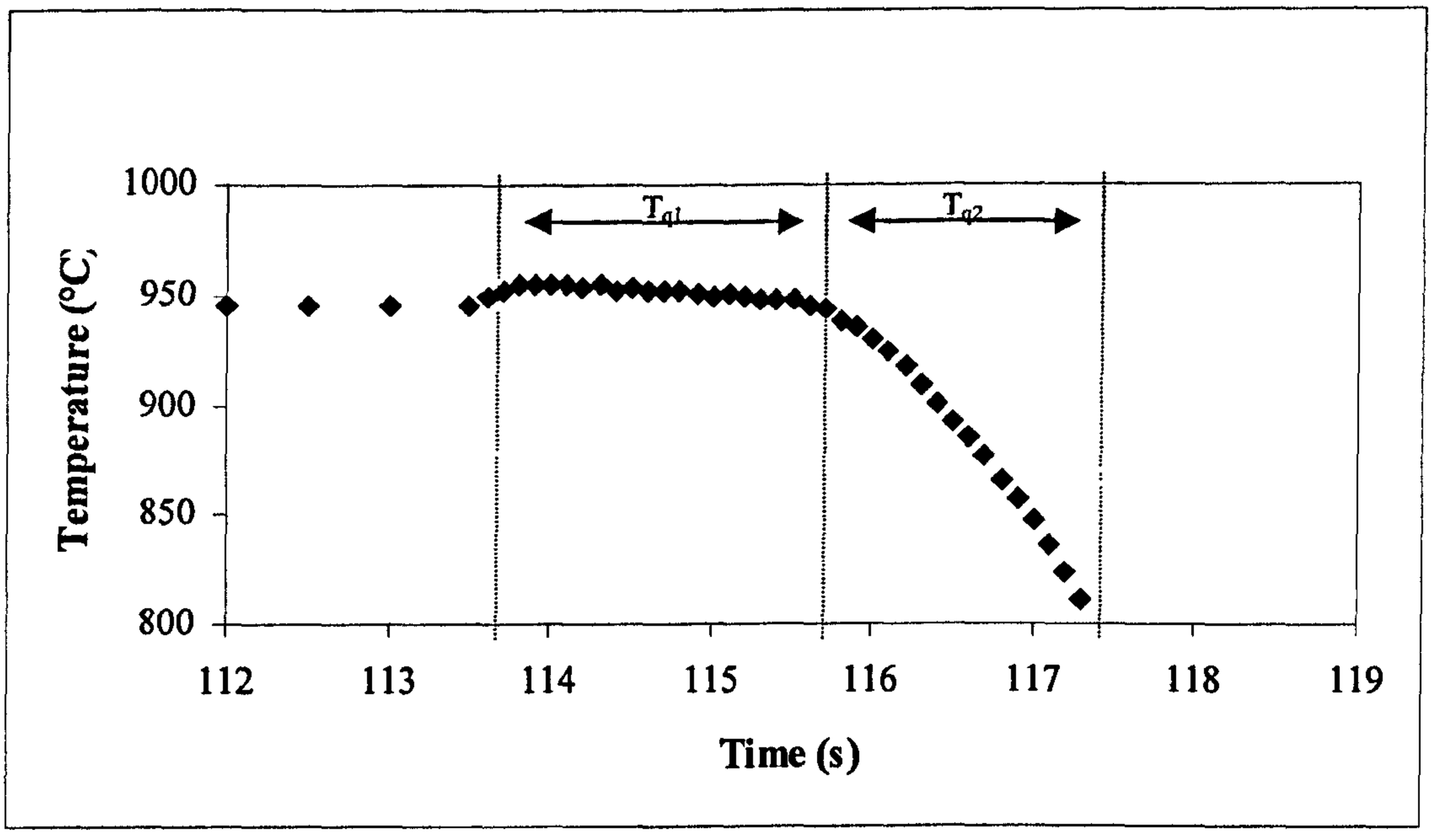

Figure 5.9: This plot shows typical quench data, in this case from the 950°C-100-dd test. The time to quench involves a movement time (T_{q1}) and a time for the water to reduce the temperature (T_{q2}). Here T_{q1} is around 2 seconds, while T_{q2} is around 1.5 seconds, making a time from the end of the test to below 800°C of around 3.5 seconds.

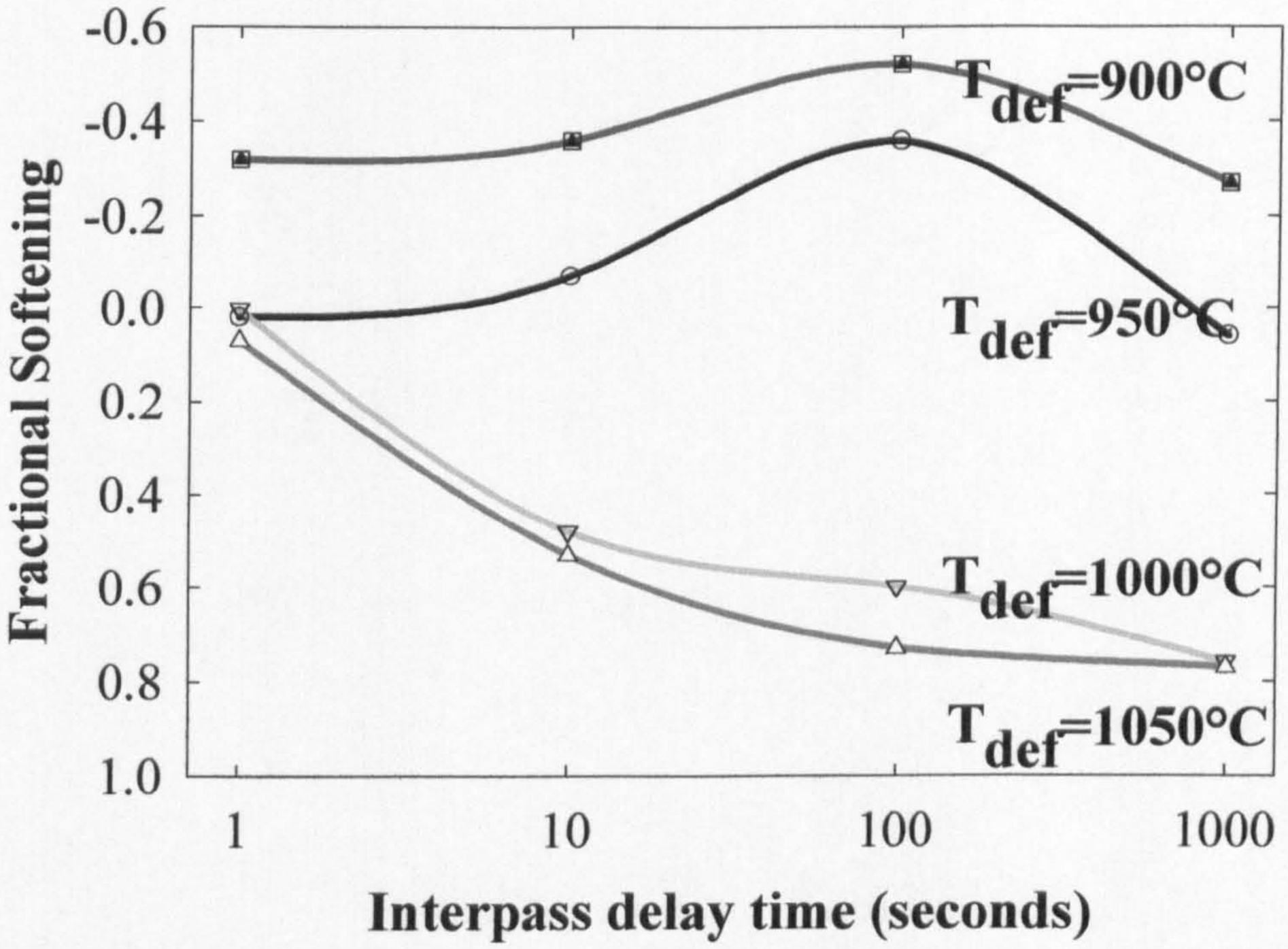

Figure 5.10: Fractional softening data derived from the true stress-true strain double deformation curves. Softening/hardening response can be seen as a function of time and temperature.

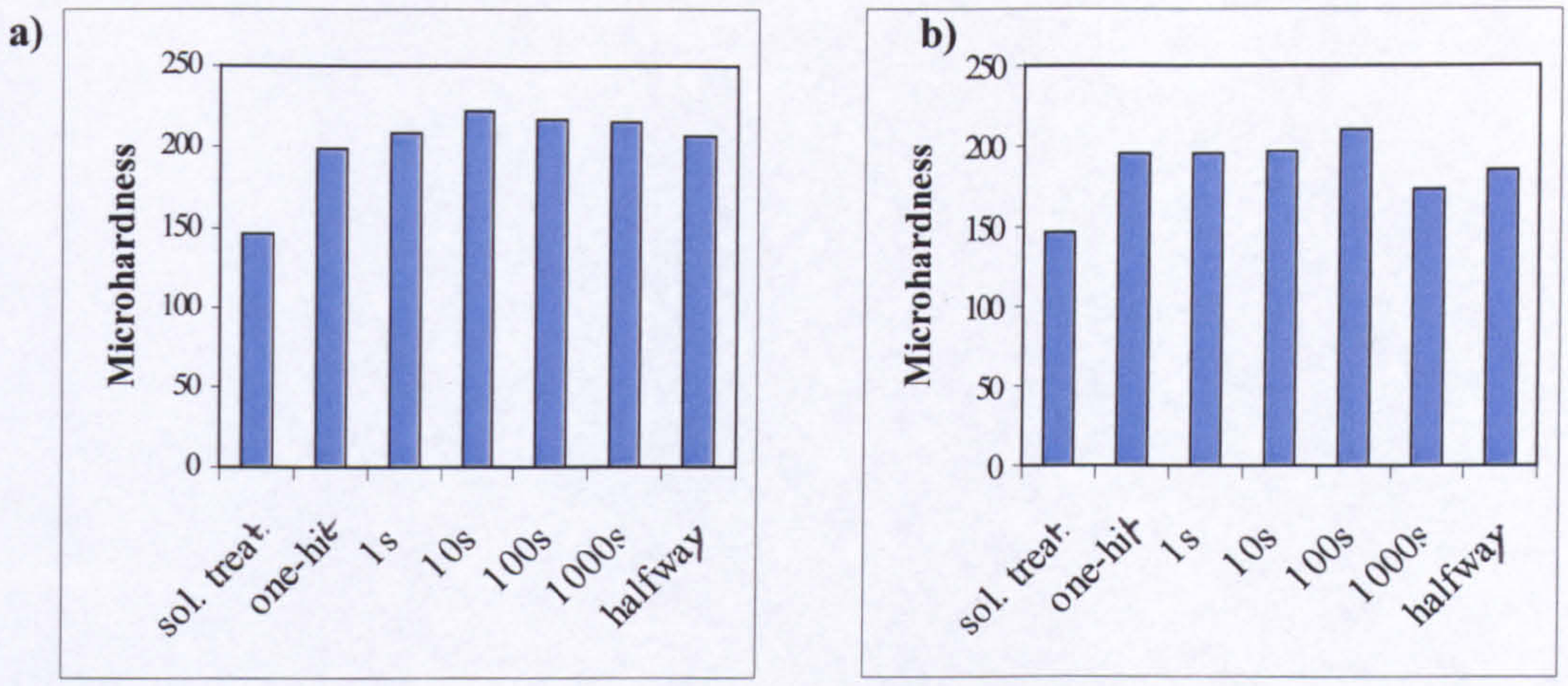

Figure 5.11: Microhardness values measured following testing at a) 900°C and b) 950°C.

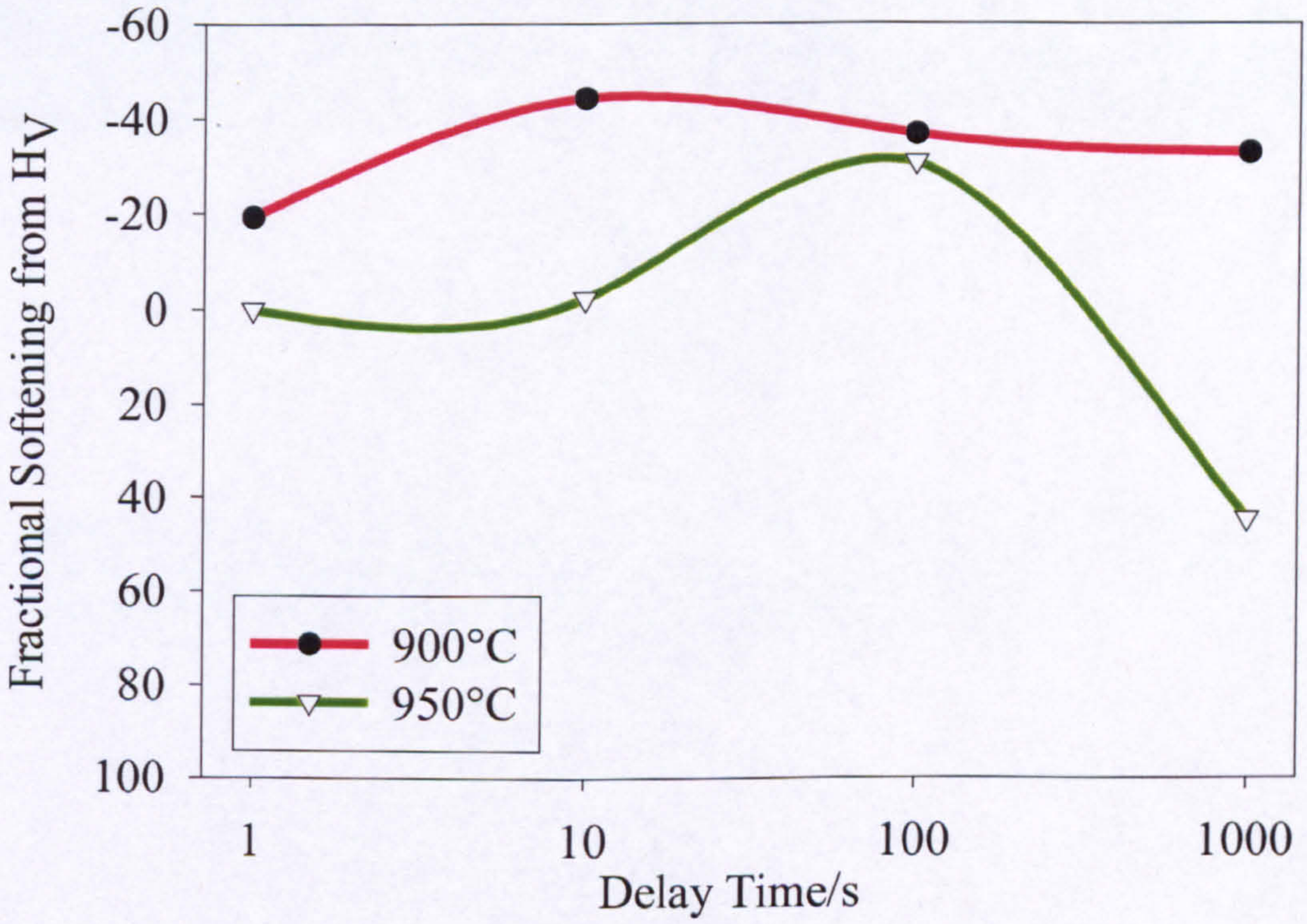

Figure 5.12: Fractional softening kinetics observed following microhardness testing of double deformation Fe-30Ni-Nb testpieces.

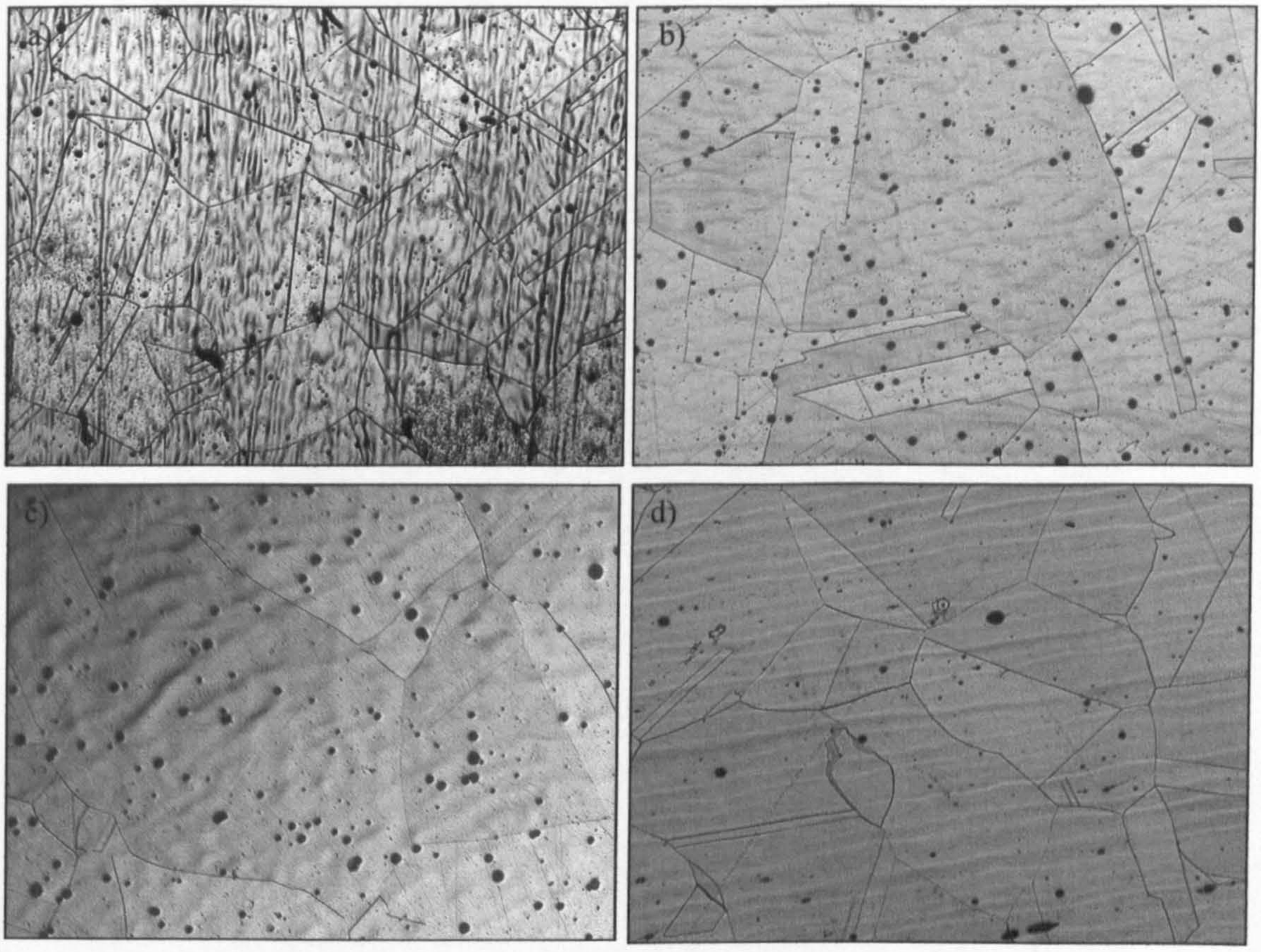

Figure 5.13: Optical micrographs showing the effect of temperature on reheated grain size for a) 8 minute anneal; b) 17 minute anneal; c) 29 minute anneal; PSC testpiece head (which underwent thermal treatment of reheat and test schedule).

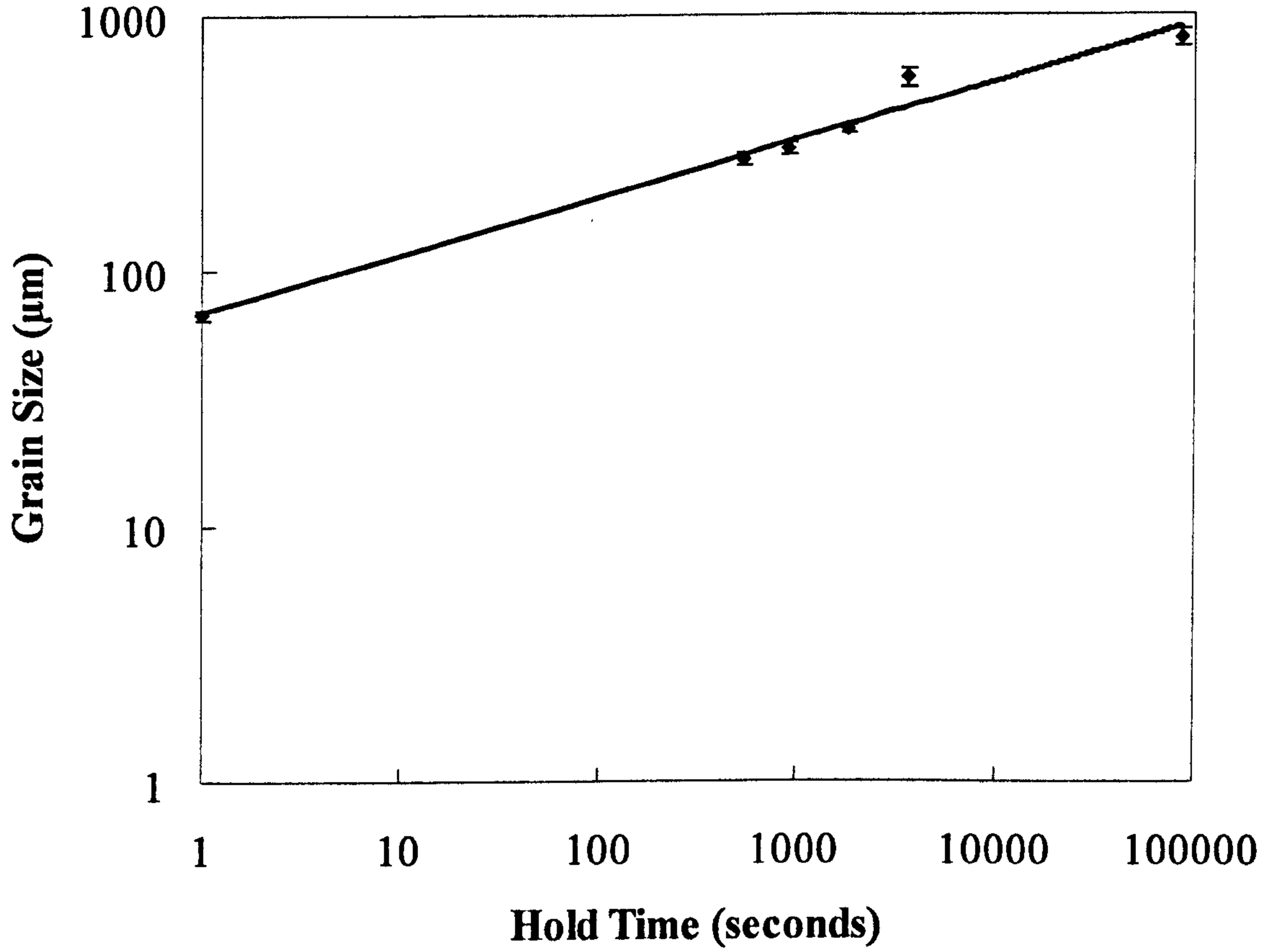

Figure 5.14: Grain growth kinetics seen in Fe-30%Ni-Nb at a temperature of 1250°C for different holding times. Regression curve fitted to experimental data.

200μm

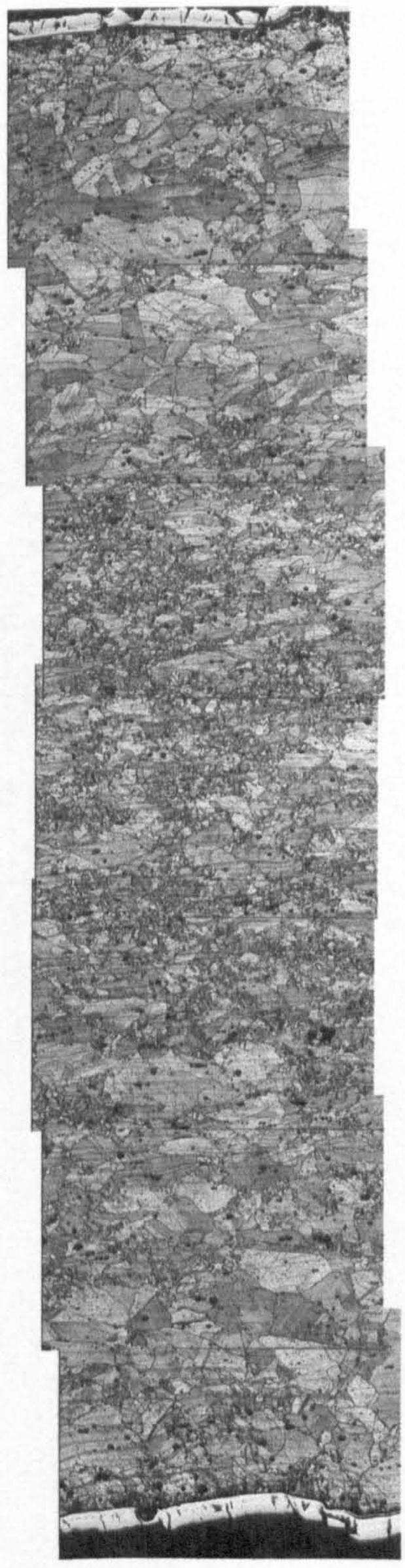

200μm

Figure 5.15: Optical micrographs showing the effect of deformation conditions on recrystallisation kinetics observed following double deformation testing of Fe-30Ni-Nb. These images were taken of specimens tested at different test temperatures, but conditions were otherwise (almost) identical. The deformation conditions were as follows: (a)T_{def}=900°C, t_{delay}=100s, strain=0.25+0.25, ER=10s^{-1}, which gave Xv=0; (b)T_{def}=1000°C, t_{delay}=1000s, strain=0.25+0.25, ER=10s^{-1}, giving Xv=0.39.

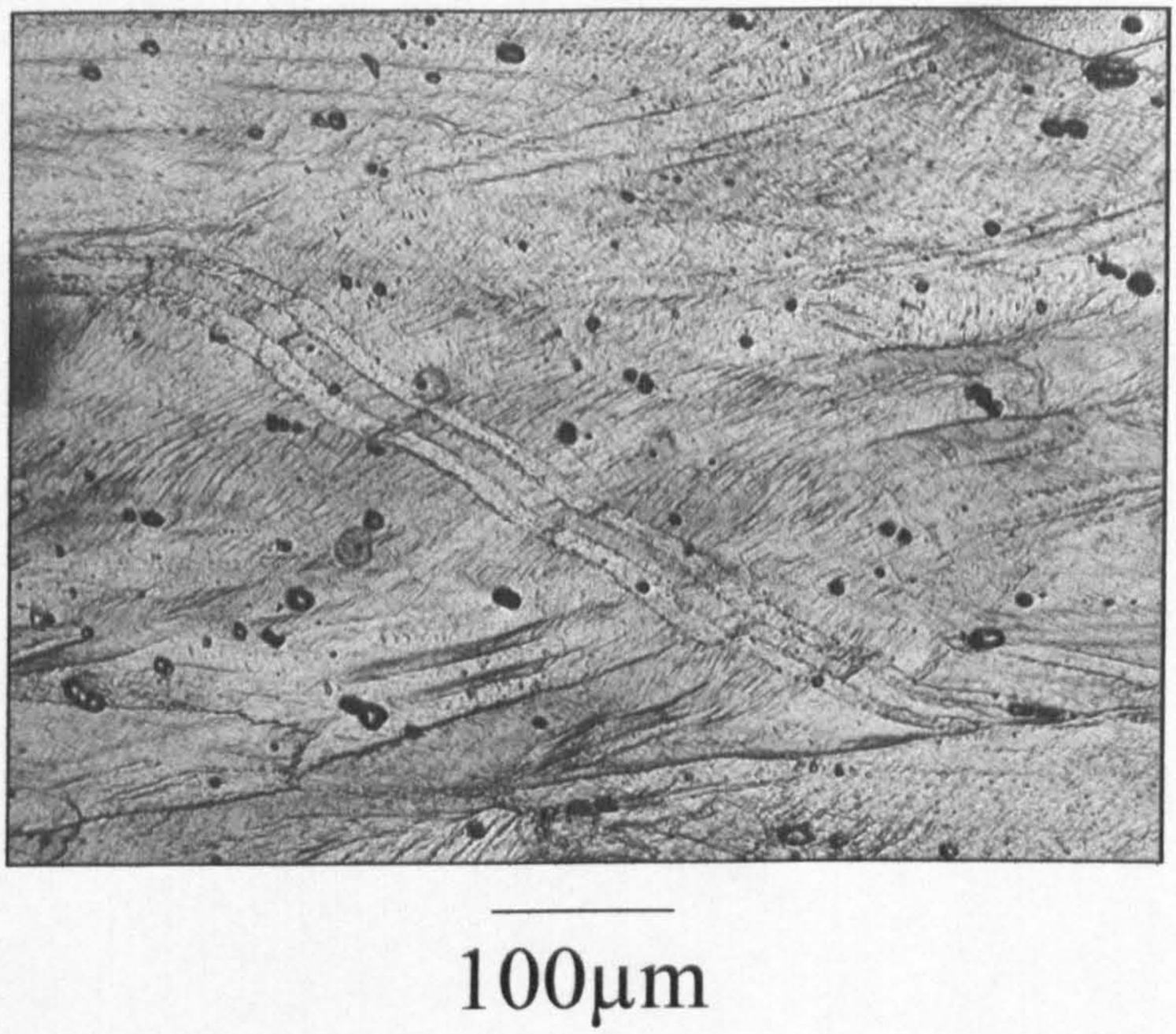

Figure 5.16 : Deformed twin boundaries seen in 900-1-DD specimen.

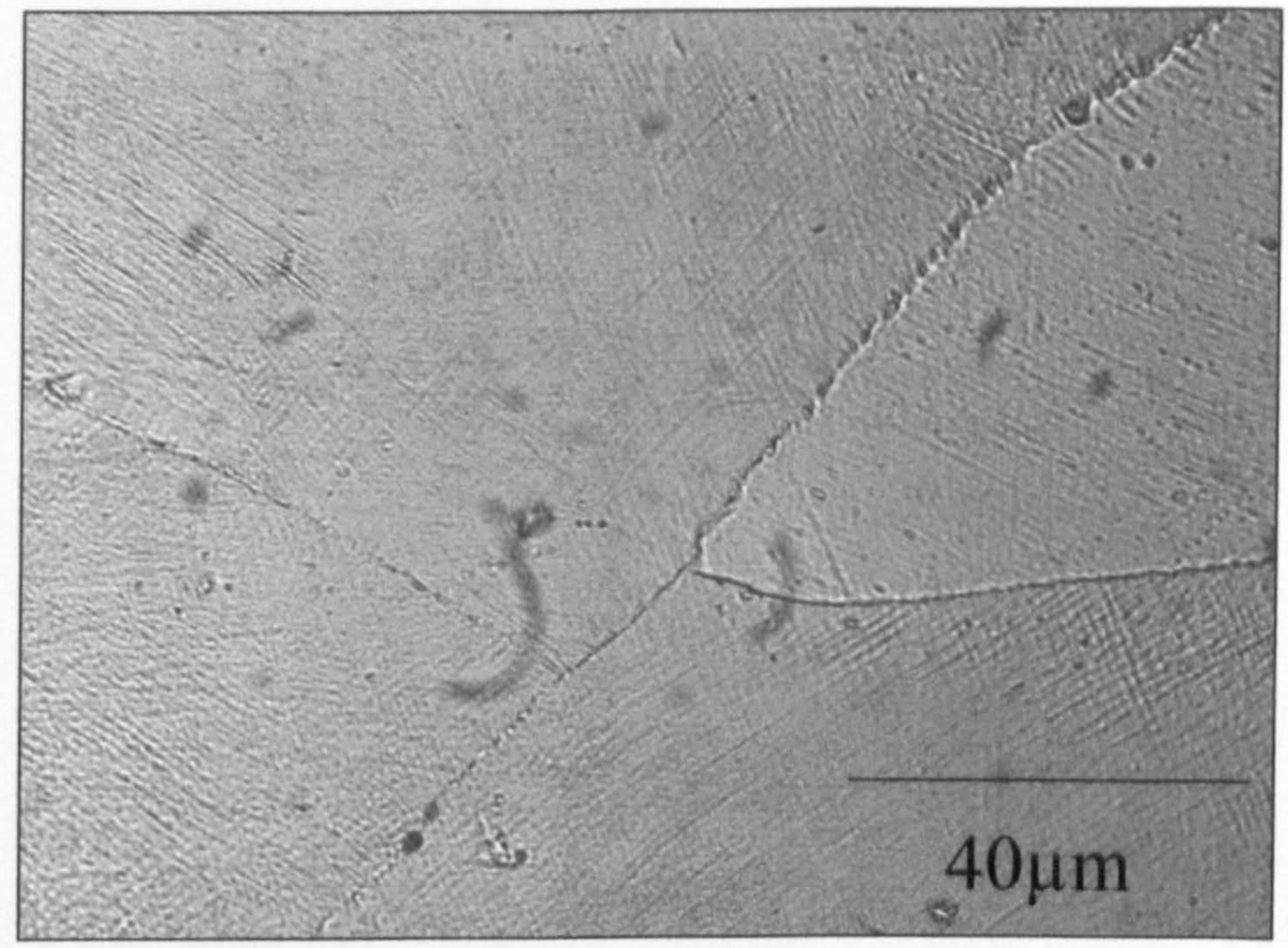

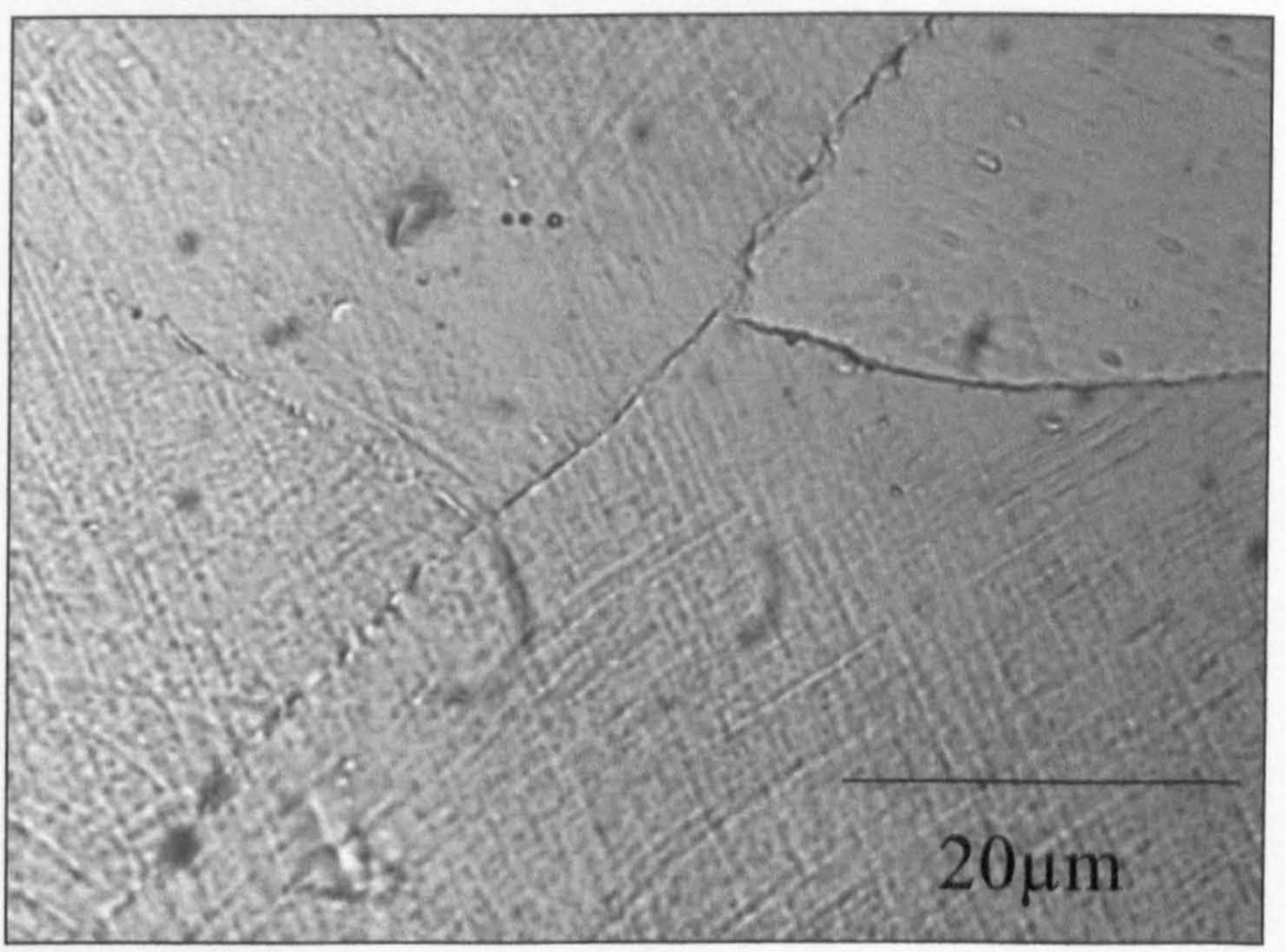

Figure 5.17: Grain boundaries and triple points in 950-1-HHQ sample. No recrystallisation was observed in this specimen. Note the presence of deformation bands and crossed microbands, seen here in the optical microscope.

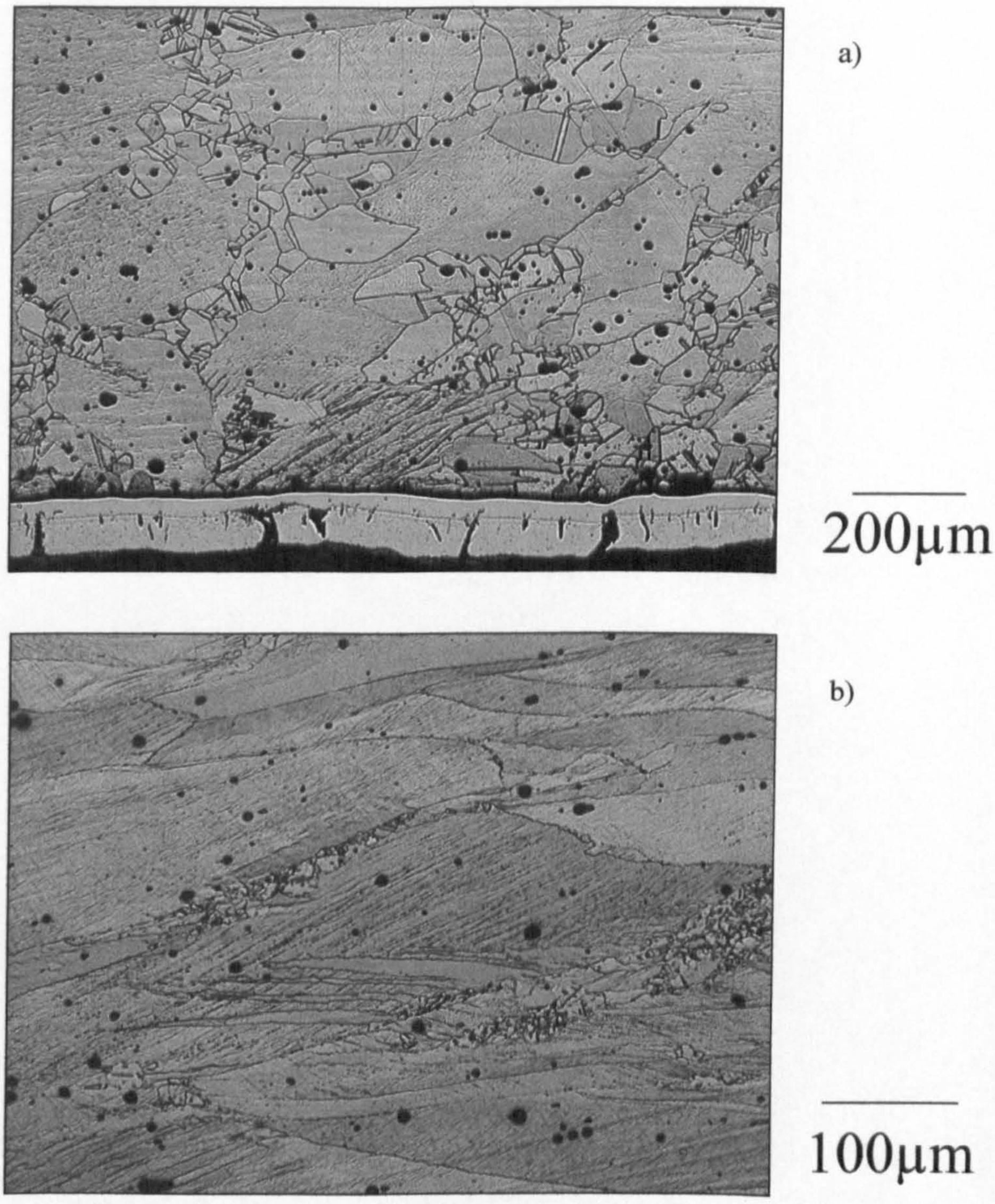

Figure 5.18: Optical micrographs showing the preferential nucleation of recrystallisation along grain boundaries in Fe-30%Ni-Nb. Samples shown are: a) 1050-SD, and b) 900-1000-DD.

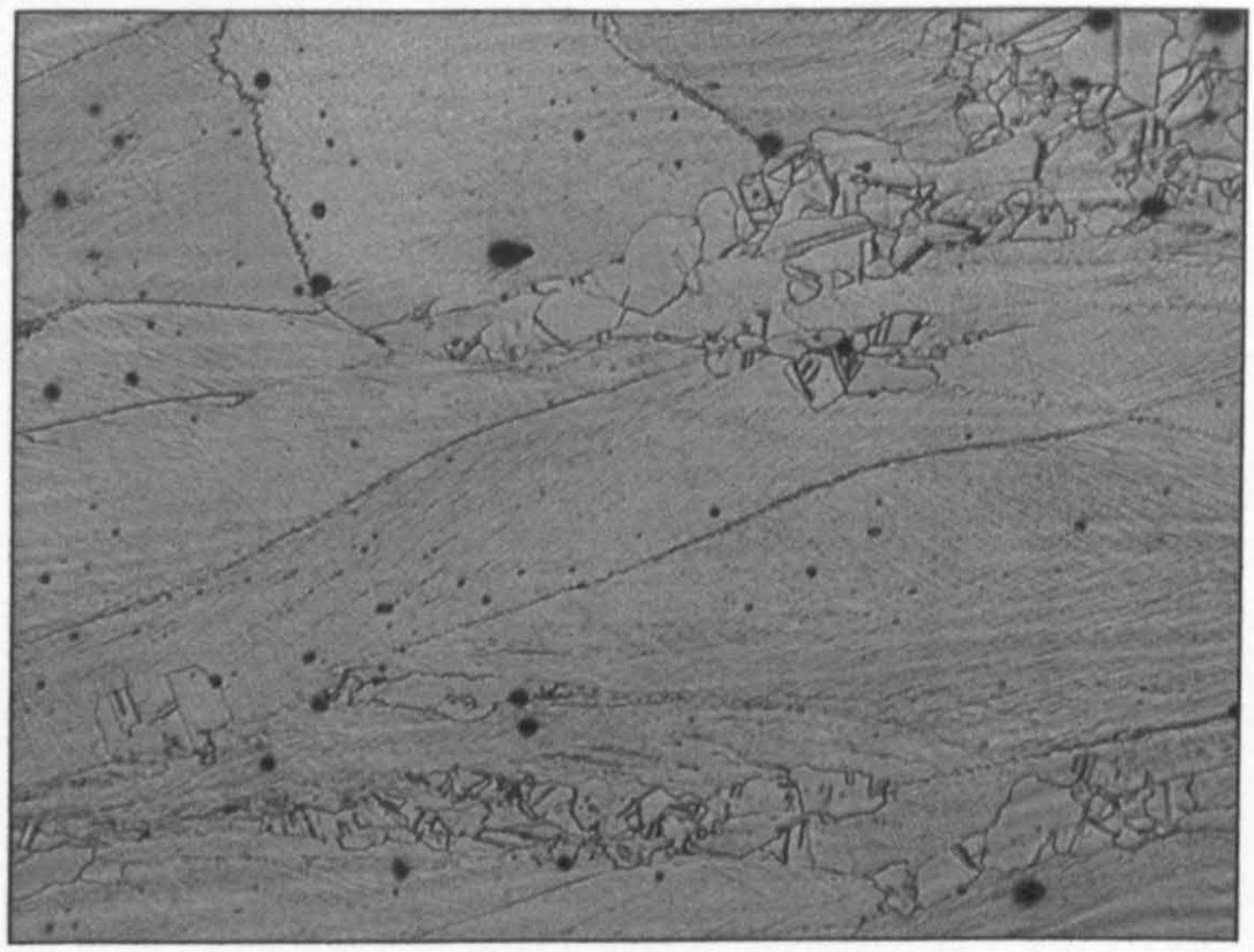

a)

100μm

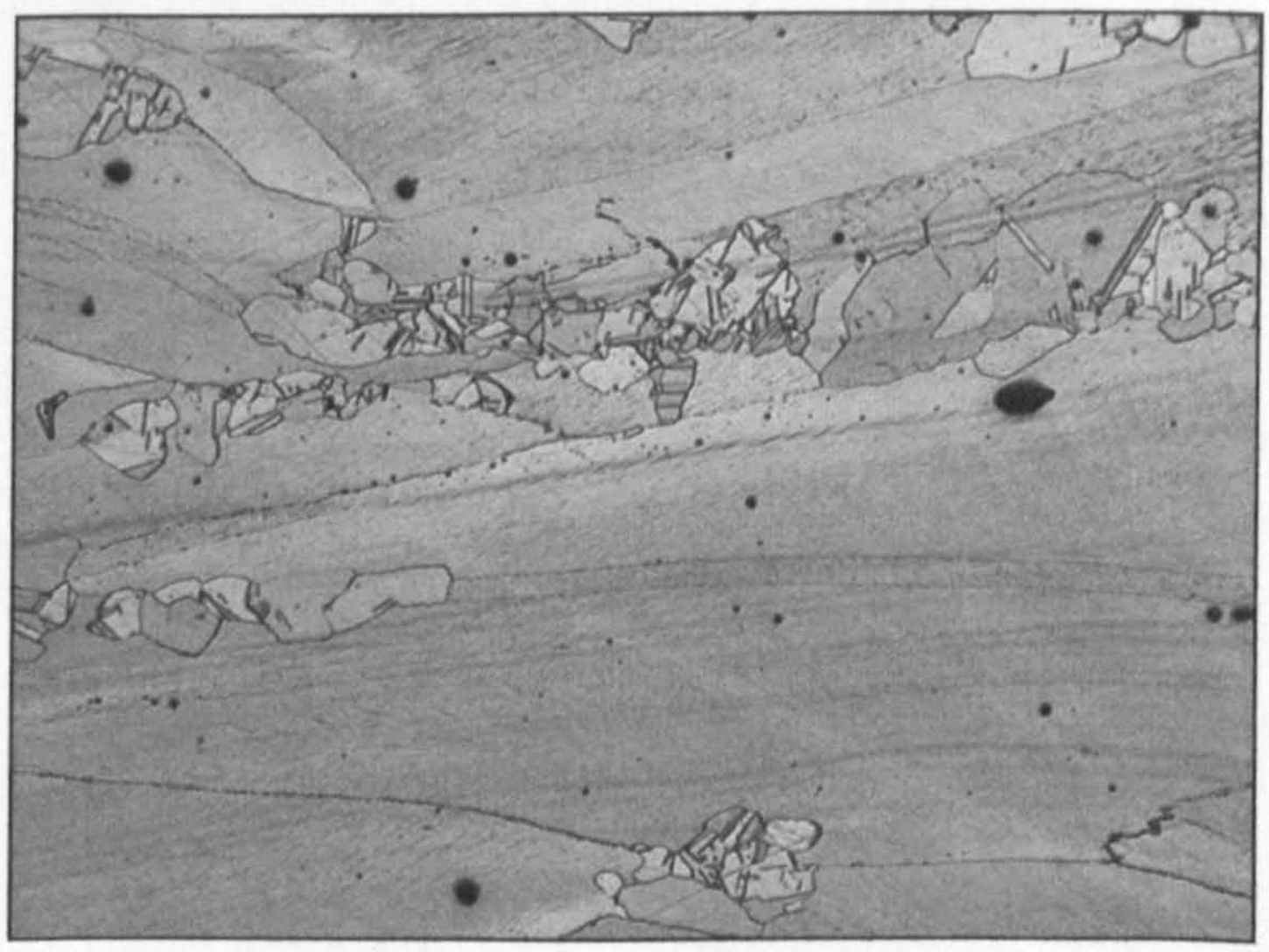

b)

100μm

Figure 5.19: Optical micrographs showing preferential nucleation of recrystallisation on a) deformation bands in sample 950-SD, and b) deformed twin boundaries seen in sample 950-1-DD.

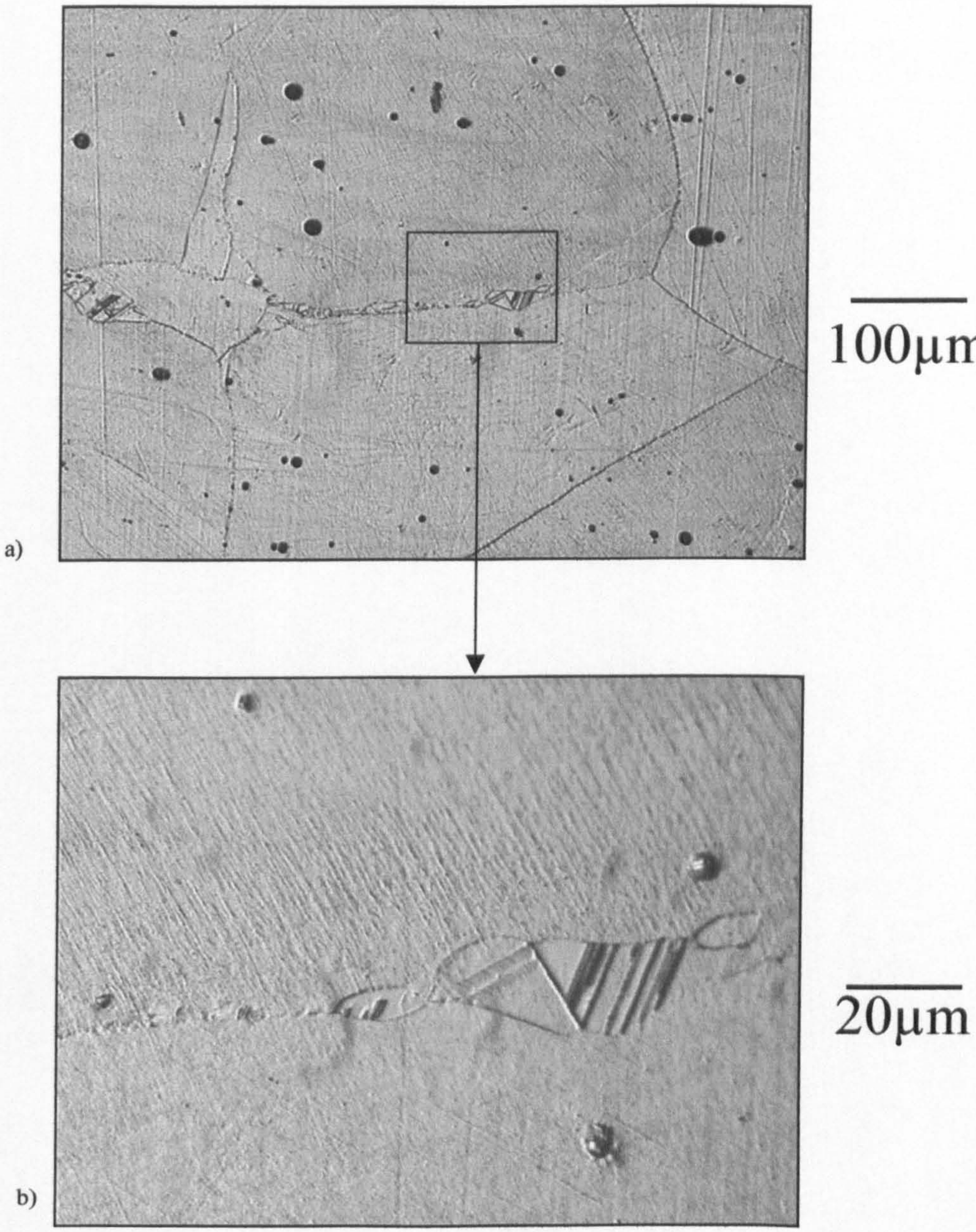

Figure 5.20: Grain boundary nucleation seen in 950-1-HHQ sample. Image seen in b) is a higher magnification shot of a).

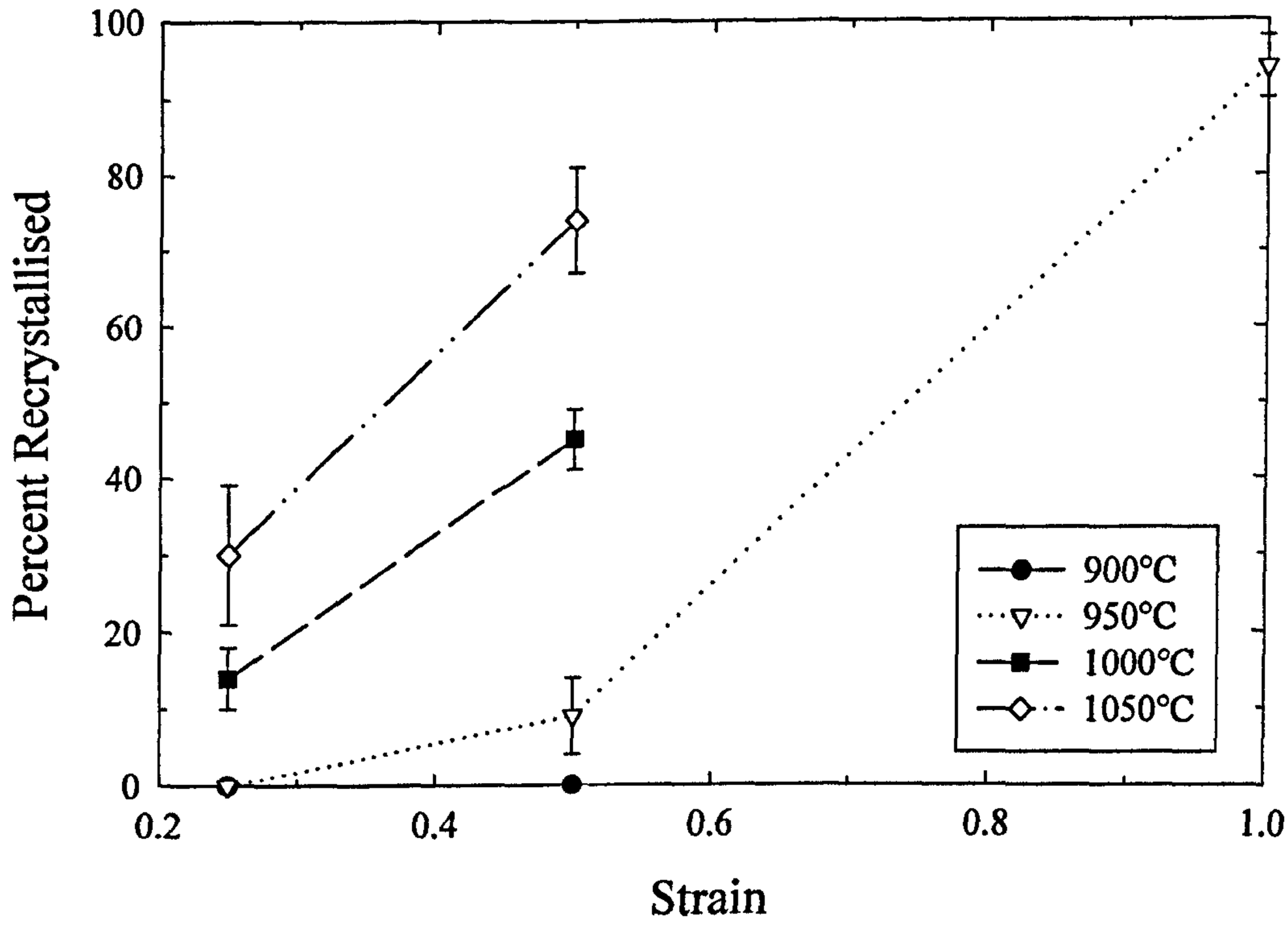

Figure 5.21: Plot showing the effect of strain on the extent of static recrystallisation following single deformation tests on Fe-30%Ni-Nb. Excepting the deformation temperature, the test conditions were otherwise equivalent. The strain rate used was $10s^{-1}$ for all tests.

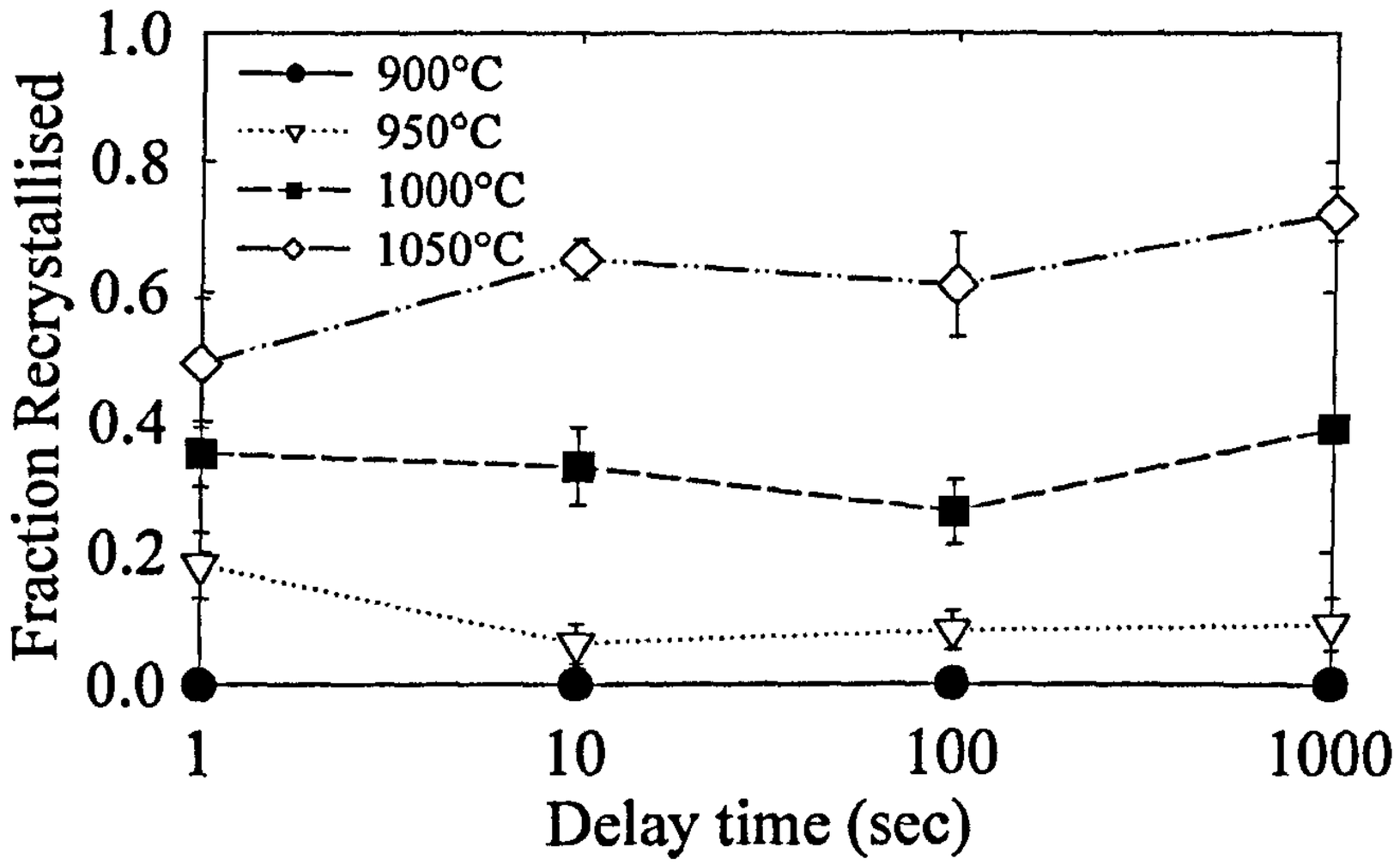

Figure 5.22: Plot showing the effect of delay time on recrystallisation for double deformation testing of Fe-30%Ni-Nb.

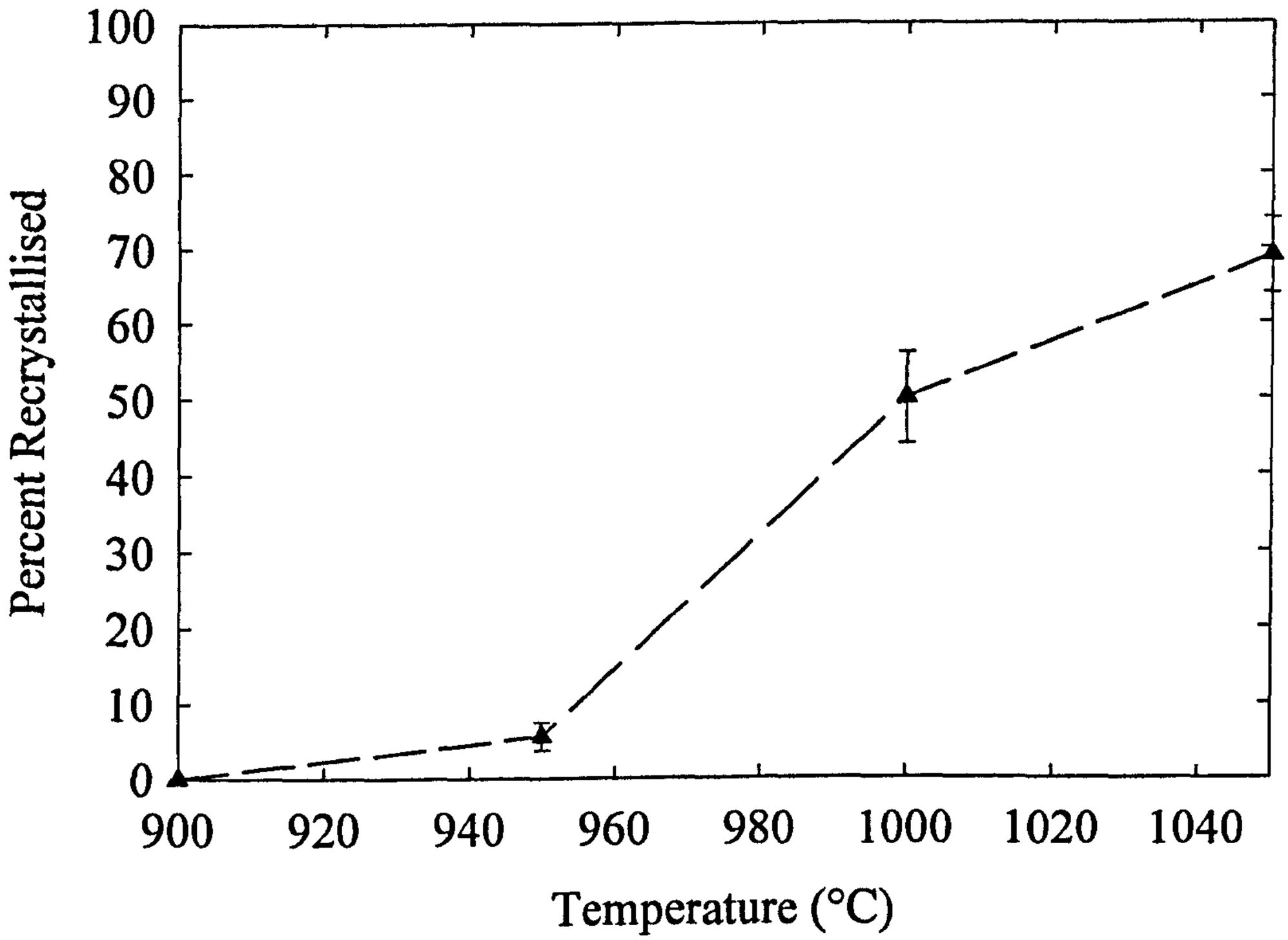

Figure 5.23: Plot showing the effect of temperature on recrystallisation for the hit-hold-quench (HHQ) specimens strained to 0.25 at 10 s^{-1}. The hold time for all temperatures was 10 seconds.

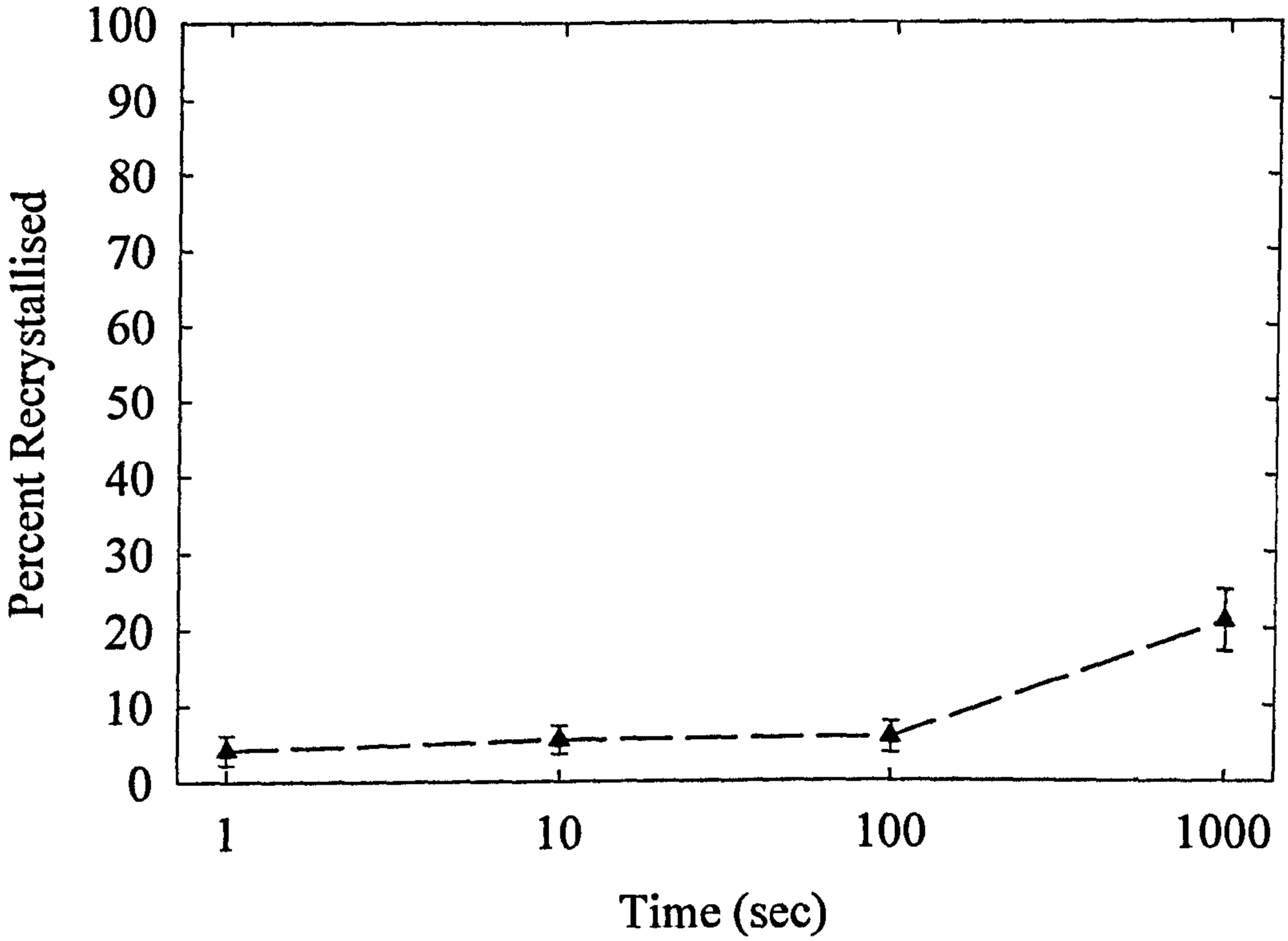

Figure 5.24: Plot showing the effect of hold time on recrystallisation kinetics for the isothermal hit-hold-quench (HHQ) specimens. Test temperature was 950°C for all hold times, while the strain given was 0.25, at a rate of $10s^{-1}$.

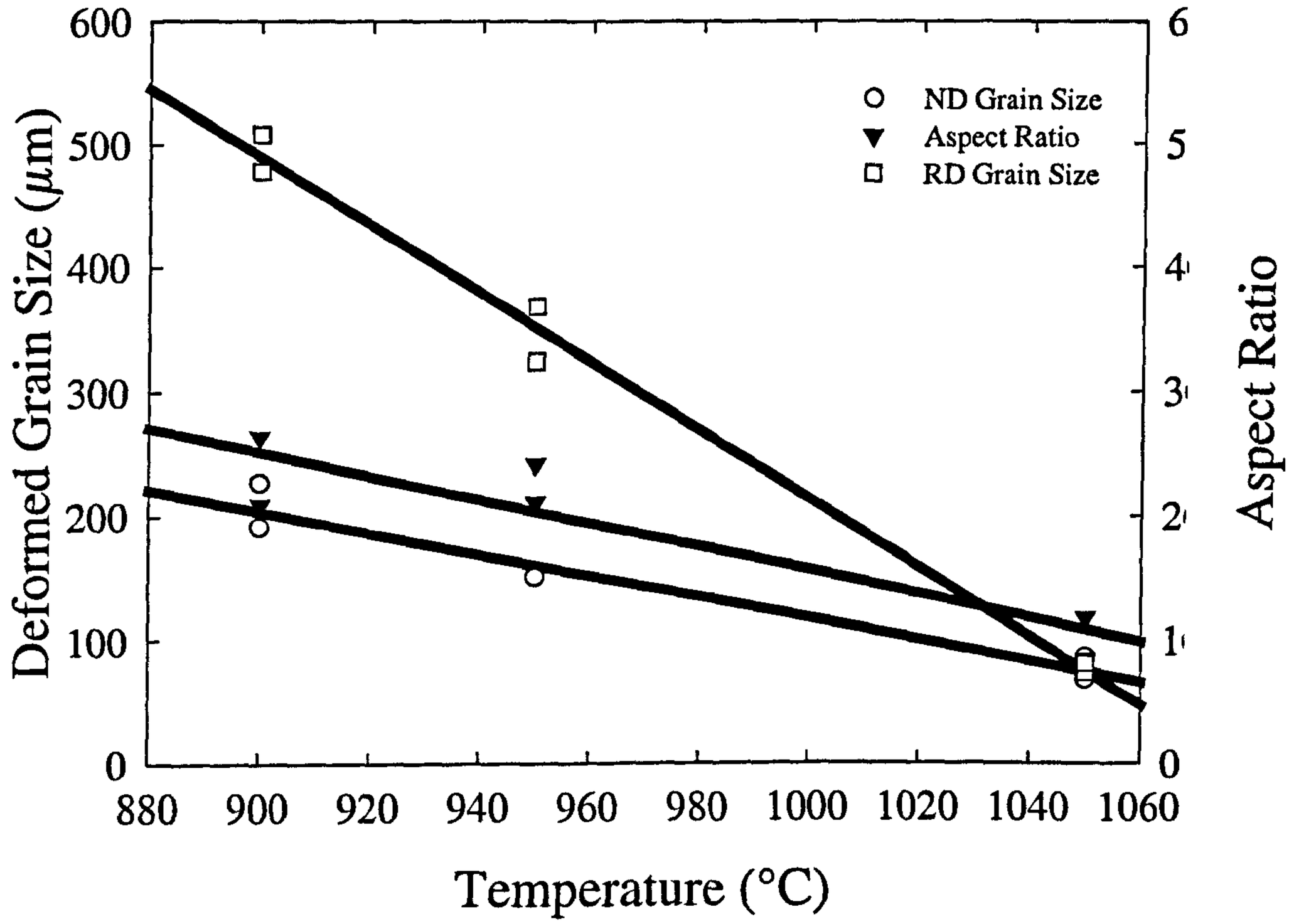

Figure 5.25: Effect of temperature on deformed grain size, and the resulting grain aspect ratio. ND refers to the grain size in the compression direction, while RD refers to the grain size in the longitudinal direction.

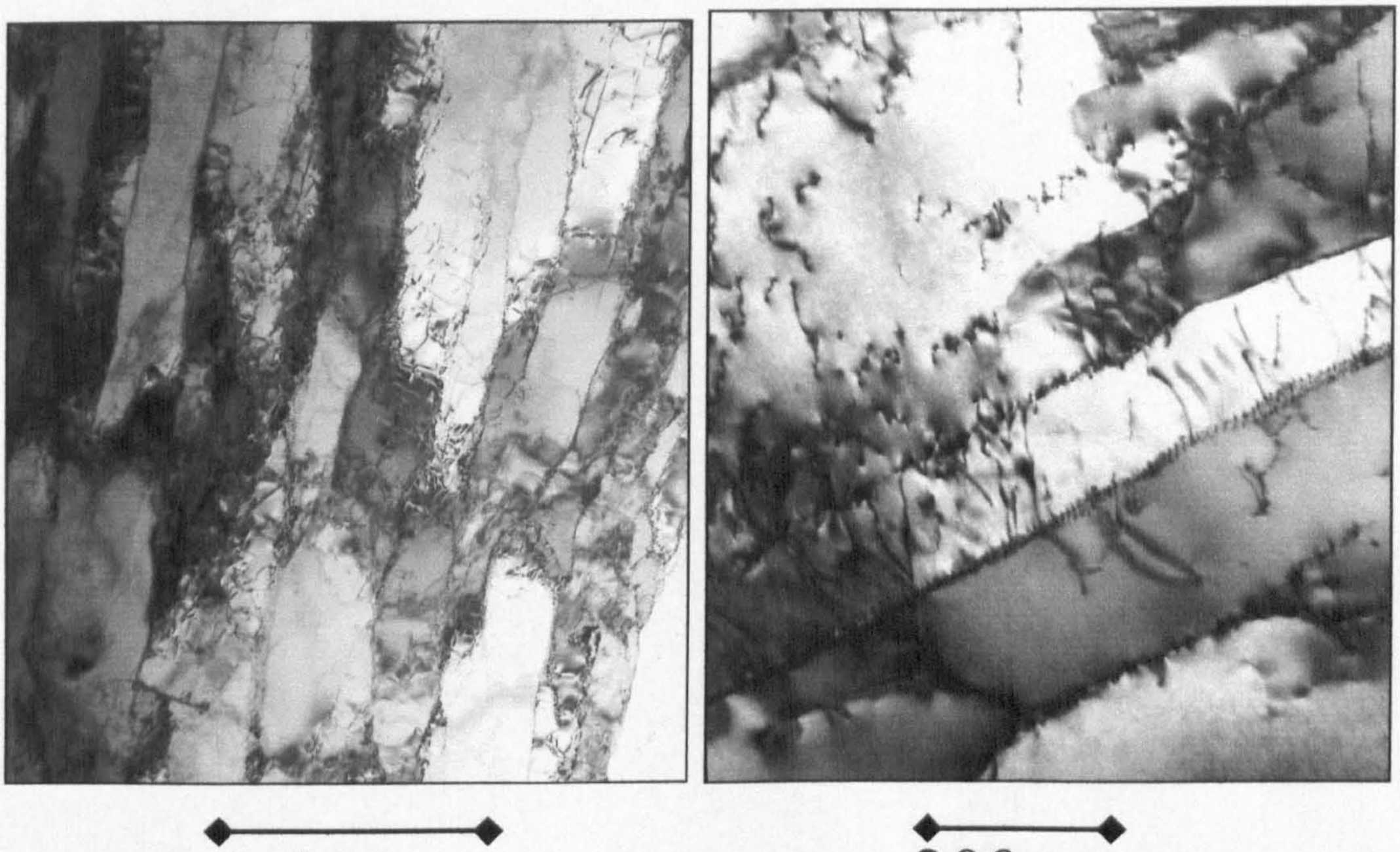

Figure 5.26: TEM micrographs of thin foils showing deformed substructure seen in sample 900-10s-DD. These images show very diffuse boundaries, where individual dislocations can be picked out.

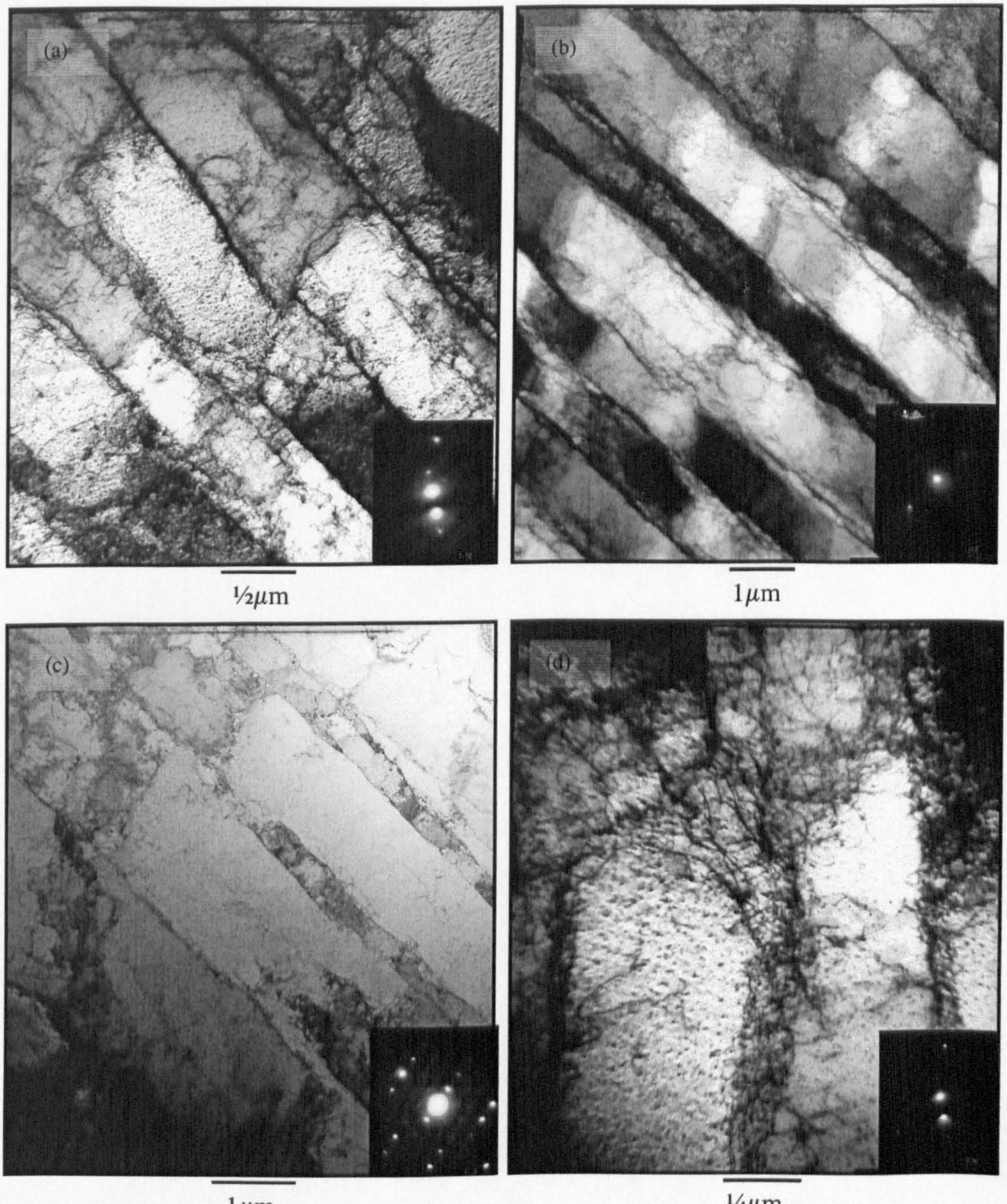

Figure 5.27: TEM micrographs showing microband structure seen in different regions of sample 950-100s-DD. Note the difference in appearance of the boundaries, and in particular how diffuse the walls appear, although they are viewed at different angles and different sample thicknesses. Images a) and b) show fairly loose dislocations making up the microband walls. In c), the dislocation walls are much more densely packed giving well-defined boundaries, while in d) they appear to be very diffuse, and individual dislocations can be easily picked out.

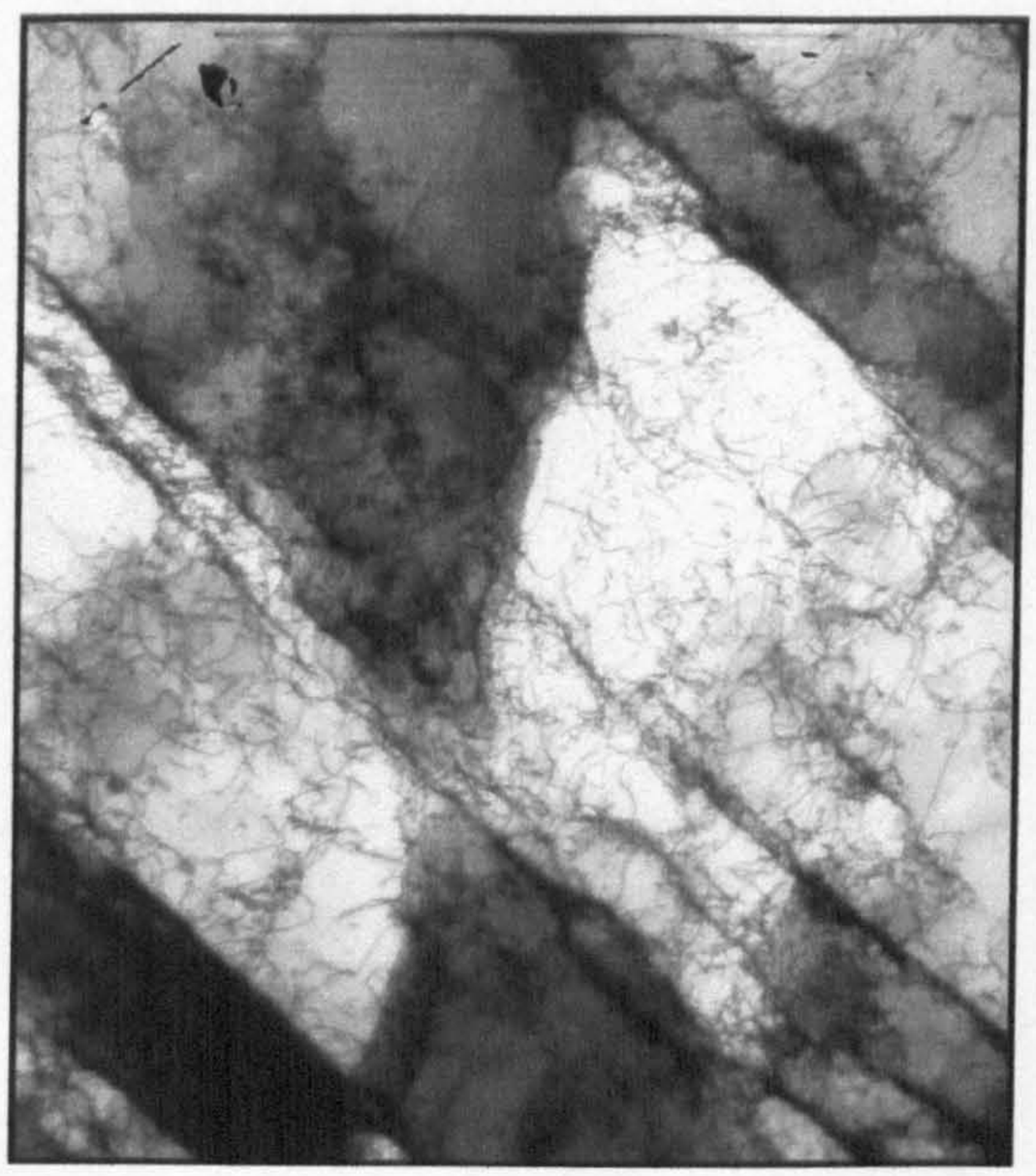

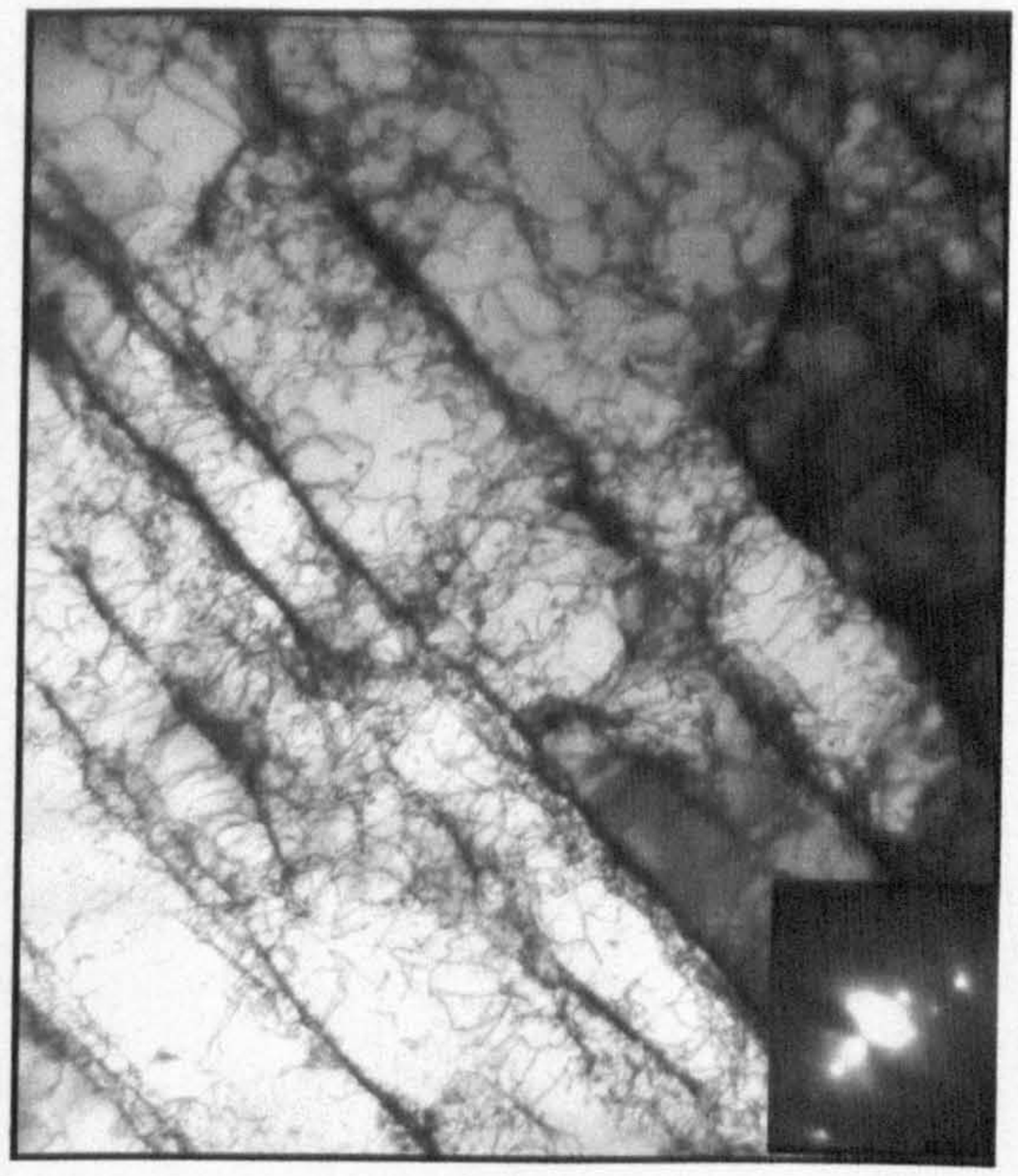

Figure 5.28: TEM micrographs showing deformed substructure seen in different regions of sample 950-100s-DD. Note how diffuse the walls appear. These images show very diffuse boundaries, where individual dislocations can be picked out.

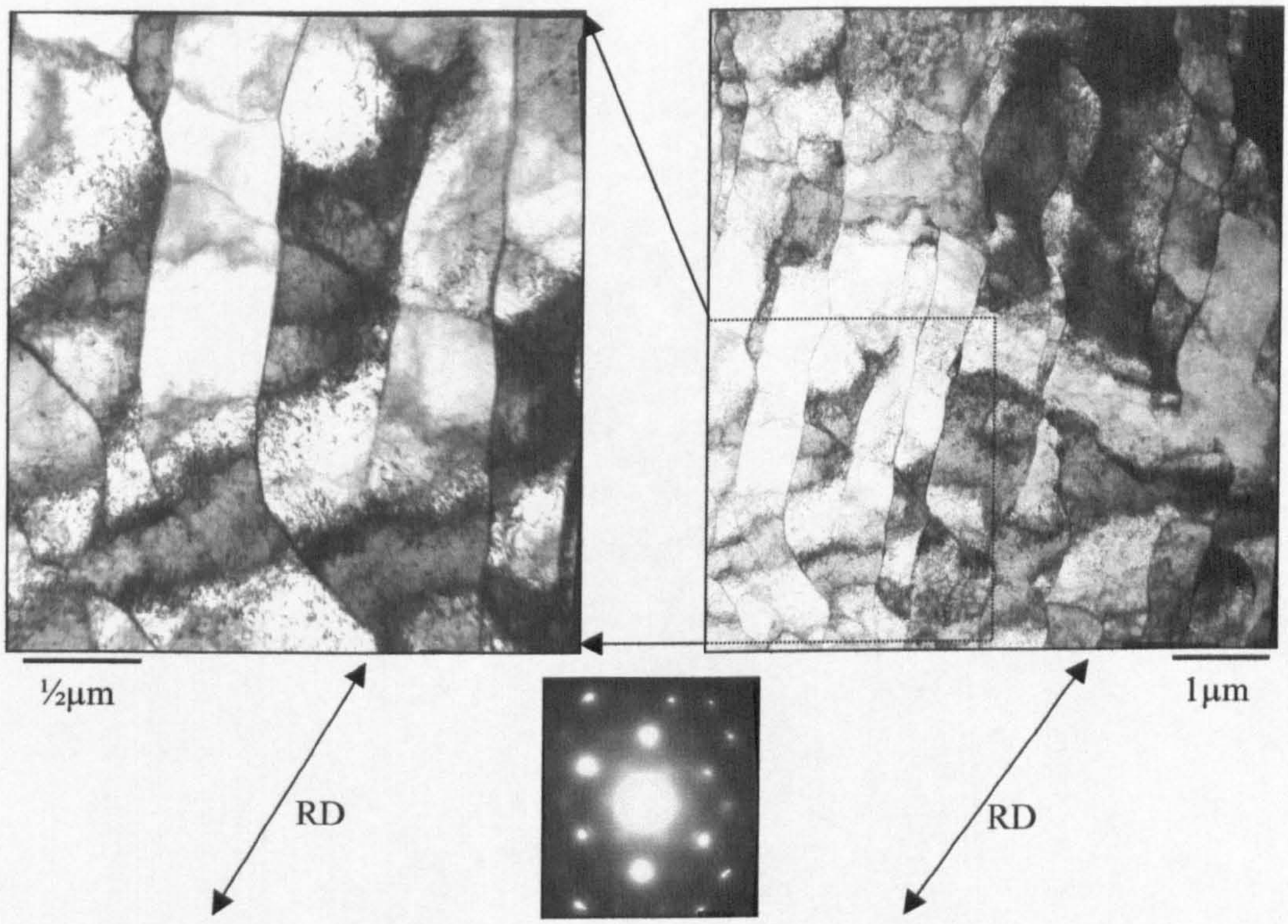

Figure 5.29: TEM micrographs showing microbands seen in sample 950-100s-DD imaged close to a [110] zone. The effective rolling direction is marked, and the angle the microbands make to the RD in this image is ~30°.

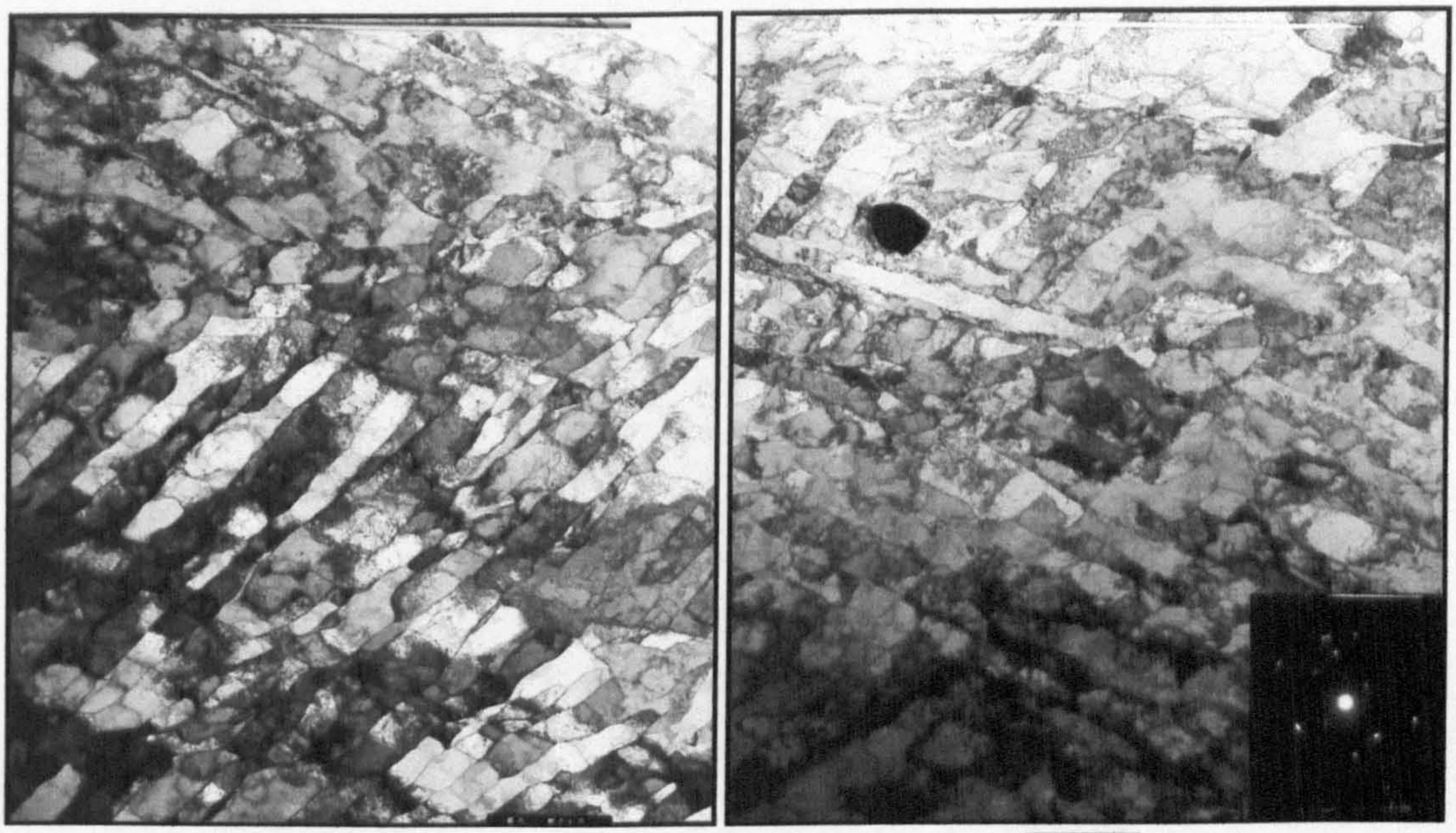

2μm 2μm

Figure 5.30: TEM micrographs showing deformed substructure in sample 950-100s-DD. Image a) shows a region where two sets of microbands meet. Image b) shows a large, undissolved particle within the microband structure.

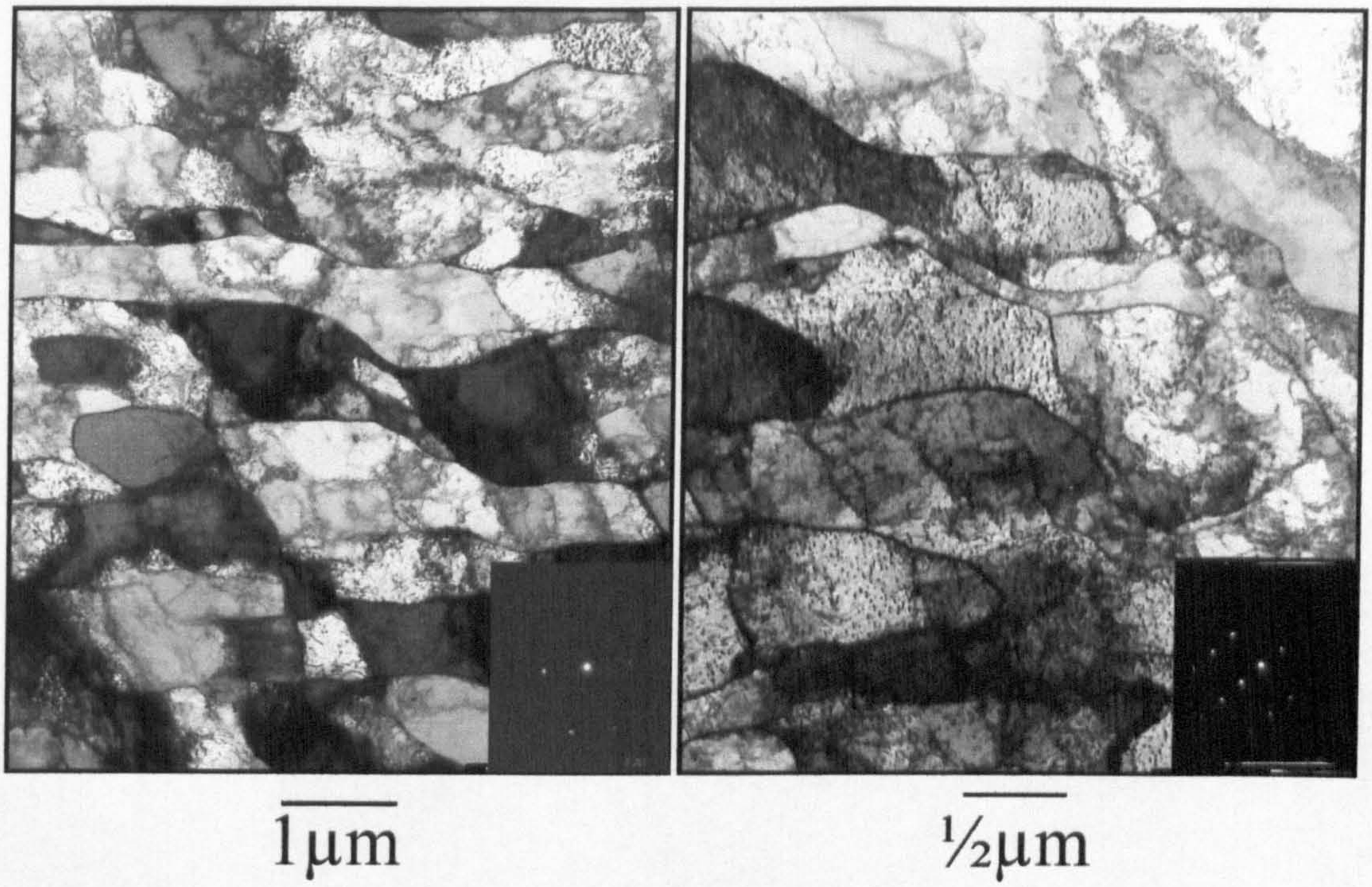

Figure 5.31: TEM micrographs showing deformed substructure in sample 950-100s-DD.

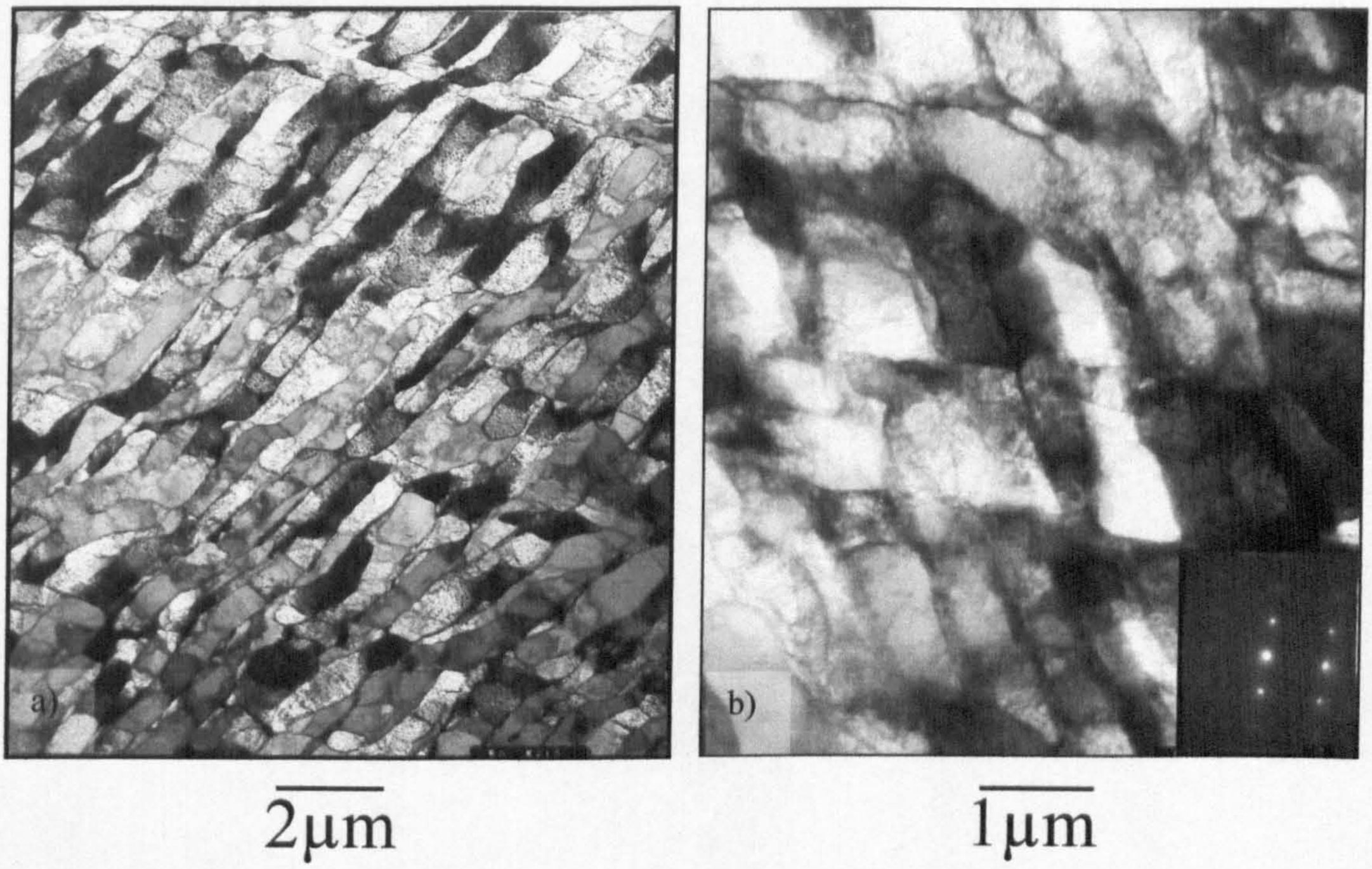

Figure 5.32: TEM micrographs showing deformed substructure in sample 950-100s-DD.
a) Microband structure.
b) Image showing where two sets of microbands intersect to give the appearance of a more equiaxed subgrain structure.

Figure 5.33: TEM micrograph of a thin foil showing the substructure in sample 1050-SD. These images show very well-defined subgrain walls.

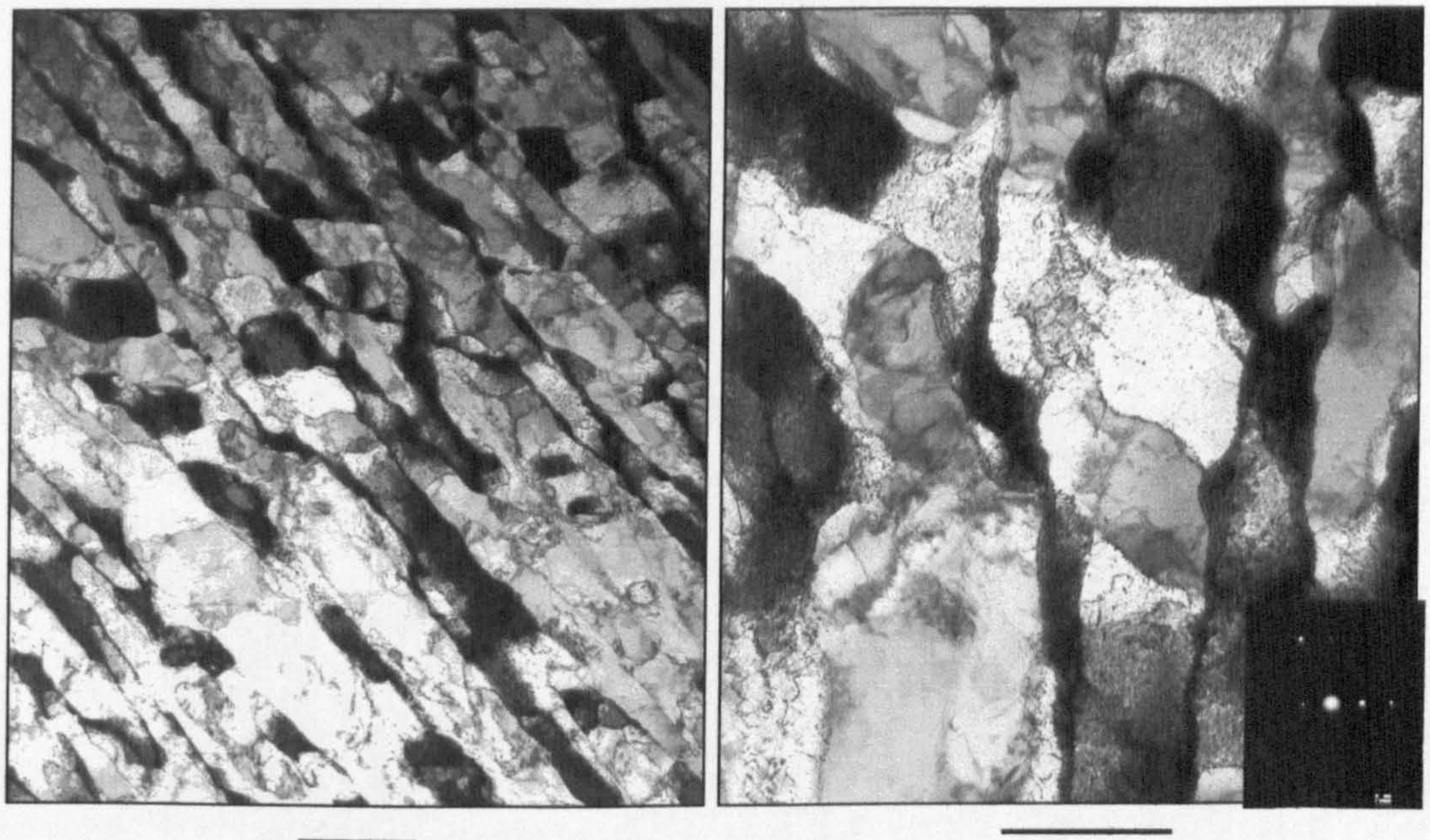

Figure 5.34: Subgrain structure seen in 1050-100-DD specimen. Note the presence of a microbanded substructure.

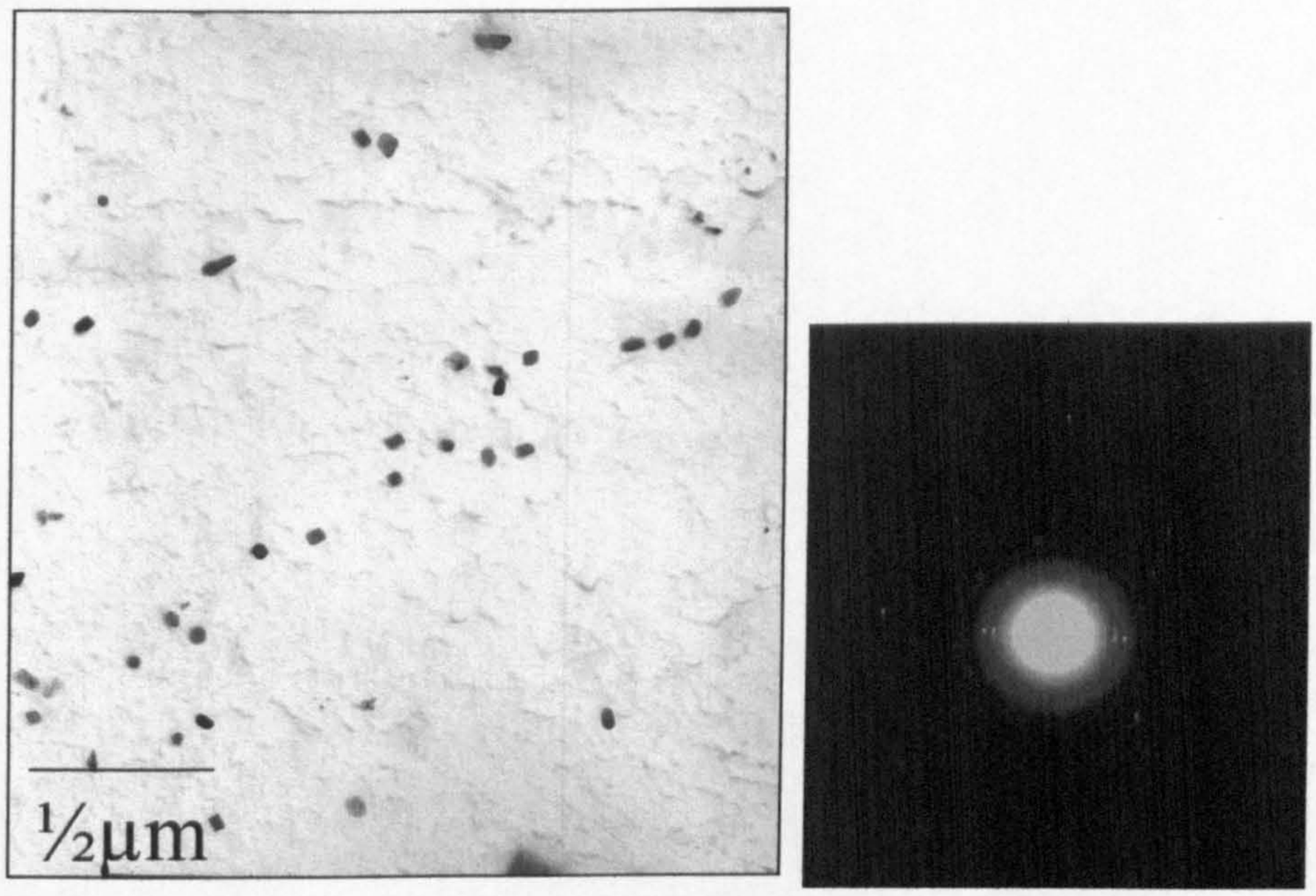

Figure 5.35: TEM micrograph showing strain induced precipitation in Fe-30%Ni-Nb. The specimen shown was from sample 950-1000-DD. The diffraction pattern was indexed as NbC.

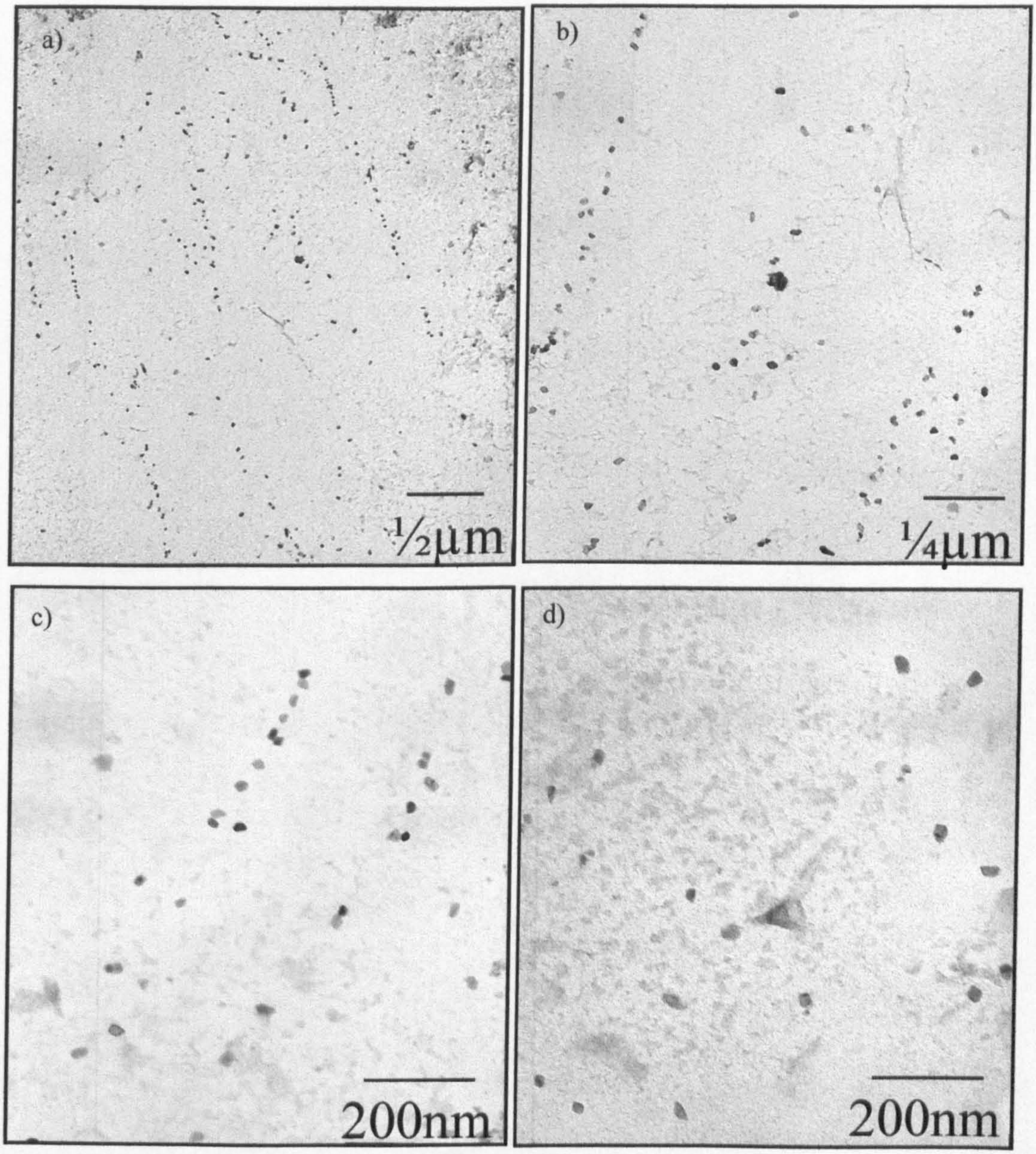

Figure 5.36: TEM micrographs showing precipitation in sample 950-100s-HHQ. Images a) and b) show a linear distribution of precipitates, while c) and d) show the arrangement of the precipitated particles more closely.

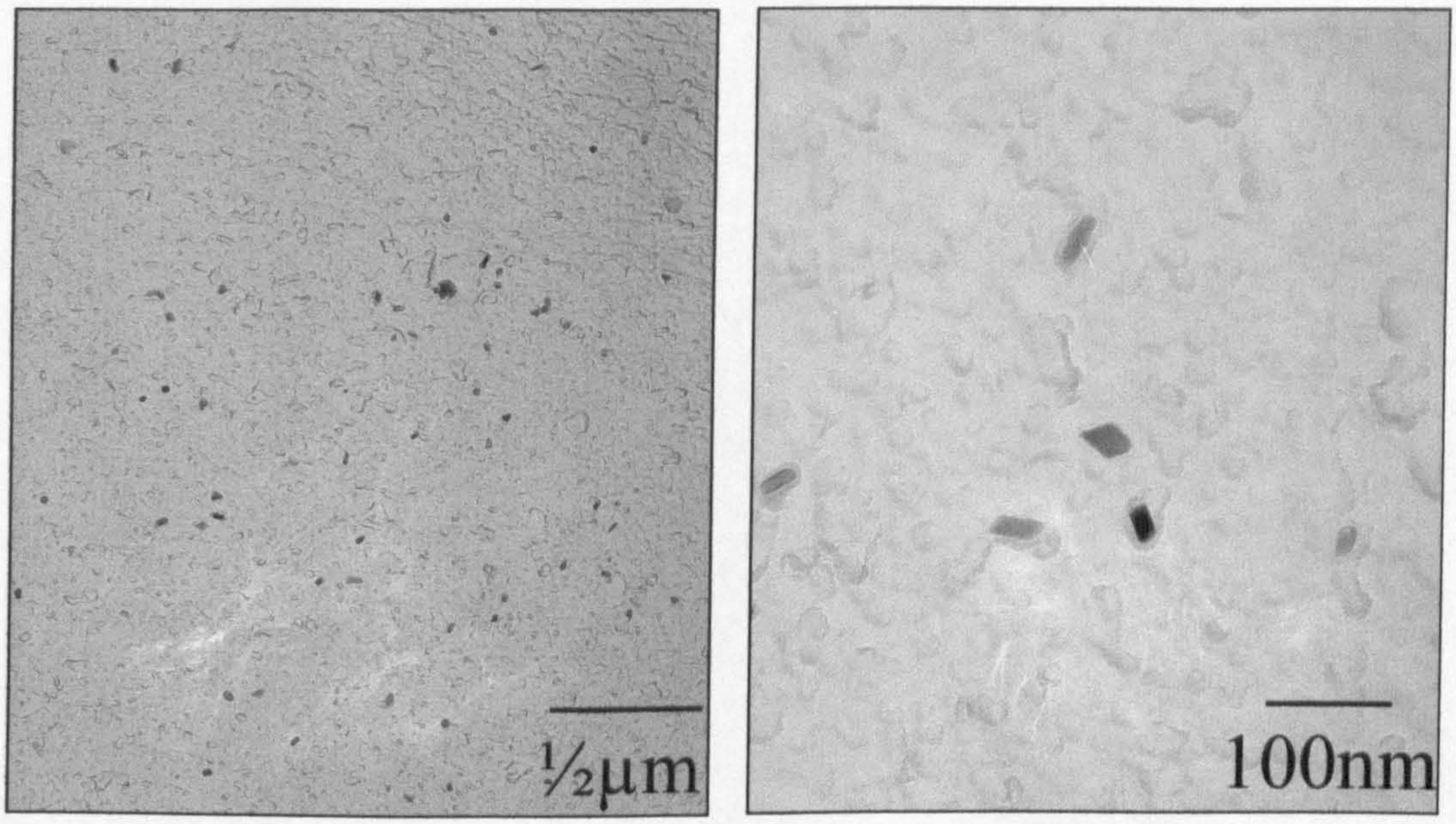

Figure 5.37: TEM micrographs showing strain-induced precipitation in replicas of sample 950-100-DD. The image seen in a) shows precipitation in a cell-like distribution, while b) shows the particles at a higher magnification.

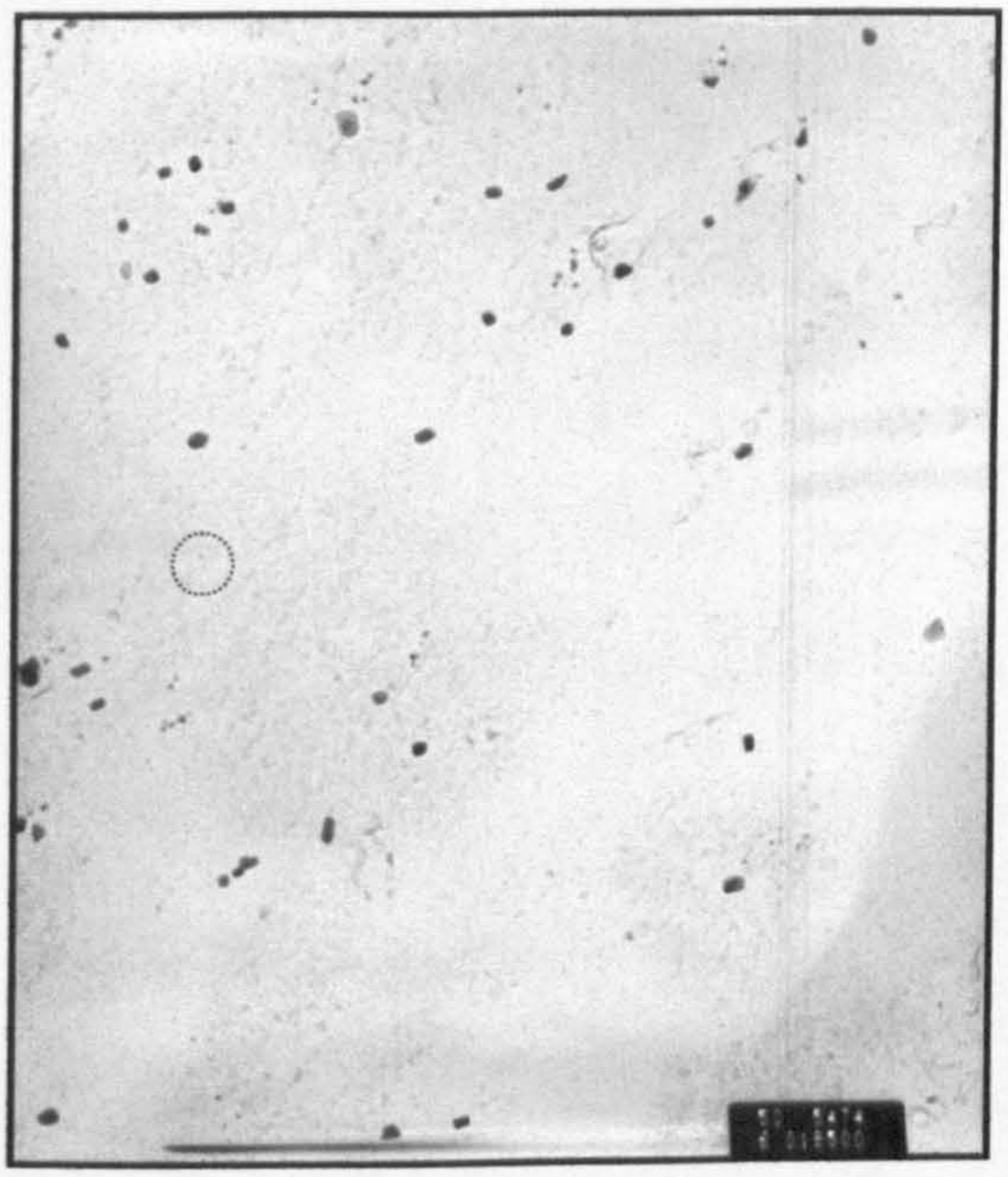

1μm

Figure 5.38: TEM micrograph showing particles of differing size. Many particles are ~30nm, while finer ones exist (circled) at below 5nm. This image was taken of a replica from sample 950-1000-DD.

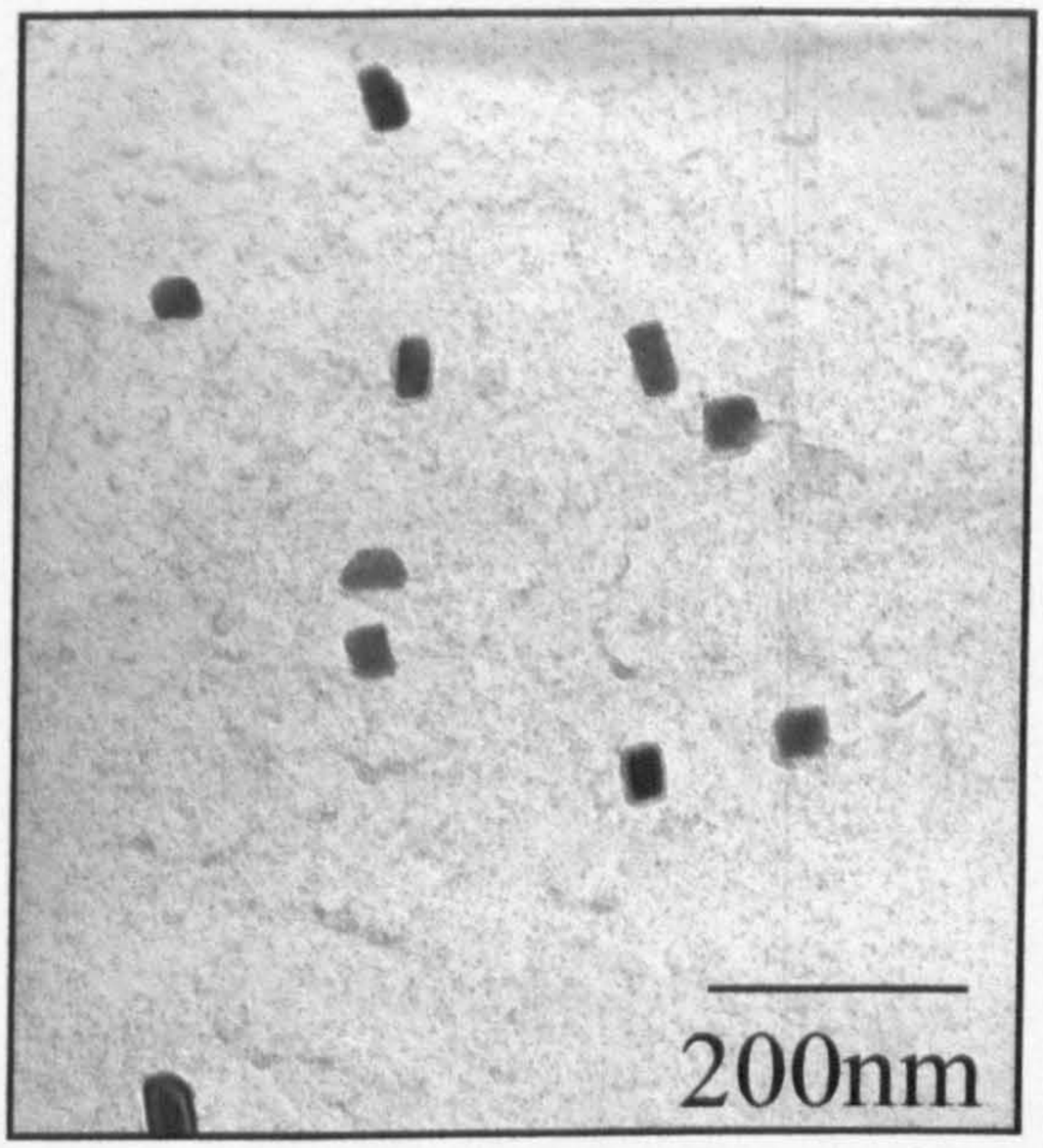

Figure 5.39: TEM micrograph showing precipitated particles in sample 950-1000-DD. The particles seen here appear to be of mainly cubic morphology.

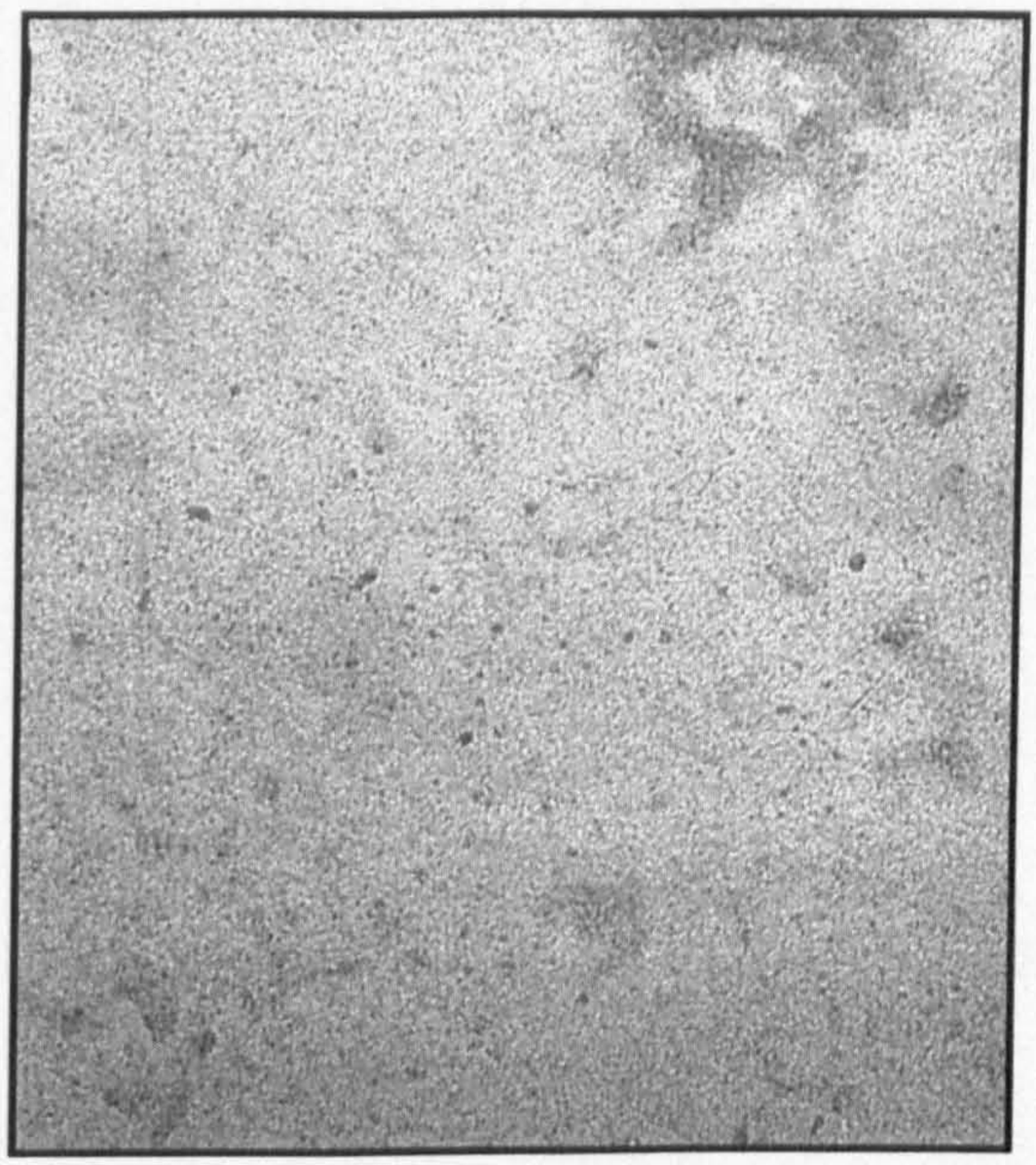

Figure 5.40: TEM micrographs showing precipitation in sample 950-1s-HHQ. The particles in this sample are very small, hard to see, and difficult to count accurately.

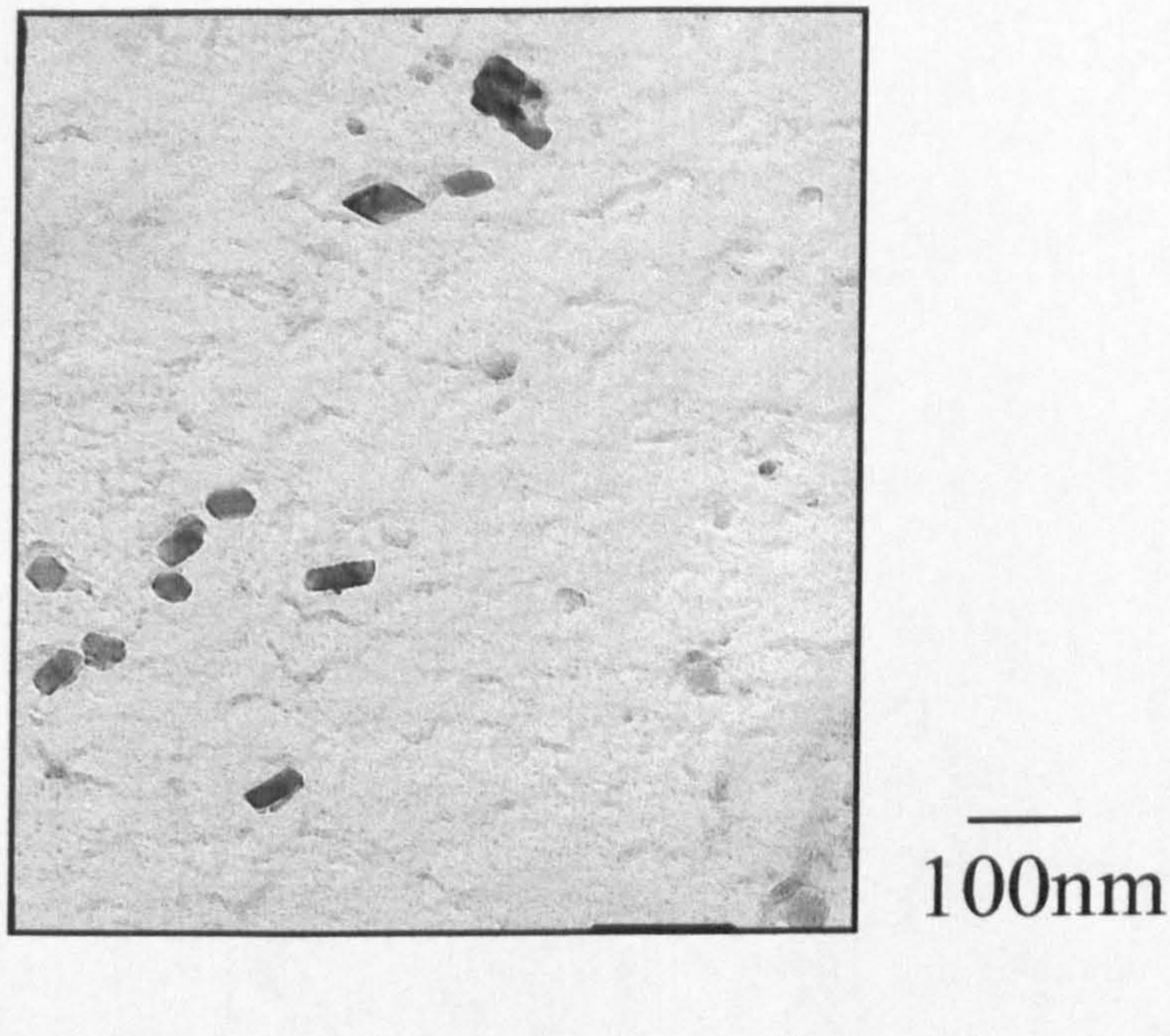

Figure 5.41: TEM micrographs showing precipitation in sample 950-1000s-HHQ. There are many midsize particles present in this sample. This image shows the variety of particle morphologies present.

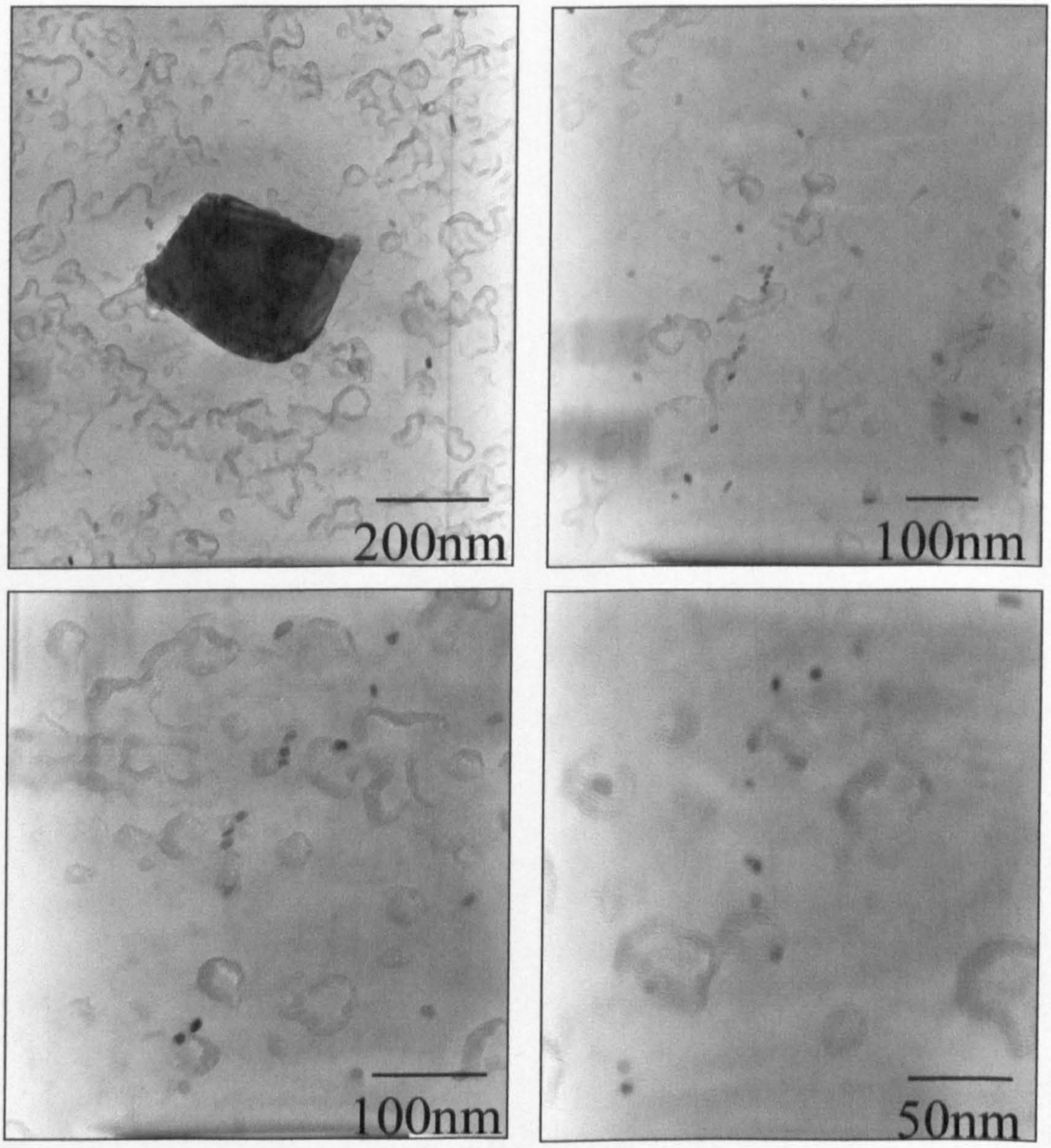

Figure 5.42: TEM micrographs showing precipitation in a sample strained to 0.5 at 900°C, held 10s and quenched. Image a) shows an undissolved niobium particle. Images b) to d) show fine-scale strain-induced precipitation.

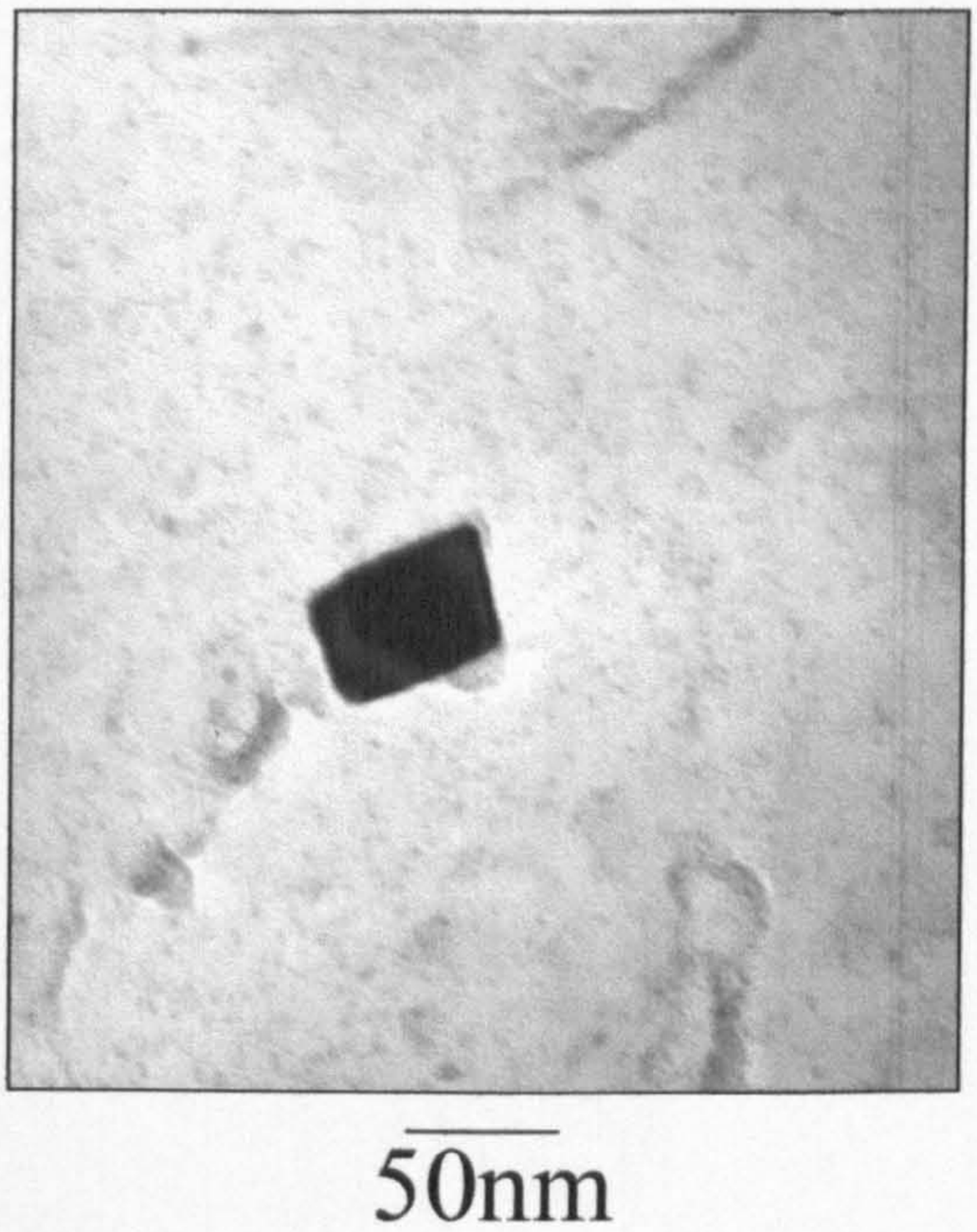

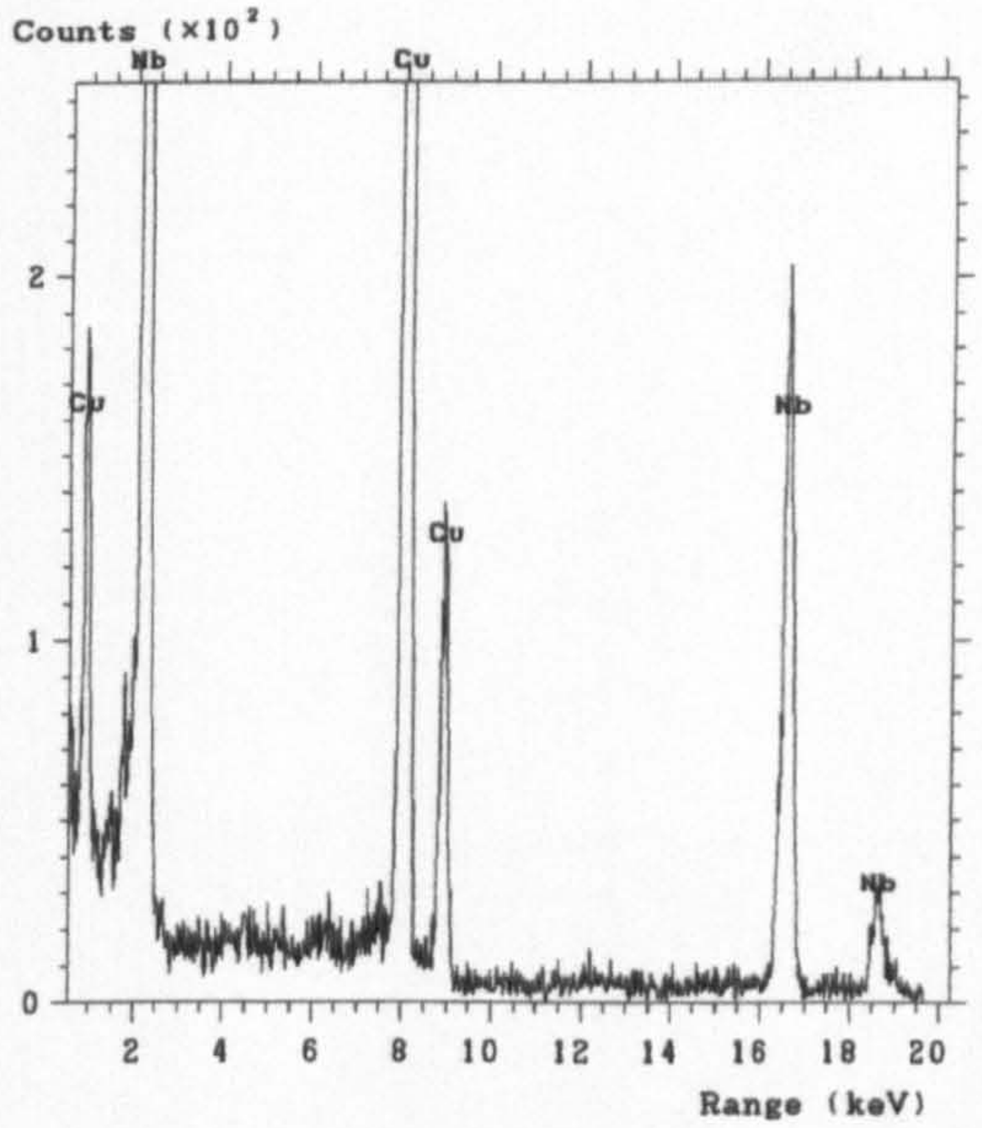

Figure 5.43: TEM micrograph/ EDS analysis of a cuboid particle in sample 950-1000-dd. This shows the presence of niobium, while the copper trace is from the supporting grid.

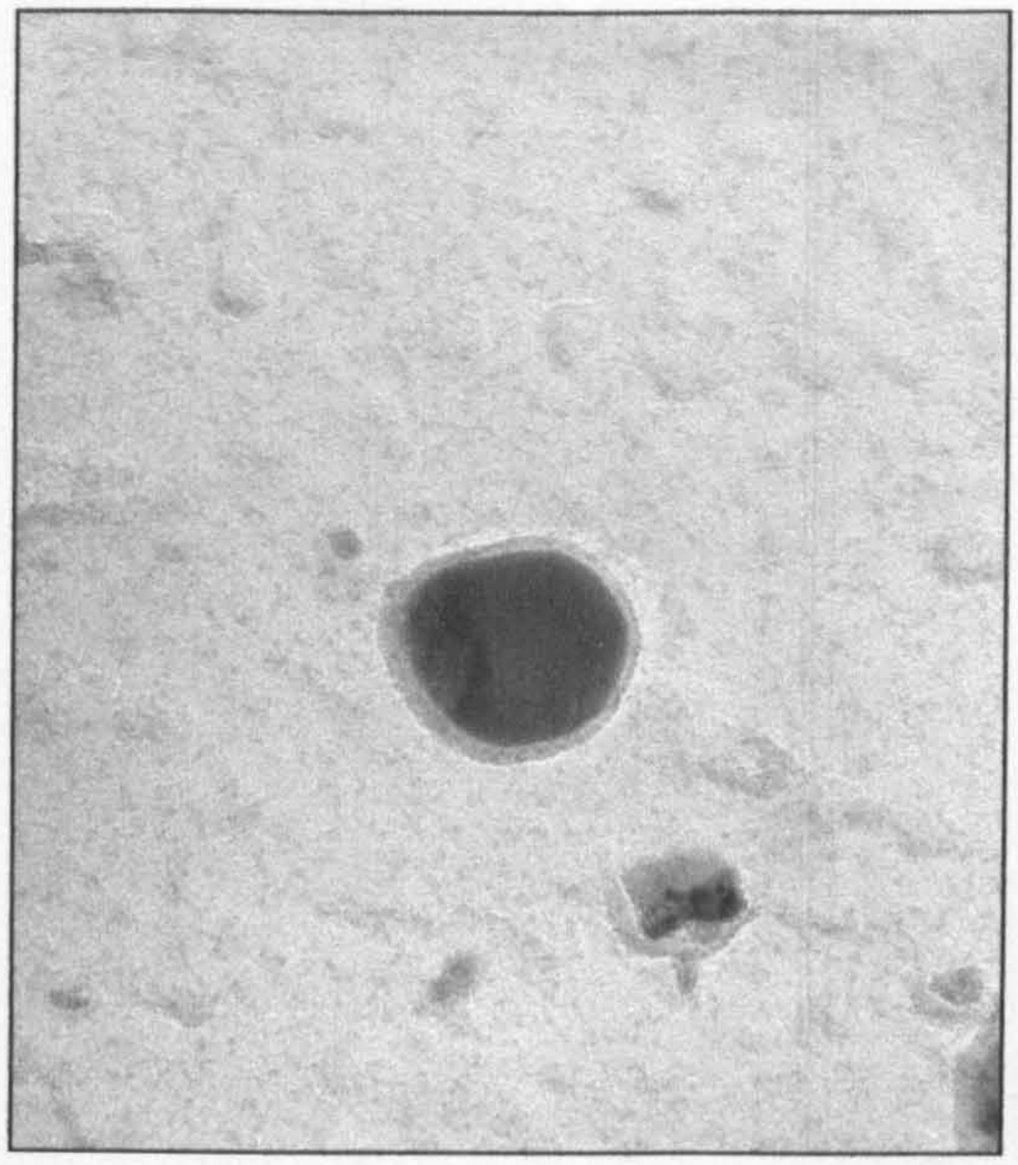

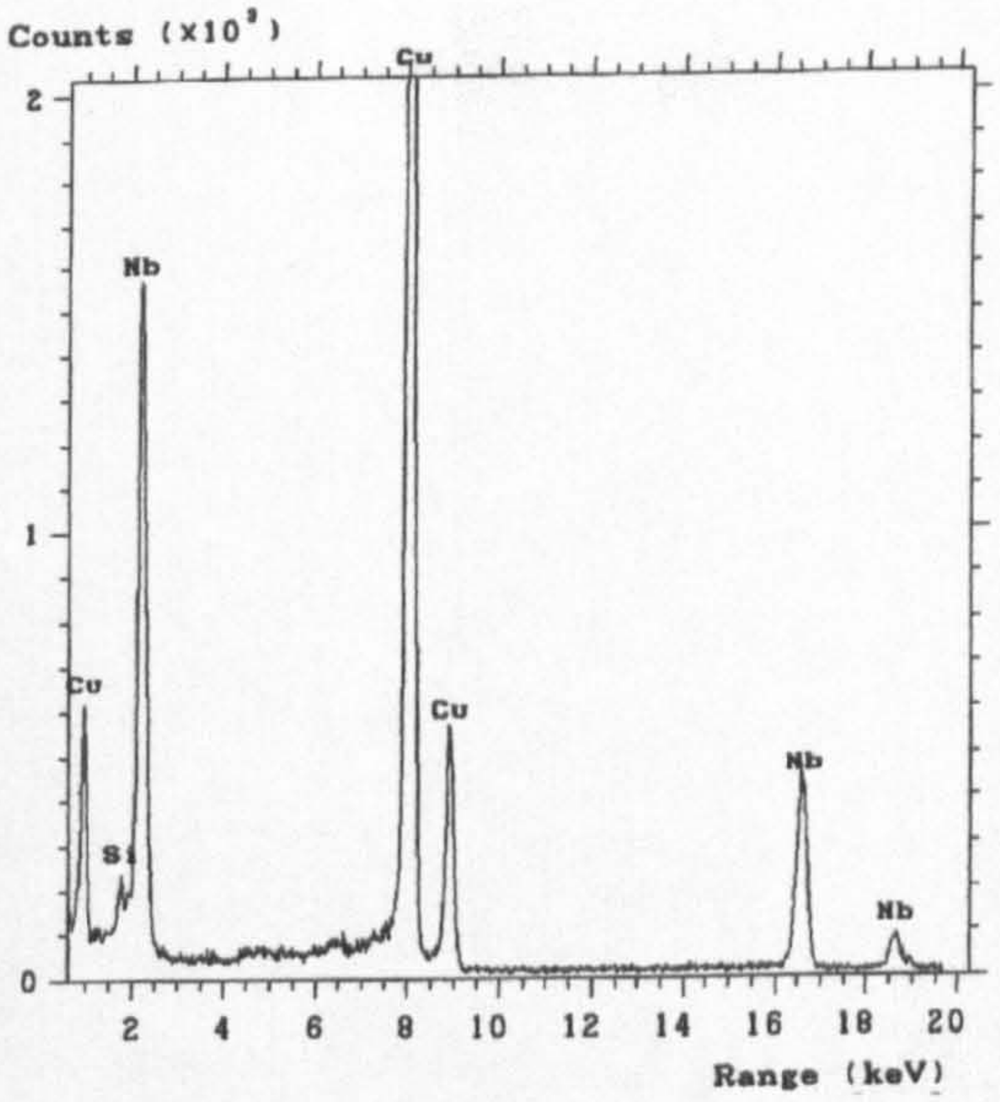

Figure 5.44: TEM micrograph/ EDS analysis of a rounded particle in sample 950-1000-dd. This shows the presence of niobium. The copper is from the supporting grid, while the silicon trace is believed to be present within the carbon film.

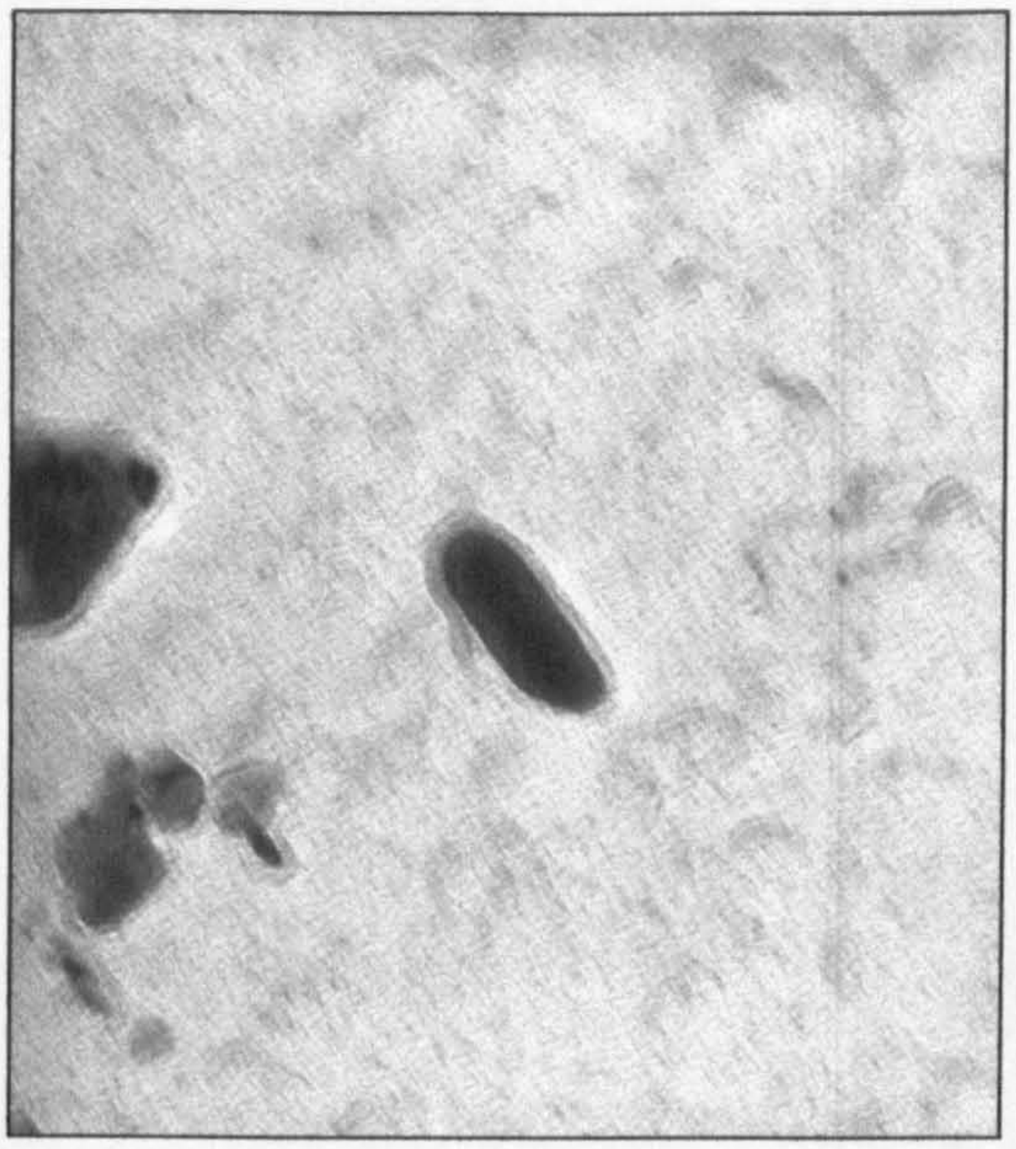

Figure 5.45: TEM micrograph/ EDS analysis of an elongated particle in sample 950-1000-DD. This shows the presence of niobium. The copper is from the supporting grid.

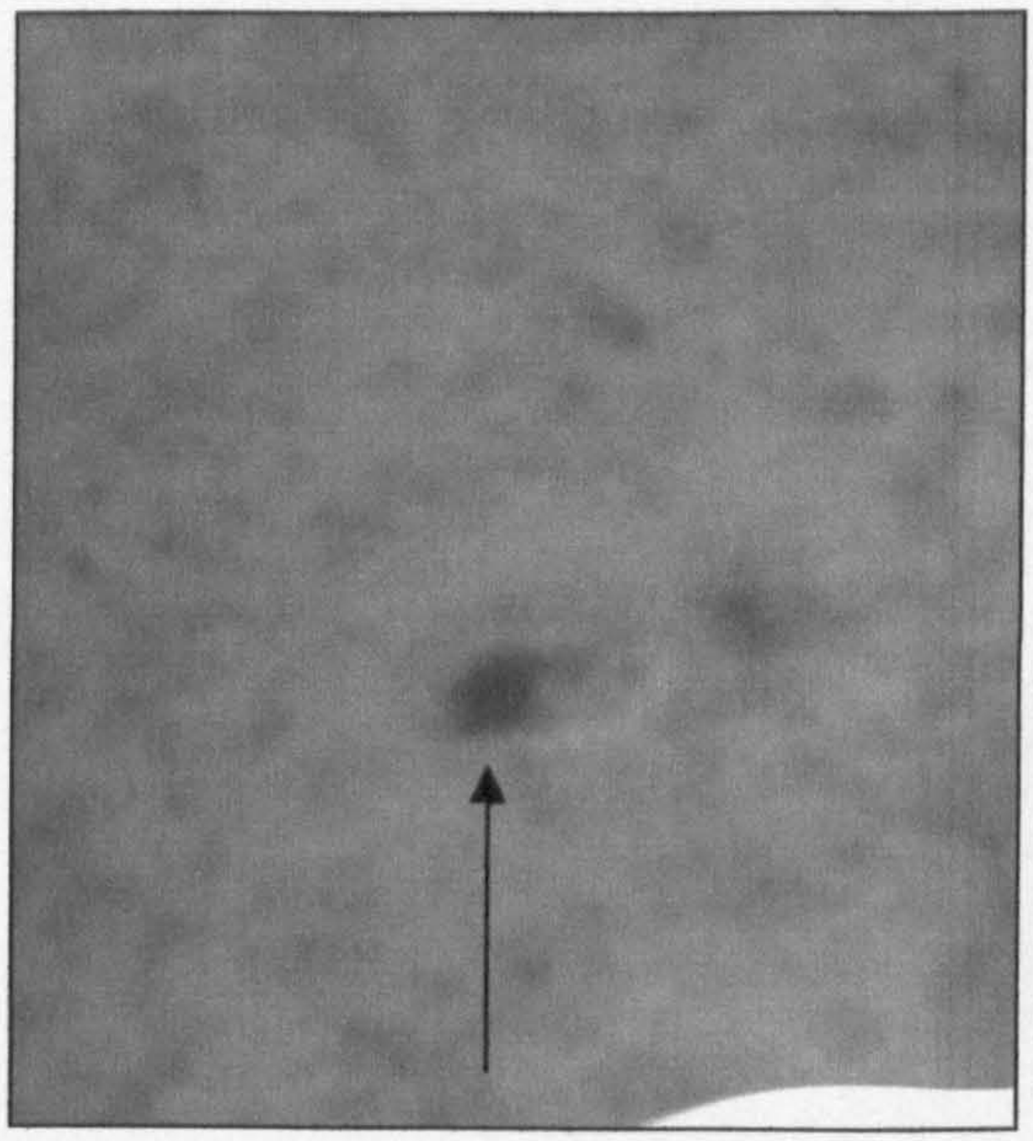

Figure 5.46: TEM micrograph and EDS analysis of a fine particle (arrowed) in sample 950-1000-DD. This confirms that Nb is present. The Cu peak is from the supporting grid.

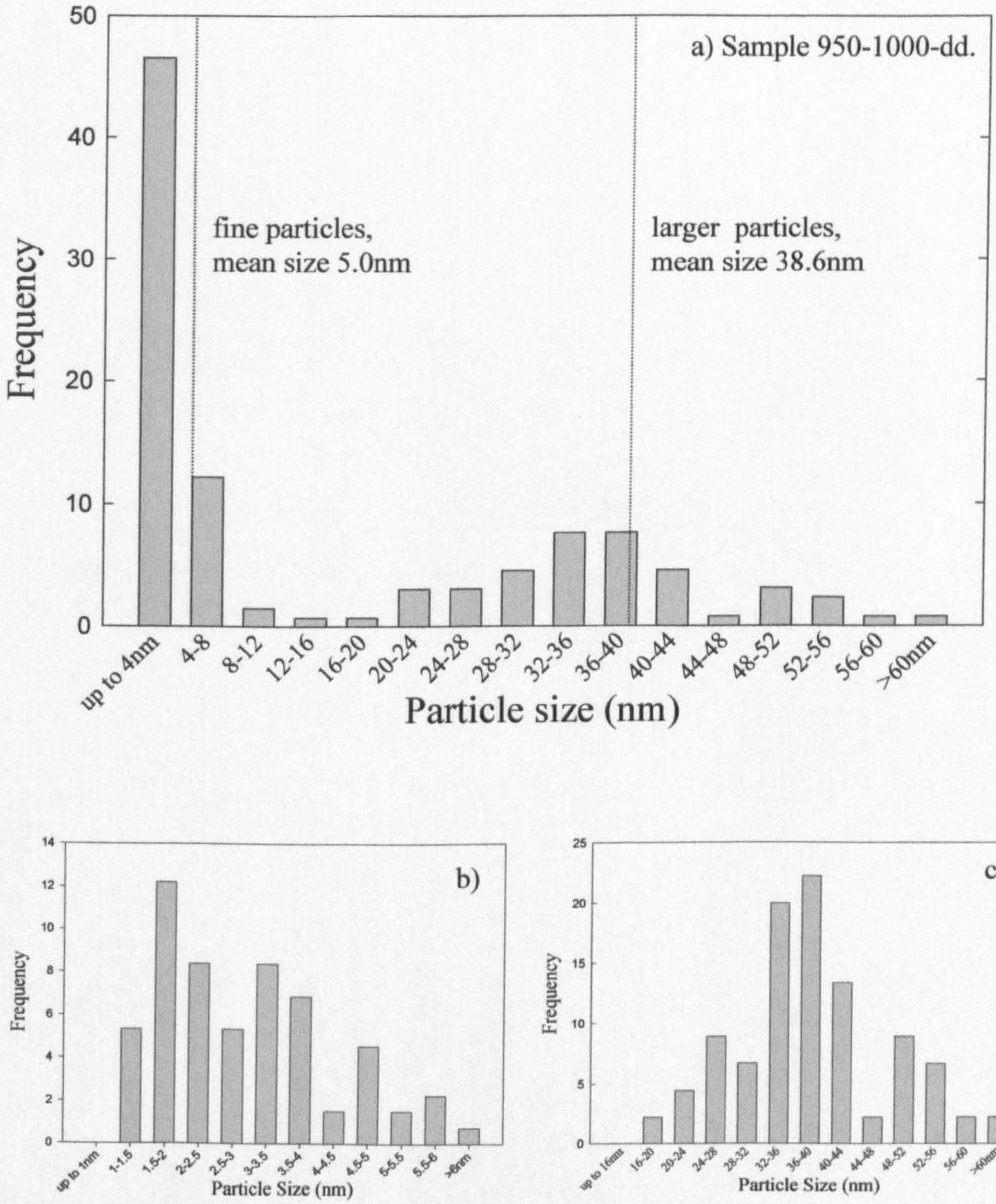

Figure 5.47: Particle size distribution found in sample 950-1000-dd. a) Shows the whole precipitate size distribution, which shows a bimodal population, while b) and c) show the frequency data for the two populations separately.

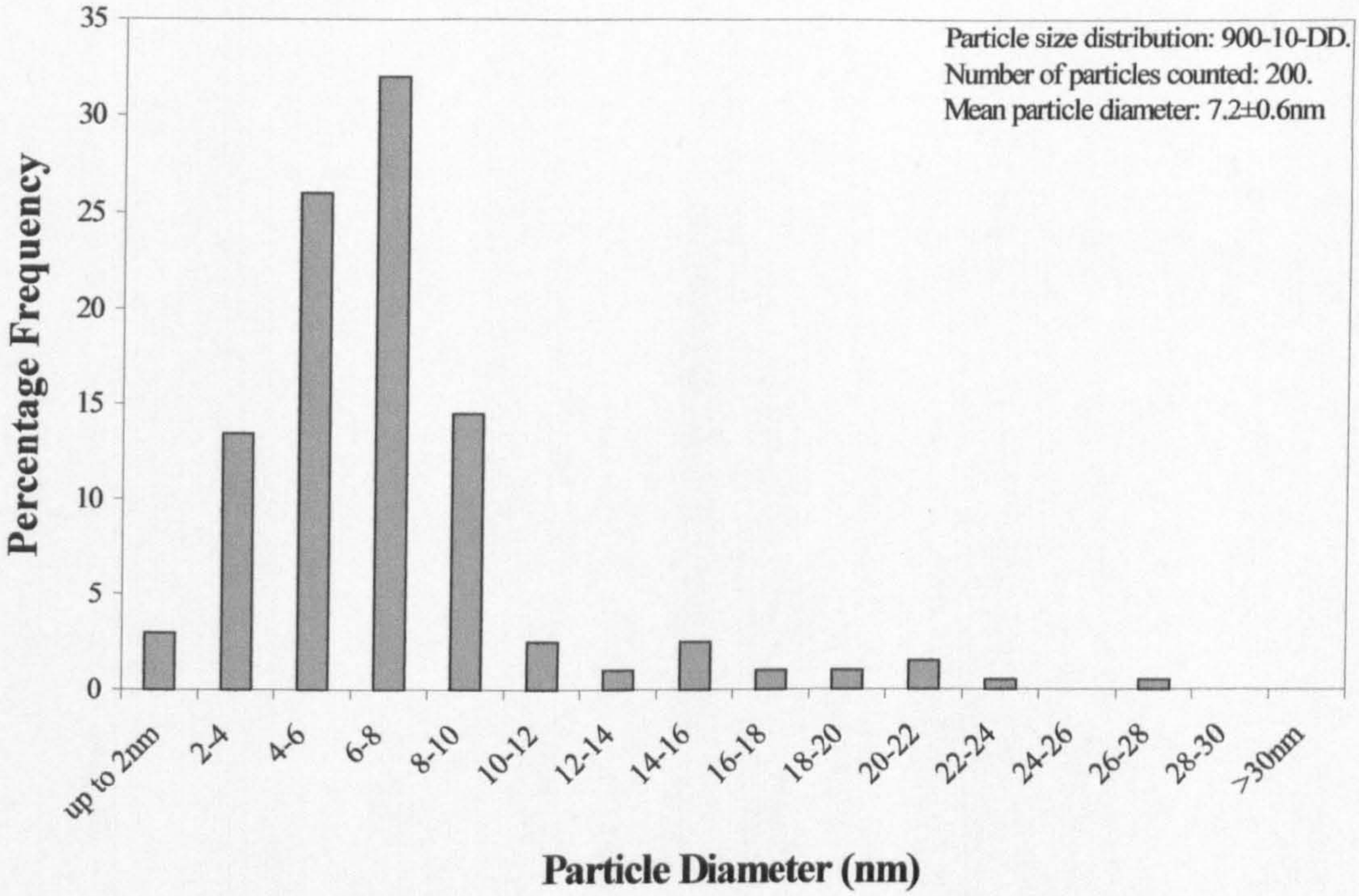

Figure 5.48: Particle size distribution measured from TEM analysis of extraction replicas for sample 900-10-DD.

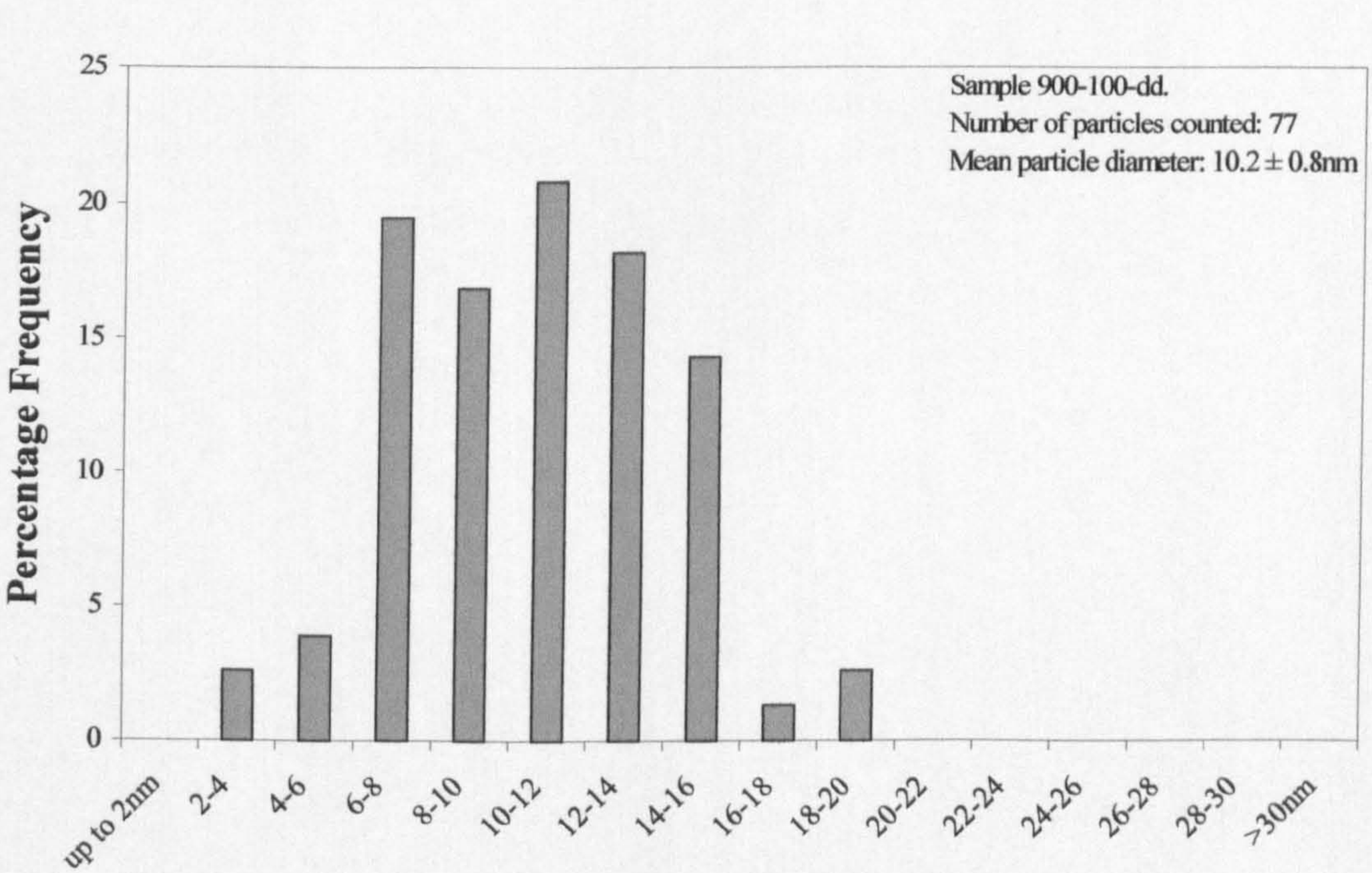

Figure 5.49: Particle size distribution measured from TEM analysis of extraction replicas for sample 900-100-DD.

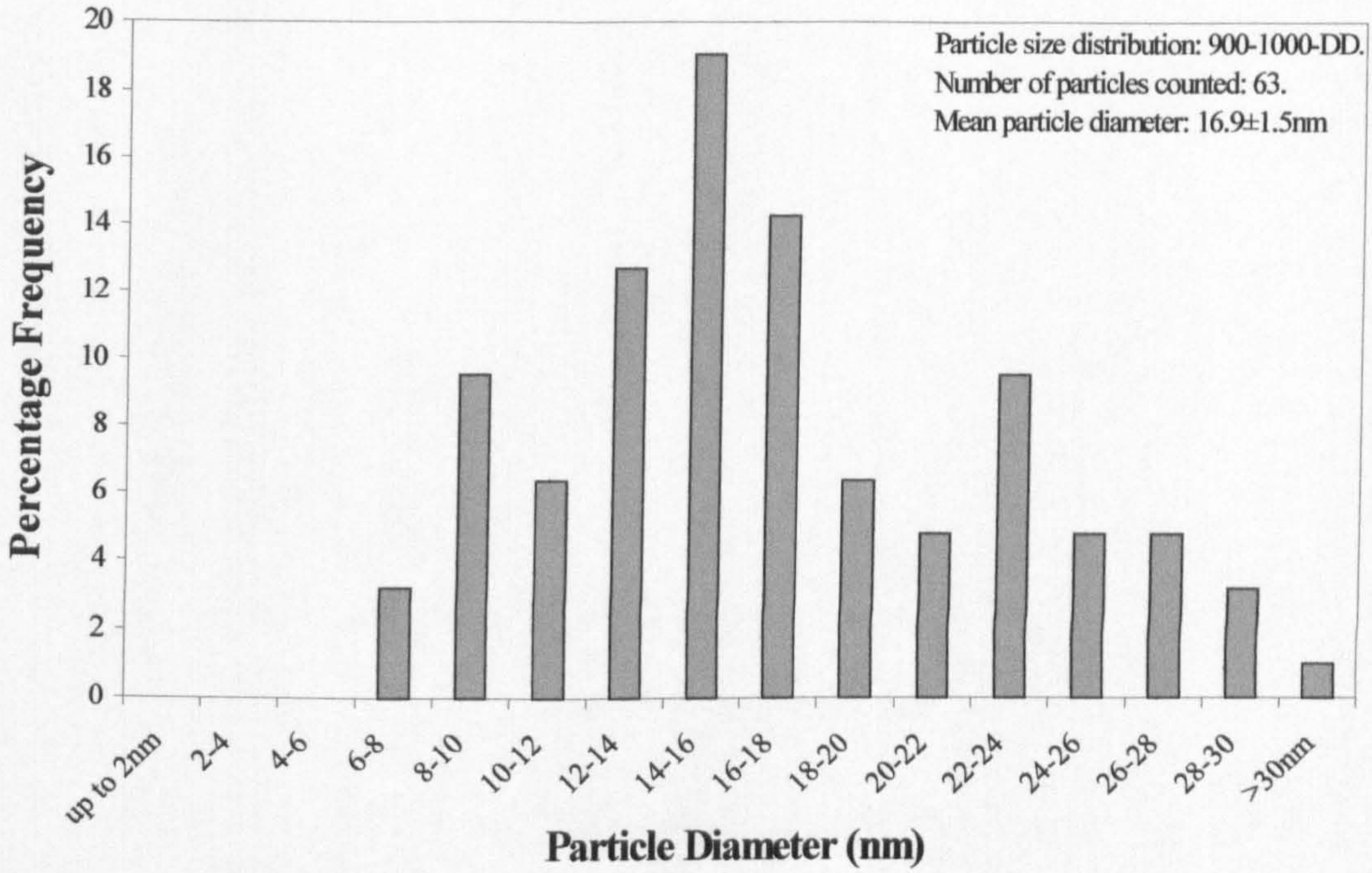

Figure 5.50: Particle size distribution measured from TEM analysis of extraction replicas for sample 900-1000-DD.

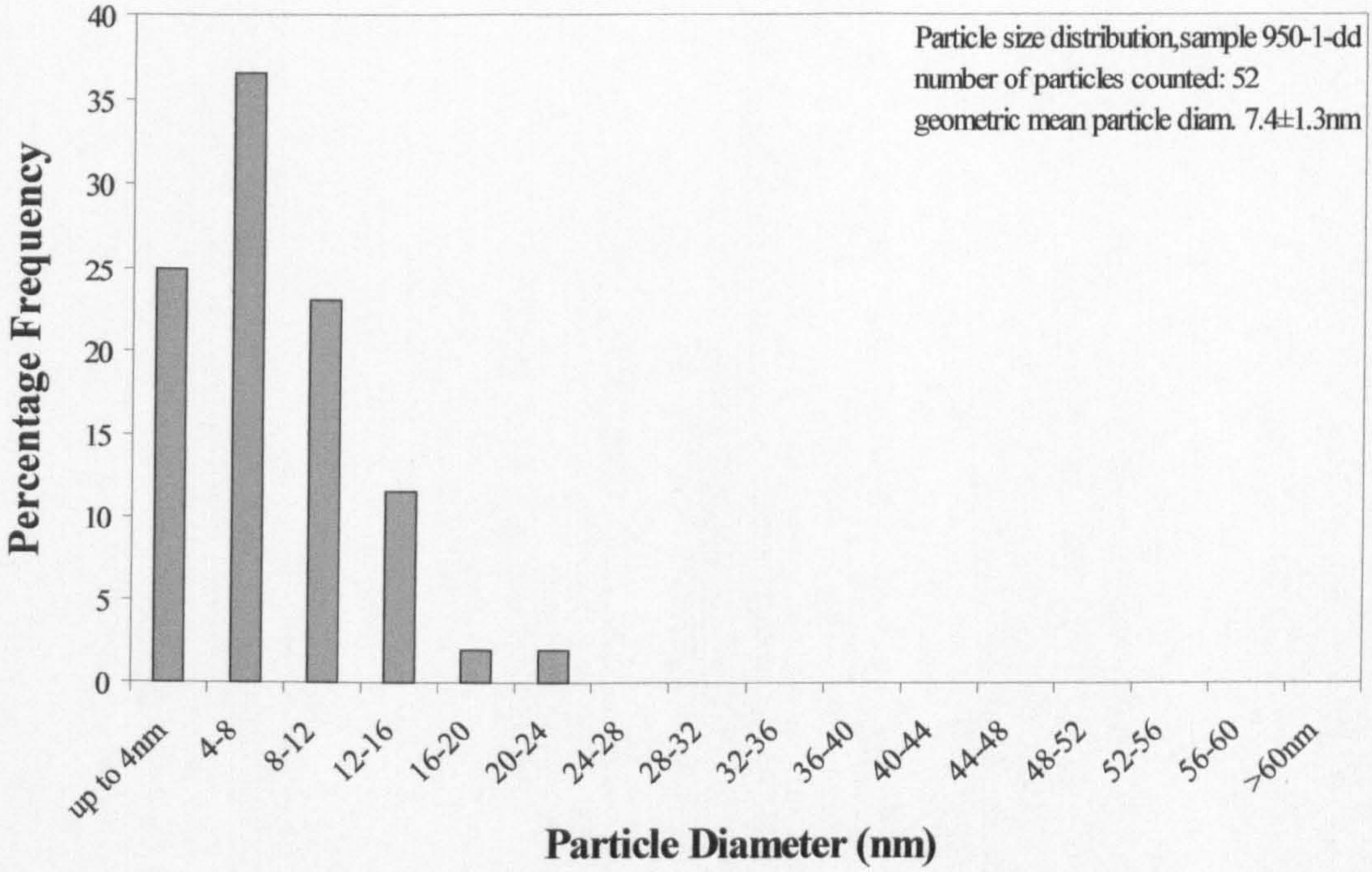

Figure 5.51: Particle size distribution measured from TEM analysis of extraction replicas for sample 950-1-DD.

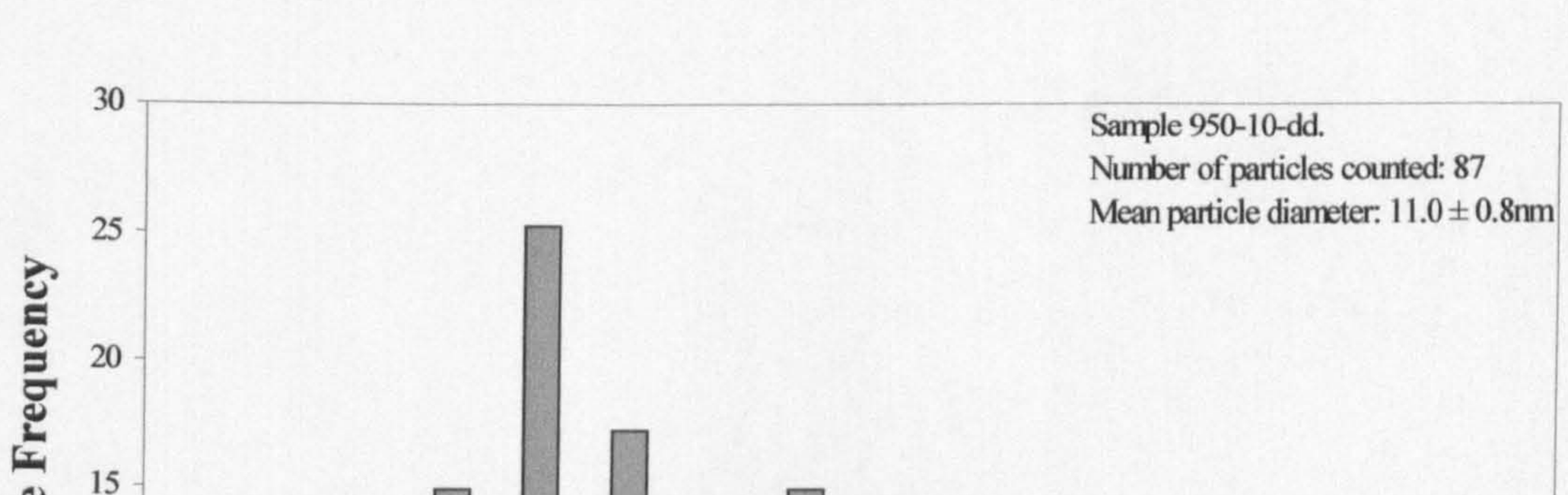

Figure 5.52: Particle size distribution measured from TEM analysis of extraction replicas for sample 950-10-DD.

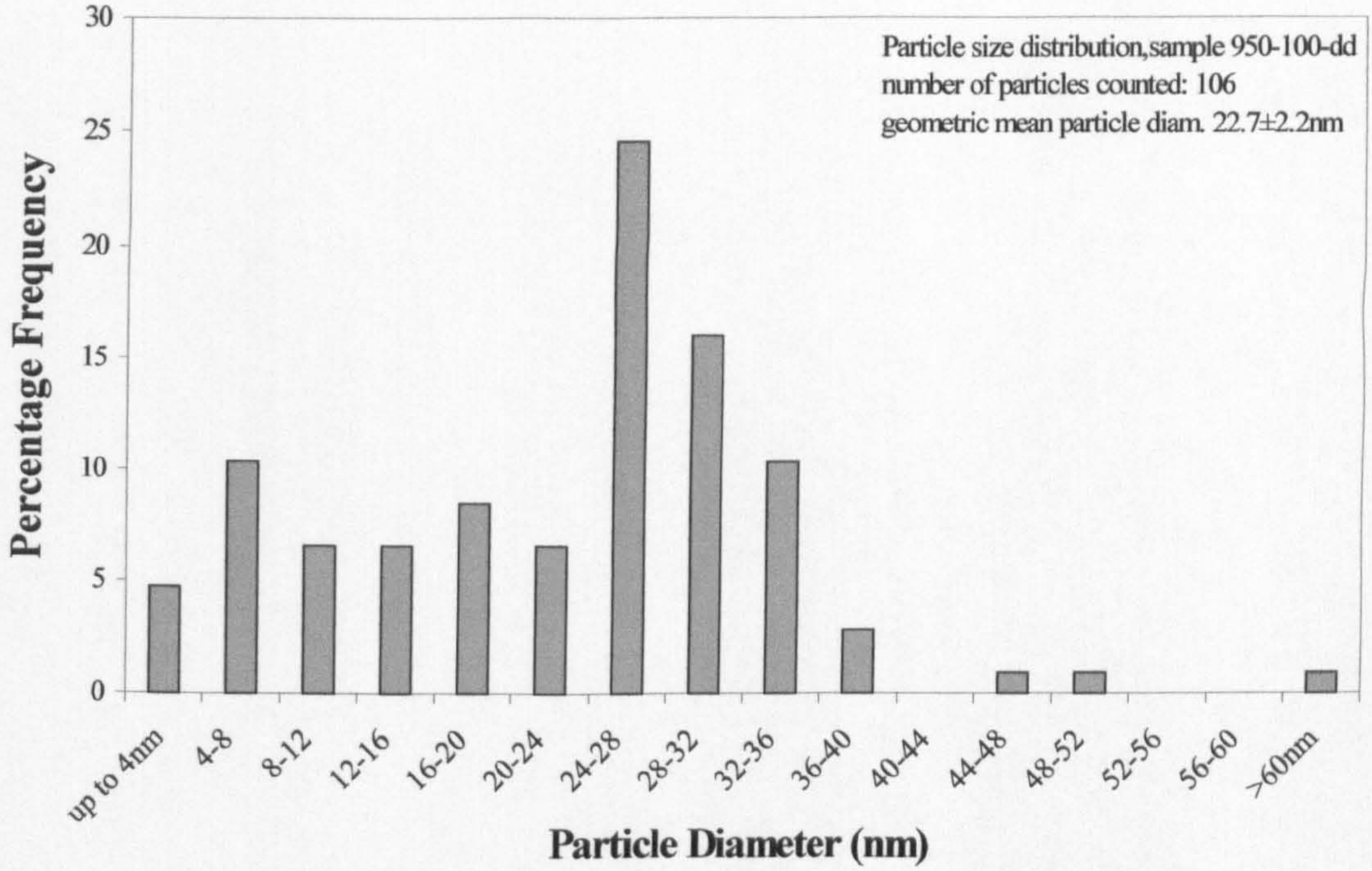

Figure 5.53: Particle size distribution measured from TEM analysis of extraction replicas for sample 950-100-DD.

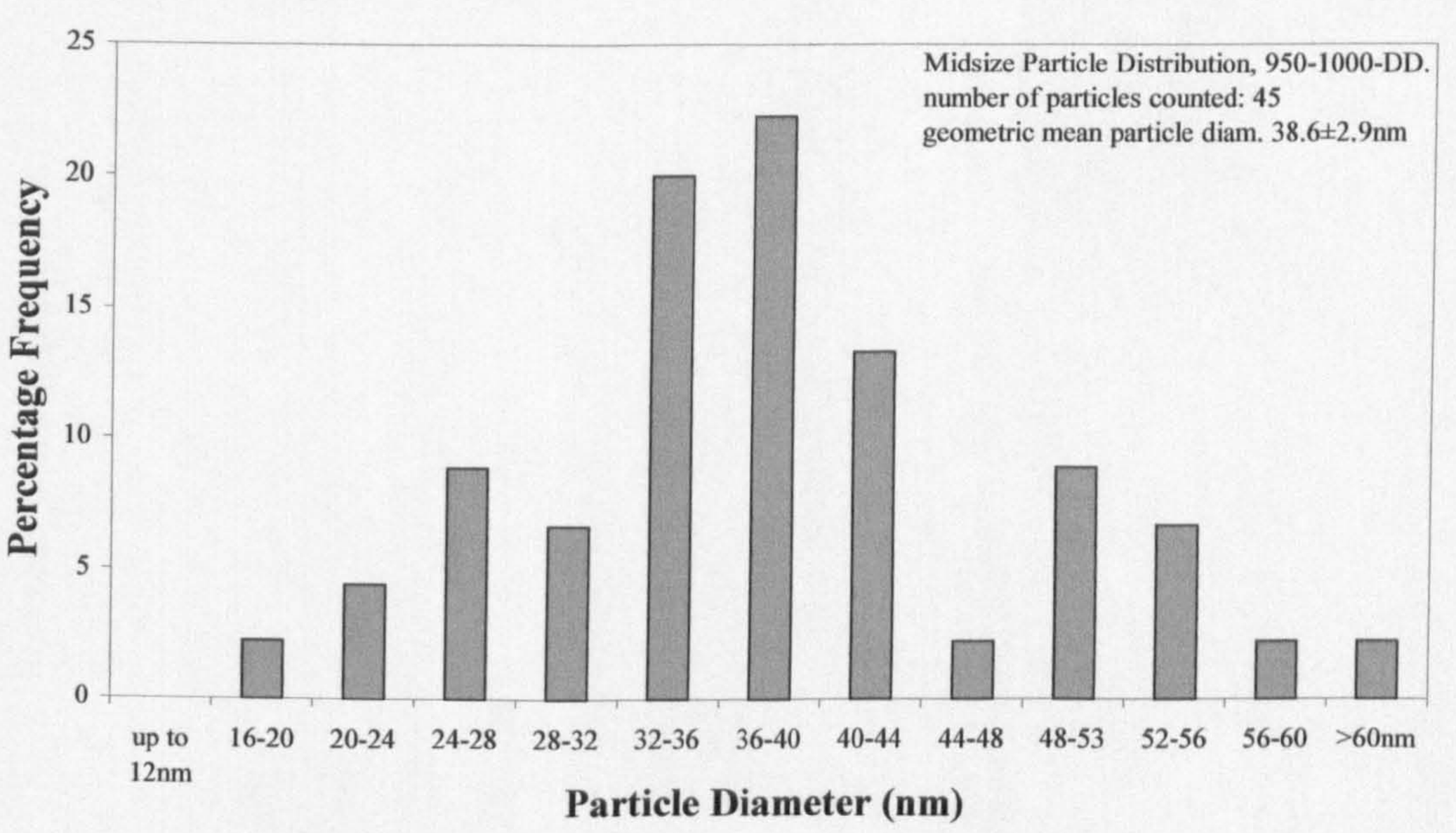

Figure 5.54: Particle size distribution measured from TEM analysis of extraction replicas for sample 950-1000-DD.

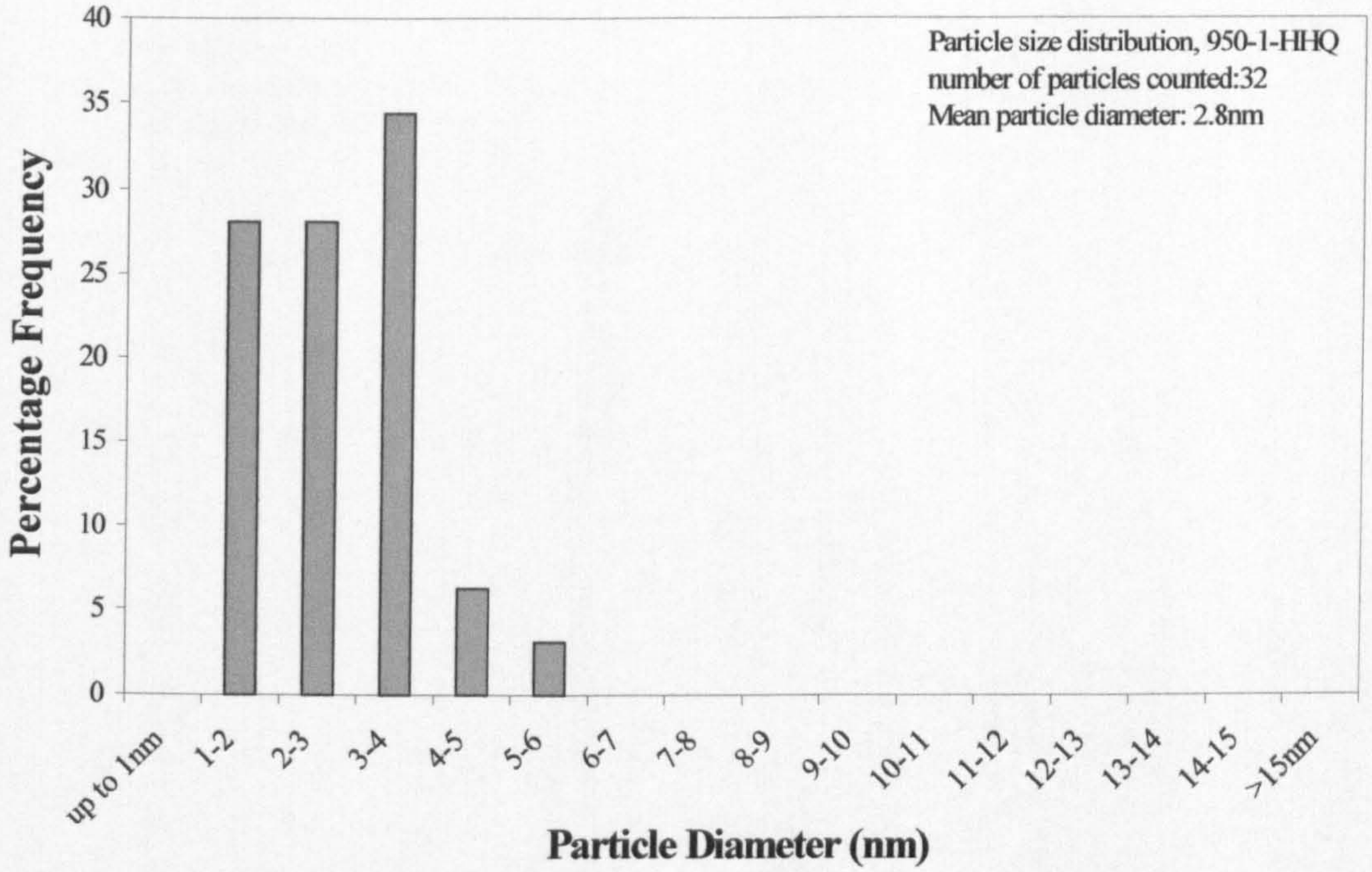

Figure 5.55: Particle size distribution measured from TEM analysis of extraction replicas for sample 950-1-HHQ.

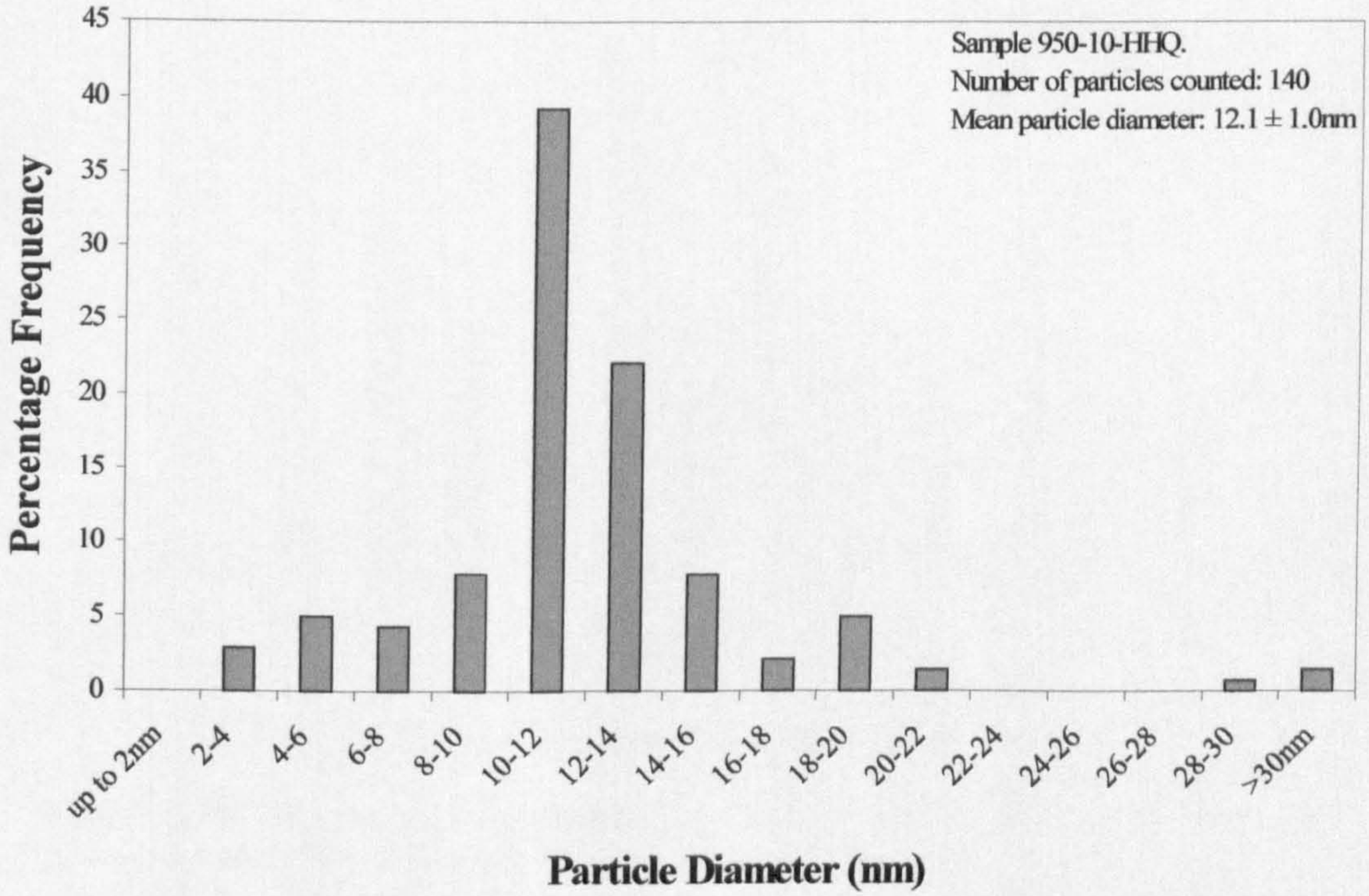

Figure 5.56: Particle size distribution measured from TEM analysis of extraction replicas for sample 950-10-HHQ.

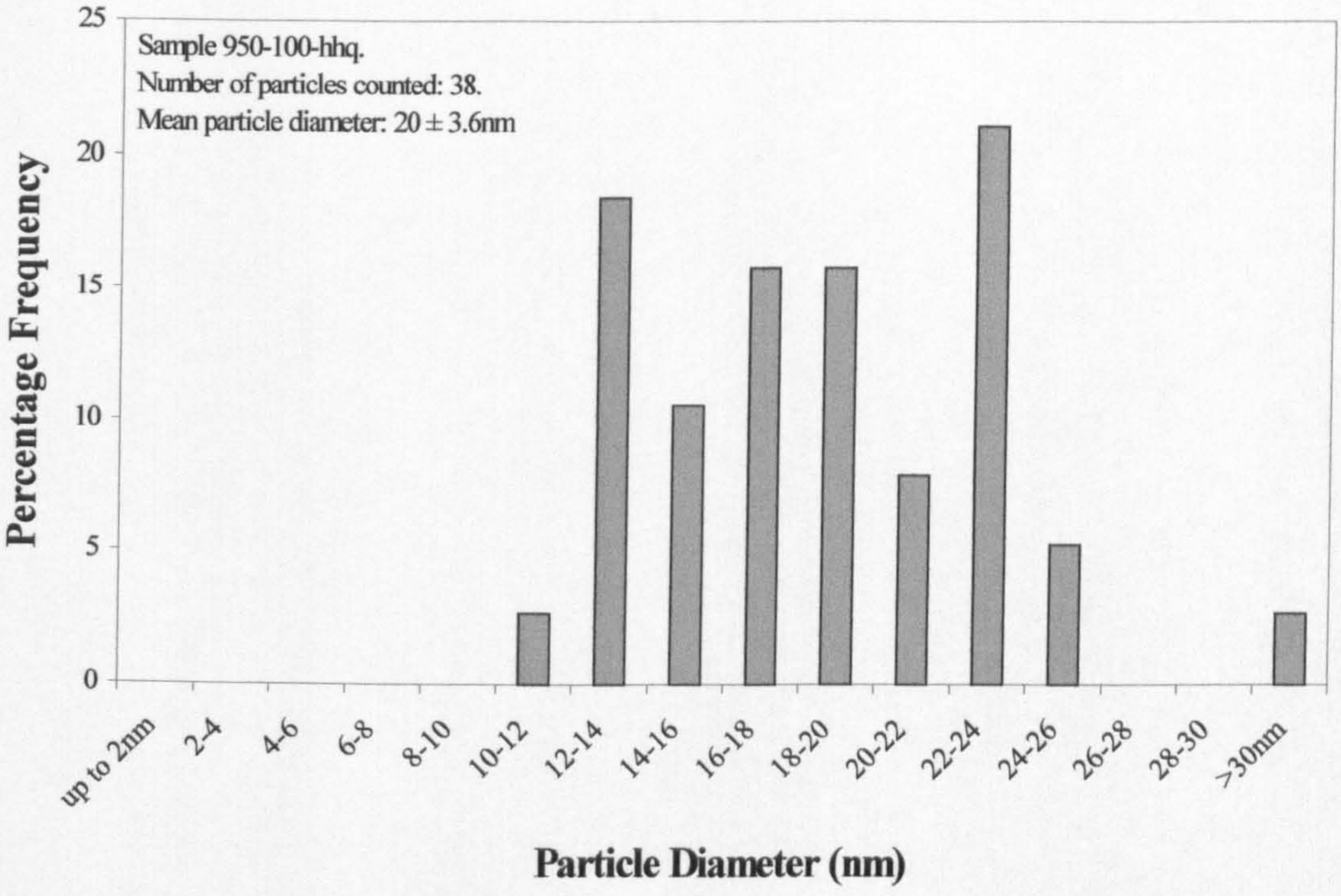

Figure 5.57: Particle size distribution measured from TEM analysis of extraction replicas for sample 950-100-HHQ.

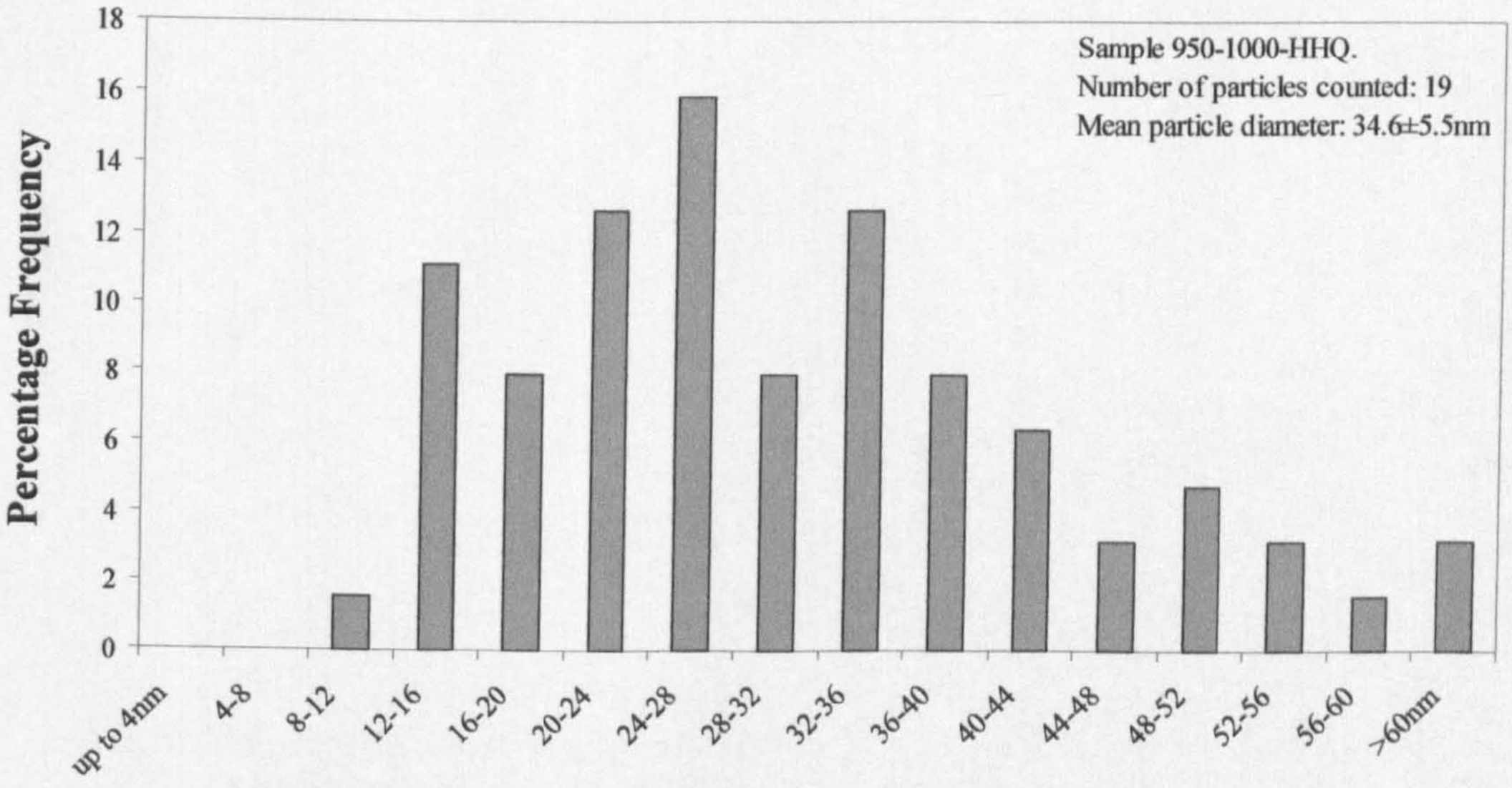

Figure 5.58: Particle size distribution measured from TEM analysis of extraction replicas for sample 950-1000-HHQ.

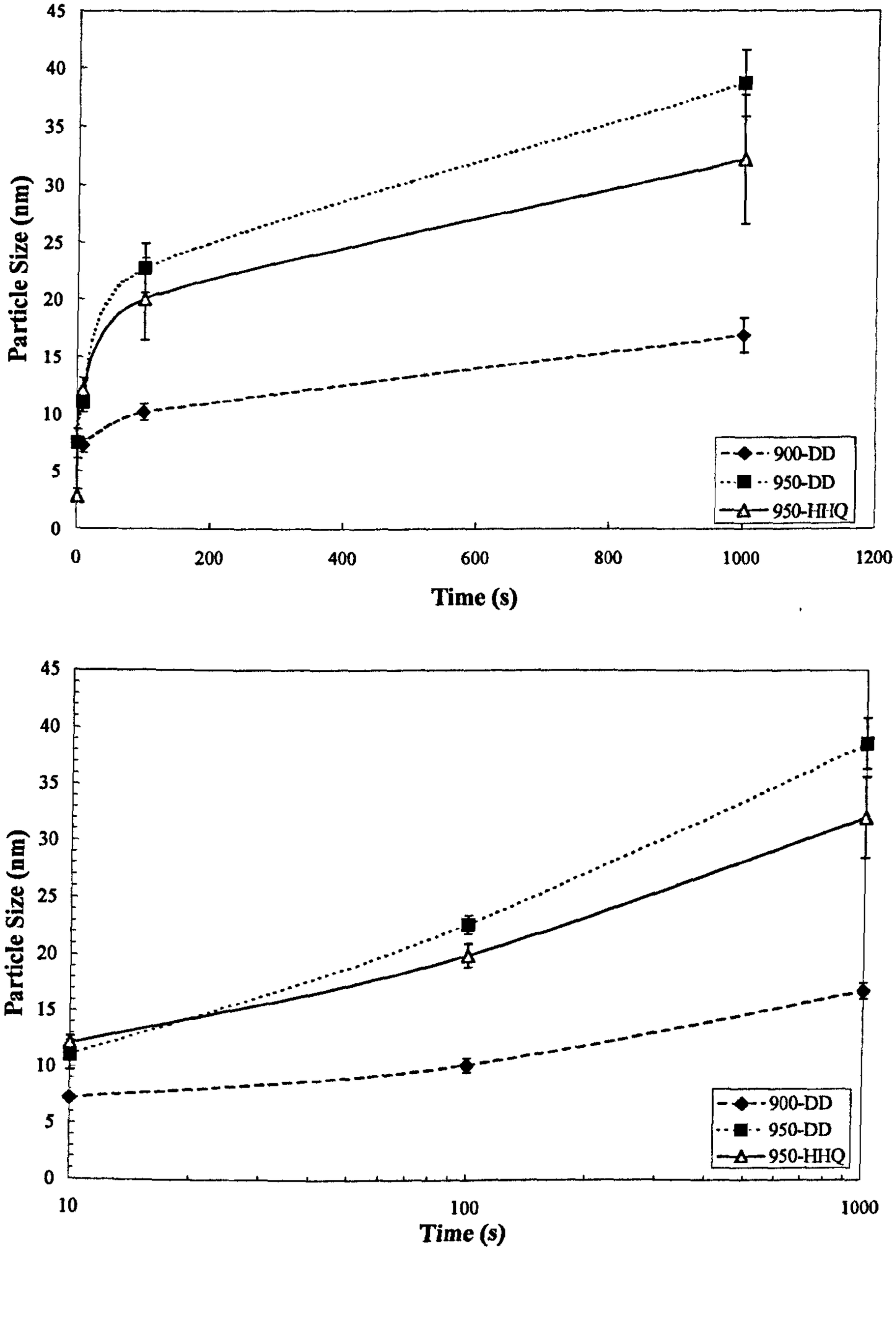

Figure 5.59: Particle coarsening measured from TEM investigations of carbon replicas of 900 and 950°C specimens, presented on a linear scale in a), and a log scale in b).

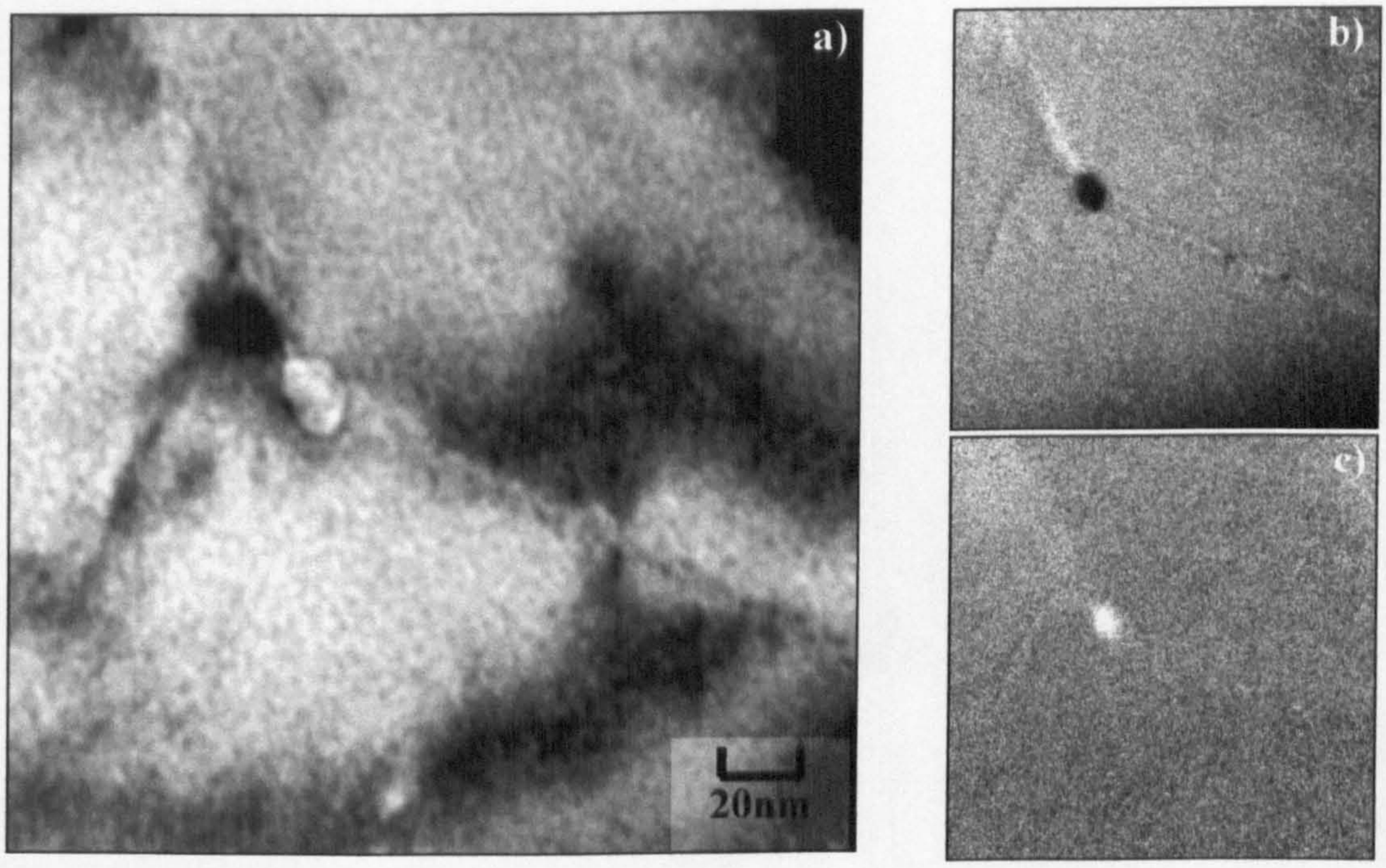

Figure 5.60: Electron spectroscopic imaging of Fe-30%Ni-Nb foils. a) Shows zero loss filtered bright field image of a double-hit specimen deformed at 950°C to a strain of ε =0.45+0.45, with a 100s interpass delay time. b) shows the iron M-edge jump ratio image, while c) shows the niobium L-edge jump ratio image.

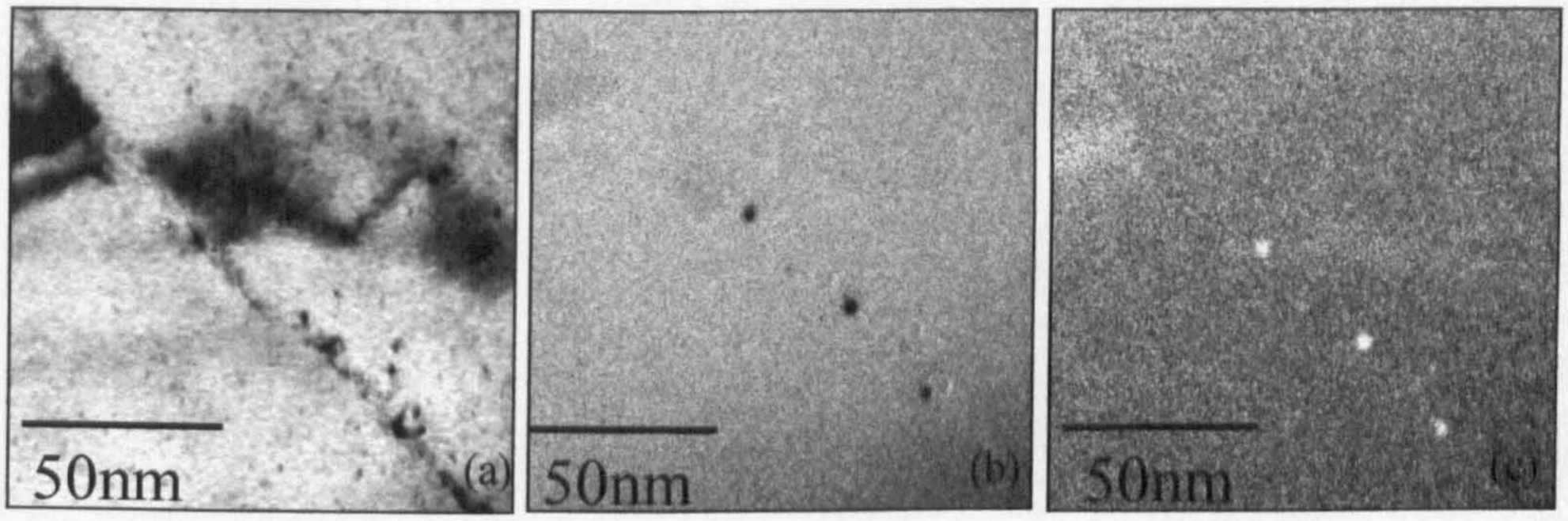

Figure 5.61: Spectroscopic imaging of deformed Fe-30Ni-Nb:(a) Zero loss filtered bright field image of grain boundary in sample prestrained to ε=0.45 at 950°C, at a strain rate of $10s^{-1}$, held for 100s, then strained to ε=0.9, quenched to room temperature; (b) Fe M-edge jump ratio image; (c) Nb L-edge jump ratio image.

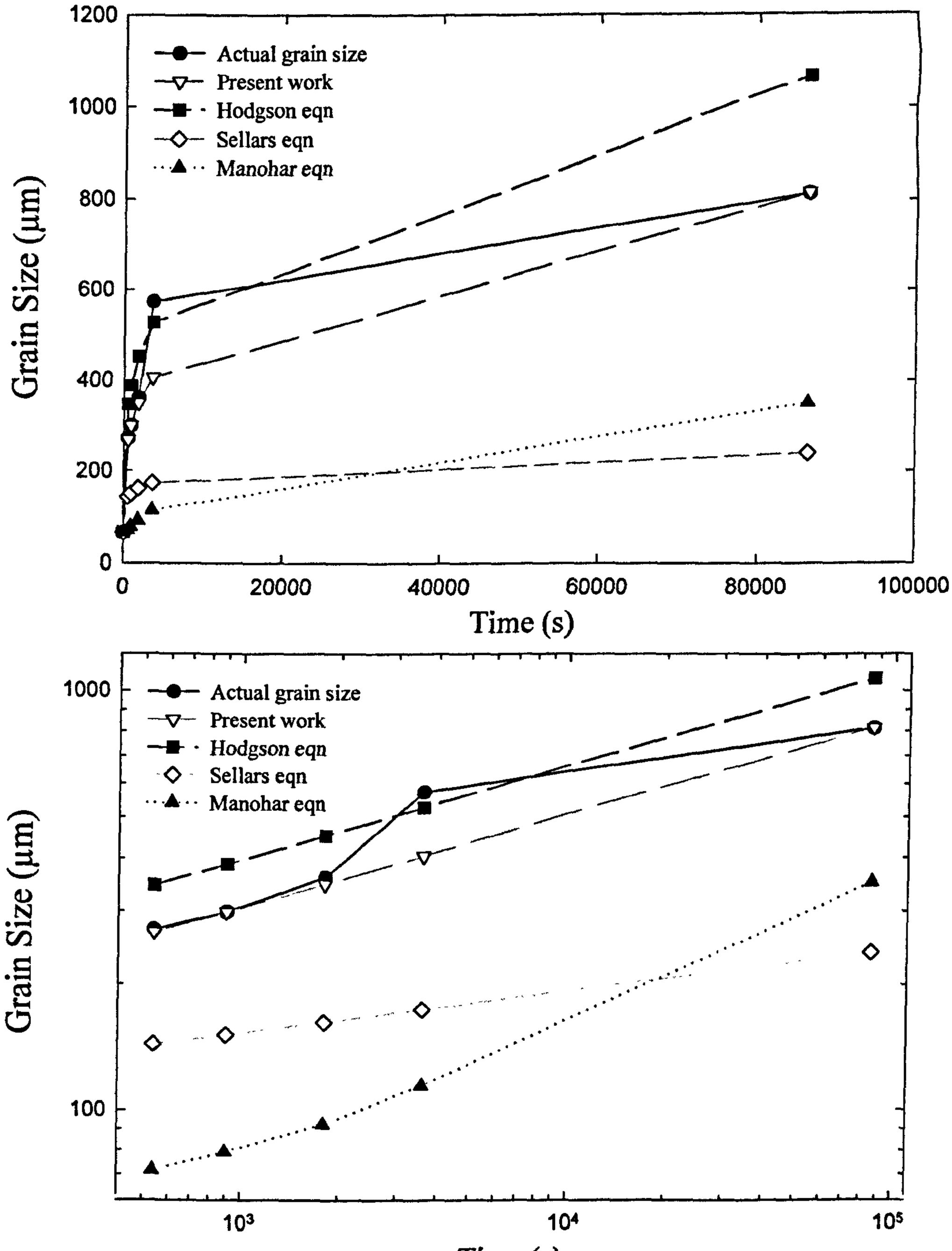

Figure 6.1: A comparison of the present grain growth equation with the values predicted by equations found in the literature. Both plots show the same data plotted on normal and logarithmic axes. The actual experimental data is also recorded. The equations from the literature were from Hodgson and Gibbs (1992), Sellars (1980), Manohar *et al.* (1996).

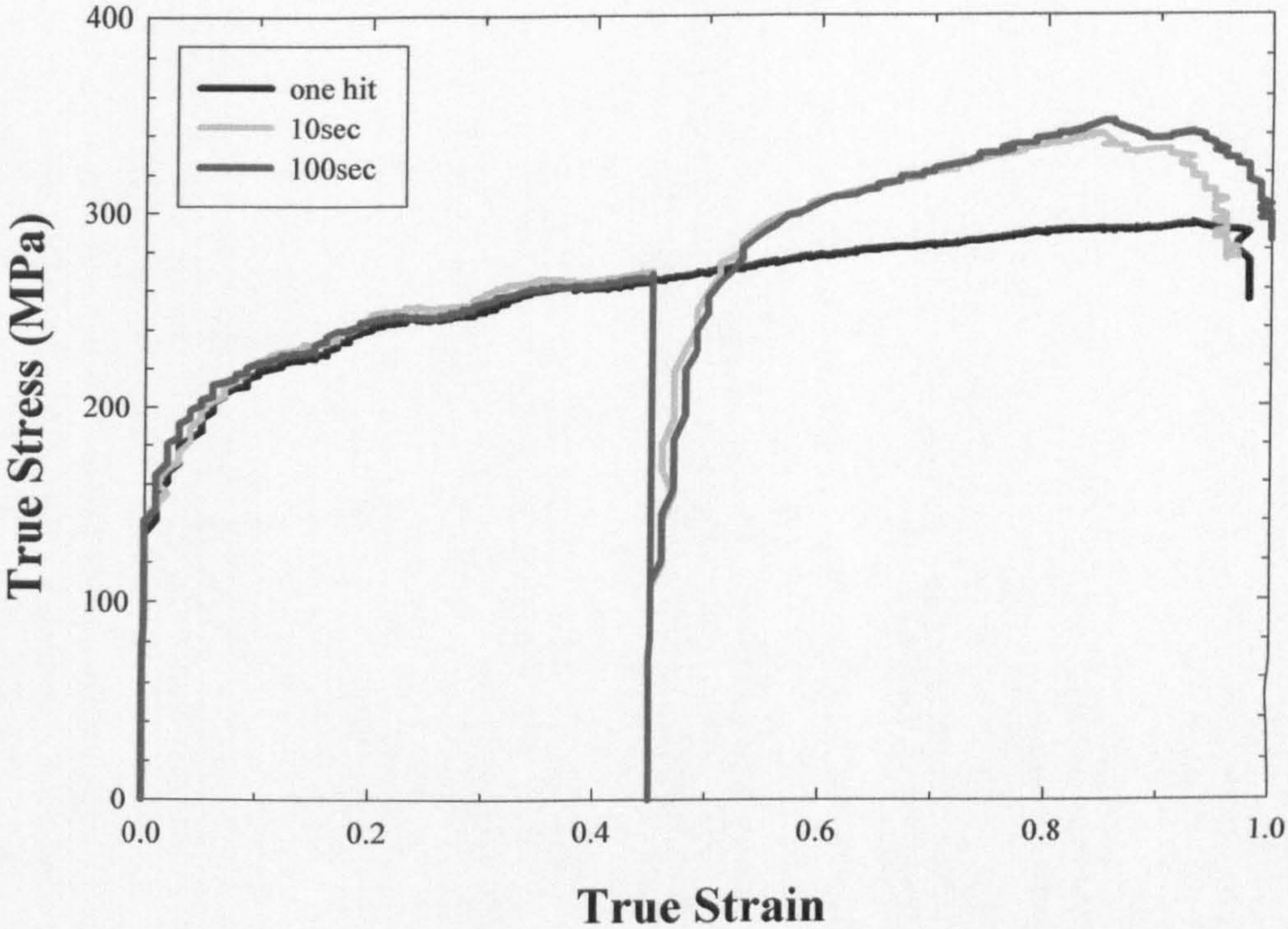

Figure 6.2: True stress-true strain curves for Fe-30%Ni-Nb at 950°C at a strain rate of $10s^{-1}$. The single deformation test was to a strain of 0.9, while the double deformation tests were pre-strained to 0.45, held for 10 or 100s, then restrained to an overall strain of 0.9.

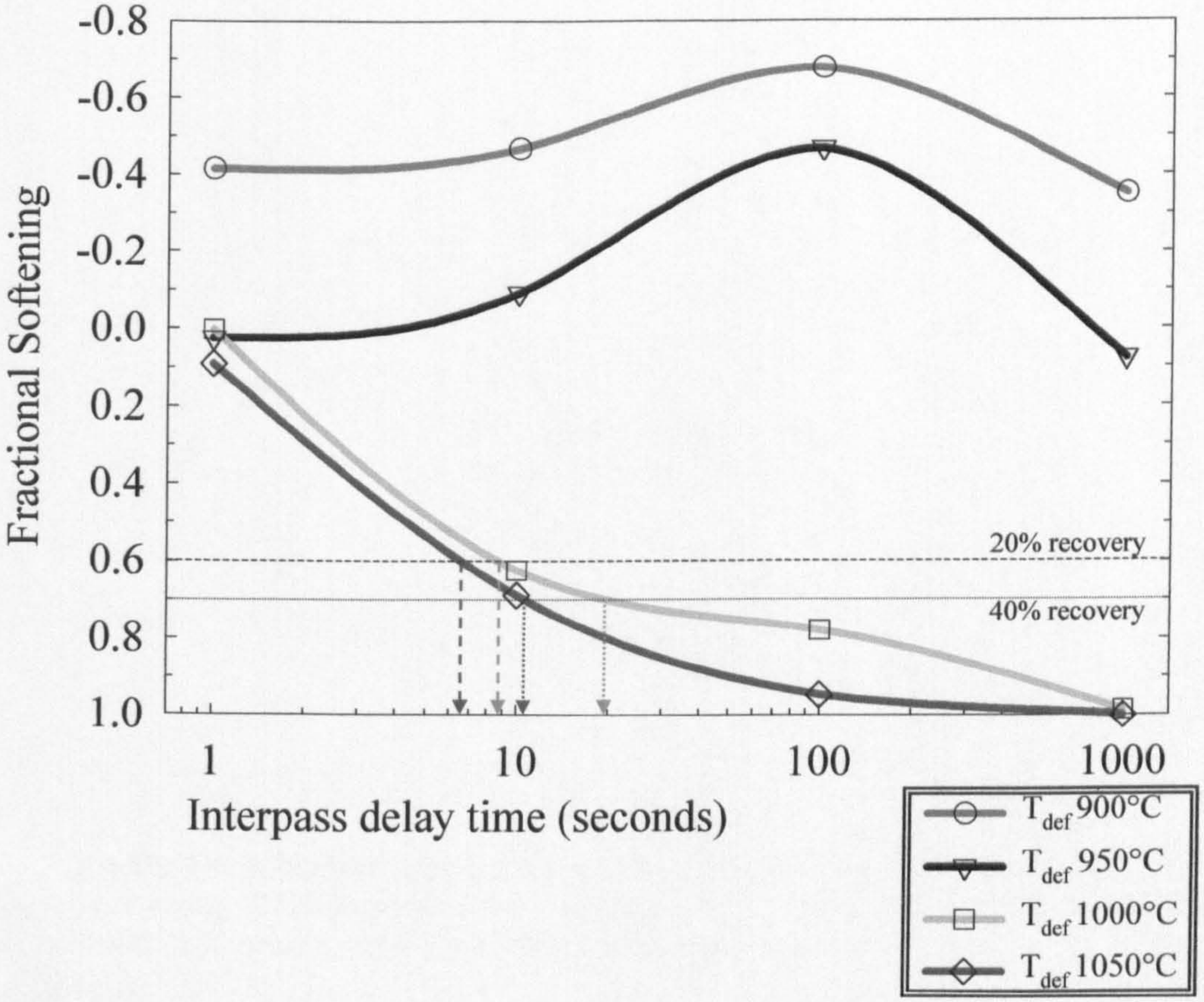

Figure 6.3: Normalised fractional softening-time plot. Dashed horizontal lines depict softening equivalent to t_{50} allowing for 20% and 40% softening by recovery (equal to 60% and 70% overall softening). The drop lines show the estimated t_{50} times for 1000°C and 1050°C.

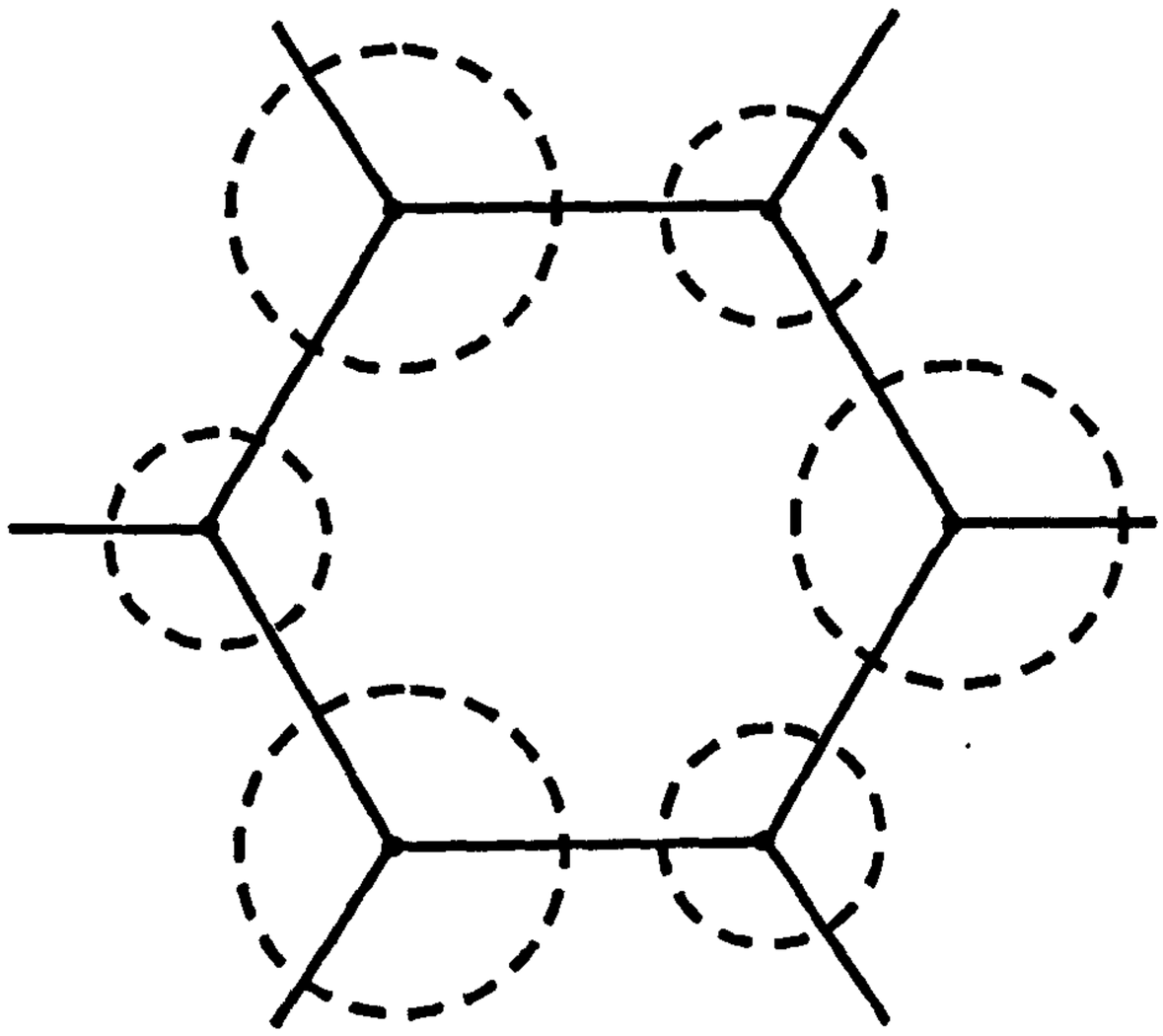

Figure 6.4: Schematic diagram showing the effect of dislocation nodes on precipitate coarsening. The dashed lines show the extent of the solute depleted regions around 1nm and 1.5nm particles on dislocation nodes [Dutta *et al.* 2001].

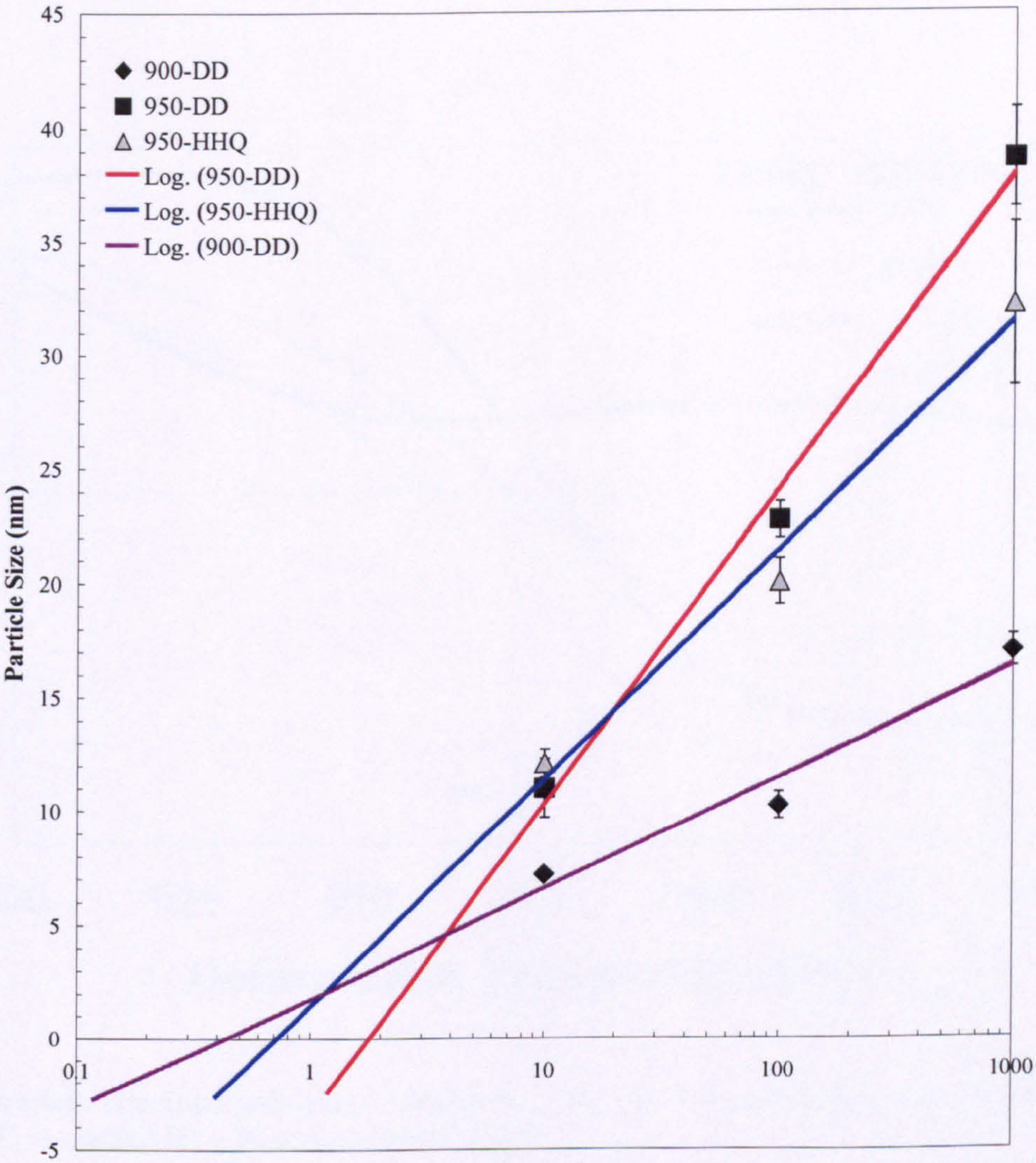

Figure 6.5: Plot showing particle size as a function of time. The best-fit line for each data set has been extrapolated back to a particle size of zero. It is assumed that this is the precipitation nucleation time.

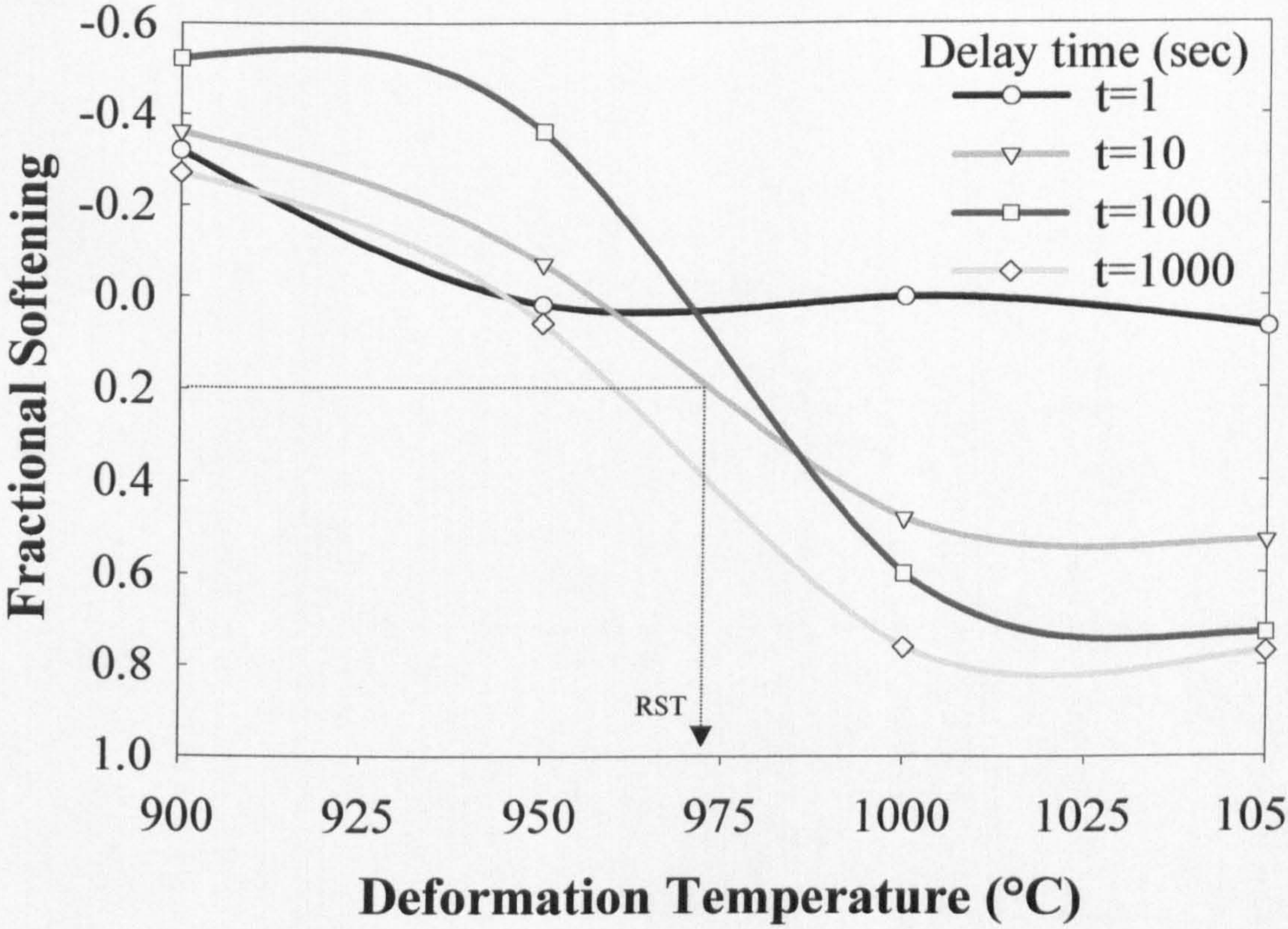

Figure 6.6: Fractional softening – temperature plot. The recrystallisation stop temperature (RST) is marked for a 10 second interpass time.

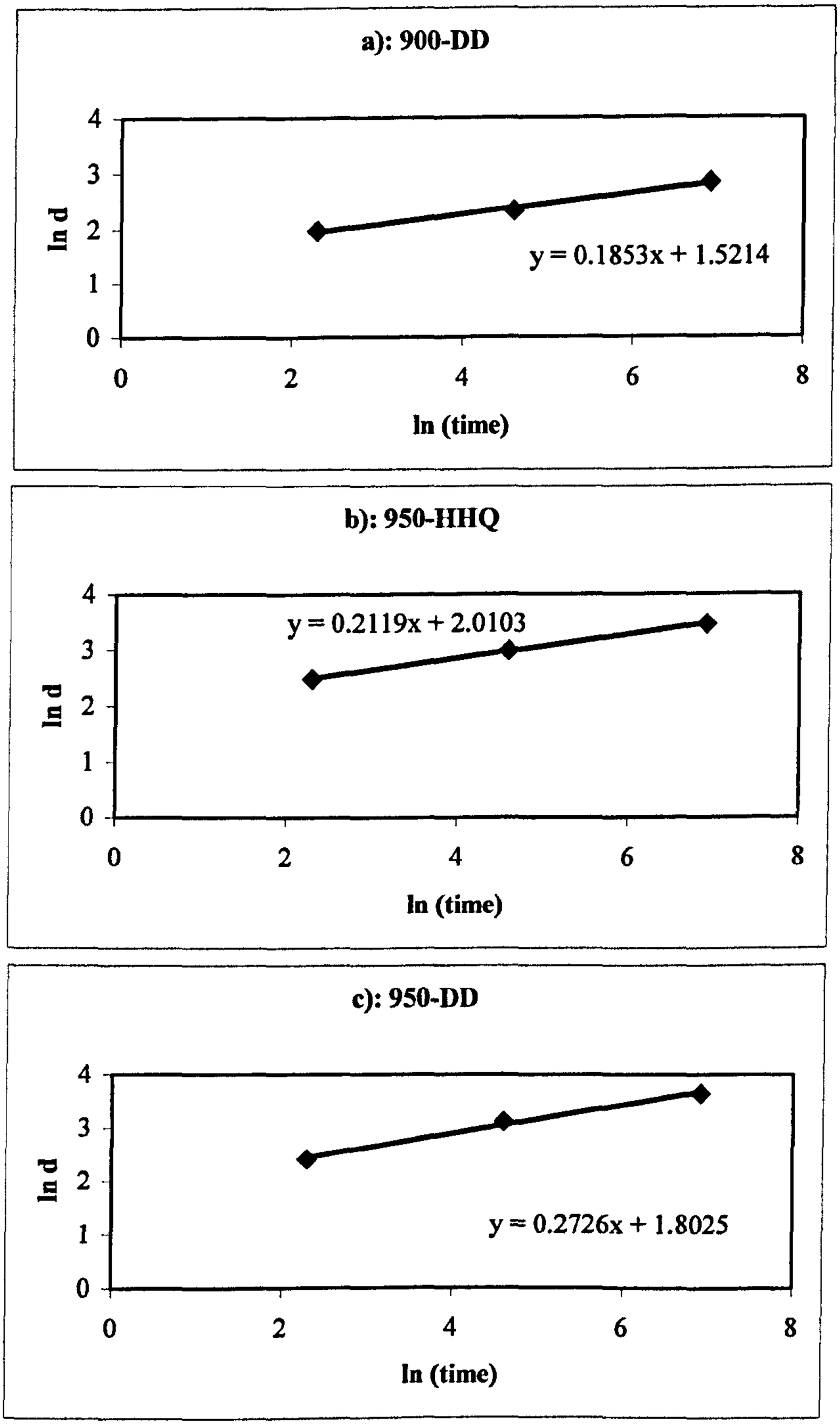

Figure 6.7:Particle coarsening plots for tests at a) 900°C double deformation, b) 950°C double deformation and c) 950°C hit-hold-quench. The equations shown are the best-fit trendlines for the data. The slope of these curve-fits gives the coarsening kinetics exponent.

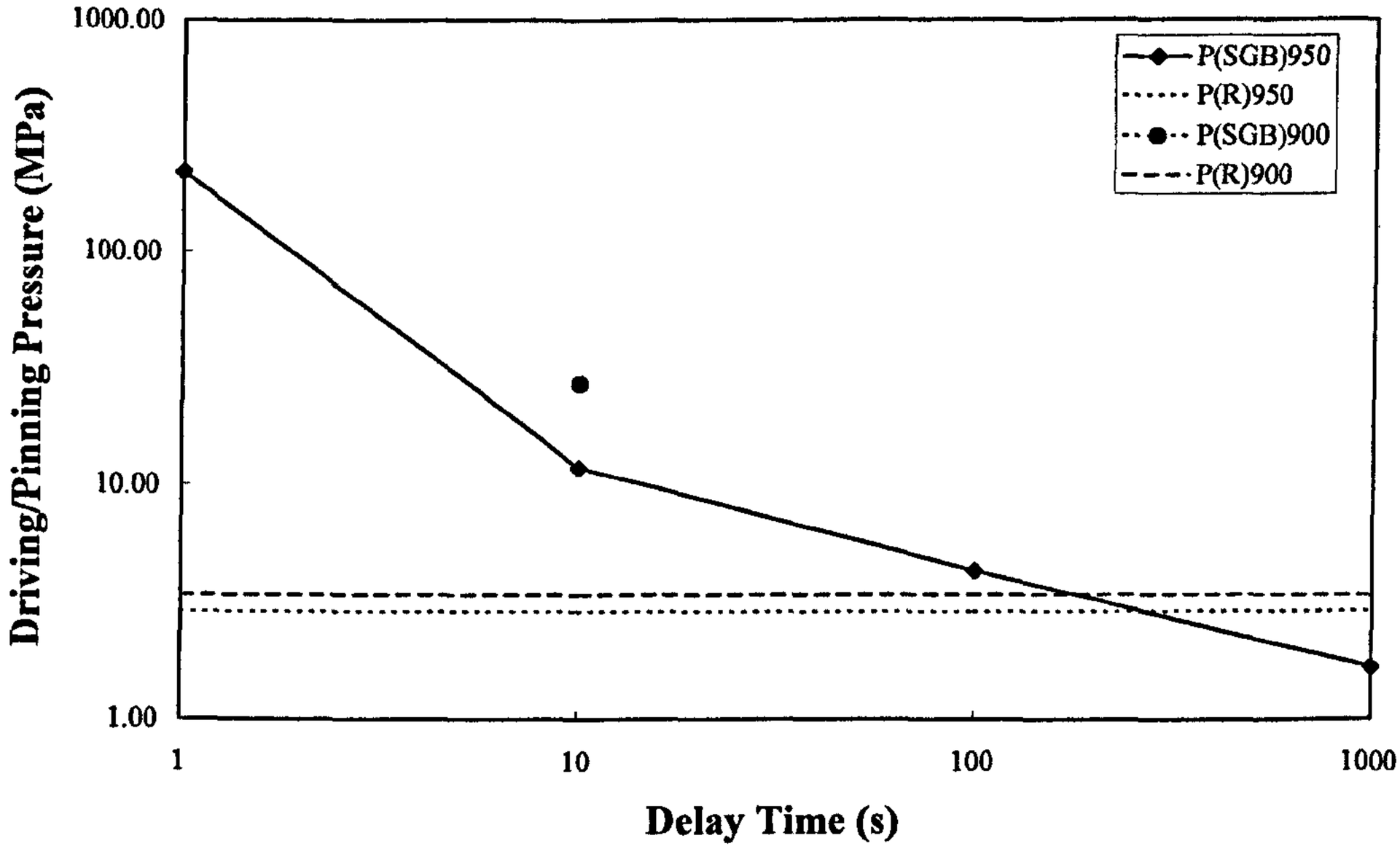

Figure 6.8: Calculated values of recrystallisation driving force (P_R) and pinning force due to fine NbC particles precipitated heterogeneously on the subgrain boundaries (P_{SGB}) at deformation temperatures of 900 and 950°C.

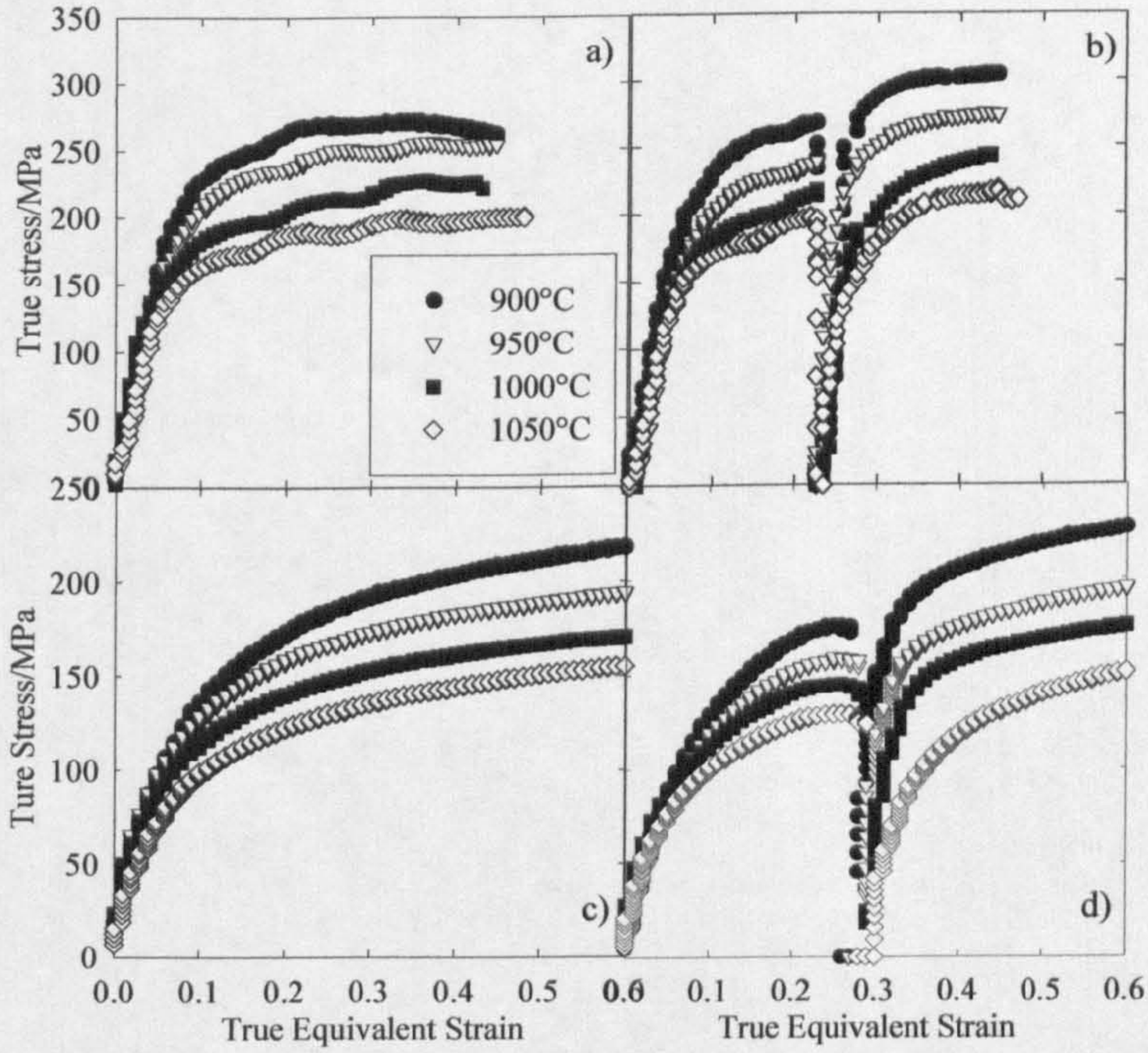

Figure 6.9: Single-hit and double-hit (10 second interpass) flow curves for microalloyed Fe-30Ni (a, b) and C-Mn-Nb steels (c, d), deformed at a strain rate of 10/s. The composition of the C-Mn-Nb steel is (in wt.%): Fe-0.08%C-1.43%Mn-0.29%Si-0.09%Nb-0.008%N.